Title:
Search for supersymmetry using a diphoton plus ETmiss final state with the ATLAS detector in proton-proton collisions at 7 TeV center-of-mass energy

Author:
Damiani, Daniel Scott

Acceptance Date:
01-01-2012

Series:
UC Santa Cruz Electronic Theses and Dissertations

Degree:
Ph.D., PhysicsUC Santa Cruz

Advisor:
Nielsen, Jason

Committee:
Schumm, Bruce, Seiden, Abraham

Permalink:
http://escholarship.org/uc/item/0wf2j4g6

Abstract:

Copyright Information:

UNIVERSITY OF CALIFORNIA
SANTA CRUZ

SEARCH FOR SUPERSYMMETRY USING A DIPHOTON PLUS $E_{\mathrm{T}}^{\mathrm{miss}}$ FINAL STATE WITH THE ATLAS DETECTOR IN PROTON-PROTON COLLISIONS AT 7 TEV CENTER-OF-MASS ENERGY

A dissertation submitted in partial satisfaction of the
requirements for the degree of

DOCTOR OF PHILOSOPHY

in

PHYSICS

by

Daniel Scott Damiani

June 2012

The Dissertation of Daniel Scott Damiani
is approved:

Professor Jason Nielsen, Chair

Professor Bruce Schumm

Professor Abraham Seiden

Dean Tyrus Miller
Vice Provost and Dean of Graduate Studies

Table of Contents

List of Figures

List of Tables

Abstract

Search for supersymmetry using a diphoton plus $E_{\mathrm{T}}^{\mathrm{miss}}$ final state with the ATLAS detector in proton-proton collisions at 7 TeV center-of-mass energy

by

Daniel Scott Damiani

A search for supersymmetry with a diphoton plus $E_{\mathrm{T}}^{\mathrm{miss}}$ final state is conducted using $4.8\,\mathrm{fb}^{-1}$ of collision data collected by the ATLAS detector at a center-of-mass energy of $\sqrt{s} = 7\,\mathrm{TeV}$ at the LHC in 2011. At least two photon candidates with $E_{\mathrm{T}} > 50\,\mathrm{GeV}$ are required, and in addition three separate signal regions are defined which are geared towards high-mass gluino or squark production decaying to a high-mass neutralino, high-mass gluino or squark production decaying to a low-mass neutralino, and direct gaugino production. Each of the three signal regions is optimized for sensitivity to the targeted scenario by tuning requirements on $E_{\mathrm{T}}^{\mathrm{miss}}$, H_{T}, and $\Delta\phi$ between the photon and the $E_{\mathrm{T}}^{\mathrm{miss}}$. The Standard Model contribution is estimated using data-driven methods, and no significant excess above Standard Model expectations is observed in any of the signal regions.

This lack of an excess is interpreted in two different flavors of gauge mediated supersymmetry breaking. In the case of general gauge mediation with a bino-like lightest neutralino, gluino masses up to 1070 GeV are excluded at 95 % CL where the lightest neutralino mass is between 50 GeV and the gluino mass. Squark masses are also excluded in this model up to 910 GeV at 95 % CL for lightest neutralino masses between 50 GeV

and the squark mass. The SPS8 benchmark slope, a minimal gauge mediation model, is also considered and Λ, which is the effective scale at which supersymmetry is broken, up to 197 TeV is excluded at 95 % CL.

To Sara Forestieri,

for being there for me always.

Acknowledgments

None of the work in this dissertation would have been possible without all of the tireless assistance and encouragement from Jason Nielsen, my advisor. In addition to Jason, I would like to thank Abe Seiden, Bruce Schumm, Alex Grillo and everyone else at SCIPP for opportunity to do this, and for putting up with me for the last five years. I am also extremely grateful for Jovan Mitrevski's and Gabriel Hare's guidance in navigating the wilds of all of ATLAS's software. I also could not have done this without Peter Manning and all of his support, both scientific and personal.

I would also like to express my gratitude to the following individuals for the indispensable parts they played in bringing together the analysis which forms this dissertation:

- Bruce Schumm for leading it all and dealing with the sometimes silly levels of bureaucracy.
- Jason Nielsen and Osamu Jinnouchi for their work on the SUSY cross section calculations.
- Martin Wildt for all his work on the limit setting.
- Jack Bradmiller-Feld and Brig Williams for all their work on the electron-to-photon fake rate and the electroweak control sample.
- Helenka Przysiezniak for all of her various work on the signal systematics.

- Maria Teresa Dova and Francisco Alonso for all of their work on the trigger and photon isolation systematics.

- Jovan Mitrevski, Helen Hayward, and Wolfgang Ehrenfeld for all their contributions to the previous two iterations of the analysis.

Last but not least, I want to thank Sara, Hal, Ben, and Peter for keeping me sane through all of this.

Part I

Theoretical Motivation

Chapter 1

Introduction

Since the creation of the first cyclotron in 1932, particle colliders have provided a wealth of information and insights into the physical world. Experimental data from particle colliders provided the experimental evidence needed to develop the current best model describing the elementary particles and their interactions, the Standard Model.

When the Large Hadron Collider (LHC), the worlds current highest energy collider located at near Geneva, Switzerland, collided protons for the first time at a center-of-mass energy of $\sqrt{s} = 7\,\text{TeV}$, a promising new frontier was opened. The unlocking of this new high energy frontier offers the potential to answer interesting new questions about the nature of physics, including the question of what, if any, new physical insights there are beyond the current Standard Model.

One avenue of new physics on which the LHC may provide some illumination is known as supersymmetry (SUSY). Supersymmetry is a proposed symmetry of the universe that relates particles of different spin. In other words it implies a symmetry

between particles with integer spin, known as bosons, and half integer spin, known as fermions. Under this scheme each fermion of the Standard Model would have a bosonic *superpartner* with all other quantum numbers and mass preserved and vice versa. Such a theory is intriguing because it poses elegant solutions to lingering questions to which the Standard Model cannot provide answers, such as "what is dark matter," and "Why are the quantum corrections to the mass of the Higgs boson so large?"

Unfortunately, there is a problem with supersymmetry. If the superpartners of the Standard Model particles truly have the same mass, why have they not been observed experimentally? This issue can be escaped if SUSY is a broken symmetry, and the superpartners therefore acquire a large mass as a result of the symmetry breaking. One interesting class of broken supersymmetry models is referred to as gauge mediated supersymmetry breaking (GMSB). In GMSB the superpotential is broken at a very high scale in a so-called hidden sector that does not couple directly to the fields of the Standard Model. However, it does posses a set of massive messenger fields that are charged under the Standard Model gauge interactions and also couple to the hidden sector. The breaking of SUSY is therefore transmitted to the superpartners via the Standard Model gauge interactions, hence the name gauge mediated supersymmetry breaking.

Gauge mediated models of SUSY breaking are interesting because they can provide phenomenologically compelling experimental signatures. In cases of SUSY where so called R-parity[1] is conserved there exists a lightest supersymmetric partner, the LSP,

[1] The conservation of R-parity also has motivations in that it suppresses the decay of the proton within a supersymmetric framework.

which is stable. In cases where the LSP is only very weakly interacting with the particles of the Standard Model, it can potentially provide a dark matter candidate, as well as provide a striking experimental signature.

This striking signature is due to the fact the incoming particles colliding in a particle collider have approximately no net momentum in the direction transverse to the axis of the collision. This implies that the particles produced in the collision have zero net transverse momentum. If an event contains an effectively non-interacting particle this will be observed in the detector as a vectoral imbalance in the transverse energy, which is referred to as missing transverse energy or $E_{\mathrm{T}}^{\mathrm{miss}}$. SUSY particles must be pair produced in a collision due to R-parity, and each SUSY particle will then decay via a cascade to an LSP, which will be observed in an event with missing transverse energy.

Collisions producing SUSY particles produced in the framework of GMSB have other distinctive signatures in addition to missing energy. The event signature is generally governed by the next-to-lightest superpartner, the NLSP, which are created as part of the SUSY cascade decay and decay to the LSP by emitting a Standard Model particle. In many flavors of GMSB this emitted particle can be a photon a very large fraction of the time. In that case such SUSY events will produce a diphoton plus $E_{\mathrm{T}}^{\mathrm{miss}}$ signature in the detector. This is a particularly exciting signature, since known Standard Model processes produce this signature very rarely.

This dissertation focuses on a search for such diphoton plus $E_{\mathrm{T}}^{\mathrm{miss}}$ signatures using $4.8\,\mathrm{fb}^{-1}$ of the $\sqrt{s} = 7\,\mathrm{TeV}$ collision data collected by the ATLAS detector at the LHC in 2011. Chapter 2 provides additional details on the Standard Model of

particle physics, while Chapter 3 highlights further details on SUSY and gauge mediated supersymmetry breaking in particular. This is followed by a description of the state of previous experimental searches for various flavors of the GMSB in Chapter 4. The next two chapters, 5 and 6, provide background info on the Large Hadron Collider and the ATLAS detector. The remaining chapters detail the aspects of the analysis procedure used in this search and the results thereof.

Chapter 2

The Standard Model

The Standard Model of particle physics is an $SU(3)_C \times SU(2)_L \times U(1)_Y$ gauge theory. At this time it provides the most complete description of observed fundamental particles and their interactions. No direct experimental evidence of physics beyond the Standard Model has been observed, however certain aspects of the theory as well indirect observations may hint at new physics at higher energies. This chapter will provide a brief description of the interactions and particles of the Standard Model as well as highlight some of the issues that may lead one to believe that new physics beyond the Standard Model is required.

2.1 Gauge Bosons

The interactions of the Standard Model are mediated by a set of spin-1 force carriers, also known as the gauge bosons. These are the photon, the $W^{\pm}$ and Z^0 bosons, and the gluons which mediate the electromagnetic, weak [1, 2, 3], and strong

forces, respectively. The weak force is interesting in that it only operates on left-handed particles and right-handed anti-particles. Also, unlike the gluon and photon, which are massless, the weak force bosons have a large mass due to the spontaneous breaking of the electroweak symmetry via the Higgs mechanism [4, 5, 6].

In electroweak gauge theory with unbroken symmetry, the B bosons carries the weak hypercharge, and the three $W^{\pm,0}$ bosons carry the weak isospin. The B^0 and W^0 weak eigenstates mix, as shown in Eq. 2.1, to form the familiar γ and Z^0 mass eigenstates

$$\begin{pmatrix} \gamma \\ Z^0 \end{pmatrix} = \begin{pmatrix} \cos\theta_W & \sin\theta_W \\ -\sin\theta_W & \cos\theta_W \end{pmatrix} \begin{pmatrix} B^0 \\ W^0 \end{pmatrix}, \tag{2.1}$$

where θ_W is the weak mixing angle. As a result of the electroweak symmetry breaking, the $W^{\pm}$ and Z^0 bosons acquires masses given by the tree-level relation in Eq. 2.2 [7].

$$m_Z^2 = \frac{m_W^2}{\cos\theta_W{}^2} \tag{2.2}$$

2.2 Higgs Boson

The Standard Model predicts the existence of one fundamental scalar (spin-0) particle, referred to as the Higgs boson. The existence of the Higgs is postulated from the apparent spontaneous breaking of the electroweak symmetry. This arises from the existence of a complex scalar doublet field with a non-zero vacuum expectation value (vev). Three of the four degrees of freedom of the Higgs field breaks the symmetry of 3 out of the four generators of the $SU(2) \times U(1)$ symmetry, and are then absorbed by

the $W^{\pm}$ and Z^0 bosons, giving the weak bosons their mass. The remaining unabsorbed component of the field is then the Higgs boson [4, 5, 6].

To date the Higgs boson is the only particle predicted by the Standard Model that has not yet been observed in an experimental setting. There are however recent observations from the LHC which appear to be consistent with those expected from the decay of the Higgs, but the statistics are not yet sufficient to claim discovery [8, 9].

2.3 Quarks and Leptons

The remaining particles in the Standard Model are the quarks and leptons, which are spin-$\frac{1}{2}$. The fermions gain their masses via a Yukawa coupling to the Higgs. Both the quarks and the leptons come in three generations. For the leptons the first generation consists of the electron (e), and the electron neutrino (ν_e). The next two generations are the muon (μ) plus its neutrino (ν_μ) and the tau (τ) plus its neutrino (ν_τ). The electron, muon, and tau have both left-handed plus right-handed states, while neutrinos, which have no mass under the Standard Model, have only left-handed states (or right-handed states for anti-neutrinos) [10]. Experimentally neutrinos have been observed to have some small mass, though there are ways this can be patched into the Standard Model without needing a light right-handed neutrino [11].

The six flavors of quark are called up (u), down (d), strange (s), charm (c), bottom (b), and top (t). Due to the nature of the strong force quarks are not observed in isolation [12], but exist in a bound states of multiple quarks. There are two general types

of quark bound states: mesons and baryons. Mesons are abound state of quark and antiquark. Three most common mesons are the pions (π^-,π^+, and π^0), which consist of combinations of up and down type quark and anti-quarks. Baryons, like protons and neutrons, are bound states of three quarks. [13].

2.4 Limitations

Although the Standard Model provides an amazingly complete explanation of current results, it has certain limitations. One issue is that 19 values, including the masses and the couplings, of the model are free parameters, and the Standard Model provides no explanation for the hierarchy of their values [14]. Two other issues for which the Standard Model does not provide a solution are the so-called hierarchy and dark matter problems, which are described in detail in Sections 2.4.1 and 2.4.2. These two issues are the most interesting from the perspective of this analysis since both can be solved by the introduction of a new symmetry of the universe. This new symmetry, which relates bosons and fermions, is known as supersymmetry and will be discussed in more detail in Chapter 3.

2.4.1 The Hierarchy Problem

The salient feature of the hierarchy is the great sensitivity of the Higgs sector to quantum corrections [15, 16, 17, 18]. The vacuum expectation value (vev) of the

Higgs field is given by Eq. 2.3.

$$\langle H \rangle = \sqrt{-m_H^2/\lambda} \tag{2.3}$$

The value of $\langle H \rangle$ is known to be approximately 246 GeV from precision electroweak measurements, which suggests that m_H^2 is on the order of $-(100\,\text{GeV})^2$ [19].

Corrections to m_H^2 arise as the result of loops involving massive particles to which the Higgs couples. A massive fermion, f, couples to Higgs by a term in the Lagrangian of $-\lambda_f H \bar{f} f$. This then provides a correction to the mass squared term of the Higgs potential, m_H^2, as shown in Eq. 2.4 [7, 19].

$$\Delta m_H^2 = -\frac{|\lambda_f|^2}{8\pi^2}\left[\Lambda_{\text{UV}}^2 + \mathcal{O}\left(\ln(\Lambda_{\text{UV}})\right) + ...\right] \tag{2.4}$$

The value Λ_{UV} is the ultraviolet momentum cutoff scale. This can be interpreted as the scale at which new physics comes in to alter the integral over the loop diagrams, which is otherwise divergent.

The terms from Eq. 2.4, which grow only logarithmically with the cutoff scale, are similar to quantum mass corrections experienced by fermions in the Standard Model [7]. The order Λ_{UV}^2 term is the problematic one and it yields, depending on the scale of Λ_{UV}, corrections orders of magnitude larger than the m_H^2 itself. If the cutoff scale is on the order of the Planck mass, then the corrections are over 30 orders of magnitude larger than m_H^2 [19]. One possible solution to this problem is to introduce a new symmetry know as supersymmetry, which will be introduced in Chapter 3.

2.4.2 Dark Matter

One very compelling hint of physics beyond the Standard Model comes from astrophysics. Current experimental evidence suggests that an additional mass on the order of five times the observed luminous matter is needed to explain observed gravitational effects, such as the rotational velocities of galaxies [20]. One possible solution is the introduction of additional massive particles that interact only weakly with the Standard Model particles. Plausible dark matter candidates can be provided by supersymmetry [21, 22].

Chapter 3

Supersymmetry

One class of theories that provide potential solutions to the issues with the Standard Model described in Section 2.4 is called supersymmetry (SUSY). Supersymmetry is an additional symmetry relating fields of different spins, in particular fermions and bosons, that arises from extending the normal Poincaré group algebra of the Standard Model with a set of anti-commutating generators

$$\left\{Q_\alpha,\, \bar{Q}_{\dot{\beta}}\right\} = 2\sigma^\mu_{\alpha\dot{\beta}} P_\mu. \tag{3.1}$$

The anti-commutation relation is shown in Eq. 3.1, where P_μ is the generator of space-time translations and σ^μ are the Pauli spin matrices. In addition the generators are spinors which carry a spin of 1/2. Versions of supersymmetry can be formulated where the number of generators, N, can be 1, 2, 4, or 8. There are difficulties with supersymmetry with $N > 1$ in four dimensions [7, 19], and only the $N = 1$ minimal supersymmetric extension to the Standard Model, called the MSSM, will be considered here.

3.1 The Minimal Supersymmetric Model

Supersymmetry postulates that all particles come in sets with one boson for every fermion. Both the mass-squared and gauge operators commute with the operators of the supersymmetry transformation implying that the boson and fermion pair share the same gauge quantum numbers and mass. Note that since all gauge quantum numbers must be equal this implies there is an individual superpartner for the left and right-handed fermions of the Standard Model. It follows that each of the Standard Model particles has a partner particle, called a superpartner, that is different in spin by 1/2 and possesses the same mass and gauge interactions [19]. If the proposed superpartners truly had the same mass and couplings as the Standard Model particles, they should have already been experimentally observed. This implies that supersymmetry must be spontaneously broken at some higher scale, which give the superpartners a mass in analogy with the $W^{\pm}$ and Z masses from electroweak symmetry breaking [7].

Introducing a new spontaneously broken symmetry while at least doubling the number of predicted particles, may somewhat unmotivated. By itself it would, if not for the elegant solutions that supersymmetry provides to some of the questions raised in Section 2.4. Potential dark matter particles can be supplied naturally in so-called *R-parity* conserving versions of supersymmetry. This concept is discussed in more depth in Section 3.3. A solution for the hierarchy problem is also provided. In analogy with Eq. 2.4, a scalar superpartner of a fermion couples to the Higgs by a term in the

Lagrangian of $-\lambda_S|H|^2|S|^2$. This leads to corrections to m_H^2 as shown in Eq.. 3.2 [19].

$$\Delta m_H^2 = \frac{\lambda_S}{16\pi^2}\left[\Lambda_{\mathrm{UV}}^2 + \mathcal{O}\left(\ln(\Lambda_{\mathrm{UV}})\right) + ...\right] \tag{3.2}$$

Notice that the correction in Eq. 3.2 has a different sign than Eq. 2.4. This is due to the fact that quantum loop corrections have different signs for bosons and fermions due to spin statistics. If both the left- and right-handed superpartner of f are considered, the quadratic terms of Λ_{UV} exactly cancel when $\lambda_S = |\lambda_f|^2$, which is always the case for unbroken supersymmetry [19]. This implies that for SUSY to solve the hierarchy problem it must be broken in such a way that this relationship is preserved. This can be achieved if supersymmetry is broken by adding explicit terms to the Lagragian like $m_{\mathrm{soft}}^2|S|^2$ for the scalar superpartners. These are referred to as *soft* terms, and give a mass of the scale of approximately m_{soft} to the superpartner, while only giving corrections to m_H^2 of the order:

$$\Delta m_H^2 = \frac{\lambda_S}{16\pi^2} m_{\mathrm{soft}}^2\left[\ln(\Lambda_{\mathrm{UV}}/m_{\mathrm{soft}}) + ...\right] \tag{3.3}$$

Such corrections imply that m_{soft} not be too much larger than the electroweak symmetry breaking scale in order for the correction to remain small compared to m_H^2 itself [7]. In the most general formulation of the MSSM the soft masses are merely free parameters. More complicated models based on more theoretically motivated mechanisms for the breaking of SUSY can impose more relationships on the soft masses. Some such models with phenomenology relevant to this analysis will be described in more detail in Section 3.4.

Particle Names	Spin-1/2	Spin-0
quarks/squark	$(u_L\ \ d_L)$, $(c_L\ \ s_L)$, $(t_L\ \ b_L)$ u_R, c_R, t_R d_R, s_R, b_R	$(\tilde{u}_L\ \ \tilde{d}_L)$, $(\tilde{c}_L\ \ \tilde{s}_L)$, $(\tilde{t}_L\ \ \tilde{b}_L)$ $\tilde{u}_R$, $\tilde{c}_R$, $\tilde{t}_R$ $\tilde{d}_R$, $\tilde{s}_R$, $\tilde{b}_R$
lepton/slepton	$(e_L\ \ \nu_e)$, $(\mu_L\ \ \nu_\mu)$, $(\tau_L\ \ \nu_\tau)$ e_R, μ_R, tau_R	$(\tilde{e}_L\ \ \tilde{\nu}_e)$, $(\tilde{\nu}_L\ \ \tilde{\nu}_\mu)$, $(\tilde{\tau}_L\ \ \tilde{\nu}_\tau)$ $\tilde{e}_R$, $\tilde{\mu}_R$, $\tilde{e}_\tau$
Particle Names	Spin-1	Spin-1/2
gluon/gluino	g	$\tilde{g}$
W boson/wino	$W^\pm\ W^0$	$\tilde{W}^\pm\ \tilde{W}^0$
B boson/bino	B^0	$\tilde{B}^0$
Particle Names	Spin-0	Spin-1/2
Higgs/higgsino	$(H_u^+\ \ H_u^0)$ $(H_d^0\ \ H_d^-)$	$(\tilde{H}_u^+\ \ \tilde{H}_u^0)$ $(\tilde{H}_d^-\ \ \tilde{H}_d^-)$
Particle Names	Spin-2	Spin-3/2
graviton/gravitino	G	$\tilde{G}$

Table 3.1: A table of the Standard Model particles and their corresponding superpartners [19]. The names, spins, and short-hand symbols used for each are also shown. Particles shown together in parentheses represent doublet states.

3.2 The Sparticles

This section lists all the sparticles of the MSSM, and describes some relevant phenomenology for the analysis. The superpartners of the Standard Model particles are nicknamed *sparticles*, which is short for supersymmetric particles. A list of all the sparticles and their Standard Model partner are show in Table 3.1.

Before discussing the sparticles themselves it must be mentioned that Higgs sector must be extended in the MSSM. If there is only one Higgs partner/superpartner pair then the electroweak force would develop a gauge anomaly [19]. This can be avoided by introducing two Higgs doublets, each with its own vacuum expectation value. The parameter $\tan(\beta)$ is the ratio of the Higgs' vacuum expectation values. The H_u doublet

couples only to up-type quarks, while the H_d couples only to the down-type quarks. The physical Higgs mass state of the Standard Model, h^0 is linear combination of H_u^0 and H_d^0.

The superpartners of the fermions are referred to as *sfermions*, which stands for the oxymoronic *scalar fermion*. The individual sfermions are named in the same fashion, such as the *stau* for the tau lepton and the *stop* for top quark. As implied by the use of the word scalar in their name, all sfermions are spin-0. Also, as was noted in Section 3.1, both the left and right-handed fermions have their own superpartners, since all superpartners share the gauge quantum and left and right-handed fermions have different gauge quantum numbers. Excepting the third generation, which mix between the left and right-hand sfermions due to large Yukawa couplings, the masses of the left and right-handed are quite degenerate [19].

The superpartners of the Standard Model gauge and Higgs bosons are designated by the suffix *-ino*. The superpartner of the gluon, the gluino, is also a mass eigenstate because there are no other colored gauginos to mix with. This is not the case for the bino, winos, or higginos. The bino, neutral wino, and the two neutral higgsinos mix to form four neutral mass eigenstates called neutralinos. The neutralinos are designated by the symbols $\tilde{\chi}_1^0$, $\tilde{\chi}_2^0$, $\tilde{\chi}_3^0$, and $\tilde{\chi}_4^0$ with the numbering to the subscript ordering them from smallest to largest mass. The charged winos and higginos mix to form mass eigenstates which are called charginos. They are designated by the symbols $\tilde{\chi}_1^\pm$ and $\tilde{\chi}_2^\pm$.

3.3 R-Parity

One potential problem with the MSSM is the presence of renormalizable coupling which violate baryon number (B) and lepton (L). Such terms are potentially disastrous as they would allow proton decay, which has not been observed experimentally. If such terms exist the couplings must be very small since the lifetime of the proton is known to be longer than 10^{31} to 10^{33} years [14]. Introducing a concept known as R-parity can mitigate this issue. If R-parity, as shown in Eq. 3.4, is conserved, then renormalizable baryon and lepton violating couplings in the MSSM are disallowed.

$$P_R = (-1)^{3(B-L)+2s} \tag{3.4}$$

The R-parity of all Standard Model particles is even, while for all sparticles it is odd. This has several interesting consequences. One is that sparticles can only be produced in pairs from collisions of Standard Model particles. The other is that the decay of sparticles must always include at least one other sparticle. The lightest supersymmetric particle (LSP) is therefore required to be stable. This is especially interesting because this LSP can provide a solution to the dark matter problem discussed in Section 2.4.2 [21, 22]. Experimentally, the LSP can be interesting because in the cases where it is non-interacting this will appear as missing energy in the detector. Only R-parity conserving versions of SUSY are further considered in this analysis.

3.4 Gauge Mediated Supersymmetry Breaking

The class of SUSY models which are of interest for this paper are known as gauge mediated supersymmetry breaking models (GMSB) [23, 24, 25, 26, 27, 28]. The general characteristic of these models is that supersymmetry is spontaneously broken in a hidden sector by a field, which does not directly couple to the MSSM, and has a non-zero vacuum expectation value of $\langle F \rangle$ which does not directly couple to the MSSM. This breaking is communicated to the MSSM by a set of massive messenger fields which couple to both the hidden sector and the MSSM via the $SU(3)_C \times SU(2)_L \times U(1)_Y$ gauge interactions [19].

One of the interesting features of all GMSB models is a light gravitino LSP. The gravitino, $\tilde{G}$, is the spin $\frac{3}{2}$ superpartner to the graviton. If SUSY is unbroken the gravitino should be massless like the graviton. The spontaneous breaking of supersymmetry gives rise to a Nambu-Goldstone fermion, called the goldstino, in an analogy to the Goldstone boson of the electroweak symmetry breaking [19]. The gravitino then acquires a mass, as shown in Eq. 3.5 [7, 19] where m_P is the Planck mass, by absorbing the goldstino. In the cases where the next-to-lightest superpartner (NLSP) is a neutralino with a large bino admixture, the NLSP will decay to the gravitino by emitting a photon.

$$m_{\tilde{G}} \sim \langle F \rangle / m_P \tag{3.5}$$

Two classes of GMSB models are examined as part of this analysis. These

two models are called minimal gauge mediation (MGM) described in Section 3.4.1 and general gauge mediation described in Section 3.4.2. Minimal gauge mediation models were explored extensively at the Tevatron [29, 30], while general gauge mediation was first explored experimentally at the LHC [31, 32]. These models are interesting from the perspective of this analysis because they can produce quite dramatic experimental signatures.

3.4.1 Minimal Gauge Mediation

In minimal gauge mediation the parameters of the MSSM are defined by five free parameters. These five parameters are m_{mes}, N_5, Λ, the sign of the higgsino mass term (μ), and $\tan(\beta)$. The parameters m_{mes} and N_5 relate to the messenger field which communicates the SUSY breaking from the hidden sector. These are mass of the messengers and number of messenger fields respectively. The parameter $\Lambda = \langle F \rangle / m_{\text{mes}}$ is the effective scale of the supersymmetry breaking [33]. A general feature of minimal gauge mediation is that $\tilde{\chi}_1^0$ is mostly bino-like in its mixing. For low values of $\tan(\beta)$ and $N_5 = 1$, the lightest neutralino is also the NLSP. Another interesting feature is that the colored sparticles are significantly more massive the neutralinos and charginos. This has the effect that production at colliders proceeds generally via electroweak channels, which is not ideal at a proton-proton collider like the LHC.

A specific minimal gauge mediation scenario was examined as part of this analysis. This model is one of a series of benchmark SUSY scenarios devised to provide common comparison points for experiments when interpreting their results in terms of

supersymmetry [33]. This benchmark point was designated SPS8. The SPS8 model has one free parameter, Λ. The other parameters are set as follows: $m_{\text{mes}} = 2\Lambda$, $N_5 = 1$, $\tan(\beta) = 15$, and $\mu > 0$. This scenario provides a neutralino NLSP with a large admixture of bino, which decays with a high branching fraction to γ plus $\tilde{G}$.

3.4.2 General Gauge Mediation

A relatively newer class of gauge mediation models is known general gauge mediation (GGM) provides even more interesting features than MGM models like SPS8. Its most interesting feature is the removal of the hierarchies between the gauginos themselves and between the gauginos and the squarks while still preserving the gravitino LSP [34, 35]. The soft masses for the particles can be set explicitly, in the same manner as is done for the plain MSSM. This opens up a potentially huge additional range of parameter space to explore, such as non bino-like neutralino NLSPs, or relatively small mass splittings between the neutralinos and the squarks/gluinos. For the purposes of this analysis the scenario with lighter colored particles and a bino-like NLSP is the most interesting.

For this analysis GGM scenarios were examined where there was a bino-like neutralino NLSP and then either light gluinos or squarks. All other particles of the MSSM were pushed to high mass in an attempt to decouple them. The purpose of this procedure was attempt to limit the relevant parameters to just the mass scale of the colored sparticle produced and the mass of the neutralino NLSP.

3.5 Experimental Signatures

This section discusses how diphoton plus $E_{\mathrm{T}}^{\mathrm{miss}}$ signatures arise in certain sets of SUSY parameter space. Due to R-parity sparticles are produced in pairs a at colliders. Both sparticles then proceed down to the NLSP via a cascade decay of sparticles. Standard Model particles are emitted at each step of the cascade, and the identity of those particles depends on the SUSY mass spectrum. In GMSB both NLSPs in the event will then decay to a Standard Model particle plus a gravitino. In cases where the NLSP is a neutralino with a high admixture of bino, the other particle in the decay will be a photon giving a potential diphoton signature in the event.

Since the gravitino does not interact on the length scale of a particle detector and collision events start with no net momentum in the transverse direction, the gravitinos can create an apparent vectoral imbalance in the transverse component of the energy detected in the event. This imbalance is referred to as missing transverse energy or $E_{\mathrm{T}}^{\mathrm{miss}}$. This combined with two photons is a fairly unique signature that occurs rarely in the Standard Model.

The particles emitted in the cascade can also assist to differentiating such events from Standard Model events. In scenarios like SPS8, the sparticles produced are generally neutralinos, charginos, or sleptons which can lead to the appearance of leptons and gauge bosons in the event. In the specific cases of the GGM explored for this analysis the produced squark or gluino must decay via emitting quarks to NLSP because of the choice of mass spectrum. This leads to a large amount energy deposited

in the detector via jets, which are the sprays of particles created in the hadronization of produced quarks.

3.6 Cross Section Calculations

All the SUSY cross section values used in this analysis are based on the standard calculation method used by the ATLAS SUSY group [36], which themselves are designed to conform to the PDF4LHC recommendations [37]. A different procedure is used for the calculations depending on the type of production process. Strong production processes including gluino-gluino and squark-squark production are the only processes types considered for the GGM scenario. The SPS8 scenario contains a wider array of contributing processes than the GGM scenario. These other production processes are calculated in a different manner than the strong production.

In the case of gluino-gluino and squark-squark production the cross sections are calculated to next-to-leading order in the strong coupling constant with the addition of next-to-leading-logarithmic soft gluon emission terms [38, 39, 40, 41, 42]. This will be referred to as NLO+NLL production cross-sections. In the case of squark-squark production, the squark mass used is obtained by averaging over the light squark masses in the first two generations, and then the resulting cross-section scaled based upon the number of light squarks. Stop and sbottom production are not considered in the production cross section calculations. The gluino-gluino and squark-squark production cases are treated independently. To deal with this the cross-sections of both scenarios

are calculated in a decoupling regime where the mass of the heavier colored sparticle type is pushed to infinity for purposes of the calculation. This is done out of a desire to decouple the resulting cross-section from any sensitivity to the particular masses of the heavier colored sparticles. All other processes are calculated at next-to-leading order (NLO) using `PROSPINO` [38].

The actual cross section calculation is derived by using the 68% CL ranges of the `CTEQ6.6` [43] (including the uncertainty on α_S which is added in quadrature), and `MSTW2008` [44] PDF error sets. The factorization and renormalization scales are also increased and decreased by a factor of two and this is used as an additional uncertainty. The appropriate uncertainties from the factorization and renormalization scale are then added in quadrature to each of the errors from the PDF sets. The extent of the envelope is then taken as the maximum range of the two PDF plus scale error sets. The nominal cross-section value used is the middle point of the envelope, and the error is taken as half the extent of the envelope. This is done to conform as closely as possible to the PDF4LHC recommendations [37]. The detailed cross-section values and errors for all the points studied in the GGM and SPS8 parameter are included in Section 8.3.

Chapter 4

Previous Results

Previous diphoton plus $E_{\mathrm{T}}^{\mathrm{miss}}$ search results from several experiments are presented in this chapter. Although the current best results from the Tevatron are presented in Section 4.1, the exclusions they provide on SUSY parameter space have been superseded by results from the LHC experiments [45, 31, 46, 32]. The current best publicly released results from the LHC experiments ATLAS and CMS are also presented in Sections 4.2 and 4.3, respectively. The current best result from CMS is based upon the full 2011 proton-proton collision dataset, and is most comparable to the analysis which is the focus of this document.

4.1 Tevatron Results

The most recent results from both the CDF and D0 experiments at the Tevatron provide constraints on the SPS8 model introduced in Section 3.4.1. The CDF result is based upon $2.6\,\mathrm{fb}^{-1}$ of proton-antiproton collisions at a center-of-mass energy

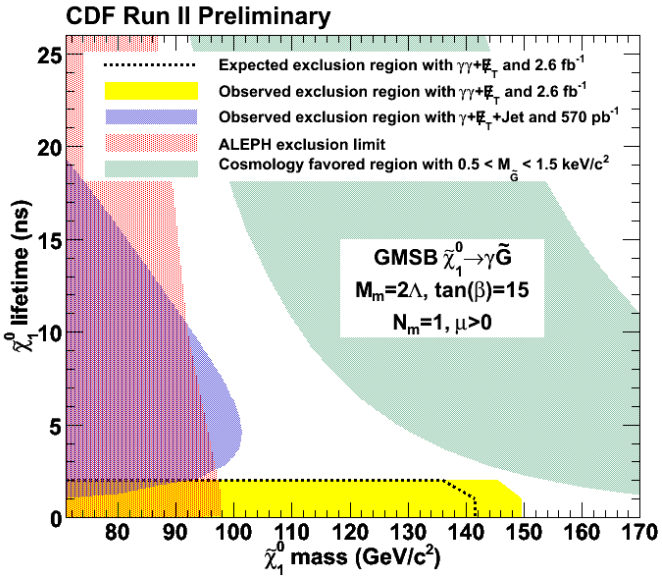

Figure 4.1: Plot of the expected and observed exclusion region in the mass and lifetime of the $\tilde{\chi}_1^0$ in SPS8 from the 2.6 fb^{-1} CDF diphoton plus $E_{\mathrm{T}}^{\mathrm{miss}}$ result [29].

of $\sqrt{s} = 1.96$ TeV [29]. The quoted expected background for the CDF diphoton search is 1.4 ± 0.4 events of which 0.9 ± 0.4 and 0.5 ± 0.2 events are due to electroweak and QCD standard model backgrounds, respectively. No events are observed in the analysis, which allows CDF to place a limit on the mass of the $\tilde{\chi}_1^0$ of 149 GeV at 95% CL for a $\tilde{\chi}_1^0$ with a lifetime of less than 2 ns. A plot of the exclusion region from CDF is shown in Fig. 4.1. This $\tilde{\chi}_1^0$ mass corresponds to a value for Λ of ~ 107 TeV for the SPS8 model.

The best constraint on the SPS8 scenario provided by a Tevatron experiment comes from D0 [30]. This result is based upon 6.3 fb^{-1} of proton-antiproton collisions at a center-of-mass energy of $\sqrt{s} = 7$ TeV. The D0 analysis requires two photons with p_{T} greater than 25 GeV in an event, and then compares the $E_{\mathrm{T}}^{\mathrm{miss}}$ distribution to that expected from standard model backgrounds. Three bins in $E_{\mathrm{T}}^{\mathrm{miss}}$ used for this

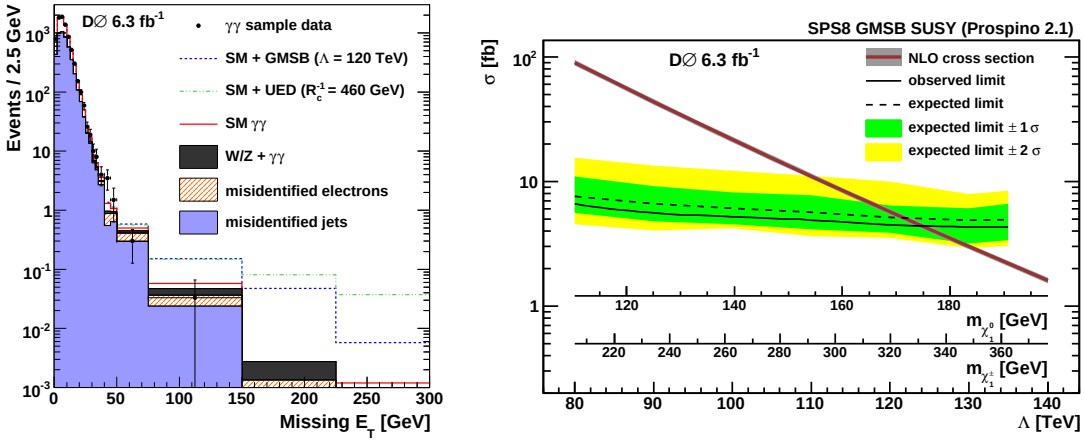

Figure 4.2: The $E_{\mathrm{T}}^{\mathrm{miss}}$ distribution of observed diphoton events overlaid with the expected backgrounds (left) and the expected and observed exclusion region in the mass of the $\tilde{\chi}_1^0$ and Λ in SPS8 (right) from the 6.3 fb^{-1} D0 diphoton plus $E_{\mathrm{T}}^{\mathrm{miss}}$ result [30].

comparison are 35–50, 50–75, and >75 GeV. The expected number of Standard Model background events for these three $E_{\mathrm{T}}^{\mathrm{miss}}$ bins are quoted as 11.9 ± 2.0, 5.0 ± 0.9, and 1.9 ± 0.4, respectively. The breakdown of these expected background contributions between electroweak and QCD sources is 2.3 ± 0.5 and 9.6 ± 1.9 for the 35–50 GeV bin, 1.5 ± 0.3 and 3.5 ± 0.8 for the 50–75 GeV bin, and 0.8 ± 0.1 and 1.9 ± 0.4 for the $E_{\mathrm{T}}^{\mathrm{miss}}$ greater than 75 GeV bin. The observed number of events for each of the three bins is 18, 3, and 1 events. This allows D0 to exclude values of Λ less than 124 TeV for the SPS8 model at 95% CL. This corresponds to a $\tilde{\chi}_1^0$ mass of ~ 175 GeV in the SPS8 model scenario. The $E_{\mathrm{T}}^{\mathrm{miss}}$ of the D0 diphoton sample and a plot of the exclusion reach in the SPS8 scenario can be seen in Fig. 4.2.

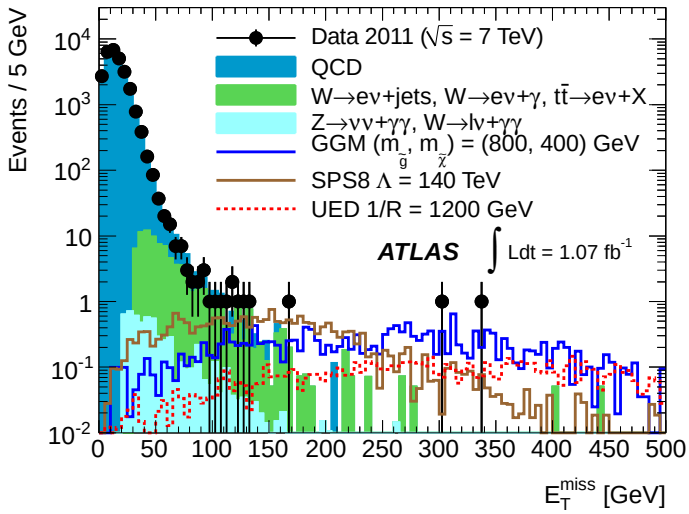

Figure 4.3: The $E_{\mathrm{T}}^{\mathrm{miss}}$ distribution of observed diphoton events overlaid with the expected Standard Model backgrounds from the $1.07\,\mathrm{fb}^{-1}$ ATLAS diphoton plus $E_{\mathrm{T}}^{\mathrm{miss}}$ result [46]. Includes an overlay of the $E_{\mathrm{T}}^{\mathrm{miss}}$ distributions of representative GGM (blue) and SPS8 (brown) points taken from Monte Carlo.

4.2 ATLAS Results

The most recent publicly released diphoton plus $E_{\mathrm{T}}^{\mathrm{miss}}$ result from the ATLAS collaboration was based upon $1.07\,\mathrm{fb}^{-1}$ of $\sqrt{s} = 7\,\mathrm{TeV}$ proton-proton collision data collected in the spring and early summer of 2011 [32]. The currently discussed analysis is an improvement upon this result, utilizing an improved analysis and the full 2011 collision data set. The result based on $1.07\,\mathrm{fb}^{-1}$ of data is itself an update of an earlier analysis of the collision data collected in 2010 [46].

A diphoton trigger was used to collect the data sample used for the analysis. The analysis required that each event have two reconstructed photon candidates with $p_{\mathrm{T}} > 25\,\mathrm{GeV}$ and $E_{\mathrm{T}}^{\mathrm{miss}} > 125\,\mathrm{GeV}$. The expected Standard Model background was broken down into three separate categories for modeling. The electroweak component,

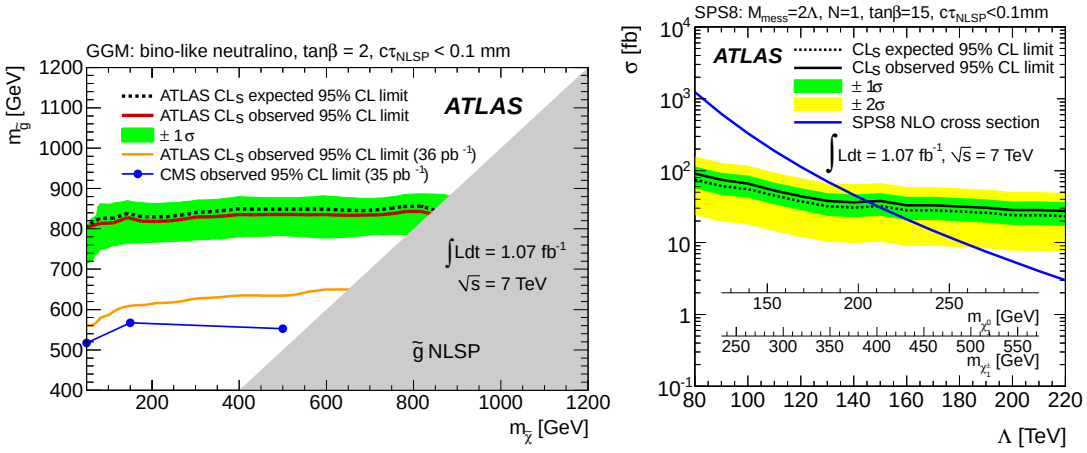

Figure 4.4: Plot of the expected and observed exclusions in the GGM (left) and SPS8 (right) theory scenarios from the 1.07 fb^{-1} ATLAS diphoton plus $E_{\mathrm{T}}^{\mathrm{miss}}$ result [46].

representing $W \to e\nu + \mathrm{X}$ and $t\bar{t}$ events, and the QCD component, representing dijet, γ+jet, and $\gamma\gamma$ events, were modeled using a data driven method. The third component, which was modeled using Monte Carlo, corresponds to $W \to \ell\nu + \gamma\gamma$ and $Z \to \nu\nu + \gamma\gamma$ events. This general methodology was also used in the analysis presented in this document (see Chapter 10 for more details on the background modeling).

The total expected background for the 1.07 fb^{-1} ATLAS result was 4.1 ± 0.6 coming from 0.8 ± 0.3 expected QCD background events, 3.1 ± 0.5 electroweak background events, and 0.23 ± 0.05 total $W \to \ell\nu + \gamma\gamma$ and $Z \to \nu\nu + \gamma\gamma$ background events. The $E_{\mathrm{T}}^{\mathrm{miss}}$ distribution of the selected diphoton events overlaid with that of the various expected background and signal contributions can been seen in Fig. 4.3. A total of 5 diphoton events with $E_{\mathrm{T}}^{\mathrm{miss}} > 125$ GeV were observed. From this limits are placed on the mass of the gluino of $m_{\tilde{g}} > 805$ GeV at 95% CL for all masses of the lightest neutralino in the range $50\,\mathrm{GeV} < m_{\tilde{\chi}_1^0} < m_{\tilde{g}}$ in the GGM theory scenario described

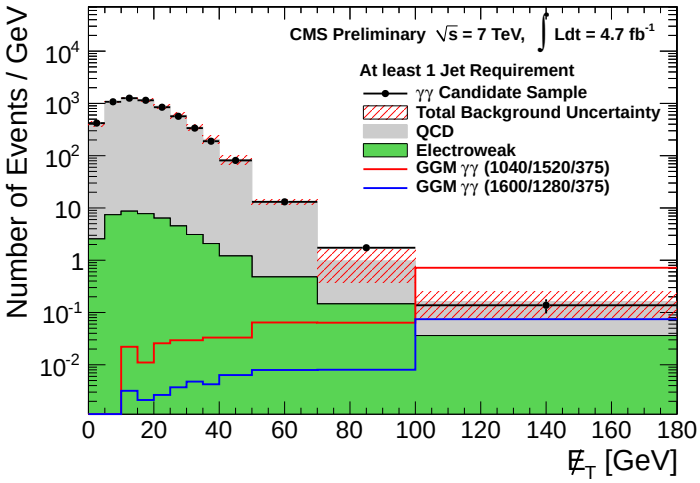

Figure 4.5: The $E_{\mathrm{T}}^{\mathrm{miss}}$ distribution of observed diphoton events overlaid with the expected Standard Model backgrounds from the $4.7\,\mathrm{fb}^{-1}$ CMS diphoton plus $E_{\mathrm{T}}^{\mathrm{miss}}$ result [31]. Includes an overlay of the $E_{\mathrm{T}}^{\mathrm{miss}}$ distributions of two representative GGM points in red and blue taken from Monte Carlo.

in Section 3.4.2. These limits on the mass of the gluino also assume a squark mass of 1.5 TeV. Limits of $\Lambda > 145\,\mathrm{TeV}$ are also placed on the SPS8 theory scenario, which corresponds to a $\tilde{\chi}_1^0$ mass of $\sim 205\,\mathrm{GeV}$. Limit plots for both the GGM and SPS8 scenarios for the $1.07\,\mathrm{fb}^{-1}$ analysis can be seen in Fig. 4.4.

4.3 CMS Results

The CMS collaboration has released, as of the time of this writing, the current best public results for a diphoton plus $E_{\mathrm{T}}^{\mathrm{miss}}$ analysis This analysis used a data sample of $4.7\,\mathrm{fb}^{-1}$ of $\sqrt{s} = 7\,\mathrm{TeV}$ proton-proton collision data collected in 2011 [31]. It was collected using a diphoton trigger. The CMS analysis requires the selection of two reconstructed photons candidates, requiring at least one photon with $p_{\mathrm{T}} > 40\,\mathrm{GeV}$ and

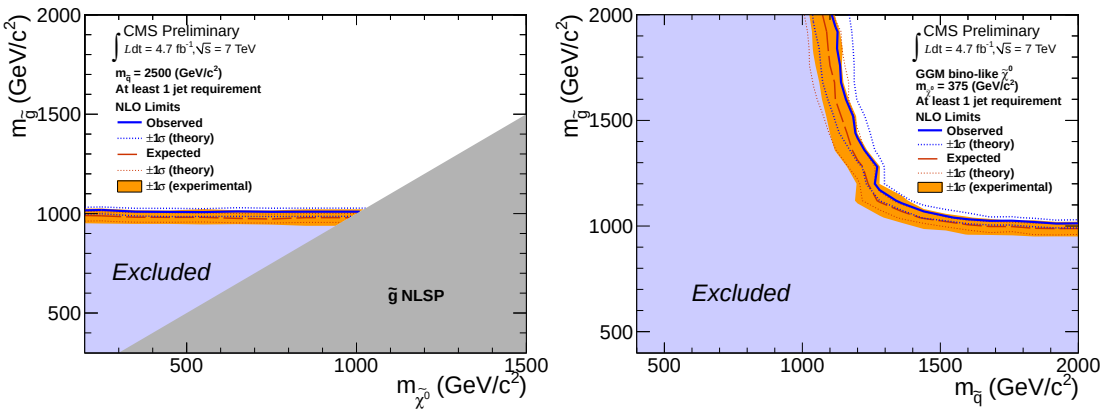

Figure 4.6: Plot of the expected and observed exclusions in a $m_{\tilde{g}}$ versus $m_{\tilde{\chi}_1^0}$ plane (left) and a $m_{\tilde{g}}$ versus $m_{\tilde{q}}$ plane (right) in the GGM theory scenario from the $4.7\,\mathrm{fb}^{-1}$ CMS diphoton plus $E_{\mathrm{T}}^{\mathrm{miss}}$ result [31]. The $m_{\tilde{g}}$ versus $m_{\tilde{q}}$ plane assumes a mass of the lightest neutralino of $m_{\tilde{\chi}_1^0} = 375\,\mathrm{GeV}$.

a second with $p_{\mathrm{T}} > 25\,\mathrm{GeV}$ in a event. Both photons are required to be in the range $|\eta| < 2.5$. Additional, the event is required to contain a reconstructed hadronic jet with $p_{\mathrm{T}} > 30\,\mathrm{GeV}$ and $|\eta| < 2.6$. Events are also required to have $E_{\mathrm{T}}^{\mathrm{miss}} > 100\,\mathrm{GeV}$.

The Standard Model backgrounds are modeled using a data-driven approach. The QCD contribution is modeled using a sample of two fake photons. The $E_{\mathrm{T}}^{\mathrm{miss}}$ shape of this fake photon sample is then normalized to the diphoton sample in the region of $E_{\mathrm{T}}^{\mathrm{miss}} < 20\,\mathrm{GeV}$ to obtain the estimated contribution at high $E_{\mathrm{T}}^{\mathrm{miss}}$. The electroweak background is modeled using an electron plus photon sample which is reweighted by an electron-to-photon fake rate. The total expected Standard Model background quoted for the CMS analysis is 13.0 ± 4.3 events. This comes from 10.1 ± 4.2 expected QCD background events and 2.9 ± 1.0 expected electroweak background events. The observed number of diphoton events with $E_{\mathrm{T}}^{\mathrm{miss}} > 100\,\mathrm{GeV}$ is 11. The $E_{\mathrm{T}}^{\mathrm{miss}}$ distribution of

diphoton events can be seen in Fig. 4.5, and exclusions in the GGM parameter space can be seen in Fig. 4.6. In the $m_{\tilde{g}}$ versus $m_{\tilde{\chi}_1^0}$ plane, which is most comparable to the ATLAS result in Section 4.2, gluino masses of less than $\sim 1\,\text{TeV}$ are excluded at 95% CL. This $m_{\tilde{g}}$ versus $m_{\tilde{\chi}_1^0}$ plane also assumes a squark mass of 2.5 TeV. From the $m_{\tilde{g}}$ versus $m_{\tilde{q}}$, squark masses of less than $\sim 1.1\,\text{TeV}$ have been excluded at 95% for all gluino masses less than 2 TeV.

Part II

Experimental Setup

Chapter 5

The Large Hadron Collider

Particle collisions can provide an excellent probe of fundamental physics. These collisions must occur at high energies in order to produce the Higgs boson or other massive particles, such as those predicted by SUSY, at an appreciable rate. Particle accelerators are used to accelerate and then collide particles creating a myriad of additional particles, which can then be studied. The collisions used in this dissertation were generated at the Large Hadron Collider (LHC) at $\sqrt{s} = 7\,\text{TeV}$ in 2011. This accelerator is located at CERN, near Geneva, Switzerland.

The CERN Council granted initial approval of the LHC project in December of 1994 [47]. The 26.7 km circumference tunnel of the LEP accelerator is used to house the LHC beam-line. Unlike LEP, which was an electron-positron collider, the LHC collides protons. Protons lose less energy losses due to synchrotron radiation than electrons in a curved accelerator. Due to the smaller energy loss, protons can be more easily accelerated to high energies. First collisions at the LHC were achieved in November

2009 with collisions at a center-of-mass energy of $\sqrt{s} = 7\,\text{TeV}$ coming later on March 30th 2010 [48].

5.1 LHC Design

The LHC consists of two beams of protons traveling around the LHC storage ring in opposite directions. The protons in the beams are confined in bunches with a minimum spacing of 25 ns. There are a total of 3564 bunch spaces per beam in the LHC ring. Not all bunches can be filled with protons due to the manner in which the LHC is filled and the need to preserve a gap of $3\,\mu$s of empty bunches for aborting the beam. The filling of the LHC results in trains of 72 consecutive filled bunches, separated from the next train by a gap of 12 bunches. Nominally 2808 out of the 3564 bunches per beam can be filled with protons at one time. The designed beam intensity is 1.15×10^{11} protons per bunch, which gives a design peak luminosity of $L = 10^{34}\text{cm}^{-2}\text{s}^{-1}$ in the nominal fill configuration. Higher intensity bunches up to 1.7×10^{11} protons per bunch are possible, and would increase the achievable luminosity to $L = 2.3 \times 10^{34}\text{cm}^{-2}\text{s}^{-1}$ [47].

The protons are injected into the LHC from the injector chain at a proton energy of 450 GeV, and then must be accelerated up to the desired energy. For more info on the accelerators making up the injector chain, please see Section 5.1.1. The design center-of-mass energy for proton-proton collisions at the LHC is $\sqrt{s} = 14\,\text{TeV}$, implying a proton energy of 7 TeV in each beam. To reach this energy a peak field of 8.33 T must be reached in the dipole magnets. This energy has not yet been achieved

with the LHC due to an issue with safely achieving the needed currents in the magnet system. For details on this please see Section 5.1.3.

5.1.1 Injector Chain

The protons are accelerated to progressively higher energies in four different machines before injection into the LHC storage ring. The first step is the Linac2 which accelerates the protons to 50 MeV. This is followed by the Proton Synchrotron Booster, the Proton Synchrotron, and the Super Proton Synchrotron (SPS), which accelerate the protons to 1.4 GeV, 25 GeV, and 450 GeV respectively. From the SPS the beams are injected into the LHC ring via two ∼2.5 km long transfer lines [47].

5.1.2 The LHC Ring and Experiments

The LHC ring is divided into 8 octants, as can be seen in Fig. 5.1. Each octant consists of one straight and one arced section. The straight sections, which are ∼528 m in length, are where the beam crossings for the experiments and other utility operations like cleaning and dumping the beam occur [47]. In four of these straight sections, the beams cross to provide collisions in interaction regions designated IR1, IR2, IR5, and IR8. The kicker magnets for dumping the beams are located in IR6. IR3 and IR7 are used primarily for cleaning of the beam, and IR4 houses the RF system for accelerating the protons, as well as the feedback system for tuning beam parameters [47].

The four main experimental detectors are located at the four interaction regions. Two of the experiments, ATLAS at IR1 and CMS at IR5, are general purpose

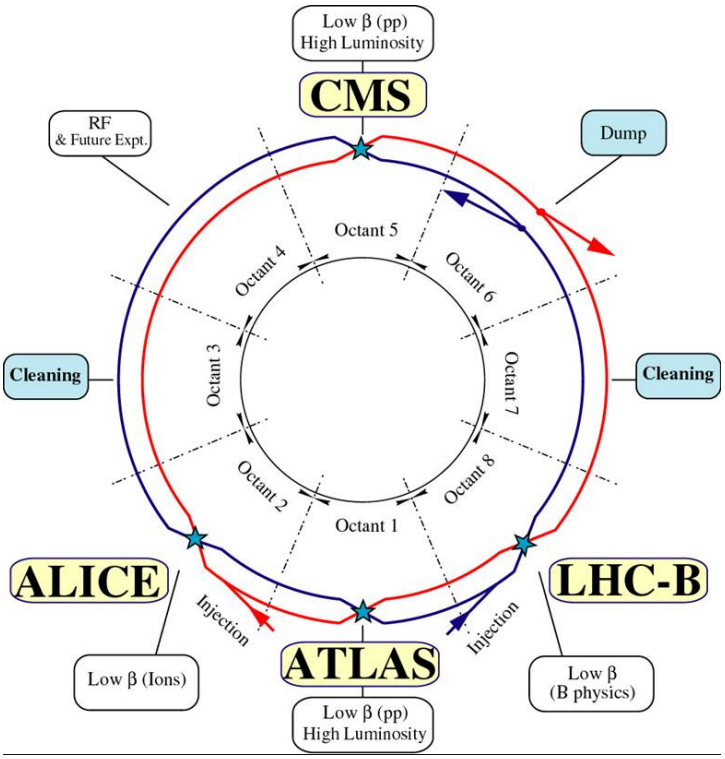

Figure 5.1: A schematic of the LHC storage ring [47]. The four main interaction regions are located in octants 1, 2, 5, and 8. The four main experimental detectors ATLAS, ALICE, CMS, and LHCb are located at these interaction regions. The beam dump is located in octant 6.

detectors designed for sensitivity to a wide range of physics. The other two experiments, ALICE at IR2 and LHCb at IR8, are more specialized. ALICE is intended to study collisions of heavy ions, and LHCb is designed to study physics related to the bottom quark. The interaction regions housing ATLAS and CMS are designed for high luminosity, the quoted nominal machine luminosity of $L = 10^{34}\text{cm}^{-2}\text{s}^{-1}$, while the interaction regions for ALICE and LHCb are designed for a lower luminosity [47].

5.1.3 Magnet Incident

The LHC has been unable to reach its design center-of-mass energy of $\sqrt{s} = 14\,\text{TeV}$ due to a flaw in the interconnects between magnets. This problem was discovered on September 19th 2008 during a powering test when an electrical arc occurred in one of the magnets, causing a helium release and damage to a greater than 700 m section of the beam-line [49]. The cause of this incident was a faulty interconnect between two magnets, which was estimated to have a resistance of $\sim 220\,\text{n}\Omega$, outside the design specification of $< 0.6\,\text{n}\Omega$ due to poor soldering [49]. Additional flawed interconnects were also found between other magnets. During the shutdown in 2009, interconnects were repaired in 4 octants with partial repairs in a 5th. Additional repairs still needed in the remaining octants will be performed after the 2012 run [50]. The unrepaired splices limit the amount of current that can be safely put in the magnets, limiting the maximum field and therefore the energy of the beams.

5.2 LHC Performance

The LHC ran at a center-of-mass energy of $\sqrt{s} = 7\,\text{TeV}$ for most of the 2010 and 2011 runs[1]. The highest instantaneous luminosity reached by the LHC in 2010 at $\sqrt{s} = 7\,\text{TeV}$ was $L = 2.07 \times 10^{32}\text{cm}^{-2}\text{s}^{-1}$ [51]. This was with 368 filled bunches per beam, of which 348 were colliding in ATLAS and CMS. The highest instantaneous luminosity reached by the LHC in 2011 at $\sqrt{s} = 7\,\text{TeV}$ was $L = 3.65 \times 10^{33}\text{cm}^{-2}\text{s}^{-1}$ [51].

[1]For the 2012 LHC run, which is beyond the scope of this analysis, the center-of-mass energy was raised to $\sqrt{s} = 8\,\text{TeV}$.

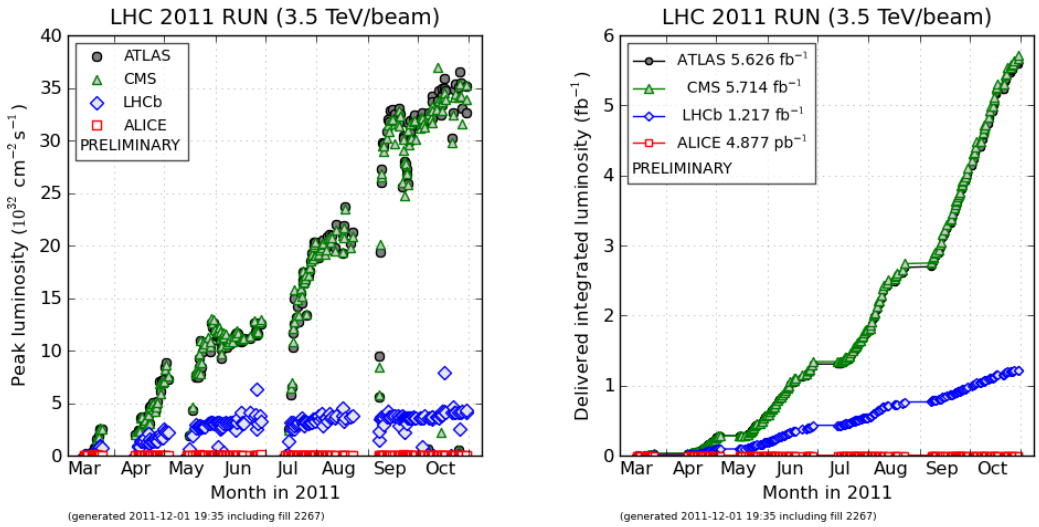

Figure 5.2: Plots of the peak instantaneous (left) and integrated (right) luminosity delivered by the LHC to the various detectors versus time during proton-proton running in 2011 [51].

This was with 1380 filled bunches per beam with a minimum spacing of 50 ns between filled bunches. Of these filled bunches 1331 were colliding in ATLAS and CMS. The total integrated luminosity delivered to ATLAS and CMS was 5.626 fb^{-1} and 5.714 fb^{-1} respectively[2] [51]. Plots of the instantaneous and integrated luminosity over time can be seen in Fig. 5.2.

[2] $1\,\text{fb}^{-1} = 10^{39}\,\text{cm}^{-2}$

Chapter 6

The ATLAS Detector

The ATLAS (**A** **T**orodial **L**HC **A**pparatu**S**) experiment is one of the four main particle detectors at the LHC. It is along with CMS (**C**ompact**M**uon**S**olenoid) one of two general purpose particle detectors designed for sensitivity to an wide range of physics. ATLAS is located in an underground cavern at point 1 on the LHC ring. The detector is very large weighing in at over 7000 tonnes, and is 25 meters in height and 44 mm in length [52]. A computer generated image of the ATLAS detector can be seen in Fig. 6.1.

The ATLAS detector is comprised of several different sub-components that cover various roles in the detection of particles produced by the LHC collisions. The innermost section of the detector with respect to the beam pipe are the tracking detectors (see Section 6.1), which provides tracking and momentum measurement of charged particles. The other major detector sections are the calorimeters (see Section 6.2), which provide energy measurements of both charged and neutral particles, and the

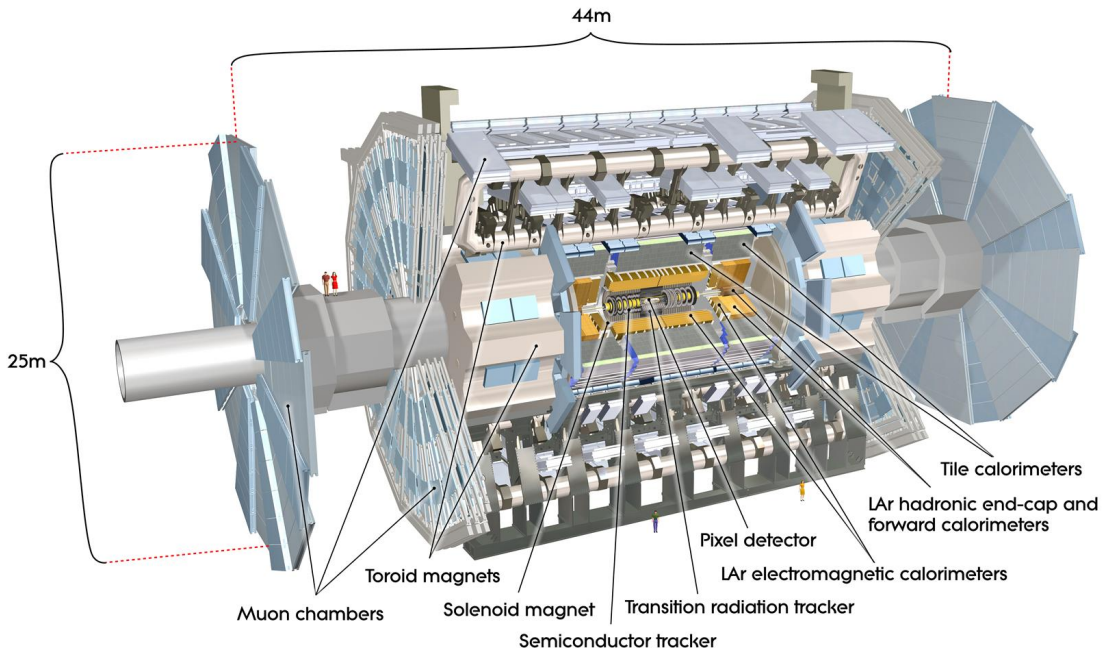

Figure 6.1: Cutaway view of the ATLAS detector with labels of the various components and subdetectors [53].

muon detectors, which measure the momentum of muons (see Section 6.3). Generally, the subdetectors making up ATLAS are subdivided into barrel and endcap regions to provide maximal coverage around the interaction point. In addition ATLAS has a multi-level trigger system for determining which events should be read-out and recorded. A more detailed description of the trigger system is included in Section 6.5.

The standard coordinate system used in ATLAS is presented here. The origin of the coordinate system is taken as the nominal beam interaction point[1]. In the Cartesian coordinate system based off this origin, the z-axis lies along the direction of the beam-line. The positive direction in z is defined as the one moving counter-clockwise

[1]The actual collisions occur over a region, due to the physical size of the proton bunches. In addition the center of this interaction region is not necessarily at the nominal origin

along the beam-line when viewing the LHC from above. The x and y directions lie in the plane transverse to the beam-line. The positive direction in x is defined as the direction pointing towards the center of the LHC ring, and the positive direction in y is defined as pointing towards the surface [52].

Other important variables in the coordinate system are ϕ, θ, η, and ΔR. The variables ϕ and θ represent the azimuthal and polar angle with respect to the z-axis, respectively. The pseudorapidity, η, is defined as $\eta = -\ln[\tan(\theta/2)]$. The variable ΔR is the distance between two positions in η-ϕ space, which is defined as $\Delta R = \sqrt{\Delta\eta^2 + \Delta\phi^2}$ [52].

6.1 Inner Detector

The portion of the ATLAS detector closest to the beam in terms of radius is a series of tracking detectors known collectively as the inner detector. The overall envelope of the inner detector extends to a radius of 1.15 m, and out to 3.5 m in both directions in z. The actively instrumented volume is smaller and ranges from 50.5 mm to 1066 mm in radius for the barrel and from 88.8 mm to 1004 mm in z for the endcaps [52]. Diagrams highlighting the components of the inner detector can be seen in Fig. 6.2. The primary function of the tracking detectors is to detect tracks from charged particles passing through the inner detector volume in the range of $|\eta| < 2.5$. These tracks can then be used to measure the momentum of the particles leaving the track and to determine the position of the actual collision vertex. The tracking detectors are also capable of

providing some additional information used in identifying the type of particles that created by the tracks.

The three primary tracking detectors going outwards in radius are the pixel detector, the silicon microstrip detector (SCT), and the transition radiation tracker (TRT). Detailed descriptions of these three can be found in Section 6.1.1 for the pixels, Section 6.1.2 for the SCT, and Section 6.1.3 for the TRT. A magnet system, which provides a 2 T solenoidal magnetic field for momentum determination in the tracker is located outside the inner detector. Details on the solenoid magnet are provided in Section 6.1.4.

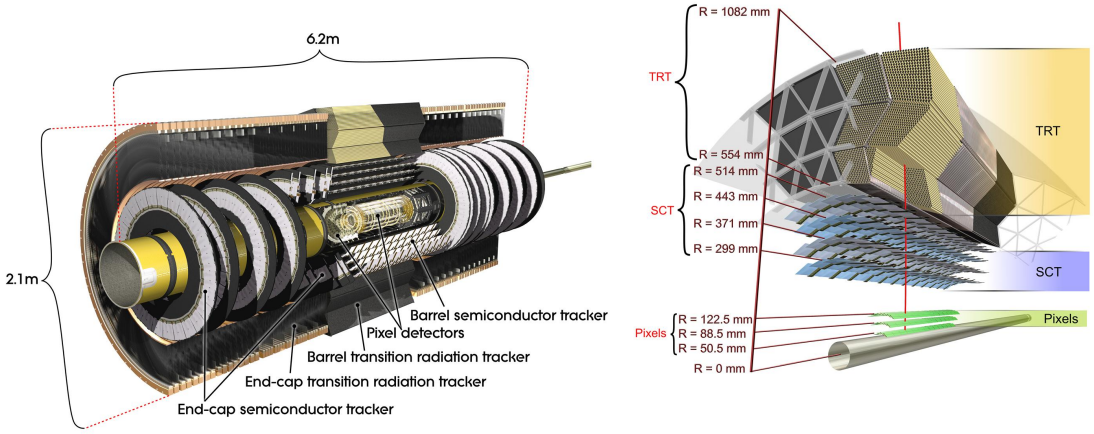

Figure 6.2: Cutaway view of the ATLAS inner detector with labels of the various subdetectors (left) and a radial view of the subdetector barrel components with labels of their distance from the beam pipe (right) [53].

6.1.1 Pixel Detector

The innermost tracking detector is the pixel detector. It consists of three concentric cylindrical barrel layers and six endcap disks, which form a ring around the

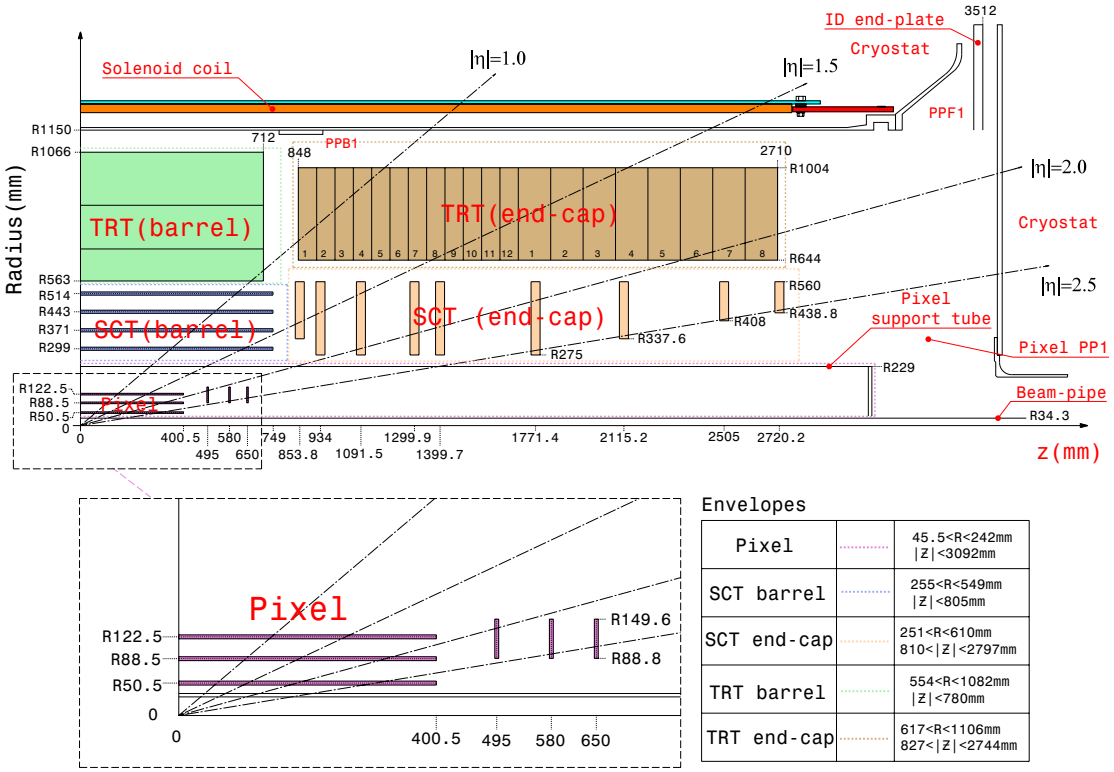

Figure 6.3: Quarter-section of the ATLAS inner detector showing the positions of all the subdetector layers [52].

beam pipe. The three barrel layers are at radii of 50.5 mm, 88.5 mm and 122.5 mm, while the endcap disks are positioned at ±495 mm, ±580 mm and ±650 mm in the z-direction [52]. The position of the pixel layers can be seen in the schematic diagram in Fig. 6.3.

Each layer of the pixels is made up of modules. The pixel barrel layers contain a total of 1456 modules, while the endcap disks contain 288 modules. Each pixel module contains 46080 independent readout channels, called pixels, on its silicon sensor. The area of the sensor corresponding to most of these pixels is $50 \times 400\,\mu\text{m}^2$[22]. The nominal

[2]Approximately 10 % of the pixels have an area of $50 \times 600\,\mu\text{m}^2$.

resolution of the pixels is $\sim$12 μm [52].

6.1.2 Silicon Strip Detector

The silicon microstrip detector (SCT) surrounds the pixels and provides additional tracking. The barrel of the SCT contains four layers at approximate radii of 299 mm, 371 mm, 443 mm, and 498 mm. Each of the SCT endcaps consists of 9 disks whose positions in the $|z|$-direction range from 854 mm to 2720 mm. The SCT contains a total of 4028 modules in the SCT with 2112 in the barrel section and 1976 in the endcaps.

Similar to the pixel detectors the active elements of the SCT are silicon sensors; however unlike the pixels the individual strips provide accurate position measurement in only one direction in the plane of the module. Each side of a SCT module has 768 active strips with a pitch of 80 μm. The nominal resolution of the SCT strips is 17 μm in the lateral direction and 580 μm in the longitudinal direction of the strip. The strips on one side of the module are rotated 20 mrad with respect to the other, allowing improved resolution when combining hits from both sides [52].

6.1.3 Transition Radiation Tracker

The outermost tracking detector is the TRT. The active sensor elements are 4 mm diameter polyimide straw tubes of which there are approximately 351,000. The straws contain a 31 μm diameter gold-plated tungsten anode and 70% Xe, 27% CO_2 and 3% O_2 gas mixture [52]. Transition radiation photons emitted by electrons passing

through the TRT are absorbed by the Xenon gas mixture leading to a higher amplitude signal from electrons compared to charged hadrons. The readout of the TRT straws has two thresholds: 250 eV and 6 keV [52]. The electrons are more likely to have high threshold hits, which is how the TRT is used for electron identification.

The TRT provides coverage for tracks out to $|\eta| = 2$ and measurement accuracy of each straw is 130 μm in the $R - \phi$ plane. Tracks within the acceptance of the TRT should pass through at least 36 straws. An exception to that is in the barrel-to-endcap transition region, $0.8 < |\eta| < 1.0$, where tracks only pass through at least 22 straws. From this the typical number of high threshold hits expected for an electron over 2 GeV is seven to ten [52].

6.1.4 Solenoid Magnet

The solenoid magnet is located between the TRT and the electromagnetic calorimeter in ATLAS, and its field allows for momentum measurement in the inner detector. It provides a 2 T solenoidal field directed along the z-axis which results in the tracks of charged particles bending primarily in the ϕ direction. The solenoid is a superconducting NbTi coil cooled to 4.5 K and has a nominal operating current of 7.730 kA. It uses the steel of the hadronic calorimeter as its flux return [52].

6.2 Calorimeters

The purpose of the calorimeters in ATLAS is to absorb and measure the energy of all the known particles except for muons and neutrinos produced in the collisions.

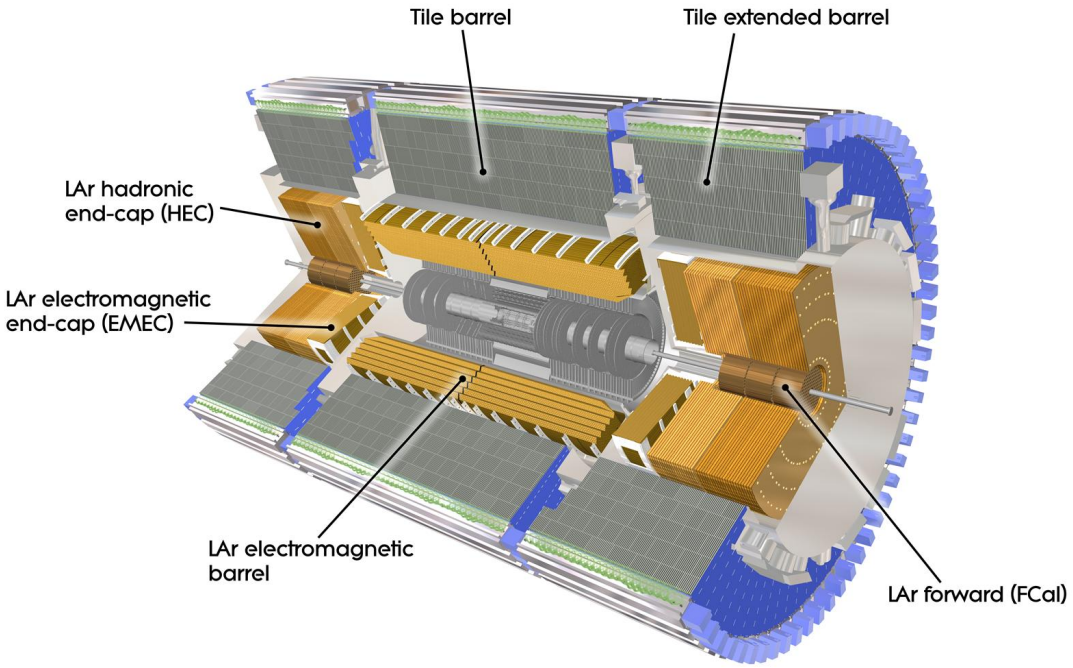

Figure 6.4: Cutaway view of the ATLAS calorimeters with labels of the various parts of the LAr and Tile calorimeters [52].

The energy deposits in the calorimeter allow for the identification of photons, electrons, and hadronic jets. Also, since the incoming partons of the protons have no significant transverse component to their momentum, the net momentum in the transverse direction of the particles coming from the collision should be zero. Missing energy in the transverse direction can then be used to infer the presence a non-interacting particle, therefore making the accurate measurement of the energy of all particles from the collision important. To this end the calorimeters have the largest acceptance of any of the detectors in ATLAS with coverage in the range of $|\eta| < 4.9$ [52]. A diagram of the ATLAS calorimeters with labels for the various sub-components can be seen in Fig. 6.4.

The innermost layer of the calorimeter, referred to as the EM calorimeter, is designed to absorb non-hadronic, electromagnetically interacting objects such as electrons and photons. It has a total thickness of at least 22 radiation lengths (X_0) of material over the barrel portion and a thickness of at least $24\,X_0$ in the endcaps [52]. The EM calorimeter is composed entirely out of the liquid-argon technology described in Section 6.2.1, and provides coverage out to $|\eta| = 3.2$.

The hadronic calorimeter is located outside of the EM calorimeter, and is designed to absorb the hadrons making up jets. There is a total of approximately 9.7 nuclear interaction lengths (λ) between the interaction point and the outer edge of the instrumented portion of hadronic calorimeter barrel, and approximately $10\,\lambda$ in the endcaps [52]. The hadronic calorimeter provides coverage out to $|\eta|$ of 4.9. This coverage is provided by both of liquid-argon technology as well as tile technology described in Section 6.2.2.

6.2.1 Liquid Argon Calorimeter

The liquid-argon (LAr) calorimeter provides all of the coverage of the electromagnetic calorimeter and a portion of the coverage of the hadronic calorimeter. The electromagnetic portion of the LAr uses lead as the absorber and liquid argon as the active material. The electromagnetic calorimeter covers the range $|\eta| < 3.2$ with between 2 and 4 sampling layers including the presampler. The presampler extends to 1.8 in $|\eta|$. After the presampler, the finely segmented first sampling covers the ranges $|\eta| < 1.4$ and $1.5 < |\eta| < 2.4$. This portion of the first sampling is referred to as the

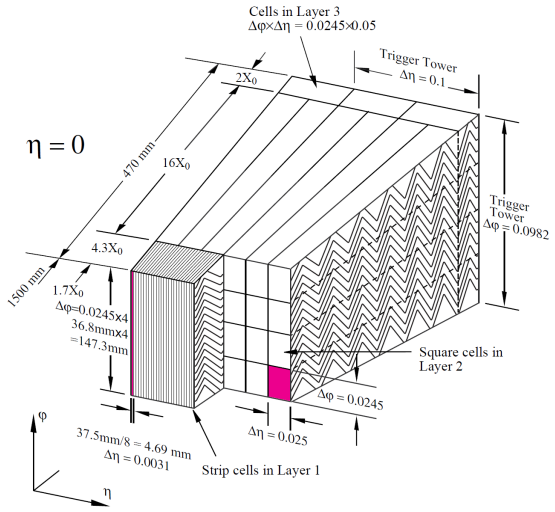

Figure 6.5: Schematic of the various sampling layers of the ATLAS LAr electromagnetic calorimeter [52].

strips and are particularly important in differentiating photons from hadronic jets. The segmentation of the strips varies from $0.025/8 \times 0.1$ to $0.025/4 \times 0.1$ in $\Delta\eta \times \Delta\phi$. The second sampling of the provides the majority of the energy measurement of electrons and photons, as well as the electromagnetic component of jets. The segmentation of the second layer varies from 0.025×0.025 to 0.1×0.1 in $\Delta\eta \times \Delta\phi$. Lastly, the segmentation of the third electromagnetic calorimeter layer is 0.050×0.025 in $\Delta\eta \times \Delta\phi$ over its entire acceptance. A figure showing a schematic of the sampling layers of the LAr electromagnetic calorimeter can be seen in Fig. 6.5. Also the LAr electromagnetic calorimeter contains 9344 channels in the presampler and 163968 channels in the remaining three layers [52].

The endcap portion of the hadronic calorimeter is also a LAr calorimeter, which uses copper for its absorber. It has four sampling layers and extends over the

range $1.5 < |\eta| < 3.2$. The hadronic endcap calorimeter segmentation is 0.1×0.1 in $\Delta\eta \times \Delta\phi$ for $1.5 < |\eta| < 2.5$, and has a slightly coarser segmentation of 0.2×0.2 in the range $2.5 < |\eta| < 3.2$. It also has a total of 5632 readout channels.

6.2.2 Tile Calorimeter

The tile calorimeter is a sampling calorimeter with steel used as the absorber and scintillator as the active material used for energy measurement. The ratio of steel to scintillator by volume is 4.7:1. The entirety of the barrel portion of the hadronic calorimeter is provided by the tile calorimeter. The tile calorimeter provides coverage with three sampling layers in the range $|\eta| < 1.7$. The segmentation of the first two layers of the calorimeter is 0.1×0.1 in $\Delta\eta \times \Delta\phi$, and 0.2×0.1 in the outer most sampling layer. There are 5760 individual readout channels in the $|\eta| < 0.8$ region of the tile calorimeter. In the outer $0.8 < |\eta| < 1.7$ portions there are 2046 channels on each side of the detector for a total 4092.

6.2.3 Forward Calorimeter

The forward most portion of the hadronic calorimeter is also provided by liquid-argon using a copper-tungsten absorber. It provides coverage over the range $3.1 < |\eta| < 4.9$. The forward calorimeter has three samplings. The segmentation of the first sampling is the finest with a segmentation of at least 3.0×2.6 in $\Delta x \times \Delta y$. The other two layers have segmentation of at least as small as 3.3×4.2 for the second and 5.4×4.7 for the third. For the lowest $|\eta|$ portions of all three layers, the segmentation

is approximately four times finer [52].

6.3 Muon Detectors

The muon system in ATLAS consists of four different detector types: monitored drift tubes (MDT), cathode strip chambers (CSC), resistive plate chambers (RPC), and thin gap chambers (TGC). The MDT's and CSC's together provide coverage out to $|\eta| = 2.7$ for precision track measurement. The RPC's and TGC's together cover out to $|\eta| = 2.7$ and provide a secondary measurement of the muon as well as the muon triggering[3]. The magnetic field for momentum measurement is provided by the large barrel toroids in the region $|\eta| < 0.4$ and by the smaller endcap toroids in the $1.6 < |\eta| < 2.7$ region. The field in the intermediate region of $1.4 < |\eta| < 1.6$ is combination of both the barrel and endcap fields. The bending power of the field is much less in this intermediate region than in the barrel or endcaps [52].

6.4 Luminosity Detectors

The primary online luminosity measurement in ATLAS is provided by the LUCID detector, which stands for **LU**minosity measurement using **C**erenkov **I**ntegrating **D**etector. LUCID consists of two detectors, one on each side of ATLAS along the beamline. The each detector consists of 20 aluminum Cerenkov tubes filled with C_4F_{10} placed around the beam pipe at $\pm 17\,\mathrm{m}$ from the interaction point. The Cerenkov light from

[3]The coverage in $|\eta|$ is only out to 2.4 when used for triggering.

each tube is collect and amplified by a photomultiplier tube [52].

LUCID measures the relative luminosity by counting particles coming from the interaction, which should be proportional to the number of proton interactions in that crossing. The detector has two particle counting modes. One were it counts particles by using the pulse height in each tube to determine the number of particles in that tube. The other mode is to assume only one particle enters the tube at a time[4], and then count every hit tube as one particle. With proper calibration LUCID has the capability to measure the luminosity to within 5% [52].

6.5 Trigger System

The bunch spacing for the LHC is 25 ns which translates to a potential event rate of 40 MHz. Keeping all of these events is impossible, both from the perspective of reading out all these events and processing and storing them. The final rate that can be readout and stored permanently is on the order of 400 Hz. Fortunately, not all bunch crossing produce interesting collisions, so many events can be discarded. Quickly and accurately deciding which events are interesting is the role of the trigger system.

The trigger system for ATLAS has three levels, Level-1 (L1), Level-2 (L2), and the event filter [52]. The L1 trigger is the lowest level of the triggers. This trigger consists of a custom hardware implementation that makes the trigger decision. The L1 analyzes events by looking quickly at a simplified set of the information from the calorimeters and muon systems to identify possible electrons, photons, jets, or muons

[4]This true to within a few percent at luminosities less than $\sim 10^{33}\text{cm}^{-2}\text{s}^{-1}$

above some p_{T} threshold. If such candidate trigger objects are found the event is passed on to the L2 trigger. The L1 trigger reduces the event to less than 100 kHz [52].

Events passing the L1 are then passed on to the L2 trigger. This trigger examines specific regions of interest (RoI's) of the detector which were passed to it by the level L1 trigger based on trigger objects seen by it. The full detector information from the RoI is then used to make a decision on the event. The L2 trigger reduces the event rate to about 3.5 Hz [52]. The final step in the trigger is then the event filter, which uses the full event information over the whole detector to decide if the event will be recorded. It uses fairly complex algorithms, which are in many cases very similar to those used in the eventual offline reconstruction of the events.

Not all events passing a particle trigger step's requirements are necessarily passed on. Some triggers are prescaled and only some fraction of events that have objects passing the trigger requirement are forwarded on. This is done because keeping all events passing that criteria would result in too high of a rate for that trigger step, but at least some of those events are still desired. In order for an event to be recorded it must pass all the steps of at least one chain of triggers from L1 to the event filter, including any prescales.

Part III

The Analysis

Chapter 7

Object Selection

This chapter highlights the criteria used to define the various reconstructed objects or other event observables used in this analysis. The ATLAS reconstruction software [54] provides a series of information on the observed signals in the detector, which are used to interpret these signatures as physical particles. Four classes of candidate objects are considered in this analysis: photons, electrons, jets, and muons. The criteria for the four classes of candidate objects can be found in Section 7.1 for photons, Section 7.2 for electrons, Section 7.3 for jets, and Section 7.4 for muons.

Since what happened in any one event cannot be known with certainty, these candidate objects may not represent what truly created the detector signature in question. Most object selection criteria are based upon the recommendations from the groups in ATLAS responsible for the corresponding reconstruction algorithms and the optimization thereof. The goal of these selection criteria is to accept objects where the interpretation is correct while rejecting ones where it is not. A discussion of the

motivation for the selection criteria that differ from the previous iterations of this analysis [46, 32] can be found in Section 9.3.

The same physical signature in the detector has the potential to pass more than one of these object criteria. When there is overlap of two or more objects, only one interpretation of that object must be chosen to avoid double counting of the object's energy. A concrete example of this is that photons and electrons will also generally pass the jet selection criteria, and these jets should be removed. The detailed methodology for this procedure is described later in Section 9.1.1.

Several event observables do not correspond directly to candidate particles in the events, but are nonetheless useful for distinguishing SUSY events from non-SUSY events. These are the missing transverse energy ($E_{\mathrm{T}}^{\mathrm{miss}}$), the angular distance in ϕ between objects ($\Delta\phi$), and the total visible transverse energy (H_{T}), which are described in detail in Sections 7.5, 7.6, and 7.7 respectively.

7.1 Photons

The photon selection is designed to identify photons produced in the decay of a neutralino NLSP. The selection is tuned to reject real photons from backgrounds such as those produced by the hard bremsstrahlung of an electron or the decay of neutral pions. The photon selection relies heavily upon the shape of the shower in the calorimeter and on calorimeter isolation requirements to distinguish photons from hadronic jets. The tracking is used to distinguish photons from electrons, both of which produce similar

showers in the calorimeter.

7.1.1 Sliding-Window Clustering Algorithm

The calorimeter clusters used to make photons in the ATLAS reconstruction are created by the sliding-window clustering algorithm [55]. The clusters are of a fixed size in η and ϕ and are limited to $|\eta| < 2.5$. The size of the cluster depends on its location and whether its associated photon converted. An unconverted photon in the barrel has a clustering window defined to be 3×5 cells in η and ϕ in the second sampling of the EM calorimeter. Converted photons in the barrel have a 3×7 window because of the expected spread in ϕ of the conversion electrons due to the magnetic field. A cluster which is 5×5 cells wide in the second sampling is used for all photon types in the endcap. The change to 5 cells in η reflects the smaller-sized cells in the endcap. The width in ϕ is the same for all photons in the endcap because the magnetic field causes less separation there. The energy of the cluster is the sum of all calorimeter cells that fall within the window.

7.1.2 Photon Identification Criteria

A host of discriminating variables (listed in Table 7.1) are used to reject jets which may fake photons. The cuts placed on these variables are parametrized in η of the photon as measured in the second sampling of the EM calorimeter. For details on these variables please see Refs. [56] and [57]. There are two main categories of cuts on these discriminating variables used in this analysis, which will be referred to as *PhotonLoose*

Category	Name	Description
Hadronic Leakage	R_{had_1}	Ratio of E_{T} in the first sampling of the hadronic calorimeter to E_{T} of the EM cluster (used only for $\lvert\eta\rvert < 0.8$ and $\lvert\eta\rvert > 1.37$)
	R_{had}	Ratio of E_{T} in all samplings of the hadronic calorimeter to E_{T} of the EM cluster (used only for $0.8 < \lvert\eta\rvert < 1.37$)
EM 2nd Sampling	R_{η}	Ratio in η of energies in 3×7 versus 7×7 cells
	R_{ϕ}	Ratio in ϕ of energies in 3×3 versus 3×7 cells
	w_2	Width of the shower in η
EM 1st Sampling	$w_{s\,3}$	Shower width for three strips around the strip with the maximum energy
	$w_{s\,\mathrm{tot}}$	Width of the shower in η
	F_{side}	Fraction of energy outside of the three central strips
	ΔE	Difference between the energy in the second maximum strip and the minimum strip energy between the first and second maxima
	E_{ratio}	Ratio of the difference in energy of the first and second maxima over the sum of the energy in the first and second maxima

Table 7.1: The discriminating variables used for photon identification along with their descriptions [56]. There are three categories of cuts: hadronic leakage, shower shapes in the second sampling of the EM calorimeter, and shower shapes in the finely segmented first sampling (a.k.a. the strips).

and *PhotonTight* requirements. The requirements are such that all photons passing *PhotonTight* also pass *PhotonLoose*. Photons passing these requirements are referred to as *Loose* or *Tight* photons.

7.1.2.1 Loose Criteria

The *Loose* photon criteria is valid over a range of $|\eta| < 2.47$. Only R_{had_1} (R_{had}), R_{η}, and w_2 are are used to define the *PhotonLoose* requirement. The exact cuts made on each of the variables is parametrized in η and are summarized in Table 7.2. No

differentiation is made between converted and unconverted photons at the *Loose* level.

Upper bound of bin in $\|\eta\|$	0.6	0.8	1.15	1.37	1.52	1.81	2.01	2.37	2.47
R_{had_1} (R_{had})	0.010	0.010	0.010	0.008	0.010	0.025	0.015	0.014	0.019
R_η	0.927	0.912	0.925	0.916	0.750	0.906	0.920	0.908	0.915
w_2	0.012	0.012	0.013	0.013	0.025	0.015	0.013	0.013	0.012

Table 7.2: Values of the cuts on the discriminating variables, which make up the *PhotonLoose* criteria, parametrized in $|\eta|$.

7.1.2.2 Tight Criteria

The *PhotonTight* requirement is a tighter subset of the *PhotonLoose* requirement, but is not valid over the whole range used by the *PhotonLoose* requirement. The ranges $1.37 < |\eta| < 1.52$ and $|\eta| > 2.37$ are excluded because the finely segmented first layer of the calorimeter (strips) is absent in those regions [56]. Most of the added cuts in *PhotonTight* utilize the strips to aid in rejecting deposits coming from π^0's by identifying the two slightly separated photons. Unlike the *PhotonLoose* requirement, a separate set of cuts is used for converted and unconverted photons in *PhotonTight*, since converted photons generally have a wider shower shape in the ϕ direction due to the electron and positron bending in the magnetic field. The exact values for these cuts are included for unconverted and converted photons in Tables 7.3 and 7.4, respectively.

7.1.2.3 Identification Correction for Monte Carlo

The distributions of some of the discriminating variables described in Section 7.1.2 differ between data and Monte Carlo. The differences can be approximated

Upper bound of bin in $\|\eta\|$	0.6	0.8	1.15	1.37	1.52	1.81	2.01	2.37
R_{had_1} (R_{had})	0.0089	0.007	0.006	0.008	–	0.019	0.015	0.0137
R_η	0.950784	0.9398	0.9418	0.9458	–	0.932066	0.928	0.924
R_ϕ	0.954	0.95	0.59	0.82	–	0.93	0.947	0.935
w_2	0.0107194	0.011459	0.010759	0.011359	–	0.0114125	0.0110	0.0125
$w_{s\,3}$	0.66	0.69	0.697	0.81	–	0.73	0.651	0.610
$w_{s\,\mathrm{tot}}$	2.95	4.4	3.26	3.4	–	3.8	2.4	1.64
F_{side}	0.284	0.36	0.36	0.514	–	0.67	0.211	0.181
ΔE	92	92	99	111	–	92	110	148
E_{ratio}	0.63	0.84	0.823	0.887	–	0.88	0.710	0.780

Table 7.3: Values of the cuts on the discriminating variables, which make up the *PhotonTight* criteria for unconverted photons, parametrized in $|\eta|$.

Upper bound of bin in $\|\eta\|$	0.6	0.8	1.15	1.37	1.52	1.81	2.01	2.37
R_{had_1} (R_{had})	0.00748	0.007	0.00489	0.008	–	0.0149	0.015	0.011
R_η	0.940784	0.9268	0.9298	0.9308	–	0.918066	0.924	0.913
R_ϕ	0.400	0.426	0.493	0.437	–	0.535	0.479	0.692
w_2	0.0116194	0.011359	0.012859	0.012659	–	0.0138125	0.012	0.0129
$w_{s\,3}$	0.697	0.709	0.749	0.78	–	0.773	0.672	0.644
$w_{s\,\mathrm{tot}}$	2.8	2.95	2.89	3.14	–	3.7	2.0	1.48
F_{side}	0.32	0.428	0.483	0.51	–	0.508	0.252	0.215
ΔE	200	200	122	86	–	123	80	132
E_{ratio}	0.908	0.911	0.808	0.803	–	0.67	0.915	0.962

Table 7.4: Values of the cuts on the discriminating variables, which make up the *PhotonTight* criteria for converted photons, parametrized in $|\eta|$.

by a simple shift in the discriminating variables (DV) as shown in Eq. 7.1.

$$\triangle\,\mu^i = \left\langle DV^i_{\mathrm{DATA}} \right\rangle - \left\langle DV^i_{\mathrm{MC}} \right\rangle . \tag{7.1}$$

The values of the discriminating variables are shifted in the Monte Carlo, and the identification cuts from Section 7.1.2 are reapplied. The photon identification efficiency is thus adjusted to better match the one measured in data. The shifts $\triangle\mu^i$ are the standard shifts used in ATLAS for analyses with photons and are taken from Ref. [58]. These shifts are measured using data from the entire 2011 run and Monte Carlo samples JF17, JF35, and JF70, which include various dijet and photon plus jet processes. The corrections are measured by selecting tight, isolated photons in those samples and

comparing the discriminating variable distributions.

7.1.3 Kinematic Requirements

The transverse momentum, p_{T}, of photon candidates is required to be greater than 50 GeV. This helps to eliminate to some degree the misidentification of electrons from Z and W decays as photons. All photons are required to have $|\eta| < 1.81$ but not be in the region $1.37 < |\eta| < 1.52$, which is the gap region between the barrel and endcap portions of the calorimeter. The η used for this cut is that of the photon as measured in the second sampling of the EM calorimeter, the same one used in the parametrization of the identification cuts in Section 7.1.2, because this is a calorimeter acceptance cut. In all other cases the η of the photon refers to the one assigned to the photon object by the reconstruction software. In the case of unconverted photons η is calculated from the vector connecting the barycenters of the energy in the first and second sampling of the EM calorimeter. For unconverted photons, where the track or tracks coming from the conversion vertex each contain four or more silicon hits, the η direction is determined by extrapolating from the calorimeter cluster to the conversion vertex. The value of η for converted photons with tracks not fulfilling that requirement is calculated in the same manner as unconverted photons.

7.1.4 Conversions

The significant amount of material in the inner detector in ATLAS, shown in Fig. 7.1, causes approximately 40% of all photons to convert before they reach the EM

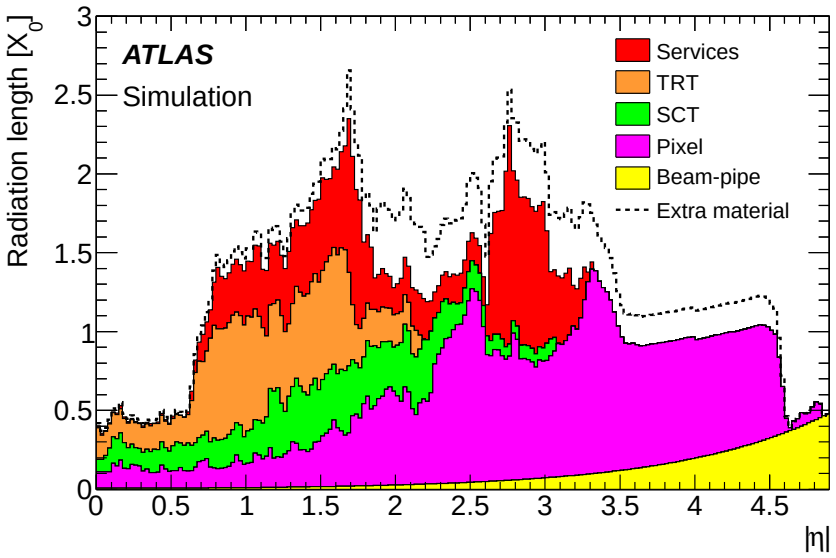

Figure 7.1: The amount of material, in units of radiation lengths, X_0, encountered by a particle before reaching the EM calorimeter as a function of η [59].

calorimeter [52]. Two categories of photons are reconstructed in ATLAS: single-track and double-track. Double track conversions cover the case where both electron tracks are found and associated with the photon cluster. The conversion vertex is then the extrapolated intersection point of the two tracks. Single-track conversions cover the case where only one of the tracks is found and associated to the cluster. This can happen, for instance, when the conversion is very asymmetric and one of the electrons has low p_{T}. The conversion vertex of a single-track conversion is considered to be the innermost hit on the track, and this innermost hit is not allowed to be in the b-layer of the pixels. Single-track conversions can faked by electrons if early hits on its track are missed due to intrinsic inefficiency or dead detector elements. The earlier hits on a track may also be missed because of a momentum change of the electron due to material interactions.

Electrons are often reconstructed as converted photons in areas where the pixel b-layer is dead. For example, single-track conversion vertices are located at the point of the first track hit. Single-track conversion vertices at the b-layer are vetoed, but those at other layers are accepted. Hence, dead b-layer modules result in an excess of electron tracks being reconstructed as single-track conversion vertices. If the dead b-layer pixel modules are taken into account by counting them as hits on conversion tracks, the number of fake single-track conversions (and two-track conversions to a lesser degree) can be significantly reduced in areas with dead pixel modules. The effect of this requirement on the SUSY samples used in this analysis is a less than 0.2 % loss in efficiency. When this requirement is applied in conjunction with the identification criteria discussed in Section 7.1.2 the letters AR are appended to the designation, e.g. *PhotonTight* to *PhotonTightAR*.

In addition to the requirement above, a converted photon must have no pixel hits on any associated tracks in order to be considered a photon. This no-pixel-hit requirement significantly reduces the rate at which true electrons are misidentified as photons even compared to the dead pixel hit requirement. Details on the effectiveness of this requirement are included in Section 9.3.3.

7.1.5 Isolation

A calorimetric isolation requirement is also applied to photons to further reduce fakes from hadronic jets. The isolation cut is based on the amount of transverse energy deposited in a cone of $\Delta R = 0.2$ around the photon from which the energy of the photon

cluster itself has been subtracted. Some additional corrections are made to the value of the energy in the cone to account for energy leakage of the photon outside its cluster and extra energy from pileup. The pileup correction is parametrized in terms of the number of reconstructed collision vertices in the event. These isolation corrections are a standard set recommended by the e/gamma combined performance group [60, 61]. The actual isolation requirement is that the transverse calorimeter energy in the cone after corrections must be less than 5 GeV.

7.1.6 Cleaning

Several cleaning cuts are applied to remove photons with clusters affected by calorimeter problems, and therefore likely fake or poorly measured. The standard recommendations from the ATLAS e/gamma combined performance group are used [60]. The standard recommendations for photons included two sets of cuts. Any photons failing either set of cleaning cuts described below are not counted as a photon for the purposes of this analysis.

The first set of photon cleaning cuts (similar cuts are also applied to electrons) are referred to in ATLAS as the object quality cuts. A photon fails the object quality cuts if any cells in its cluster have dead high voltage. A photon also fails the cuts if its cluster contains a cell with dead readout electronics in either the first or second sampling. Lastly, a photon will fail the object quality cuts if any of the cells in the cluster core, defined to be the central 3×3 cells in the second sampling, or any of the central eight cells of the cluster in the first sampling are masked out of the readout for

any reason.

Beyond the object quality described above, a photon fails the cleaning cuts if it has a cluster time $|t| > (10 + 2/|E_{\text{clus}}|)$ ns, where E_{clus} is the energy of the photon cluster in GeV. This cut is to remove photons due to non-collision backgrounds such as cosmics. Finally a photon also fails if more than 80% of its energy comes from cells with a Q-factor over 4000[1], as shown in Eq. 7.2, and either $R_\phi > 1.0$ or $R_\eta > 0.98$.

$$\frac{\sum_{\text{cluster}} E_{\text{cell}}(Q > 4000)}{\sum_{\text{cluster}} E_{\text{cell}}} > 0.8 \tag{7.2}$$

7.1.7 Photon Types

There are two main types of photons used in this analysis that will be referred to as baseline photons and pseudo-photons. Both types of candidate photons are required to pass the η and ϕ requirements from Section 7.1.3, as well as the requirements on conversions from Section 7.1.4, photon isolation from Section 7.1.5, and photon cleaning from Section 7.1.6.

The only difference between the two photon candidate types are the requirements on the shower shapes. The baseline photons are required to pass the *PhotonTightAR* identification requirements defined in Section 7.1.2, while the pseudo-photons are only required to pass the *PhotonLooseAR* identification requirements. There is an additional requirement that pseudo-photon candidates must also fail either the cuts on F_{side} or $w_{s\,3}$ which are part of the tight requirement. This ensures that the two candidate

[1]The cell Q-factor measures the difference between the measured pulse shape and the predicted pulse shape that is used to reconstruct the cell energy. The signal in cells with a large Q-factor is likely to be due to noise.

photon types are orthogonal.

The baseline photons are selected in all sub-samples in this analysis. This is not the case for the pseudo-photons which are only used in some of the control samples used to model the QCD background as described in Section 10.1 of Chapter 10.

7.2 Electrons

Electrons are important in the this analysis, as they are a major source of fake high p_{T} photons and can also appear in some cases as part of the cascade in SUSY decays. Electrons are quite similar to photons from the perspective of their calorimeter deposit. Due to the similar calorimeter deposits between photons and electrons the main differentiation is performed with the tracking. As with photons the electron selection criteria relies heavily upon the shape of the shower in the calorimeter and calorimeter isolation requirements to distinguish them from hadronic jets. The calorimeter isolation and cleaning cuts placed on electrons in this analysis are also very similar to the requirements placed on photons.

7.2.1 Electron Identification Criteria

A host of discriminating variables based on the shower shapes and track matching are used to reject fake electrons. For the shower shapes a sub-sample of the discriminating variables for photons, as shown in Table 7.1, are used, though with different cut values. The cuts placed on these variables are parametrized in η of the electron, as measured in the second sampling of the EM calorimeter, and the E_{T} of the electron.

The tracking based discriminating variables used are the number of hits on the track in various detectors, the $\Delta\eta$ or $\Delta\phi$ between the cluster and the track, the energy of the cluster over the momentum of the track (E/p), and the transverse impact parameter of the track, d_0. For details on these variables please see Ref.s [62] and [60]. There are two main categories of cuts on these discriminating variables used in this analysis, which will be referred to as *ElectronMedium++* and *ElectronTight++* requirements. The requirements are such that all electrons passing *ElectronTight++* also pass *ElectronMedium++*. Electrons passing these requirements are referred to as *Medium++* or *Tight++* electrons.

7.2.1.1 Medium++ Criteria

The *Medium++* electron criteria is valid over a range of $|\eta| < 2.47$. The shower shape discriminating variables used in *ElectronMedium++* are $R_{\mathrm{had_1}}$ (R_{had}), R_η, w_2, $w_{s\,\mathrm{tot}}$, and E_{ratio}. These cuts are parametrized in η and E_{T} of the electron. The *ElectronMedium++* criteria requires a $\Delta\eta < 0.005$ for the track match and a transverse impact parameter of the track $d_0 < 5.0\,\mathrm{mm}$. The requirements on the number of hits in the pixel plus SCT detectors is shown in Table 7.5. Also if the electron is within the TRT acceptance, there is a requirement on the fraction of its TRT hits which must be high threshold hits, as shown in Table 7.6.

Detector	$\lvert\eta\rvert < 2.01$	$\lvert\eta\rvert \geq 2.01$
B-layer	≥ 1	≥ 0
Pixels	≥ 1	≥ 2
Pixels + SCT	≥ 7	≥ 7

Table 7.5: The *ElectronMedium++* requirements on the number of silicon hits on an electron track.

Upper bound of bin in $\lvert\eta\rvert$	0.1	0.625	1.07	1.304	1.752	2.0
TRT_{high}/TRT	0.05	0.05	0.05	0.06	0.08	0.08

Table 7.6: The *ElectronMedium++* requirements, as a function of the η of the track, on the fraction of TRT hits on the track that are high threshold hits. For electrons with $|\eta| > 2.0$, which is outside the TRT acceptance, this cut is not applied.

7.2.1.2 Tight++ Criteria

The *ElectronTight++* requirement is defined as a tighter subset of the *ElectronMedium++* requirement. The *Tight++* electron criteria is valid over a range of $|\eta| < 2.47$. The shower shape discriminating variables used in *ElectronTight++* are identical to *ElectronMedium++*, but with tighter cuts in some cases. These cuts are parametrized in η and E_{T} of the electron. The *ElectronTight++* criteria requires a $\Delta\eta < 0.005$ for the track match, a $\Delta\phi < 0.015$ for the track match, a transverse impact parameter of the track $d_0 < 1.0\,\mathrm{mm}$, and a requirement on the E/p of the track. The E/p cut is parametrized in η and E_{T} of the electron. The requirements on the number of hits in the pixel plus SCT detectors is shown in Table 7.7. If the electron is within the TRT acceptance, there is also a requirement on the fraction of its TRT hits which must be high threshold hits, as shown in Table 7.8. The final additional requirement of the

ElectronTight++ is that there is not also a converted photon interpretation matched to the electron's cluster.

Detector	$\|\eta\| < 2.01$	$\|\eta\| \geq 2.01$
B-layer	≥ 1	≥ 1
Pixels	≥ 1	≥ 2
Pixels + SCT	≥ 7	≥ 7

Table 7.7: The *ElectronTight++* requirements on the number of silicon hits on an electron track.

Upper bound of bin in $\|\eta\|$	0.1	0.625	1.07	1.304	1.752	2.0
TRT_{high}/TRT	0.08	0.085	0.085	0.115	0.13	0.155

Table 7.8: The *ElectronTight++* requirements, as a function of the η of the track, on the fraction of TRT hits on the track that are high threshold hits. For electrons with $|\eta| > 2.0$, which is outside the TRT acceptance, this cut is not applied.

7.2.2 Kinematic Requirements

The p_{T} of electron candidates is required to be greater than 25 GeV. All electrons are required to have $|\eta| < 2.47$ and not lie in the calorimeter gap region $1.37 < |\eta| < 1.52$. The η used for this acceptance cut is is one measured in calorimeter in the same manner as for photons. In all other cases the η of the electron refers to the measured η assigned to the electron's track[2]In some cases, as described in Section 7.2.3, tighter requirements are imposed on electron p_{T} and η.

[2]The official e/gamma group recommendations are to use the η of the track except when the track has fewer than four hits in the silicon detectors. In that case the η of the calorimeter cluster is used.

7.2.3 Electron Types

There are two main types of electrons used in this analysis that will be referred to as baseline electrons and photon-replacement electrons. Both types of candidate electrons are required to pass an isolation requirement that is identical to the photon requirement from Section 7.1.5 and the object quality portion of the photon cleaning requirement from Section 7.1.6.

The difference between the two electron candidate types is in the kinematic and identification requirements. The baseline electrons are required to pass the *Electron-Medium++* identification requirements defined in Section 7.2.1 and η and E_{T} requirements in Section 7.2.2. The photon-replacement electrons are purely a sub-sample of the baseline electrons, which use the η and p_{T} requirements for photons from Section 7.1.3 and pass the *ElectronTight++* requirement.

The baseline electrons are selected and used in all sub-samples in this analysis. This photon-replacement electrons are only used in the control samples used for modeling the electroweak background as described in Section 10.2 of Chapter 10.

7.3 Jets

Jets refer to the detector signature of the spray of particles created during the fragmentation and hadronization of colored particles produced in the collisions. A hadronic jet will usually leave a series of tracks in the inner detector and energy deposits in both the electromagnetic and hadronic calorimeters roughly in a cone pointing back

to the primary vertex.

The jet reconstruction in this analysis is based on topological clusters in the calorimeter. These topological clusters differ from the sliding-window clusters used in photon and electron reconstruction, as described in Section 7.1.1, in that they are not of a fixed size, and they pull cells neighboring the seed into the jet based on a significance threshold [55]. The topoclusters are used as input for the anti-k_t jet algorithm [63] with the four-momentum recombination distance parameter set to 0.4.

Several different jet energy calibration schemes exist in the ATLAS reconstruction. The calibration applied to the jets in this analysis is the called the EM+JES calibration [64]. This starts from the electromagnetic scale energy (*emscale*) of the jet, which does not include the calorimeters' reduced response to energy deposition from hadrons. A scale factor derived from Monte Carlo as a function of the η and ϕ positions of the jets in the detector, is applied to the jet to correct the *emscale* energy of the hadronic scale. The EM+JES calibration method has poorer energy resolution, but it is easier to access the systematic uncertainties for this method [64]. Another disadvantage of this method is that energy deposits coming mostly from particles depositing their energy electromagnetically will have their energy corrected to the hadronic scale over-estimating the true energy.

The two acceptance cuts applied to jets require a $p_{\mathrm{T}} > 20\,\mathrm{GeV}$ and $|\eta| < 2.8$. These are the baseline jets used in this and many other SUSY analyses in ATLAS [65]. When referred to jets, these baseline jets are implied unless stated otherwise.

7.4 Muons

Muon candidates are reconstructed by algorithms that perform a statistical combination of a track reconstructed in the muon spectrometer with a corresponding track in the inner detector. All muon identification cuts are taken from recommendations proposed by the muon combined performance group [66]. For this analysis muons from the *STACO* muon algorithm chain are used. The muons are required to be either *Combined*, where the muon is reconstructed independently in both the muon spectrometer (MS) and the inner detector (ID), or *Segment-tagged* muons, where the MS is used to tag ID tracks as muons, without requiring a fully reconstructed MS track. The p_{T} of muons candidates is required to be greater than 10 GeV. The pseudorapidity of muons must satisfy $|\eta| < 2.4$. Muons are required to pass the *Loose* quality, as defined by the ATLAS muon combined performance group.

Additional cuts on the inner detector track quality are also applied. The inner detector track is required to have a hit in the b-layer of the pixels, unless the b-layer module through which the track would have passed is dead. An additional requirement on the pixel hits of the track is that the total number of pixel hits associated with track plus the number of dead pixel modules through which the track passed is greater than one. A similar requirement is made on the sum of the number of SCT hits on the track and the crossed dead SCT modules, except that at least six hits are required. Also the number of dead SCT modules traversed by the track must be less than three. If the inner detector track falls within the acceptance of the TRT, then an extension of the

track into the TRT is required. The following requirements are applied to the TRT track extension:

- Let $n = n_{TRT}^{hits} + n_{TRT}^{outliers}$
- Case 1: $|\eta| < 1.9$. Require $n > 5$ and $n_{TRT}^{outliers} < 0.9n$.
- Case 2: $|\eta| \geq 1.9$. If $n > 5$, then require $n_{TRT}^{outliers} < 0.9n$.

These baseline muons are identical to the muon definition used in many other SUSY analyses in ATLAS [65]. Muons are used in this analysis to veto events with cosmic muons, as discussed in Section 9.1.3, and are also included as components of the $E_{\mathrm{T}}^{\mathrm{miss}}$ and H_{T} observables discussed below.

7.5 Missing Transverse Energy

Although the interacting partons for the colliding protons may have unknown net momentum along the z direction, the net transverse momentum is assumed to be zero. As a result the vectoral sum of the transverse momentum of particles produced in the collision should be zero. In an event where this is not true, the event is said to have 'missing' transverse energy ($E_{\mathrm{T}}^{\mathrm{miss}}$). This so-called missing energy can have several different sources. The most interesting case in terms of this analysis is when a non-interacting particle[3], such as a neutrino or gravitino, is produced and exits the detector without depositing any energy. The missing transverse energy may also arise

[3]These particles are not necessarily strictly non-interacting and may interact via the weak force or gravity.

from detector effects, e.g. energy resolution, the incomplete acceptance of the detector, and cosmic rays.

For this analysis the $E_{\mathrm{T}}^{\mathrm{miss}}$ definition consists of two components: a calorimetric term and a muon term. The calorimetric $E_{\mathrm{T}}^{\mathrm{miss}}$ component is calculated from the energy deposited in calorimeter cells associated to a topocluster, up to $|\eta| < 4.9$, using Eq. 7.3. The calibration applied to these topoclusters is referred to as the local cluster weighting (LCW) calibration. The LCW calibration works by first classifying a topocluster as either electromagnetic or hadronic, based on the shower shapes of the individual topoclusters [67]. After the classification, a correction for each type is applied. This correction, derived from single pion Monte Carlo [64], accounts for the non-compensation for hadronic energy deposits and energy lost in dead material, including the cryostat [64]. The internal ATLAS name for this calorimeter based $E_{\mathrm{T}}^{\mathrm{miss}}$ definition is *MET_LocHadTopo*. Further details on this definition of the calorimeter term of the $E_{\mathrm{T}}^{\mathrm{miss}}$ can be found in Ref. [68].

$$\begin{aligned} E_{\mathrm{x}}^{\mathrm{miss,calo}} &\equiv -\sum_{i=1}^{N_{\mathrm{cell}}} E_i \sin\theta_i \cos\phi_i \\ E_{\mathrm{y}}^{\mathrm{miss,calo}} &\equiv -\sum_{i=1}^{N_{\mathrm{cell}}} E_i \sin\theta_i \sin\phi_i \\ E_{\mathrm{T}}^{\mathrm{miss,calo}} &\equiv \sqrt{\left(E_{\mathrm{x}}^{\mathrm{miss,calo}}\right)^2 + \left(E_{\mathrm{y}}^{\mathrm{miss,calo}}\right)^2} \end{aligned} \tag{7.3}$$

In addition to the calorimetric term described above (*MET_LocHadTopo*), a muon contribution made up of two terms is also included. These two muon terms are the standard ones prescribed by the $E_{\mathrm{T}}^{\mathrm{miss}}$ combined performance group [69]. The first muon

term, *MET_MuonBoy*, is derived from the transverse energy of reconstructed muons passing a set of selections in the event. Only muons with $|\eta| < 2.7$ are considered. The muons with $|\eta| < 2.5$ are required to be *Combined* muons, and the p_{T} used for these *Combined* muons depends on their isolation. If a muon is within $\Delta R < 0.3$ of a reconstructed jet it is considered non-isolated. For isolated muons the vectoral components of the p_{T} of the *Combined* muon are used in the *MET_MuonBoy* term, and the energy deposited in the calorimeter by the muon is treated in another term. For non-isolated muons, since the muon's calorimeter deposit cannot be resolved from that of the jet, the p_{T} of the muon spectrometer track, which is measured after the energy loss in the calorimeter, is used. Finally, muons in the range $2.5 < |\eta| < 2.7$ are not required to be *Combined* muons because this is outside the η acceptance of the inner detector. The vectoral components of the p_{T} of the muon spectrometer track are used, and no distinction is made between isolated and non-isolated muons. The second muon related term, *MET_RefMuon_Track*, represents the energy deposited in the calorimeter by isolated muon tracks. This is subtracted from the $E_{\mathrm{T}}^{\mathrm{miss}}$ to avoid double counting of the energy from isolated muons in *MET_MuonBoy* with that from the topoclusters. The muon terms are added to the *MET_LocHadTopo* term as shown in Eq. 7.4 to obtain the value of the missing transverse energy used in this analysis.

$$
\begin{aligned}
E_{\mathrm{x}}^{\mathrm{miss},\mu} &\equiv MET\_MuonBoy(x) - MET\_RefMuon\_Track(x) \\
E_{\mathrm{y}}^{\mathrm{miss},\mu} &\equiv MET\_MuonBoy(y) - MET\_RefMuon\_Track(y) \\
E_{\mathrm{x(y)}}^{\mathrm{miss}} &\equiv E_{\mathrm{x(y)}}^{\mathrm{miss,calo}} + E_{\mathrm{x(y)}}^{\mathrm{miss},\mu} \\
E_{\mathrm{T}}^{\mathrm{miss}} &\equiv \sqrt{\left(E_{\mathrm{x}}^{\mathrm{miss}}\right)^2 + \left(E_{\mathrm{y}}^{\mathrm{miss}}\right)^2}
\end{aligned} \tag{7.4}
$$

For details on the optimization of the cuts on $E_{\mathrm{T}}^{\mathrm{miss}}$ please see Section 9.3.

7.6 Angular Distance Between Objects

The angular distance between two objects in the coordinate ϕ is defined in Eq. 7.5.

$$
\Delta\phi_{1,2} \equiv \begin{cases} |\phi_1 - \phi_2 - 2\pi| & \text{if } \phi_1 - \phi_2 \geq \pi \\ |\phi_1 - \phi_2 + 2\pi| & \text{if } \phi_1 - \phi_2 < -\pi \\ |\phi_1 - \phi_2| & \text{if } -\pi \leq \phi_1 - \phi_2 < \pi \end{cases} \tag{7.5}
$$

A cut on the angular distance in ϕ between a photon and the $E_{\mathrm{T}}^{\mathrm{miss}}$ is particularly useful in rejecting events in which the $E_{\mathrm{T}}^{\mathrm{miss}}$ arises from energy mismeasurement of the photon. Details on this cut and its optimization are included in Section 9.3.

7.7 Total Visible Transverse Energy

The total visible transverse energy (H_{T}) observable is defined as the scalar sum of the p_{T} of all the baseline selected photon, electron, jet, and muon candidates in the

event. This observable is calculated after the overlap removal described in Section 9.1.1 is applied in order to avoid double counting. Also, in samples in which pseudo-photons are selected, their p_{T} is added into the H_{T} as well. The H_{T} seen in an event is expected to be large for many SUSY scenarios compared to the expected Standard Model backgrounds. For the optimization of the cuts on the H_{T} observable please see Section 9.3.

Chapter 8

Data and Monte Carlo Samples

Both real collision data recorded by the ATLAS detector and simulated collision events were used in this analysis. The modeling of the backgrounds is done primarily using the real data itself with some minor contributions estimated via simulated Monte Carlo samples. See Chapter 10 for further details on the modeling of the backgrounds. Simulated samples are also used to study the expected characteristics of the signal events. The following chapter contains a detailed description of the real collision data sample in Section 8.1. Similar details for the background and signal Monte Carlo samples are included in Sections 8.2 and 8.3, respectively.

8.1 Collision Data Set

The data used for this analysis were taken from the proton-proton collisions at $\sqrt{s} = 7\,\text{TeV}$ recorded by the ATLAS detector during run periods B and D-M from the 2011 run. The data from periods B and D-K was originally reconstructed at the

Tier-0[1]. with release 16 of the ATLAS offline software. This was incompatible with the version of the software used to reconstruct the later data periods. As a result periods B and D-K were reprocessed in November 2011[2]. The standard Tier-0 reconstruction was used for the runs in periods L and M, except for a few runs which required reprocessing [3]. All runs used in this analysis were reconstructed in a version of the ATLAS offline software that is compatible with release 17.0.3.X.

In order for events to be recorded they must pass a trigger chain as described in Section 6.5. This analysis uses a diphoton trigger that requires two photons passing the loose shower shape requirements[4] and with a transverse momentum of at least 20 GeV[5]. This particular trigger was chosen because it was the diphoton trigger with the loosest selection requirements that was unprescaled during the entire 2011 run.

In addition to the trigger requirements, a standard set of criteria based upon the status of the detectors is applied to ensure that the data used is of high quality. These requirements are applied at the level of individual luminosity blocks, and are based on both conditions information and performance measurements from the data runs. Based on various sets of these criteria, lists can be generated of the luminosity blocks which are considered usable. These are referred to as Good Run Lists (GRL). Events not falling in luminosity blocks considered good by the GRL used are rejected.

The GRL used for this analysis[6] requires that all of the detector systems, which

[1]Tier-0 is the designation of the CERN computing facility that reconstructs the raw ATLAS data [54].
[2]Reprocessing tags `r2603` or `r2713` for reprocessing campaign `pro10`.
[3]Reconstruction tags `f402+`. Runs using tag `f415` were reprocessed.
[4]These shower requirements are equivalent to the *PhotonLoose* criteria from Section 7.1.2.1.
[5]The internal ATLAS name for this trigger is `EF_2g20_loose`.
[6]`data11_7TeV.periodAllYear_DetStatus-v36-pro10_CoolRunQuery-00-04-08_Susy_ph_met.xml`

have an influence on the reconstruction of the event objects as defined in Chapter 7, are performing within nominal tolerances. The solenoid and toroid magnet systems are required to be operating at their nominal field values. This ensures that the p_{T} of reconstructed electrons and muons is well measured. It is also required that the reconstruction algorithms themselves are performing as expected. The trigger systems used for the photon triggers are also all required to be functioning nominally for all luminosity blocks to be used.

Using the GRL and trigger prescale values if applicable, the effective integrated luminosity can be calculated. This value is merely the sum of the official luminosity value determined by ATLAS[7] for each luminosity block passing the GRL. Assuming the trigger used was unprescaled, this value is then the effective luminosity of the data set. If this is not the case, then for any luminosity block where the trigger was prescaled, the value of the luminosity is scaled by the fraction of events passing the trigger that were kept. This scaled value of the luminosity is then used in the sum instead.

The effective integrated luminosity of the data sample used for the current analysis is 4812.34 pb^{-1}. A precise breakdown of the integrated luminosity per run period can be seen in Table 8.1. The integrated luminosity of the runs considered for this analysis before the application of the GRL is 4934.39 pb^{-1}, so the efficiency of the GRL selection is 97.5%.

[7]Please see Ref. [70] for details on the official ATLAS luminosity calculation.

Period	Run range	Luminosity [pb^{-1}]
B	178044–178109	11.7
D	179710–180481	166.7
E	180614–180776	48.8
F	182013–182519	136.1
G	182726–183462	537.5
H	183544–184169	259.5
I	185353–186493	386.2
J	186516–186755	226.4
K	186873–187815	600.1
L	188902–190343	1401.9
M	190503–191933	1037.6
Total	178044–191933	4812.3

Table 8.1: Integrated luminosity for 2011 after applying the GRL used in this analysis. For each data taking period the run range and the integrated luminosity are given in units of pb^{-1}.

8.2 Background Monte Carlo Samples

A range of simulated Monte Carlo (MC) events, representing various Standard Model processes, were used in this analysis. The events were generated with various MC generation programs and put through the standard ATLAS detector simulation [54]. Prior to the reconstruction step additional collision events are overlaid in proportions corresponding to the actual conditions during the 2011 run. These samples were used mostly for optimization of the selection criteria and cross check studies. Excepting a few minor cases, MC samples were not used to estimate the Standard Model background contributions for the analysis. A list of all the Standard Model MC samples used can be seen in Tables 8.2, 8.3, and 8.4.

8.2.1 Electroweak Boson Samples

Events with $W^{\pm}$ or Z bosons plus any number of jets where the electroweak boson decays leptonically have the potential to fake a diphoton plus $E_{\mathrm{T}}^{\mathrm{miss}}$ signature via the misidentification of electrons as photons. Fake photons from leptonic decays of taus to electrons is also a possibility. Other than $Z \to ee$ all of these processes should have significant intrinsic missing transverse energy. These Monte Carlo events were generated with the `ALPGEN` [71] Monte Carlo generator (version 2.13) with up to five-parton matrix elements. Showering and fragmentation were then provided by `HERWIG` [72, 73] version 6.5.1, and the underlying event by `JIMMY` [74]. Next-to-next-to-leading order (NNLO) K-factors for these samples are derived using the FEWZ program [75]. The leading-order cross sections and NNLO K-factors for the $W^{\pm}$ or Z boson samples can be found in Table 8.2.

In addition to the $W^{\pm}$ or Z bosons plus jets samples, $W^{\pm} + \gamma$ or $Z + \gamma$ MC were used. These events are assumed to mimic the diphoton signature mostly via one fake photon coming from an electron. In the case of the $W^{\pm} \to \ell\nu + \gamma$ events there is significant real $E_{\mathrm{T}}^{\mathrm{miss}}$ from the neutrino. The $W^{\pm} + \gamma$ samples were generated using `ALPGEN` in a similar manner to the $W^{\pm}+$jets samples. For the $Z + \gamma$, leading-order matrix elements were calculated using `MadGraph` 4 [76]. The program `PYTHIA` 6.4.23 [77] was used for the parton showering and fragmentation. No NLO K-factors were used for either the $W^{\pm} + \gamma$ or $Z + \gamma$ samples. The cross sections for these MC samples can be seen in Table 8.2.

Process	Generator	Cross Section [pb]	NLO K-factor
$W \to e\nu + \text{jets}$	Alpgen+Jimmy	8748.5	1.20
$W \to \tau\nu + \text{jets}$	Alpgen+Jimmy	8749.3	1.20
$W + \gamma$	Alpgen+Jimmy	289.1	–
$Z \to ee + \text{jets}$	Alpgen+Jimmy	858.1	1.25
$Z \to \tau\tau + \text{jets}$	Alpgen+Jimmy	858.4	1.25
$Z \to ee + \gamma$	MadGraph+Pythia	8.67	–
$Z \to \mu\mu + \gamma$	MadGraph+Pythia	8.67	–
$Z \to \tau\tau + \gamma$	MadGraph+Pythia	1.41	–
WW	Herwig	10.3	–
ZZ	Herwig	1.28	–
WZ	Herwig	2.16	–
$t\bar{t}$	MC@NLO	145.49	1.146

Table 8.2: Electroweak boson and top Monte Carlo samples used in this analysis, including leading-order (or NLO for $t\bar{t}$) cross section times branching ratio and the NNLO K-factor when available.

8.2.2 Top Quark Samples

Events containing $t\bar{t}$ are also a significant background to the diphoton plus $E_{\mathrm{T}}^{\mathrm{miss}}$ analysis. In a similar manner to electroweak boson plus jet events, a diphoton plus $E_{\mathrm{T}}^{\mathrm{miss}}$ signature arises generally by the misidentification of at least one electron as a photon. The $t\bar{t}$ MC samples were generated with the full next-to-leading order `MC@NLO` [78, 79] generator. Showering and fragmentation were then provided by `HERWIG`, and the underlying event by `JIMMY`. Next-to-next-to-leading order (NNLO) K-factors, as calculated in Ref. [80], are used to correct the NLO MC calculations. The cross sections and NNLO K-factors used for $t\bar{t}$ can be found in Table 8.2

8.2.3 QCD Samples

Separate photon+jet and diphoton samples were used for this analysis. The photon+jet samples were generated in a similar manner to the $W^{\pm}$ and Z samples using `ALPGEN`. Parton showering and fragmentation were simulated by the `HERWIG` event generator with `JIMMY` generating the underlying event. A generator-level requirement of two narrow[8] jets with $p_T > 20\,\text{GeV}$ is applied for all the photon+jet samples. The prompt diphoton sample was generated in `PYTHIA`. This sample included the hard subprocesses $gg \to \gamma\gamma$ and $q\bar{q} \to \gamma\gamma$ with a generator level cut of 15 GeV of transverse momentum on at least two prompt photons. No scaling of the cross section to NLO was used for either the photon+jet(s) and diphoton samples.

Process	Generator	Cross Section [pb]
$\gamma\gamma$	Pythia	114.94
γ + 1 parton	Alpgen+Jimmy	7737
γ + 2 partons	Alpgen+Jimmy	6627
γ + 3 partons	Alpgen+Jimmy	2656
γ + 4 partons	Alpgen+Jimmy	1059
γ + 5 partons	Alpgen+Jimmy	267

Table 8.3: QCD and direct photon Monte Carlo samples used in this analysis, including cross section times branching ratio and the number of events in each sample.

8.2.4 Irreducible Background Samples

Events containing $W \to \ell\nu + \gamma\gamma$ and $Z \to \nu\nu + \gamma\gamma$ are also simulated and used. Of all the MC processes described so far they are the only ones used directly in the background estimation. These samples are referred to as irreducible due to the fact

[8]This is a 0.12×0.12 rectangular grid in η and ϕ.

they produce a real diphoton plus $E_{\mathrm{T}}^{\mathrm{miss}}$ signature. The leading-order matrix element calculations for these are calculated using `MadGraph` 4. `PYTHIA` was used for the parton showering and fragmentation. Next-to-leading order cross section K-factors were used for all the irreducible samples. For the $Z \to \nu\nu + \gamma\gamma$ sample a K-factor of 2.0 ± 0.3 was used, based upon calculations in Ref. [81]. A K-factor of 3 ± 3 is applied for $W \to \ell\nu + \gamma\gamma$, which is taken from Ref. [82]. The cross sections and K-factors for the irreducible backgrounds can be seen in Table 8.4.

Process	Generator	Cross Section [pb]	NLO K-factor
$W^- \to \ell\nu + \gamma\gamma$	MadGraph+Pythia	2.93×10^{-2}	3 ± 3
$W^+ \to \ell\nu + \gamma\gamma$	MadGraph+Pythia	4.05×10^{-2}	3 ± 3
$Z \to \nu\nu + \gamma\gamma$	MadGraph+Pythia	1.46×10^{-2}	2.0 ± 0.3

Table 8.4: Irreducible Monte Carlo samples used in this analysis, including leading-order cross section times branching ratio and the NLO K-factor.

8.3 Signal Monte Carlo Samples

8.3.1 GGM Samples

As discussed in Section 3.4.2 we will consider a GGM model with a bino-like lightest neutralino. A pair two-dimensional benchmark planes in the GGM parameter space are studied in this analysis. The neutralino mass is one free parameter, and the other is either the gluino or squark mass, depending on the benchmark plane being considered. When the gluino mass is treated as a free parameter, the squark soft masses are set to 2.5 TeV. For the other case of the free squark masses, the soft masses of the left-handed squarks and down-type right-handed squarks are varied while the gluino and

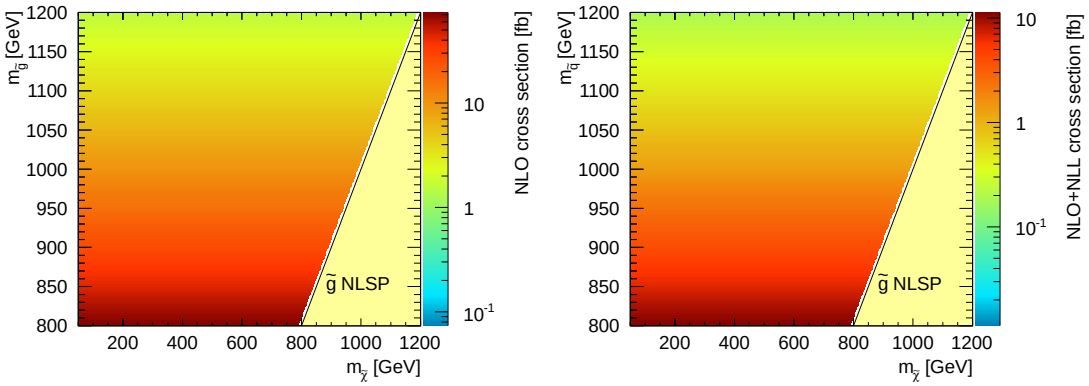

Figure 8.1: NLO+NLL cross sections for the GGM signal points as a function of the gluino and lightest neutralino mass (left) and squark and lightest neutralino mass (right).

up-type right-handed squarks are set to 2.5 TeV. The up-type right-handed squarks are treated in this manner in order to satisfy the GGM sum rules [34, 35]. The other model parameters are fixed to $M_2 = 2.5\,\text{TeV}$, $\mu = 2.5\,\text{TeV}$, $\tan\beta = 1.5$ and $c\tau_{\text{NLSP}} < 0.1\,\text{mm}$. All soft parameters are set to 2.5 TeV. The CP-odd Higgs is decoupled regime with $M_{A^0} = 2.0\,\text{TeV}$.

The full mass spectrum and the particle branching ratios and decay widths are calculated from this set of parameters using `SUSPECT` 2.41 [83] and `SDECAY` 1.3 [84]. For each signal point 5000 events are generated with the `HERWIG++` generator version 2.4.2 [85] using the MRST 2007 LO* [86] parton density functions.

In total, 228 GGM signal points are generated and half are in the $m(\tilde{g}) - m(\tilde{\chi}_1^0)$ plane with the remainder in $m(\tilde{q}) - m(\tilde{\chi}_1^0)$ plane. The gluino and squark masses range from 800 to 1300 GeV, and the neutralino mass from 50 GeV up to 10 GeV below the gluino or squark mass. Cases where the gluino is lighter than the lightest neutralino are not considered, since photons are not produced in this scenario. As an example, the

$M_{\tilde{g}}$[GeV]	σ(LO)[pb]	σ(NLO + NLL)[pb]	Uncertainty (%)	K factor
800	0.0305	0.0742	23.1	2.43
850	0.0179	0.0442	24.9	2.47
900	0.0106	0.0267	26.6	2.52
950	0.0063	0.0163	28.3	2.56
1000	0.0038	0.0100	30.0	2.61
1050	0.0023	0.0062	31.7	2.65
1100	0.0014	0.0039	33.9	2.72
1150	0.00088	0.0025	36.0	2.79
1200	0.00054	0.0016	38.6	2.87
1250	0.00034	0.00098	40.3	2.93
1300	0.00021	0.00063	42.7	3.02

Table 8.5: The total LO and NLO+NLL cross sections with uncertainties and derived K factors for GGM gluino-bino signal points.

full SUSY particle mass spectrum for the $m(\tilde{\chi}_1^0) = 450\,\text{GeV}$, $m(\tilde{g}) = 1000\,\text{GeV}$ signal point is listed in Table A.3 in Section A.1. The LO cross sections were calculated by `HERWIG++` for the different signal points, which ranges from 0.03 pb to 0.2 fb for gluino masses from 800 GeV to 1300 GeV, respectively. The different mass combinations and the LO cross sections are also listed in Table A.1 in Section A.1. The cross sections have only a very slightly dependence on the neutralino mass. For the GGM model with a bino-like NLSP considered here, the dominant production is colored; therefore the cross section is determined by the gluino or squark mass depending on the sample. Since all but the lightest neutralino are pushed to high mass in this scenario, direct neutralino pair production has a comparatively tiny cross section, and is ignored. When these GGM MC samples were produced, depending on which particle was light, only the contributing gluino-gluino or squark-squark final states were turned on.

The signal cross sections for GGM grid points are calculated to next-to-leading

$M_{\tilde{q}}$[GeV]	σ(LO)[pb]	σ(NLO + NLL)[pb]	Uncertainty (%)	K factor
800	0.0049	0.0102	28.5	2.08
850	0.0028	0.0060	30.5	2.13
900	0.0016	0.0036	32.9	2.20
950	0.00094	0.0021	35.3	2.27
1000	0.00056	0.0013	37.8	2.35
1050	0.00033	0.00080	40.4	2.43
1100	0.00020	0.00049	43.1	2.53
1150	0.00012	0.00031	45.8	2.63
1200	0.00007	0.00019	48.6	2.76
1250	0.00004	0.00012	51.5	2.89
1300	0.00002	0.00008	54.3	3.04

Table 8.6: The total LO and NLO+NLL cross sections with uncertainties and derived K factors for GGM squark-bino signal points.

order including soft gluon emission to next-to-leading-logarithmic order (NLO+NLL). Please refer to Section 3.6 for a detailed description of the calculation method. The cross sections for the points in the gluino-bino grid are shown in Fig. 8.1 and Table 8.5 together with the error, LO cross section, and the derived K factor. No dependence on the gaugino mass is expected. In the production of the GGM gluino-bino signal samples only the gluino-gluino production is considered, hence only this process is considered for the NLO+NLL calculation. The cross sections for the grid points of the squark-bino grid are shown in Table 8.6. For these points only squark production is considered and used for the NLO+NLL calculations.

8.3.2 SPS8 Samples

The representative minimal GMSB model used in this analysis is SPS8, which was introduced in Section 3.4.1. In this model the only free parameter is Λ. The

Λ[TeV	σ(LO)[pb]	σ(NLO/NLO + NLL)[pb]	Uncert. (%)
50	11.6	18.2	6.1
60	4.14	6.53	6.3
70	1.71	2.69	6.3
80	0.794	1.23	6.4
90	0.403	0.609	6.3
100	0.221	0.324	6.1
110	0.129	0.184	5.8
120	0.0795	0.110	5.5
130	0.0512	0.0684	5.2
140	0.0340	0.0442	4.9
150	0.0232	0.0294	4.7
160	0.0162	0.0202	4.7
170	0.0115	0.0141	4.7
180	0.00830	0.00998	4.8
190	0.00606	0.00717	4.7
200	0.00444	0.00512	4.9
210	0.00330	0.00378	5.0
220	0.00246	0.00280	4.9
230	0.00185	0.00210	5.2
240	0.00140	0.00157	5.2
250	0.00106	0.00118	5.2

Table 8.7: The total LO and NLO (NLO+NLL for strong production components only) cross sections and uncertainties for the SPS8 signal points.

other model parameters are fixed to $M_{\text{mes}} = 2\Lambda$, $N_{\text{mes}} = 1$, $\tan\beta = 15$, $\mu > 0$ and $C_{\text{grav}} = 1$. This trajectory in Λ ensures a neutralino NLSP with a high branching fraction to photons.

The full mass spectrum, the branching ratios, and the width of the decays are calculated from this set of parameters using `ISAJET` [87] version 7.80. For each signal point 10000 events are generated with the `HERWIG++` generator version 2.4.2 [85] using the MRST 2007 LO* parton density distributions. In total, 21 signal points from $\Lambda = 50\,\text{TeV}$ to $\Lambda = 250\,\text{TeV}$ in steps of $10\,\text{GeV}$ were generated. Unlike the GGM parameter space,

all the possible supersymmetric final states are included as possibilities when the events are generated. Neutralino/chargino and slepton final states almost completely dominant for the higher values of Λ, but some of the points lower in the range have non-negligible contributions from strongly produced final states. As an example the full SUSY particle mass spectrum for the $\Lambda = 140\,\text{TeV}$ signal point is listed in Table A.12 in Section A.2. The LO cross section ranges from 11 pb to 1 fb for the given range in Λ. All cross sections are listed in Table A.11 in Section A.2.

The signal cross sections for SPS8 grid points are calculated to NLO+NLL in an almost identical manner as the GGM, see Section 3.6 for details. Unlike GGM there are several distinct production processes of both the strong (NLO+NLL) and electroweak (NLO only) variety that contribute. The total cross section is taken as the sum of the individual NLO+NLL (or NLO) cross sections for each contributing process. They are shown in Table 8.7 together with the LO cross section. No K factors are shown since these cross section are the sums of several processes each with its own K factor. Since the `HERWIG++` MC is generated at leading order, the events for each of the individual processes are reweighted by the proper K factor to obtain the properly weighted acceptances for each Λ point.

Chapter 9

Event Selection and Optimization

This chapter highlights in Section 9.1 the basic selection scheme common to all the signal and control samples used in this analysis. In addition the detailed definitions of the three diphoton signal regions introduced in Chapter 1 are provided. Finally, the Monte Carlo based studies, used to optimize the cuts defining the signal regions for maximum sensitivity, are presented in Section 9.3.

9.1 Base Event Selection

The following base selection scheme is applied to each event for all signal and control samples in this analysis unless specified otherwise:

- The GRL and trigger requirement from Section 8.1. For Monte Carlo only the diphoton trigger is applied.
- The require that the reconstructed primary vertex of the event has more than 4

associated tracks.

- Events flagged with a LAr calorimeter error due to noise bursts or data integrity errors are removed. See Ref. [60] for details.
- The standard object selections are imposed. See Chapter 7 for details.
- The overlap removal steps, which are detailed in Section 9.1.1.
- The H_{T} and $\Delta\phi$ observables are calculated from the surviving selected candidate objects. See Sections 7.6 and 7.7 for details.
- The jet cleaning requirements. See Section 9.1.2 for details.
- The cosmic muon veto. See Section 9.1.3 for details.
- The LAr calorimeter hole event veto. See Section 9.1.4 for details.

The details of these selections are provided in the following sections. After this base selection various additional selection cuts are applied to define the various signal (see Section 9.2), and background control samples (see Chapter 10).

9.1.1 Overlap Removal

The same physical energy deposit in the calorimeter can be found by the reconstruction algorithms that create photon, electron, and jet candidates. In order to avoid double counting of this energy, a set of overlap removal rules between the different candidate object types must be employed. The overlap rules enumerated below take as inputs the selected photon, electron, jet, and muon candidates, as defined in Chapter 7.

The application of the overlap rules removes duplicates, therefore, setting the final number of photon, electron, and jet candidates in the event. Note that in the control samples were pseudo-photons are selected and only there, they are counted as photons for the purposes of the overlap rules. Also the cleaning jets, which are merely the normal baseline jets with the η requirement removed, are counted as jets in the overlap removal, since cleaning jets matching selected photon and electron candidates should be removed before applying the jet cleaning.

- If the clusters of a photon and an electron are found to be within $\Delta R < 0.01$, the object is interpreted as an electron and the photon is removed. This is the opposite of previous versions of this analysis [46, 32]. This new approach was taken in order to reduce the electron to photon fake rate.

- If a jet and an electron are found to be within $\Delta R < 0.2$, the object is interpreted as an electron, and the overlapping jet is removed.

- If a jet and a photon are found to be within $\Delta R < 0.2$, the object is interpreted as a photon and the overlapping jet is removed.

- If a jet and an electron are found to be within $0.2 < \Delta R < 0.4$, the object is interpreted as a jet and the electron is removed.

- If a jet and a photon are found to be within $0.2 < \Delta R < 0.4$, the object is interpreted as a jet and the photon is removed.

- If a jet and a muon are found to be within $\Delta R < 0.4$, the muon is considered a

muon from heavy flavor decay. Heavy flavor muons are not used for the cosmic veto described in Section 9.1.3, but they are used in the calculation of $E_{\mathrm{T}}^{\mathrm{miss}}$ and H_{T}.

9.1.2 Jet Cleaning

In some small fraction of events, calorimeter noise or energy deposits from cosmic rays can leave jet-like signatures in the detector. Such fakes jets can unbalance the transverse energy in an event leading to fake $E_{\mathrm{T}}^{\mathrm{miss}}$. Fake jets generally have different characteristics than jets from collisions, and can be dealt with accordingly. The jet variables useful in identifying fake jets are HECf, EMf, LArQ, HECQ, LArQ_{mean}, neg. E, ch$f$, and $\mathrm{F_{max}}$. The variables HECf and EMf are the fraction of the jet's energy in the hadronic endcap and the EM calorimeter, respectively. The value LArQ is the fraction of energy of the jet that is from cells with a Q-factor over 4000. The cell Q-factor measures the difference between the measured pulse shape and the predicted pulse shape that is used to reconstruct the cell energy. A similar quantity, HECQ, is calculated instead using only the cells in the hadronic endcap. The average LAr quality, LArQ_{mean}, is the normalization[1] of the energy weighted average of the Q-factor of the LAr cells in the jet. The negative energy, neg. E, is the sum of the energy in all the cells in the jet which have a negative energy. The jet charged fraction, ch$f$, is computed by dividing the sum of the p_{T} of all the tracks associated with the jet by the p_{T} of the jet itself. Finally, $\mathrm{F_{max}}$ is the fraction of the jet's energy in the layer of calorimeter with the

[1] It is normalized to one by dividing the average Q-factor by the maximum possible Q-factor, which is stored as a 16-bit integer.

highest energy from the jet. A standard ATLAS jet cleaning procedure, known as the *Looser* jet cleaning criteria [88, 89], is employed to find events affected by problematic jets. The jet cleaning procedure is applied to the cleaning jets, which are defined as the normal baseline jets from Section 7.3 with the η requirement lifted, after the application of the overlap removal procedure from Section 9.1.1. An event is rejected if at least one of the cleaning jets is considered a bad jet by the following criteria:

- The jet has signal consistent with sporadic noise in the hadronic endcap calorimeters and is considered a bad jet if either of the following is true:
  - HEC$f > 0.5$ and $|\text{HEC}Q| > 0.5$ and $\text{LAr}Q_{\text{mean}} > 0.8$
  - $|\text{neg.}\, E| > 60\,\text{GeV}$
- The jet has signal consistent with coherent noise in the LAr calorimeter and is considered a bad jet if the following is true:
  - EM$f > 0.95$ and $|\text{LAr}Q| > 0.8$ and $\text{LAr}Q_{\text{mean}} > 0.8$ and $|\eta| < 2.8$.
- The jet has a signal consistent with that expected from either cosmic ray or beam halo muons and is considered a bad jet if any of the following are true:
  - EM$f < 0.05$ and ch$f < 0.05$ and $|\eta| < 2$
  - EM$f < 0.05$ and $|\eta| \geq 2$
  - $\text{F}_{\text{max}} > 0.99$ and $|\eta| < 2$

Note that the η used in the jet cleaning is that of the jet measured at the *emscale*.

9.1.3 Cosmic Muon Veto

Cosmic ray muons have the potential to change the $E_{\mathrm{T}}^{\mathrm{miss}}$ in an event, both by being counted as a muon and by depositing energy in any of the calorimeters. Cosmic muons can be found in an event by looking for muons whose track does not extrapolate back to the primary collision vertex of the event. The two primary variables used are $|z_0|$ and $|d_0|$, which are the impact parameters with respect to the primary vertex in the z and the transverse directions, respectively. An event is rejected if it contains at least one baseline muon after overlap removal with a $|z_0| > 1\,\mathrm{mm}$ or $|d_0| > 0.2\,\mathrm{mm}$. This is the standard cosmic muon veto used by the SUSY group in ATLAS [65].

9.1.4 LAr Calorimeter Hole

On April 30th 2011, six calorimeter front-end boards (FEBs) were lost during a power failure, causing a hole in the LAr calorimeter acceptance. This corresponds to about 0.4% of the cells in the LAR calorimeter. The affected cells are clustered in the region $-0.1 < \eta < 1.5$ in η and $-0.9 < \phi < -0.5$ in ϕ [90]. Four of the dead FEBs were in the second sampling of the calorimeter, and two were in the third sampling. The second sampling provides most of the energy measurement for the LAr, so this is particularly bad for photons and electrons which are generally not reconstructed as a result. Jets falling in this region will generally still be identified, but most of the EM component of the jets energy will be lost. The LAr hole was present for all of data periods E through H, corresponding to $981.9\,\mathrm{pb}^{-1}$ of data or $\sim$20% of the total integrated luminosity. The four dead FEBs in the second sampling were repaired after

the end of period H, mitigating most of the problem.

This hole in the LAr affects this analysis in primarily two ways. The first is the loss of photon acceptance in the problematic region. This effect is modeled properly in the Monte Carlo, so no special procedure is required to take the signal acceptance loss into account. The other way in which the LAr hole can affect the analysis is by introducing tails in the $E_{\mathrm{T}}^{\mathrm{miss}}$ distribution due to improper measuring of the energy of jets falling in the problematic region; these tails may lead to potentially higher backgrounds. The effect of these tails is limited by vetoing events where it is determined that a significant fraction of the $E_{\mathrm{T}}^{\mathrm{miss}}$ is due to jets affected by the LAr hole. This veto is the standard SUSY group 'smart' veto [91]. This veto is considered 'smart' because it does not veto every event where a jet falls in the affected LAr region, but only those where it is estimated that the jet significantly affects the $E_{\mathrm{T}}^{\mathrm{miss}}$.

Three variables are important for determining if energy lost from a jet has affected the $E_{\mathrm{T}}^{\mathrm{miss}}$: $B_{\mathrm{cell}}^{\mathrm{corr}}$, $B_{\mathrm{jet}}^{\mathrm{corr}}$, $B_{\mathrm{dotx}}^{\mathrm{corr}}$. The $B_{\mathrm{cell}}^{\mathrm{corr}}$ variable is the fractional correction to the jet's energy estimated by using the energy averaged over neighboring cells for any dead cells in the jet. The $B_{\mathrm{dotx}}^{\mathrm{corr}}$ works in same manner as $B_{\mathrm{cell}}^{\mathrm{corr}}$, except it deals with cells that are not read out because of dead optical transmitters. Both the $B_{\mathrm{cell}}^{\mathrm{corr}}$ and $B_{\mathrm{dotx}}^{\mathrm{corr}}$ corrections are applied to the jet during reconstruction. The $B_{\mathrm{jet}}^{\mathrm{corr}}$ variable is the fractional correction to the jet's energy using a jet level shape profile from Monte Carlo to estimate the energy lost in dead cells. This correction is not applied to the jet during reconstruction. The $B_{\mathrm{jet}}^{\mathrm{corr}}$ correction gives a better estimate of the energy lost from jet due to the LAr hole than $B_{\mathrm{cell}}^{\mathrm{corr}}$ and $B_{\mathrm{dotx}}^{\mathrm{corr}}$. This is the case because the LAr hole is

a large group of contiguous dead cells and a neighboring cell based correction works poorly here. Since the $B_{\text{jet}}^{\text{corr}}$ correction is the one used to estimate the fake $E_{\text{T}}^{\text{miss}}$, the $B_{\text{cell}}^{\text{corr}}$ and $B_{\text{dotx}}^{\text{corr}}$ corrections must first be removed from the jet's energy. The estimated fake $E_{\text{T}}^{\text{miss}}$ due to a jet in the LAr hole, $E_{\text{T}}^{\text{fake}}$, is then given by Eq. 9.1.

$$E_{\text{T}}^{\text{fake}} = p_{\text{T}}^{\text{jet}} \left(1 - B_{\text{cell}}^{\text{corr}} - B_{\text{dotx}}^{\text{corr}}\right) \left(\frac{1}{1 - B_{\text{jet}}^{\text{corr}}} - 1\right) \cos\left(\phi_{\text{jet}} - \phi_{\text{met}}\right) \tag{9.1}$$

This value is estimated for each baseline jet candidate that falls in the η and ϕ region of the LAr hole. When more than one jet is present in the LAr hole, $E_{\text{T}}^{\text{fake}}$ is taken to be the sum of the contributions from each jet in the LAr hole. An event is then rejected if $E_{\text{T}}^{\text{fake}} > 10\,\text{GeV}$ and $E_{\text{T}}^{\text{fake}} > 0.1 E_{\text{T}}^{\text{miss}}$.

Since the effects of the LAr hole are properly modeled in the Monte Carlo, the procedure applied to both real data and Monte Carlo is identical. The average acceptance loss due to the smart veto across all the GGM and SPS8 signal samples is 2.8% and 1.4%, respectively [92]. For further details and studies on the LAr hole and the smart veto please see Ref. [90].

9.2 The Signal Regions

As introduced in Chapter 1, the analysis described in this document utilizes three signal regions. This is a change relative to the previous iteration of this analysis [32], which contained only one signal region. All three signal regions are based on the base event selection described in Section 9.1 with a requirement of two baseline candidate photons, as described in Section 7.1.7, in the event. The signal regions are

then defined by differing criteria placed upon the three observables $\Delta\phi\left(\gamma,\, E_{\mathrm{T}}^{\mathrm{miss}}\right)$, H_{T}, and $E_{\mathrm{T}}^{\mathrm{miss}}$, which are described in Sections 7.6, 7.7, and 7.5.

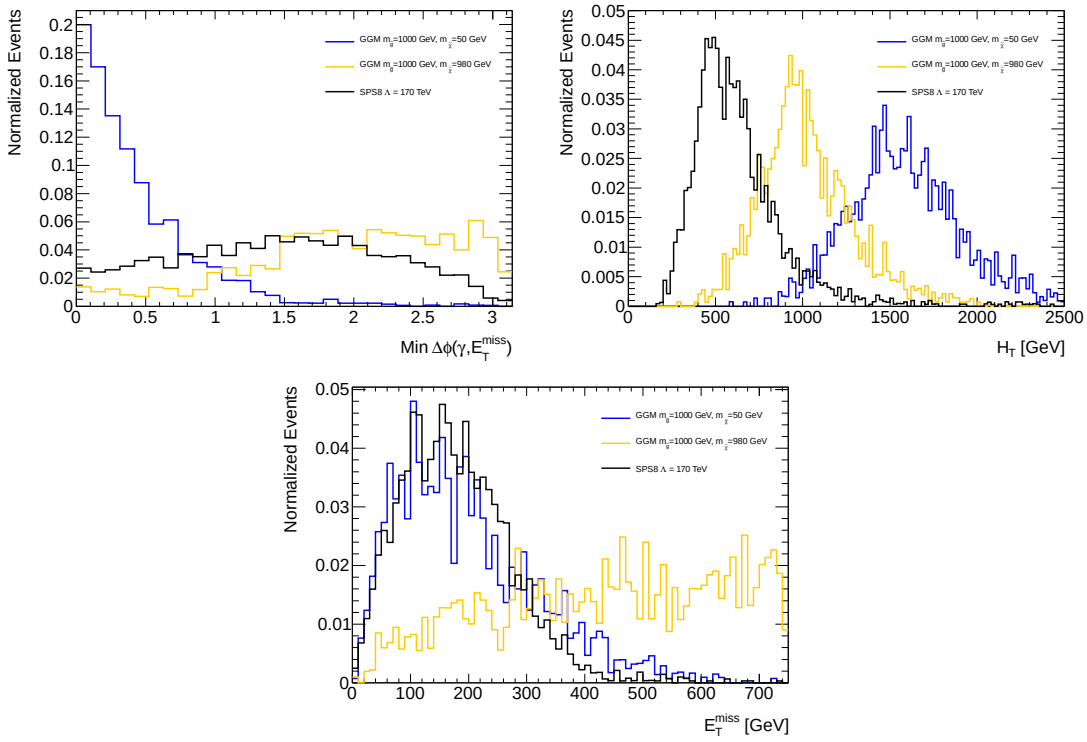

Figure 9.1: Distributions of the observables $\Delta\phi\left(\gamma,\, E_{\mathrm{T}}^{\mathrm{miss}}\right)$ (top left), H_{T} (top right), and $E_{\mathrm{T}}^{\mathrm{miss}}$ (bottom) of characteristic signal points for the different signal regions. The GGM $m(\tilde{g}) = 1000\,\mathrm{GeV}$, $m(\tilde{\chi}_1^0) = 980\,\mathrm{GeV}$ point (golden), GGM $m(\tilde{g}) = 1000\,\mathrm{GeV}$, $m(\tilde{\chi}_1^0) = 50\,\mathrm{GeV}$ point (blue), and SPS8 $\Lambda = 170\,\mathrm{TeV}$ (black) represent characteristic signal points intended to be covered signal regions A, B, and C respectively.

Signal region A is optimized for GGM scenarios where a heavy squark or gluino is produced and decays via a cascade to a lightest neutralino with a small mass difference with respect to the gluino. Signal region B is targeted to GGM scenarios where a heavy squark or gluino is produced and decays via a cascade to a neutralino NLSP with a relatively large mass separation between it and the gluino. The final signal region, C, is designed for sensitivity towards points in parameter space where direct production of

neutralinos and charginos dominates, as is generally the case with SPS8.

The distributions of the three observables for three characteristic signal points can be seen in Fig. 9.1. In terms of the $\Delta\phi$ observable the points covered by signal regions A and C generally have a good separation between the photons and the direction of the $E_{\mathrm{T}}^{\mathrm{miss}}$ in ϕ, since the mass of the decaying neutralino is generally large compared to its p_{T}. This is not the case for scenarios covered by signal region B, where the mass of the neutralino can often be small compared to its p_{T}, limiting the usefulness of this observable for this signal region. The H_{T} is generally large for all the GGM points where pairs of massive gluinos or squarks are produced. The points with large values of $m(\tilde{\chi}_1^0)$ generally have slightly lower values of H_{T} due to the generally higher fraction of the total transverse energy carried away by the gravitinos. In the case of SPS8 points, which the current analysis is sensitive to, the neutralinos and charginos produced are not significantly heavier than the $\tilde{\chi}_1^0$ [2] and generally lighter than the gluino and squark masses being probed in the GGM. As a result the H_{T} provides little differentiation from the backgrounds, as shown in Section 9.3.4, and is therefore not used in signal region C. In terms of the $E_{\mathrm{T}}^{\mathrm{miss}}$, the GGM points with a low mass neutralino and the SPS8 points have a similar distribution. Points in the GGM parameter space with a very large $m(\tilde{\chi}_1^0)$ have significantly large $E_{\mathrm{T}}^{\mathrm{miss}}$.

The values of the cuts made on the observables for each of the three signal regions was based upon Monte Carlo studies. The optimization of the cuts making up

[2]The lightest chargino and next-to-lightest neutralino are generally approximately twice the mass of the lightest neutralino. Details of the mass spectrum for a selection of SPS8 points can be seen in Section A.2 in Appendix A.

all three signal regions is described in detail in Section 9.3.4. The resulting cuts on H_{T}, $\Delta\phi\left(\gamma,\, E_{\mathrm{T}}^{\mathrm{miss}}\right)$, and $E_{\mathrm{T}}^{\mathrm{miss}}$ from the optimization for the three signal regions can be seen in Table 9.1. The results seen from applying the criteria of the three signal regions to both the real collision data and signal Monte Carlo is shown in Section 9.4.

Observable	Signal Region A	Signal Region B	Signal Region C
$\Delta\phi\left(\gamma,\, E_{\mathrm{T}}^{\mathrm{miss}}\right)$	0.5	–	0.5
H_{T}	600 GeV	1100 GeV	–
$E_{\mathrm{T}}^{\mathrm{miss}}$	200 GeV	100 GeV	125 GeV

Table 9.1: The cuts on the $\Delta\phi\left(\gamma,\, E_{\mathrm{T}}^{\mathrm{miss}}\right)$, H_{T}, and $E_{\mathrm{T}}^{\mathrm{miss}}$ observables that define the signal regions A, B, and C.

9.3 Selection Optimization

This section highlights the methods by which the selection criteria which differ compared to the previous iteration of this analysis [32] were optimized. Section 9.3.1 motivates the choice of the higher p_{T} cut of 50 GeV for this analysis, as specified in Section 7.1.3. The choice of the photon-electron overlap criteria specified in Section 9.1.1 is also an improvement compared to the previous analysis. The rationale for this choice is laid out in Section 9.3.2. The requirement that the tracks of converted photon have no hits in the pixel detector is motivated in Section 9.3.3. Lastly, the optimization procedure used to the determine the specific cuts that define the three signal regions of this analysis defined in Section 9.2 is described in Section 9.3.4.

9.3.1 Photon Transverse Momentum

The optimal p_{T} requirement for the two photons was determined via a Monte Carlo study. Several GGM and SPS8 signal points were used, and a diphoton selection was performed using a set of various p_{T} requirements. The baseline photon p_{T} requirement was 25 GeV for both photons in the $1.07\,\mathrm{fb}^{-1}$ analysis [32]. For the $t\bar{t}$, $W \to e\nu + \mathrm{jets}$, $W \to \tau\nu + \mathrm{jets}$, and $W + \gamma$ Monte Carlo samples, a photon plus electron selection is performed, and the event is given a weight of based on the η-dependent electron to photon fake rate. This fake rate varied from between $2 - 6\%$. For the QCD backgrounds, which include diphoton, dijet and γ + jet samples, a photon plus pseudo-photon selection is performed. The resulting $E_{\mathrm{T}}^{\mathrm{miss}}$ distribution from the QCD Monte Carlo is then normalized to that of the diphoton collision data in the region $E_{\mathrm{T}}^{\mathrm{miss}} < 20\,\mathrm{GeV}$. The photon p_{T} cuts are varied between 25 and 75 GeV for both the leading and subleading photon/electron/pseudo-photon. No p_{T} cuts below 25 GeV were examined due to the thresholds of the `EF_2g20_loose` trigger. A final cut requiring $E_{\mathrm{T}}^{\mathrm{miss}} > 125\,\mathrm{GeV}$ is also applied.

The expected number of background and signal events for $4.8\,\mathrm{fb}^{-1}$ of data for the various choices of the p_{T} thresholds can be seen in Table 9.2. From these values the expected significance at each point is estimated using a significance estimator defined as

$$\mathcal{S}_{\mathrm{est}} = \sqrt{2[(S+B)\ln(1+S/B) - S]}, \tag{9.2}$$

where S and B are the number of signal and background events, respectively. The values

Leading/subleading p_T cut	25/25	50/25	60/25	75/25	50/50	50/75	75/75
Total Background	24.6	20	17.6	14.7	8.0	7.0	3.0
GGM (800,150)	26.1	26.1	25.4	24.2	19.4	18.7	13.6
GGM (800,400)	29.8	29.8	29.8	29.8	28.5	28.5	26.3
GGM (800,700)	31.9	31.9	31.9	31.9	31.6	31.6	31.0
GGM (800,780)	36.7	36.7	36.7	36.6	36.6	36.6	36.6
GGM (900,50)	6.1	6.0	5.9	5.5	4.5	4.3	3.1
GGM (900,400)	9.0	9.0	9.0	8.9	8.5	8.5	7.6
GGM (900,800)	9.9	9.9	9.9	9.9	9.8	9.8	9.7
SPS8 $\Lambda = 140\,\text{TeV}$	52.4	52.4	51.7	49.4	41.9	40.4	26.2
SPS8 $\Lambda = 170\,\text{TeV}$	20.5	20.4	20.3	19.8	17.9	17.6	13.2

Table 9.2: The expected event numbers for various model-space points, as a function of the cut on the leading/subleading photon p_T.

of this estimated significance for each set of the p_{T} thresholds can be seen in Table 9.3. As can be seen from Table 9.3 the value of the significance estimator is highest for a p_{T} cut of 75 GeV on both photons for all tested signal points except the $\Lambda = 140\,\text{GeV}$ SPS8 point. However, due to worries of low statistics in the data-driven control samples used to estimate the expected Standard Model backgrounds, a lower p_{T} cut of 50 GeV on both photons was chosen. This choice of p_{T} still offers a significant improvement in sensitivity compared to a $p_{\text{T}} > 25\,\text{GeV}$ cut.

Leading/subleading p_T cut	25/25	50/25	60/25	75/25	50/50	50/75	75/75
GGM (800,150)	4.7	5.0	5.1	5.2	5.4	5.4	5.4
GGM (800,400)	5.2	5.6	5.9	6.2	7.3	7.3	9.0
GGM (800,700)	5.5	5.9	6.2	6.6	8.0	8.0	10.2
GGM (800,780)	6.2	6.7	7.0	7.4	8.9	8.9	11.5
GGM (900,50)	1.2	1.3	1.3	1.4	1.5	1.5	1.6
GGM (900,400)	1.7	1.9	2.0	2.1	2.6	2.7	3.0
GGM (900,800)	1.9	2.1	2.2	2.4	3.4	3.4	4.2
SPS8 $\Lambda = 140\,\text{TeV}$	8.5	9.0	9.3	9.4	9.9	9.9	9.0
SPS8 $\Lambda = 170\,\text{TeV}$	3.7	4.0	4.2	4.4	5.0	5.0	5.3

Table 9.3: Estimated significance, using the significance estimator from Eq.. 9.2 with signal and background numbers taken from Table 9.2, for various signal points, as a function of the cut on the leading/subleading photon p_T.

9.3.2 Photon and Electron Overlap Criteria

Previous iterations of this analysis used a overlap removal procedure different than that described in Section 9.1.1. Under the old criteria if the clusters of a photon and an electron were found to be within $\Delta R < 0.01$, the object was interpreted as photon and the electron removed. This was done to maximize the acceptance of photons, but comes at the cost of a significant increase in the electron to photon fake rate. Studies performed on Monte Carlo indicate that the current overlap criteria reduces the electron to photon fake rate in Standard Model events from between 0.046 to 0.168, depending on the η of the object, to between 0.025 and 0.075. This reduces the acceptance of real photons from SUSY signal samples by only 10-15%.

Overlap Requirement	Old	Current
$t\bar{t}$	2.5	0.8
$W \to e\nu + \text{jets}$	3.1	1.3
$W \to \tau\nu + \text{jets}$	0.3	0.1
$W + \gamma$	6.1	2.8
$Z + \gamma$	0.4	0.1
$WW/ZZ/WZ$	0.2	0.1
Total Background	12.6	5.2
GGM (900,50)	18.0 (4.3)	15.8 (5.2)
GGM (900,880)	27.4 (6.1)	23.6 (7.2)
SPS8 ($\Lambda = 170\,\text{TeV}$)	17.0 (4.1)	14.4 (4.8)

Table 9.4: Table of expected event numbers for various model-space points, as a function of the old versus current photon-electron overlap requirement, for p_T cuts of (50 GeV/50 GeV) on the two photons and $E_{\text{T}}^{\text{miss}}$ cut of greater than 125 GeV. The resulting values of the significance estimator, $\mathcal{S}_{\text{est}}$, are shown in parentheses for the signal Monte Carlo points.

The breakdown of the various contributions to the number of expected background and signal events for $4.8\,\text{fb}^{-1}$ of data for the old and new overlap criteria is

shown in Table 9.4. These numbers assume a photon p_{T} cut of 50 GeV on both photons and a $E_{\mathrm{T}}^{\mathrm{miss}}$ cut of 125 GeV. The improvement of the significance expected from this cut is determined by applying the significance estimator, $\mathcal{S}_{\mathrm{est}}$, to the expected signal and background numbers from Table 9.4. Comparing the old overlap requirement to the current one the value of the estimator goes from $4.3 \rightarrow 5.2$, $6.1 \rightarrow 7.2$, and $4.1 \rightarrow 4.8$ for the GGM ($m(\tilde{g}) = 900\,\mathrm{GeV}$, $m(\tilde{\chi}_1^0) = 50\,\mathrm{GeV}$), GGM ($m(\tilde{g}) = 900\,\mathrm{GeV}$, $m(\tilde{\chi}_1^0) = 880\,\mathrm{GeV}$) and SPS8 $\Lambda = 170\,\mathrm{TeV}$ signal points respectively.

9.3.3 Photon Pixel Hit Veto

Requiring that a converted photon have no pixel hits on any of its associated conversion tracks was devised as a potential method to reduce the rate at which electrons faked photons. The effectiveness of this requirement was tested by applying it to several signal MC points, and making the diphoton selection with and without this requirement. This was then compared to several background MC samples with electrons including $t\bar{t}$, $W \rightarrow l\nu$ + jets, $W\gamma$, $Z\gamma$, WW, ZZ, and WZ samples.

Table 9.5 shows the number of expected events for the total background and signal for various points in the GMSB model space as a function of the applied pixel hit requirement, scaled to a luminosity of $4.8\,\mathrm{fb}^{-1}$, for p_{T} cuts of (50 GeV/50 GeV) on the two photons. The resulting signal significance is shown in parentheses next to the value of the expected number of events for each signal model.

Pixel Hit Requirement	Not Applied	Applied
Total Background	5.2	4.3
GGM (900,50)	15.8 (5.2)	15.6 (5.5)
GGM (900,880)	23.6 (7.2)	23.4 (7.5)
SPS8 ($\Lambda = 170\,\mathrm{TeV}$)	14.4 (4.8)	14.2 (5.1)

Table 9.5: Table of expected event numbers for various model-space points, as a function of the application of the no pixel hit requirement, for p_T cuts of (50 GeV/50 GeV) on the two photons and $E_{\mathrm{T}}^{\mathrm{miss}}$ cut of greater than 125 GeV. The resulting values of the significance estimator, $\mathcal{S}_{\mathrm{est}}$, are shown in parentheses.

9.3.4 Signal Region Optimization

The optimization of the three signal regions discussed in Section 9.2 was performed via a Monte Carlo study. The samples used to model the Standard Model background are those listed in Tables 8.2 and 8.3. The base event selection from Section 9.1 was applied to all of these Monte Carlo samples. In order to maximize the available statistics, events with one baseline photon (see Section 7.1.7 for details) plus one photon-replacement electron (see Section 7.2.3 for details) were selected from the samples in Table 8.2. This was done because the majority of reconstructed diphoton events in these samples contain at least one photon which is due to a misidentified true electron. Each event was then reweighted by an η-dependent, electron-to-photon fake, which was extracted from $Z \to ee$ Monte Carlo. Finally, these samples were normalized to the equivalent $4.8\,\mathrm{fb}^{-1}$ using the cross sections listed in Table 8.2.

The estimated background contribution from QCD events was estimated separately using the samples in Table 8.3. Events with a single baseline candidate photon were selected. A normalization factor was then obtained, which is the ratio of the num-

ber of events with $E_{\mathrm{T}}^{\mathrm{miss}} < 20\,\mathrm{GeV}$ to the number of observed diphoton events with $E_{\mathrm{T}}^{\mathrm{miss}} < 20\,\mathrm{GeV}$ in $4.8\,\mathrm{fb}^{-1}$ of collision data. This normalization factor was the only input from the real collision data to this optimization. The QCD Monte Carlo sample was then scaled by the normalization factor.

A different representative signal Monte Carlo point was used for the optimization of each signal region. These were the GGM ($m(\tilde{g}) = 900\,\mathrm{GeV}$, $m(\tilde{\chi}_1^0) = 800\,\mathrm{GeV}$ point for signal region A, the GGM $m(\tilde{g}) = 900\,\mathrm{GeV}$, $m(\tilde{\chi}_1^0) = 50\,\mathrm{GeV}$ point for signal region B, and the SPS8 ($\Lambda = 170\,\mathrm{GeV}$ point for signal region C. The standard base event selection was applied to all three of these samples. Each event was also required to have two baseline candidate photons. These samples were then normalized to the equivalent $4.8\,\mathrm{fb}^{-1}$ using the appropriate NLO or NLO+NLL cross sections, which were discussed in Section 8.3.

	$E_{\mathrm{T}}^{\mathrm{miss}}$	H_{T}	$\Delta\phi$	Significance
A	200 GeV	600 GeV	0.6	17.7 [GGM(900,800)]
B	100 GeV	1150 GeV	–	8.4 [GGM(900,50)]
C	125 GeV	–	0.8	7.1 [SPS8 $\Lambda = 170$ TeV]

Table 9.6: Raw cut values obtained from the optimization procedure of the three signal regions.

The optimization was then performed by applying a series of candidate values for the cuts on $\Delta\phi$, H_{T}, and $E_{\mathrm{T}}^{\mathrm{miss}}$. This yielded an expected number of signal and background events for each set of potential cuts. The expected signal and background values were then used as inputs to a significance estimator defined in Eq. 9.2. The optimal set of cuts for each signal region were those that maximized the value of the

significance estimator. The optimization was found to be quite flat around the maximum in $\Delta\phi$, and so a generic cut of 0.5 was chosen for signal regions A and C. Finally, the H_{T} cut for signal region B was rounded down to 1100 GeV, leading to the final cut choices shown in Table 9.1. Also note that no $\Delta\phi\left(\gamma,\, E_{\mathrm{T}}^{\mathrm{miss}}\right)$ cut is applied for signal region B and no requirement on H_{T} is made for signal region C.

9.4 Signal Region Results

This section highlights the results of applying the base event selection from Section 9.1 and the subsequent individual signal region selections from Section 9.2 to both the 2011 collision data set specified in Section 8.1 and the GGM and SPS8 signal Monte Carlo samples described in Section 8.3. Table 9.7 shows the cut flow performed on the 2011 collision data as well as a few representative signal points. The number of Monte Carlo events are normalized to correspond to $4.8\,\mathrm{fb}^{-1}$ of data based on the appropriate NLO or NLO+NLL cross section from Section 8.3. As can be seen no events in the 2011 collision data pass the selection criteria for either signal regions A or B. Two events do pass the selection criteria from signal region C.

The various observables used to define the signal regions can be seen for collision data and example signal Monte Carlo points in Fig. 9.2 and 9.3. These distribution are shown after the diphoton selection has been applied, but prior to any of the signal region cuts. The left side of Fig. 9.2 shows the p_{T} of the leading photon candidate in each event, while the right side show the $E_{\mathrm{T}}^{\mathrm{miss}}$ distribution of the events. Similarly,

Selection	Data			GGM			SPS8		
All events			–			48.1			61.6
GRL+Trigger			1166060			27.1			44.5
Vertex			1163257			27.0			44.3
LAr Error			1159774			27.0			44.3
Jet Cleaning			1158390			27.0			44.1
Muon veto			1158256			27.0			43.9
LAr veto			1156641			26.9			43.8
Diphoton			10455			12.2			17.0
	A	B	C	A	B	C	A	B	C
$\Delta\phi$	7293	–	7293	10.8	–	10.8	14.7	–	14.7
H_{T}	117	9	–	10.8	10.5	–	6.5	0.9	–
$E_{\mathrm{T}}^{\mathrm{miss}}$	0	0	2	7.9	9.5	9.6	2.7	0.8	10.4

Table 9.7: Cut flows for 2011 collision data and select signal MC samples. The numbers shown are the number of events after each selection step. The number of MC events are scaled to the data luminosity of $4.8\,\mathrm{fb}^{-1}$ based upon the appropriate cross-section from Section 8.3. The data starts from a skim requiring, in addition to the trigger and GRL, one loose photon with $p_{\mathrm{T}} > 45\,\mathrm{GeV}$. The GGM point shown is the $m(\tilde{g}) = 1000\,\mathrm{GeV}$,$m(\tilde{\chi}_1^0) = 450\,\mathrm{GeV}$ point, while the SPS8 point shown is the $\Lambda = 170\,\mathrm{TeV}$ point.

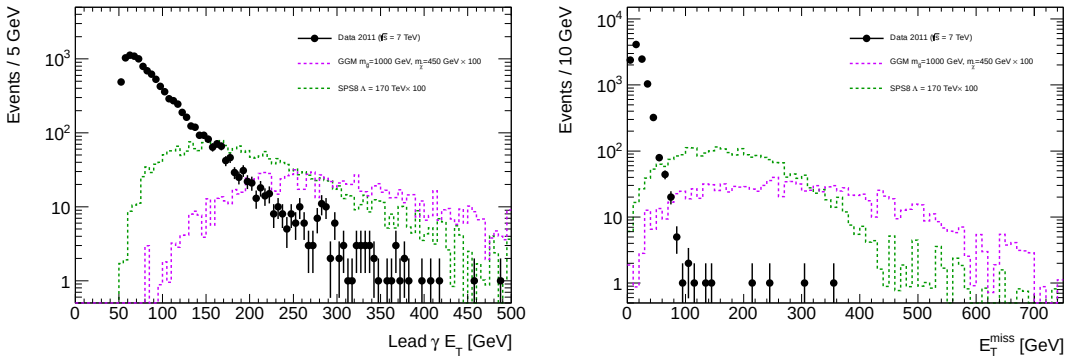

Figure 9.2: Transverse momentum of the leading photon (left) and $E_{\mathrm{T}}^{\mathrm{miss}}$ (right) for data and signal Monte Carlo. These are shown after the diphoton selection, but prior to the signal region selections. The signal points are the GGM ($m(\tilde{g}) = 1000\,\mathrm{GeV}$,$m(\tilde{\chi}_1^0) = 450\,\mathrm{GeV}$) point and the SPS8 $\Lambda = 170\,\mathrm{TeV}$ point.

Fig. 9.3 shows the H_{T} for the events on the left and the minimum of the $\Delta\phi$ between either of the two highest p_{T} photon candidates and the $E_{\mathrm{T}}^{\mathrm{miss}}$ on the right.

The $E_{\mathrm{T}}^{\mathrm{miss}}$ distribution of the data and signal Monte Carlo after applying a cut on H_{T} of either 600 GeV or 1100 GeV to the diphoton selection can be seen in Fig. 9.4. In the plot where the cut of $H_{\mathrm{T}} > 1100\,\mathrm{GeV}$ is applied, the portion with $E_{\mathrm{T}}^{\mathrm{miss}}$ greater than 100 GeV is signal region B. Two Alternative plots of the $E_{\mathrm{T}}^{\mathrm{miss}}$ distributions of the data and signal Monte Carlo can also be seen in Fig. 9.5. In both these plots a cut on $\Delta\phi\left(\gamma,\, E_{\mathrm{T}}^{\mathrm{miss}}\right)$ of less than 0.5 is imposed. A different H_{T} cuts is applied to each plot: no H_{T} cut and $H_{\mathrm{T}} > 600\,\mathrm{GeV}$. The area of $E_{\mathrm{T}}^{\mathrm{miss}} > 125\,\mathrm{GeV}$ for the plot with no H_{T} cut is signal region C, and area of $E_{\mathrm{T}}^{\mathrm{miss}} > 200\,\mathrm{GeV}$ for the plot with an H_{T} cut of 600 GeV is signal region A.

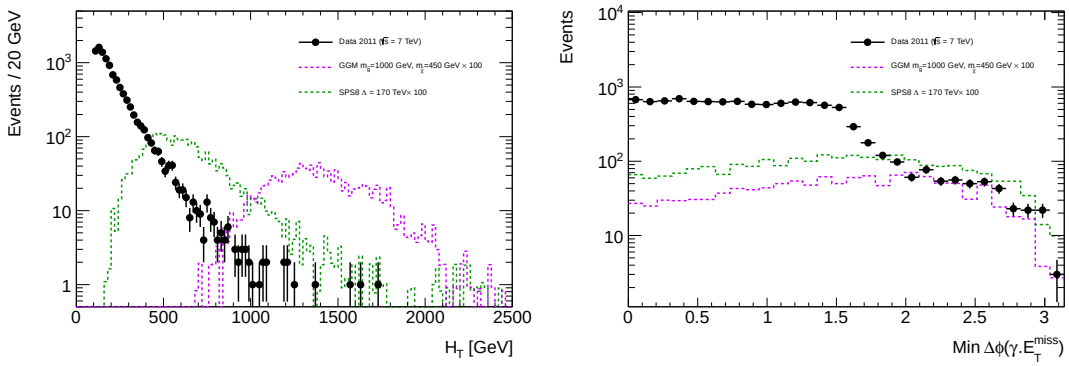

Figure 9.3: The H_{T} (left) and minimum $\Delta\phi\left(\gamma,\, E_{\mathrm{T}}^{\mathrm{miss}}\right)$ (right) for data and signal Monte Carlo. These are shown after the diphoton selection, but prior to the signal region selections. The signal points are the GGM ($m(\tilde{g}) = 1000\,\mathrm{GeV}$,$m(\tilde{\chi}_1^0) = 450\,\mathrm{GeV}$) point and the SPS8 $\Lambda = 170\,\mathrm{TeV}$ point.

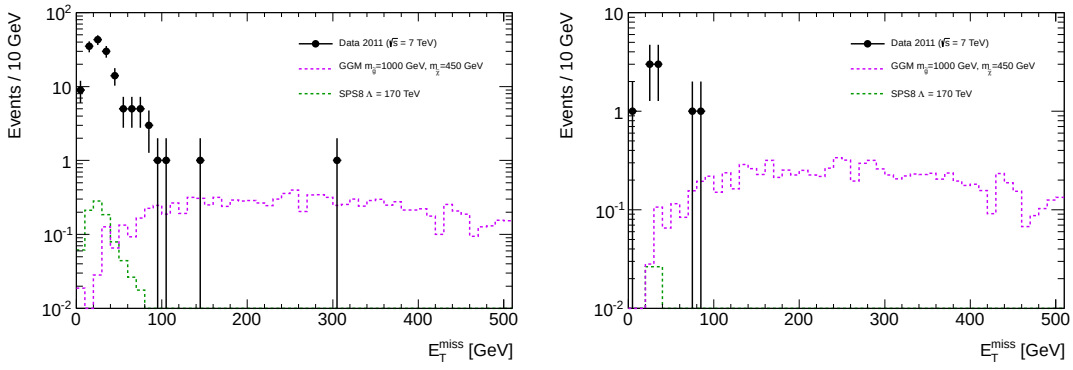

Figure 9.4: $E_{\mathrm{T}}^{\mathrm{miss}}$ distribution of data and signal Monte Carlo after a requirement of $H_{\mathrm{T}} > 600\,\mathrm{GeV}$ (left) and $H_{\mathrm{T}} > 1100\,\mathrm{GeV}$ (right). Signal region B is the area in the right-hand plot with values of $E_{\mathrm{T}}^{\mathrm{miss}} > 100\,\mathrm{GeV}$; no events are observed. Signal region A requires an additional cut of $\Delta\phi > 0.5$ (see Fig. 9.5). The signal points are the GGM ($m(\tilde{g}) = 1000\,\mathrm{GeV}$,$m(\tilde{\chi}_1^0) = 450\,\mathrm{GeV}$) point and the SPS8 $\Lambda = 170\,\mathrm{TeV}$ point.

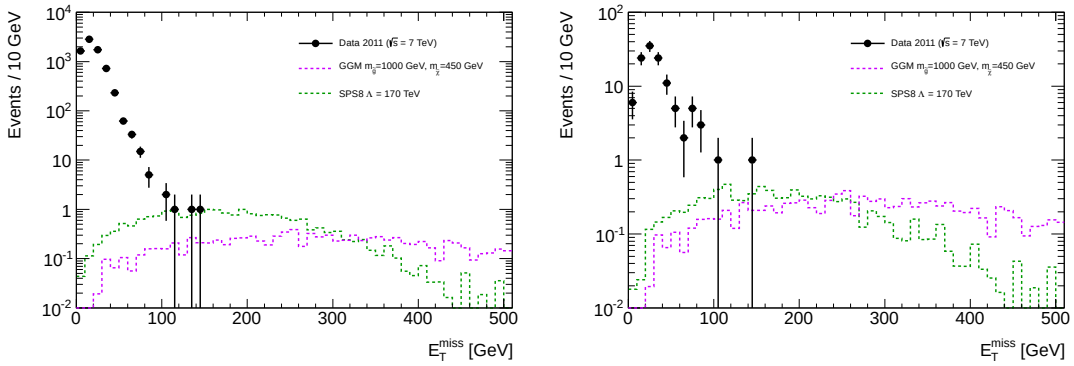

Figure 9.5: $E_{\mathrm{T}}^{\mathrm{miss}}$ distribution of data and signal Monte Carlo for all values of H_{T} (left) and for $H_{\mathrm{T}} > 600\,\mathrm{GeV}$ (right) after requiring $\Delta\phi\left(\gamma,\, E_{\mathrm{T}}^{\mathrm{miss}}\right) > 0.5$. Signal region B is the area in the left-hand plot with values of $E_{\mathrm{T}}^{\mathrm{miss}} > 125\,\mathrm{GeV}$; two events are observed. Signal region A is the region of $E_{\mathrm{T}}^{\mathrm{miss}} > 200\,\mathrm{GeV}$ in the right-hand plot; no events are observed. The signal points are the GGM ($m(\tilde{g}) = 1000\,\mathrm{GeV}$,$m(\tilde{\chi}_1^0) = 450\,\mathrm{GeV}$) point and the SPS8 $\Lambda = 170\,\mathrm{TeV}$ point.

9.4.1 Signal Region Monte Carlo Acceptances

Visual representations of the acceptances of the various signal regions for the GGM points can be seen in Fig. 9.6, 9.7, and 9.8 for signal regions A, B, and C, respectively. Detailed numerical tables of the acceptances of each GGM point for all three signal regions can be seen in Section A.1.1 of Appendix A. The acceptances of all the SPS8 points for all three signal regions can be seen in Fig. 9.9. The detailed numerical values of all these acceptances can be seen in Section A.2.2 of Appendix A.

For GGM points with a low mass for the lightest neutralino signal region B has significantly higher acceptances than A for the same points. As an example the $m(\tilde{g}) = 1300\,\mathrm{GeV}$, $m(\tilde{\chi}_1^0) = 50\,\mathrm{GeV}$ GGM point has an acceptance of 25.9 % for signal region B and only 4.1 % for signal region A. The acceptances of signal region B are generally poorer than that of signal region A for GGM points with a large value of

$m(\tilde{\chi}_1^0)$. This is especially pronounced for points with low squark or gluino masses, which is due to the inefficiency of the H_{T} cut here. For the $m(\tilde{g}) = 800\,\mathrm{GeV}$, $m(\tilde{\chi}_1^0) = 750\,\mathrm{GeV}$ GGM point signal region A has an acceptance of 21.4 % while signal region B only has one of 4.7 %.

Signal region C, which is the closest of the three to the signal region of the previous analyses [46, 32], provides slightly more uniform acceptances over the GGM parameter space than A or B though it has noticeable dip in acceptance for points with low $m(\tilde{\chi}_1^0)$. The acceptances of signal region C for the GGM are comparable to slightly greater than those of signal region A. Signal region A still provides better sensitivity to high mass neutralino points than signal region C because of the significantly lower number of expected Standard Model background events of signal region A as will be shown in Chapter 10. For GGM points with low values of $m(\tilde{\chi}_1^0)$ the acceptances of signal region B are significantly higher than those of signal region C.

The acceptances for SPS8 are the highest for signal region C as expected. Although the acceptances are quite low for the lowest points in Λ, these points have already been previously excluded as shown in Section 4.2. For points on the SPS8 slope with values of $\Lambda >= 140\,\mathrm{TeV}$ the acceptances range from 13.1 % to 21.5 %. Note that the only difference between signal region A and C is the cut on H_{T} of 600 GeV, which is the reason for the worse performance of signal region A for SPS8.

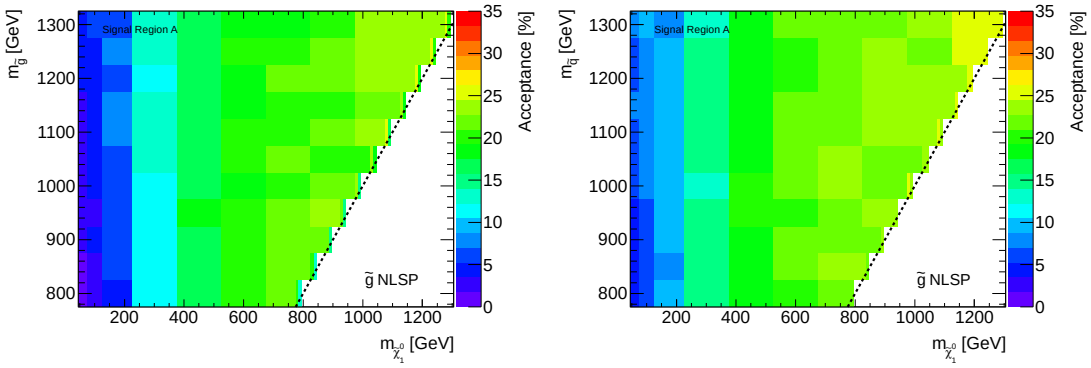

Figure 9.6: Acceptances of signal region A for all the GGM Monte Carlo signal points plotted as a function of the mass of the gluino (left) or squark (right) versus the mass of the lightest neutralino.

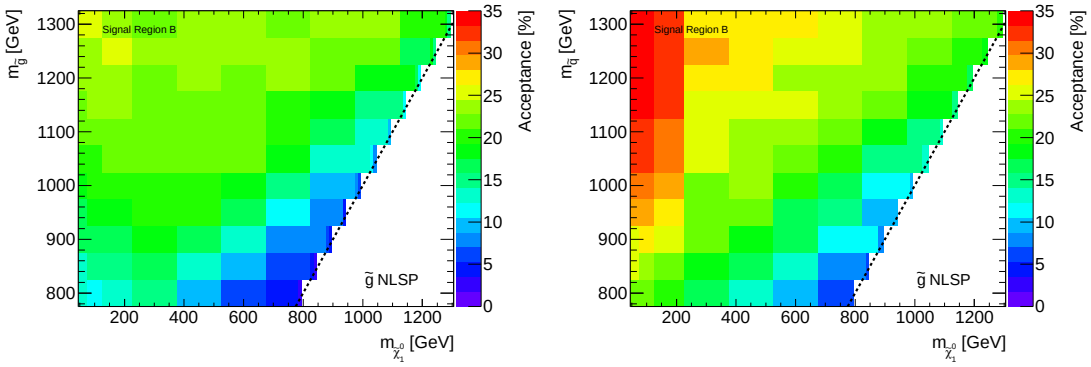

Figure 9.7: Acceptances of signal region B for all the GGM Monte Carlo signal points plotted as a function of the mass of the gluino (left) or squark (right) versus the mass of the lightest neutralino.

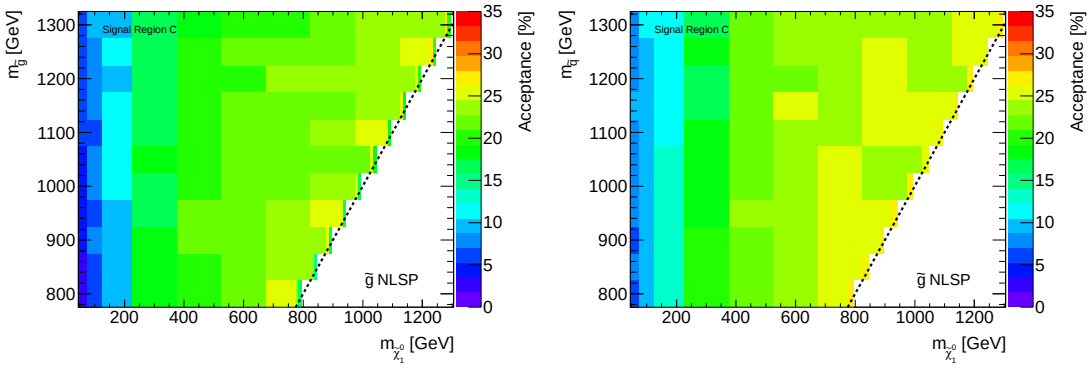

Figure 9.8: Acceptances of signal region C for all the GGM Monte Carlo signal points plotted as a function of the mass of the gluino (left) or squark (right) versus the mass of the lightest neutralino.

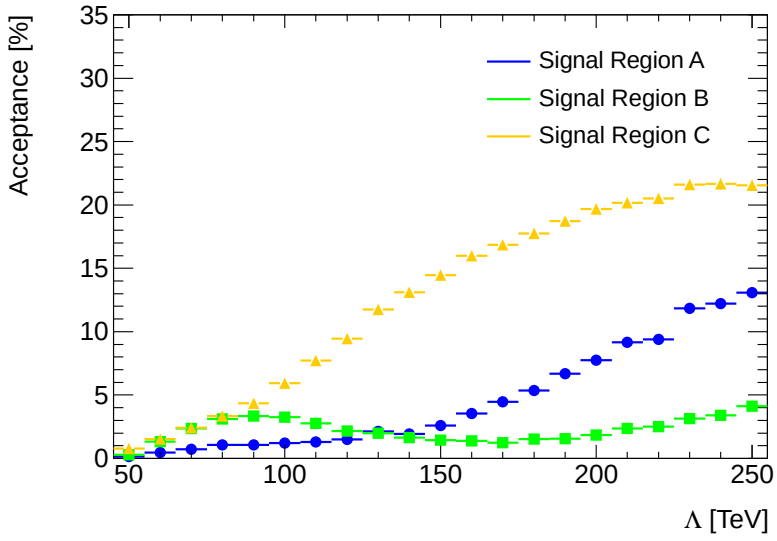

Figure 9.9: Acceptances of all three signal region for the SPS8 Monte Carlo signal points plotted as a function of Λ.

Chapter 10

The Background Model

One of the most important aspects of this analysis is the modeling and subsequent estimation of the expected contribution from Standard Model backgrounds. The observed number of events passing the selections from Chapter 9 has no meaning without a hypothesis for the expected background level. There are two grand categories of background events: events with a true diphoton plus $E_{\mathrm{T}}^{\mathrm{miss}}$ signature and events that fake that signature. Events that in some form fake the signature constitute the bulk of the expected Standard Model background, as will be shown in this chapter.

Diphoton plus $E_{\mathrm{T}}^{\mathrm{miss}}$ signatures where both the photons and the missing transverse energy are real, such as $W \to \ell\nu + \gamma\gamma$ and $Z \to \nu\nu + \gamma\gamma$, are relatively rare in the Standard Model. Those two processes have a combined NLO cross-section of $\sim 0.2\,\mathrm{pb}$ at $\sqrt{s} = 7\,\mathrm{TeV}$. This category of backgrounds is referred to as irreducible because they cannot be reduced by improvements in misidentification. Some differentiation of these backgrounds from the signal is possible, since the photons in these events are produced

by radiation, and the likelihood of having two radiated photons with high p_{T} is small. Also, in order for a $W \to \ell\nu + \gamma\gamma$ or $Z \to \nu\nu + \gamma\gamma$ event to pass the $E_{\mathrm{T}}^{\mathrm{miss}}$ of any of the signal regions, which is greater than 100 GeV in all cases, the produced vector boson is required to have a transverse momentum of its own. These irreducible background components are modeled purely from Monte Carlo, and this is discussed in more depth in Section 10.3.

Events which fake a diphoton plus $E_{\mathrm{T}}^{\mathrm{miss}}$ signature can be broken down into roughly three categories: collision events with at least one photon which is faked by an electron and $E_{\mathrm{T}}^{\mathrm{miss}}$ arising from high p_{T} neutrinos from the leptonic decay of a $W^{\pm}$ boson, collision events with real or fake photons and *fake*[1] $E_{\mathrm{T}}^{\mathrm{miss}}$ which is not due to the presence of high p_{T} neutrinos, and non-collision events. All three of theses background categories are modeled in a data driven way. The two collision event categories are the dominant source of backgrounds and are referred to as the QCD background and the electroweak backgrounds. The details on the modeling and the estimates themselves are included in Sections 10.1 and 10.2, respectively. The estimation of the collision background due to cosmic rays is described in Section 10.4, and they are found to be negligible.

The certainty with which the background estimate is known is just as important as the actual value of the background estimate. Several systematic errors are assessed on the various components to the background. These systematic errors and the

[1]The use of term *fake* here is used as a catch-all term for apparent missing transverse energy arising as the result of energy resolution effects, incomplete detector acceptance, and neutrinos produced in hadron decays which also degrade the jet energy resolution.

methodology for deriving them are described in Section 10.5. The various systematics on the background components are treated as uncorrelated, and are therefore combined by adding in quadrature. The final total background estimate and its associated uncertainties are presented in Section 10.6.

10.1 Modeling of the QCD Background

One important component of the background is due to Standard Model diphoton, photon+jet, and multi-jet events, which will be referred to as the QCD background. The apparent photons in these events can come both from both true photons and jets faking photons[2]. Another characteristic of such events is that the observed $E_{\mathrm{T}}^{\mathrm{miss}}$ is due primarily to energy resolution in the calorimeter, neutrinos from hadron decays in jets (which also degrades the energy resolution for jets), and incomplete detector acceptance. Due to the relatively poorer energy resolution of hadronic jets compared to photons and electrons, the $E_{\mathrm{T}}^{\mathrm{miss}}$ distribution of events with jets has a longer tail than in events with purely electromagnetic objects like photons and electrons.

The general strategy for modeling this background follows the same procedure as used in the previous iteration of this analysis [32]. The general prescription is to create a template $E_{\mathrm{T}}^{\mathrm{miss}}$ distribution that accurately models the shape of the QCD component of the diphoton sample. This procedure is done individually for each signal region. Three control regions are defined in order to derive this template. They are

[2]Often when a jet fakes a photon it is because a large fraction of the jet's energy was carried by neutral pions, which decay to photons; however such energy deposits are still considered fake photons for the purposes of this analysis

named two photon QCD control sample, $\mathrm{QCD}_{\gamma\gamma}$, the single photon QCD control sample, QCD_{γ}, and the dielectron control sample. The exact criteria defining the three control samples is included in Section 10.1.1.This control samples are intended to model different potential components of the QCD background. The $\mathrm{QCD}_{\gamma\gamma}$ sample is intended to model photon+jet events, while the QCD_{γ} sample is intended to more closely mimic the $E_{\mathrm{T}}^{\mathrm{miss}}$ distribution of multi-jet events. The dielectron sample is intended to model the contribution from Standard Model diphoton events, since electrons and photons have very similar energy measurement resolutions in the calorimeter. In principle the $E_{\mathrm{T}}^{\mathrm{miss}}$ template should be created from a combination of the $E_{\mathrm{T}}^{\mathrm{miss}}$ distributions of all three control samples. However, as is explained in more detail in Section 10.1.1, the dielectron control sample is not directly used in the background estimate, and only serves as a cross check for deriving systematic uncertainties.

Once a suitable $E_{\mathrm{T}}^{\mathrm{miss}}$ template has been created, all the cuts defining the specific signal region except $E_{\mathrm{T}}^{\mathrm{miss}}$ are applied to the diphoton sample. The $E_{\mathrm{T}}^{\mathrm{miss}}$ template is then normalized to the number of events within the normalization region of $E_{\mathrm{T}}^{\mathrm{miss}} < 20\,\mathrm{GeV}$ of the diphoton sample. The number of events with a $E_{\mathrm{T}}^{\mathrm{miss}}$ greater than the cut defined for the signal region is then taken for the normalized $E_{\mathrm{T}}^{\mathrm{miss}}$ template. This value then constitutes the expected QCD background component for that signal region. This procedure is explained in more depth in Section 10.1.2, and is referred to as the nominal method.

As the choice of the name for the background estimation method described above suggests there is an additional method used to calculate the QCD background.

This alternative estimation method, which is described in detail in Section 10.1.3, is necessary due to very low statistics in the control regions used to create the $E_{\mathrm{T}}^{\mathrm{miss}}$ templates for signal regions A and B. No events are present in the control regions for A or B giving a nominal background estimate of 0 events for both. This allows only for a fairly loose 90% CL upper limit to be set for the QCD background in those to signal regions, which is not particularily desirable within the limit setting formalism used for the analysis.

The alternative method involves relaxing in steps the H_{T} cuts applied to the control samples used for constructing the $E_{\mathrm{T}}^{\mathrm{miss}}$ template for each signal region. The resulting higher statistics alternative $E_{\mathrm{T}}^{\mathrm{miss}}$ templates cannot be used directly for the final estimated background number because the H_{T} and $E_{\mathrm{T}}^{\mathrm{miss}}$ distributions can be quite correlated. Instead estimates made using progressively relaxed H_{T} cuts are used to extrapolate the background prediction to the nominal value of the H_{T} cut. This method is likely a fairly conservative overestimate of the expected QCD background, so the average of the two methods is used for the predicted QCD background for signal regions A and B. A 100% systematic uncertainty is then assigned to this background contribution to cover the span between the two methods.

10.1.1 QCD Control Samples

This section describes the control samples used to construct the $E_{\mathrm{T}}^{\mathrm{miss}}$ template used for the estimation of the QCD background. All events in each control sample are required to pass the base event selection defined in Section 9.1. The exact cuts defining

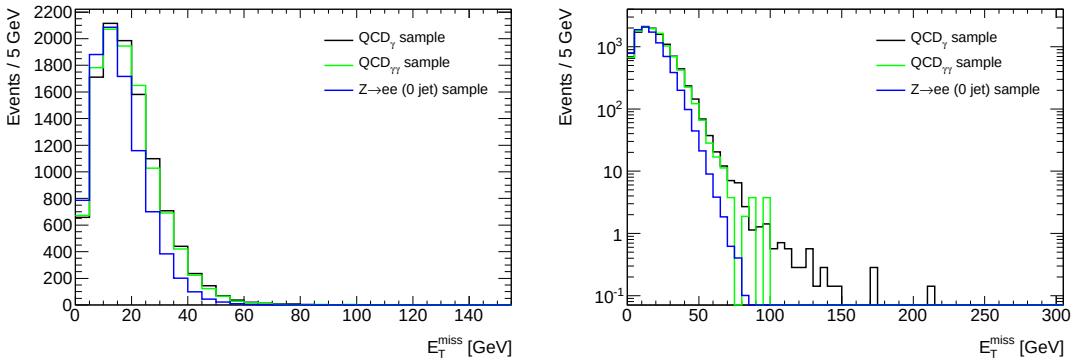

Figure 10.1: Comparison of the $E_{\mathrm{T}}^{\mathrm{miss}}$ distributions from the QCD_{γ} sample (black line), $\mathrm{QCD}_{\gamma\gamma}$ sample (green line) and the dieletron (0 jet) sample, (blue line) plotted on both a linear (left) and log (right) scale. None of the signal region specific cuts are applied in these plots. Also, the control samples are normalized to the diphoton sample for the region $E_{\mathrm{T}}^{\mathrm{miss}} < 20\,\mathrm{GeV}$.

the three different samples are each defined individually in Sections 10.1.1.1, 10.1.1.2, and 10.1.1.3. The $E_{\mathrm{T}}^{\mathrm{miss}}$ distributions of the three control samples can be seen in Fig. 10.1. The $E_{\mathrm{T}}^{\mathrm{miss}}$ distributions of the $\mathrm{QCD}_{\gamma\gamma}$ and QCD_{γ} samples are very similar though the $\mathrm{QCD}_{\gamma\gamma}$ sample has an order of magnitude less statistics than the QCD_{γ} sample. In general the dielectron control sample has a much smaller tail to its $E_{\mathrm{T}}^{\mathrm{miss}}$ distribution compared to the $\mathrm{QCD}_{\gamma\gamma}$ and QCD_{γ} samples.

The original intention was to fit a linear combination of the $E_{\mathrm{T}}^{\mathrm{miss}}$ distributions of the three control samples[3] to the low $E_{\mathrm{T}}^{\mathrm{miss}}$ region of the diphoton samples. The three distributions would then be combined in the fractions determined by the fit to create the $E_{\mathrm{T}}^{\mathrm{miss}}$ template. Both previous iterations of this analysis observed that a 100 % $\mathrm{QCD}_{\gamma\gamma} + \mathrm{QCD}_{\gamma}$ template gave the best match to the shape of the diphoton sample at

[3]The shapes of the $E_{\mathrm{T}}^{\mathrm{miss}}$ distributions of the $\mathrm{QCD}_{\gamma\gamma}$ and QCD_{γ} samples are so similar that a simple unweighted combination of them is used.

low $E_{\mathrm{T}}^{\mathrm{miss}}$ [32, 46]. As a result the $\mathrm{QCD}_{\gamma\gamma} + \mathrm{QCD}_{\gamma}$ sample is used to construct the $E_{\mathrm{T}}^{\mathrm{miss}}$ template, with the dielectron sample merely serving a cross check used in the estimation of systematic uncertainties.

10.1.1.1 Two Photon QCD Control Sample

The two photon QCD control sample is referred to as $\mathrm{QCD}_{\gamma\gamma}$ for short. Any event containing two baseline photon candidates, as defined in Section 7.1.7, is rejected to ensure this sample is orthogonal to the diphoton sample. Events are also rejected if they contain at least one baseline electron candidate, as defined in Section 7.2.3,in order to obtain a sample that is orthogonal to the electron-photon control sample, which will be described in Section 10.2. An event is then accepted into this sample if it contains exactly one baseline photon candidate plus one pseudo-photon candidate (see Section 7.1.7 for details), or the event contains exactly two pseudo-photon candidates and no baseline photon candidate.

10.1.1.2 Single Photon QCD Control Sample

The single photon QCD control sample is referred to as QCD_{γ} for short. This control sample is designed to be orthogonal to the $\mathrm{QCD}_{\gamma\gamma}$ sample as well as the other background samples. Its primary purpose is to act as a sample with a similar $E_{\mathrm{T}}^{\mathrm{miss}}$ distribution to the $\mathrm{QCD}_{\gamma\gamma}$ sample but with higher statistics. To create the sample any event with either a baseline photon candidate or a baseline electron candidate is rejected from the sample. A event is then accepted into the sample if it possesses exactly one

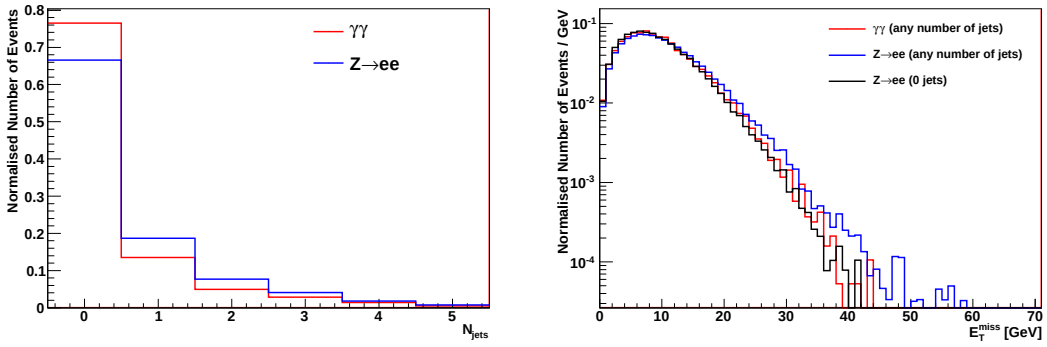

Figure 10.2: Comparison of the number of jets (left) and $E_{\mathrm{T}}^{\mathrm{miss}}$ (right) from the Standard Model diphoton Monte Carlo and $Z \rightarrow ee$ Monte Carlo samples. All distribution are normalized to an integral of one for the purposes of shape comparison.

pseudo-photon candidate.

10.1.1.3 Dielectron Control Sample

The dielectron sample is intended to mimic the $E_{\mathrm{T}}^{\mathrm{miss}}$ distribution of Standard model diphoton events. Since the calorimeter response to two electrons is approximately equivalent to that of two photons, the dielectron control sample is created by selecting $Z \rightarrow ee$ production from data events. For events to be selected in this sample, two electrons passing the baseline electron candidate criteria defined in Section 7.2.3 are required[4]. In addition it is required that both electrons have $|eta| < 1.81$, so as to match the *eta* distribution of the diphoton sample. Also, to increase the likelihood that the event is truly a $Z \rightarrow ee$ event a requirement is placed that invariant mass of the electron pair satisfy the following: $70\,\mathrm{GeV} < m_{ee} < 110\,\mathrm{GeV}$.

[4]Note that the p_{T} requirement for baseline electrons is only 25 GeV, as opposed to the 50 GeV cut used for photons. The electrons here are not required to have the same p_{T} as photons because such a requirement would leave to little statistics in the sample.

In principle the jet activity in dielectron events may differ from that of Standard Model diphoton events. This can in fact be seen in Fig. 10.2. The Standard Model diphoton events generally have a lower number of additional jets when compared to $Z \to ee$ events. Since additional jet activity in events will generally increase the tail of the $E_{\mathrm{T}}^{\mathrm{miss}}$ distribution, inclusive $Z \to ee$ events have higher tails in $E_{\mathrm{T}}^{\mathrm{miss}}$ than Standard Model diphoton events. As can also be seen in Fig. 10.2, requiring that a selected $Z \to ee$ event has no additional jets greatly improves the agreement of the $E_{\mathrm{T}}^{\mathrm{miss}}$ distributions with those of Standard Model diphotons. As a result a final requirement is placed on the dielectron sample that it contain no jets passing the baseline jet selection criteria defined in Section 7.3.

10.1.2 Nominal Method

The $E_{\mathrm{T}}^{\mathrm{miss}}$ template used for the background estimate is created by simply combining the $\mathrm{QCD}_{\gamma\gamma}$ and QCD_{γ} samples to form the combined $\mathrm{QCD}_{\gamma\gamma}$+$\mathrm{QCD}_{\gamma}$ sample. The H_{T} and $\Delta\phi\left(\gamma,\, E_{\mathrm{T}}^{\mathrm{miss}}\right)$ cuts of the three signal regions are then applied to create three separate $E_{\mathrm{T}}^{\mathrm{miss}}$ templates. The normalization region for each of the three templates is defined as $E_{\mathrm{T}}^{\mathrm{miss}} < 20\,\mathrm{GeV}$. The number of events in normalization region A for the $\mathrm{QCD}_{\gamma\gamma}$ + QCD_{γ} sample is 68 events of which 60 come from the $\mathrm{QCD}_{\gamma\gamma}$ and 8 from the QCD_{γ} sample. Similarly for normalization region B there are 2 events total both of which came from the QCD_{γ}. Lastly, the number of events in normalization region C for the $\mathrm{QCD}_{\gamma\gamma} + \mathrm{QCD}_{\gamma}$ sample is 42231 events of which 39835 come from the $\mathrm{QCD}_{\gamma\gamma}$ and 2396 from the QCD_{γ} sample. Additionally, the numbers of events in the

Template	SR A	SR B	SR C
QCD_{γ} + $\mathrm{QCD}_{\gamma\gamma}$	0 (<1.01 at 90% CL)	0 (<1.15 at 90% CL)	0.85 ± 0.30
$Z \to ee$	0	0	0.14 ± 0.05

Table 10.1: The nominal background prediction results using $E_{\mathrm{T}}^{\mathrm{miss}}$ templates from the $\mathrm{QCD}_{\gamma\gamma} + \mathrm{QCD}_{\gamma}$ and dielectron samples, for each of the three signal regions. The $\mathrm{QCD}_{\gamma\gamma} + \mathrm{QCD}_{\gamma}$ result is used for the central value of the prediction, while the difference between the $\mathrm{QCD}_{\gamma\gamma} + \mathrm{QCD}_{\gamma}$ and dielectron predictions motivate a systematic uncertainty on the QCD background estimate. Displayed errors are statistical only.

separate three normalization regions of the diphoton sample, used for the background predictions for signal regions A, B, and C, are 30, 1, and 4479 events, respectively. Neither control regions A nor B of $\mathrm{QCD}_{\gamma\gamma} + \mathrm{QCD}_{\gamma}$ contains any events. Control region C of $\mathrm{QCD}_{\gamma\gamma} + \mathrm{QCD}_{\gamma}$ does, however, contain 8 events.

For all three signal the QCD background is estimated by scaling the $\mathrm{QCD}_{\gamma\gamma} + \mathrm{QCD}_{\gamma}$ control region result by the ratio of the number of events in the diphoton and $\mathrm{QCD}_{\gamma\gamma} + \mathrm{QCD}_{\gamma}$ normalization regions. This method yields an expected background of zero events for signal regions A and B, but this result is poorly constrained from a statistical prospective. The estimates for this method on the QCD backgrounds for all three signal regions are presented in Table 10.1.

10.1.3 Alternative Method

Due to the lack of statistics in the control regions of the $\mathrm{QCD}_{\gamma\gamma} + \mathrm{QCD}_{\gamma}$ control sample for both analysis A and B, an additional method is employed for the background estimation. For this additional method the H_{T} cut for the $\mathrm{QCD}_{\gamma\gamma} + \mathrm{QCD}_{\gamma}$ control sample is relaxed in three steps. The steps are 400, 200, and 0 GeV for the

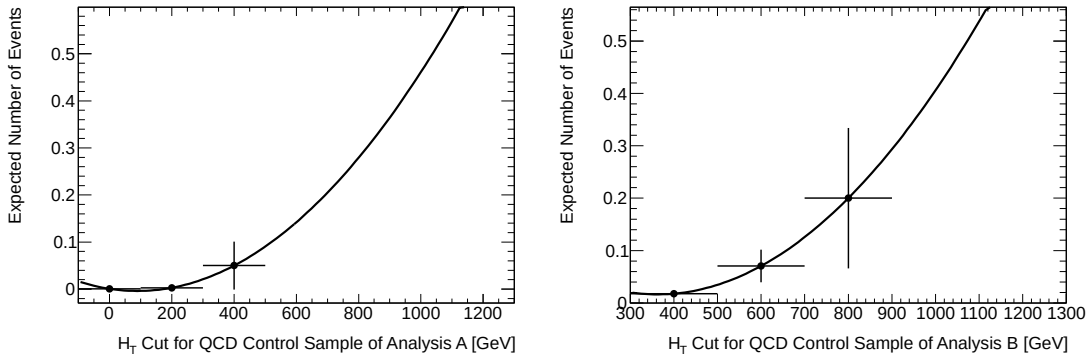

Figure 10.3: The expected QCD background values for signal regions A (left) and B (right) as a function of the relaxed H_{T} cut placed on the $\mathrm{QCD}_{\gamma\gamma}+\mathrm{QCD}_{\gamma}$ control sample. Extrapolating this dependence via a quadratic function, which is shown in black, to the H_{T} cut of the signal region yields an expectation of 0.14 and 0.54 QCD background events for signal regions A and B respectively.

signal region A estimate and 800, 600, and 400 GeV for the signal region B estimate. The resulting $E_{\mathrm{T}}^{\mathrm{miss}}$ distribution is scaled by the ratio of the nominal $\gamma\gamma$ normalization region result and the relaxed $\mathrm{QCD}_{\gamma\gamma} + \mathrm{QCD}_{\gamma}$ normalization region result to obtain an expected number of events in each signal region. This yields, for each of signal region A and B, a series of three expected values for the QCD background as a function of the relaxed H_{T} cut placed on the $\mathrm{QCD}_{\gamma\gamma} + \mathrm{QCD}_{\gamma}$ control sample. For each signal region a quadratic function is used to extrapolate this dependence to the H_{T} cut of the signal region ($H_{\mathrm{T}} > 600\,\mathrm{GeV}$ for signal region A and $H_{\mathrm{T}} > 1100\,\mathrm{GeV}$ for signal region B), as shown in Fig. 10.3.

This alternative method yields an expectation of 0.14 and 0.54 QCD background events for signal region A and B, respectively. Other functions were tested, but they gave smaller background estimates. The estimate of 0 events from the di-

rect scaling discussed in Section 10.1.2 is conservatively low. The estimate that will be used for the QCD background of signal regions A and B will be the mean of that of the two approaches. These two approaches most likely conservatively bound the true QCD background expectation. A 100% systematic uncertainty will be assigned to this combined estimate to cover the full range between the two individual estimates. The combined estimates on the QCD backgrounds for all three signal regions are presented in Table 10.2.

SR	Nominal Estimate	Alternative Estimate	Combined Estimate
A	0 (< 1.01 at 90% CL)	0.14	0.07 ± 0.07
B	0 (< 1.15 at 90% CL)	0.54	0.27 ± 0.27
C	0.85 ± 0.30	–	0.85 ± 0.30

Table 10.2: The QCD background estimates based upon the nominal (direct) and alternative (extrapolated) approaches, and the combined result. The errors quoted for signal regions A and B are the systematic that arises from comparing the two methods, while for the C analysis the error arises from the statistics of the control sample above $E_{\mathrm{T}}^{\mathrm{miss}} > 125\,\mathrm{GeV}$ cut. Other systematics uncertainties will be addressed in Section 10.5.1.

10.2 Modeling of the Electroweak Background

The electroweak background contribution consists primarily of $t\bar{t}$ and $W^{\pm}$ plus γ/jet. In these events at least one of the candidate photons is faked by a true electron and the $E_{\mathrm{T}}^{\mathrm{miss}}$ is due to high p_{T} neutrinos produced in the leptonic decay of $W^{\pm}$ bosons. This background contribution is estimated by selecting an electron-photon control sample, which is orthogonal to the standard diphoton selection. The individual cuts defining the signal regions are applied to the electron-photon sample to create a control region for

each of three signal regions. This sample is then scaled based upon a electron-to-photon scale factor derived using a tag-and-probe method on $Z \rightarrow ee$ events. The tag-and-probe method is described in more detail in Section 10.2.2. The residual contamination of the electron-photon control sample by QCD events is then subtracted to avoid double counting of backgrounds. The specifics of this subtraction procedure are described in Section 10.3, though the impact of this correction is negligible.

10.2.1 Electron-Photon Sample

All events in the electron-photon control sample are required to pass the base event selection defined in Section 9.1. The event is then required to contain exactly one baseline candidate photon from Section 7.1.7 and one candidate photon-replacement electron from Section 7.2.3. Finally, the selection cuts that define the three signal regions from Section 9.2 are applied, creating three electron-photon control regions corresponding to signal regions A, B, and C. The candidate electron is treated the same as the photon for the purposes of the $\Delta\phi$ cut in the electron-photon sample. The number of raw events appearing in the control regions are 1, 3, and 28 for regions A, B, and C respectively. A plot showing the $E_{\mathrm{T}}^{\mathrm{miss}}$ distribution before and after the various cuts defining the signal regions can be seen in Fig. 10.4 and 10.5.

10.2.2 Electron-Photon Scale Factor

The electron-to-photon scale factor is measured using a tag-and-probe method on $Z \rightarrow ee$ data events. The tag-and-probe sample is derived using all the base selections

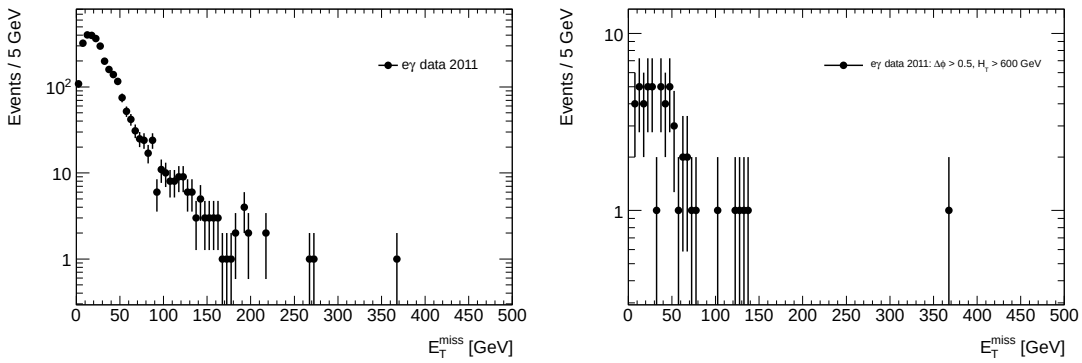

Figure 10.4: The $E_{\mathrm{T}}^{\mathrm{miss}}$ of the inclusive unscaled electron-photon control sample (left) and that same distribution after imposing cuts of $H_{\mathrm{T}} > 600\,\mathrm{GeV}$ and $\Delta\phi\left(e/\gamma,\, E_{\mathrm{T}}^{\mathrm{miss}}\right) > 0.5$. The plot on the right is the equivalent of signal region A before the $E_{\mathrm{T}}^{\mathrm{miss}}$ cut is imposed.

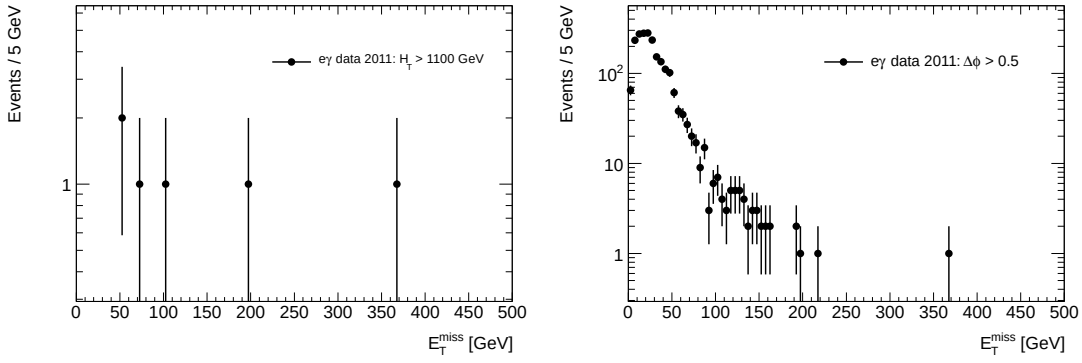

Figure 10.5: The $E_{\mathrm{T}}^{\mathrm{miss}}$ of the unscaled electron-photon control sample after imposing a $H_{\mathrm{T}} > 1100\,\mathrm{GeV}$ cut (left) and after imposing a cut on $\Delta\phi\left(e/\gamma,\, E_{\mathrm{T}}^{\mathrm{miss}}\right) > 0.5$ (right). The plot on the left is the equivalent of signal region B before the $E_{\mathrm{T}}^{\mathrm{miss}}$ cut and the right is the equivalent of signal region C before its own $E_{\mathrm{T}}^{\mathrm{miss}}$ cut.

defined in Section 9.1 with a few minor exceptions. One of these differences is that a single electron trigger is used as shown in Table 10.3. The other difference was the requirement that the event have $E_{\mathrm{T}}^{\mathrm{miss}} > 20\,\mathrm{GeV}$. A tag electron is then defined in the same manner as the photon-replacement electron, including the normal overlap removal criteria applied to electrons, with the one difference that the p_{T} requirement is lowered from 50 GeV to 25 GeV due to the p_{T} spectrum of the electrons produced in Z decays. All events are required to possess at least one tag electron. The requirements imposed on probe photons and electrons are the identical selection and overlap criteria used for baseline candidate photons and photon-replacement electrons with the difference that the p_{T} requirement is lowered to 25 GeV in both cases. If there is a probe photon in the event and the invariant mass of the tag and probe is within 10 GeV of m_Z, then is this recorded as an $e\gamma$ or γe event. It is recorded as a γe event when the photon p_{T} is higher than that of the tag electron and as an $e\gamma$ event otherwise. Alternatively, if there is a probe electron in the event and the invariant mass of the two electrons is within 10 GeV of m_Z, it is recorded as an ee event. The electron-to-photon scale factor is then derived from the number of $e\gamma$ ($N_{e\gamma}$), γe ($N_{\gamma e}$), and ee (N_{ee}) events as shown in Eq. 10.1.

$$f = \frac{N_{\gamma e} + N_{e\gamma}}{2N_{ee}} \tag{10.1}$$

The full derivation of Eq. 10.1 is included in Appendix B.

The electron-to-photon scale factor possesses some variation as a function of both the η and p_{T} of the probe. This variation can be seen in Fig. 10.6. The variation in the scale factor as function of η is far more significant than in p_{T}. For this reason, as

Run Number	Trigger
$177986 - 186755$	`EF_e20_medium`
$186873 - 187815$	`EF_e22_medium`
$188902 - 191933$	`EF_e22vh_medium1` $\|\|$ `EF_e45_medium1`

Table 10.3: The list of single electron triggers that the $Z \rightarrow ee$ tag-and-probe sample was drawn from as function of the ATLAS run number.

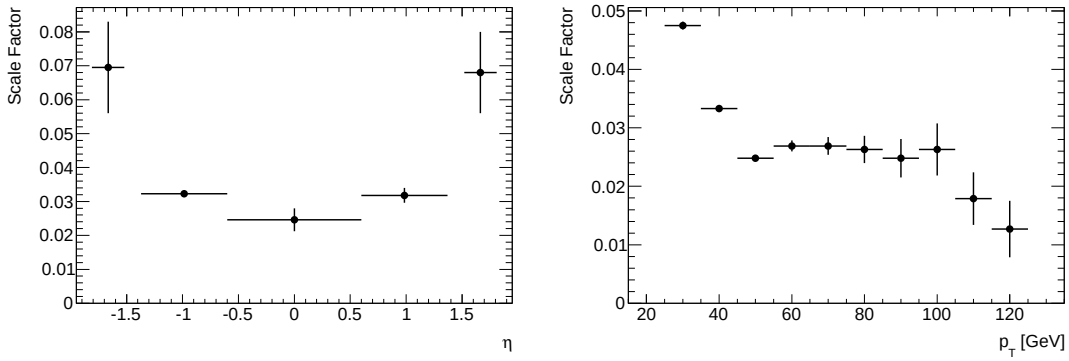

Figure 10.6: The variation of the electron-to-photon scale factor as function of the η (left) and p_{T} (right). For the η parametrization the errors included the systematic uncertainties derived in Section 10.5.4. For the p_{T} parametrization the errors are purely statistical.

was done in the previous version of this analysis [32], the electron-to-photon fake rate is parametrized in terms of the η of the probe, and integrated over all p_{T}. The effect of not parametrizing the scale factor in p_{T} is discussed later in this section.

The tag-and-probe sample is split into five bins in the η of the probe, and the scale factor is calculated for each bin individually. The η bins cover the range $-1.81 < \eta < 1.81$, excluding the crack regions of $1.37 < |\eta| < 1.52$ in which *PhotonTight* identification requirement does not exist. The value of the scale factor in all η bins can be seen in Table 10.4. The scale factor varies from a value of 0.0246 to 0.0695 being

lowest in the central barrel and highest in the endcaps. This is primarily an effect of the amount of material before the calorimeter as a function of η, as can be seen in Fig. 7.1. Each event in the electron-photon control sample is then reweighted by the appropriate scale factor based upon the η of its photon-replacement electron candidate. After this reweighting, the number of events remaining in control regions A, B, and C are 0.03, 0.09, and 0.81, but these are not the final numbers used for the electroweak background estimate. Double counting of the QCD background estimate must first be subtracted, which is discussed in Section 10.2.3.

Bin in η	$N_{\gamma e}$	$N_{e\gamma}$	$2N_{ee}$	Scale Factor
$-1.81 < \eta \leq -1.52$	911	1173	29966	0.0695 ± 0.0135
$-1.37 < \eta \leq -0.6$	1868	2603	138556	0.0323 ± 0.0007
$-0.6 < \eta < 0.6$	2725	3939	271436	0.0246 ± 0.0034
$0.6 \leq \eta < 1.37$	1870	2534	138297	0.0318 ± 0.0022
$1.52 \leq \eta < 1.81$	875	1156	29885	0.0680 ± 0.0120

Table 10.4: The electron-to-photon scale factor parametrized for the five bins in η. This parametrization is the one used in the actual calculation of the estimated electroweak background. The uncertainties shown on the value of the scale factors are derived in Section 10.5.4.

The effect of not parametrizing the scale factor in p_{T} is likely small, but it still must be considered. As can be observed from Fig. 10.6, the electron-to-photon scale factor is quite flat as a function of p_{T} in the range of $50-100\,\mathrm{GeV}$, and rises significantly for $p_{\mathrm{T}} > 5\,\mathrm{GeV}$. This is consistent with observations from the previous iteration of this analysis [32]. One novel feature is the apparent downwards trend in the scale factor versus p_{T} for values of the p_{T} greater than $100\,\mathrm{GeV}$. There were not sufficient statistics to observe such an effect in the data with the previous analysis, though Monte Carlo

studies had indicated an expected slow fall off in the scale factor at higher p_{T}. The effect in the Monte Carlo was smaller, with only a 20% drop going from p_{T} of approximately 100 GeV to 200 GeV. One caveat with this comparison is that selection criteria other than the p_{T} cut also changed with respect to the last analysis.

Bin in p_{T} [GeV]	$N_{\gamma e}$	$N_{e\gamma}$	$2N_{ee}$	Scale Factor
$25 < E_{\mathrm{T}} \leq 35$	716	4728	114505	0.0475 ± 0.0007
$35 < E_{\mathrm{T}} \leq 45$	3093	6136	276886	0.0333 ± 0.0004
$45 < E_{\mathrm{T}} \leq 55$	3082	423	141368	0.0248 ± 0.0004
$55 < E_{\mathrm{T}} \leq 65$	775	47	30564	0.0269 ± 0.0010
$65 < E_{\mathrm{T}} \leq 75$	293	25	11812	0.0269 ± 0.0015
$75 < E_{\mathrm{T}} \leq 85$	117	15	5028	0.0263 ± 0.0023
$85 < E_{\mathrm{T}} \leq 95$	53	5	2341	0.0248 ± 0.0033
$95 < E_{\mathrm{T}} \leq 105$	33	3	1367	0.0263 ± 0.0044
$105 < E_{\mathrm{T}} \leq 115$	16	0	896	0.0179 ± 0.0045
$115 < E_{\mathrm{T}} \leq 125$	6	1	550	0.0127 ± 0.0048

Table 10.5: The electron-to-photon scale factor parametrized for the ten bins in p_{T}. This parametrization is not directly used in the actual calculation of the estimated electroweak background. The uncertainties shown on the value of the scale factors are statistical only.

The primary issue is that the p_{T} cuts used for the electron-photon control sample are different than those used in the tag-and-probe sample for the current analysis. The values of the scale factor in Table 10.4, which are the ones used in the background estimate, are dominated by electrons and photons with p_{T} below the cut for the control region. This was not much of a problem in previous analyses where the p_{T} spectra of the two samples were similar. With the default cut of $p_{\mathrm{T}} > 25$ GeV, the scale factor averaged over all η is 0.0334. If the scale factor extraction is redone using a 50 GeV cut on p_{T} instead, this yields a scale factor averaged over all η of 0.0264. The nominal scale factor

is approximately 25% larger than the scale factor calculated requiring $p_{\mathrm{T}} > 50\,\mathrm{GeV}$. This 25% difference in the scale factor is covered by the systematic error that is already assigned to the electroweak background component from other sources, as detailed in Section 10.5.

10.2.3 Subtraction of the QCD Contamination

In principle there can be a large contribution to the the electron-photon control sample from $Z \rightarrow ee$ events when one of the photons is faked by an electron. These events have intrinsic $E_{\mathrm{T}}^{\mathrm{miss}}$ and therefore the tail of their $E_{\mathrm{T}}^{\mathrm{miss}}$ distribution more closely resembles that of the QCD background. For that reason these events will be accounted for by the QCD component of the background estimation, and would be double counted if included in the electroweak background component as well. This is avoided by subtracting the QCD contamination from the high $E_{\mathrm{T}}^{\mathrm{miss}}$ tails of the electron-photon sample.

The subtraction is performed on each of the three electroweak control regions separately. The first step is to count the number of electron-photon events with $E_{\mathrm{T}}^{\mathrm{miss}} < 20\,\mathrm{GeV}$ after reweighting by the appropriate scale factor and applying all the control region criteria except the $E_{\mathrm{T}}^{\mathrm{miss}}$ cut. The $E_{\mathrm{T}}^{\mathrm{miss}}$ template of the $\mathrm{QCD}_{\gamma\gamma} + \mathrm{QCD}_{\gamma}$ control sample is then normalized to have the same number of events in the $E_{\mathrm{T}}^{\mathrm{miss}} < 20\,\mathrm{GeV}$. The $E_{\mathrm{T}}^{\mathrm{miss}}$ cut for the particular control region is then applied to the normalized $E_{\mathrm{T}}^{\mathrm{miss}}$ template of the $\mathrm{QCD}_{\gamma\gamma} + \mathrm{QCD}_{\gamma}$ sample, and the number of events passing that cut is the amount that will be subtracted from that control region of the electron-photon

sample. The subtraction was found to be negligible for control regions A and B. Control region C had a larger, though still small, subtraction of 0.005 events, which yields a final electroweak background estimate for that region of 0.80 events.

This very small amount of double counting in the electroweak background control sample is a departure from the previous version of this analysis [32]. The different p_{T} requirement on the photons and electrons of the electron-photon control sample is the cause of this change. In the previous analysis where the p_{T} cut was a much lower 25 GeV, a larger fraction of $Z \to ee$ events were accepted into the control sample.

10.3 Modeling of the Irreducible Background

The irreducible background component due to Standard Model $Z \to \nu\nu + \gamma\gamma$ and $W \to \ell\nu + \gamma\gamma$ is estimated purely from Monte Carlo using leading-order `MadGraph` samples. As mentioned in Sec. 8.2.4, a K-factor of 2.0 ± 0.3 was chosen for $Z \to \nu\nu + \gamma\gamma$ and 3 ± 3 for $W \to \ell\nu + \gamma\gamma$. The large uncertainty for $W \to \ell\nu + \gamma\gamma$ is due to the large phase-space dependence of the K-factor [82]. For the $Z \to \nu\nu + \gamma\gamma$ process, a 7.5% scale uncertainty is assigned, which is taken from Ref. [81]. The irreducible background Monte Carlo samples are then normalized to a luminosity of $4.8\,\mathrm{fb}^{-1}$ using these cross-sections. After normalization the base event selection from Section 9.1 is applied to the Monte Carlo samples followed by a requirement of two baseline photons. The cuts defining the three signal regions from Section 9.3 are then applied. The normalized number of events passing the final signal region selections is then considered to be the

estimated background contribution from $Z \to \nu\nu + \gamma\gamma$ and $W \to \ell\nu + \gamma\gamma$ to that signal region.

No events pass the selections for signal regions A and B from either the $Z \to \nu\nu + \gamma\gamma$ or $W \to \ell\nu + \gamma\gamma$ Monte Carlo. This is due primarily to the H_{T} cuts which are very effective at eliminating these types of events. In a study similar to what was done for the QCD sample, the H_{T} was relaxed in several steps for each Monte Carlo sample, and the background estimates at relaxed H_{T} cuts were extrapolated to the nominal cut value. This alternate method yields estimates of the total irreducible background from signal regions A and B of less than 0.001 events. As a result this background contribution to signal regions A and B is considered negligible and therefore ignored.

A small number of events pass the signal region C criteria in both the $Z \to \nu\nu + \gamma\gamma$ and $W \to \ell\nu + \gamma\gamma$ Monte Carlo samples, leading to a non-negligible background contribution. For signal region C the predicted number of events coming from the $Z \to \nu\nu + \gamma\gamma$ process is $0.27 \pm 0.09 \pm 0.04$, while $W \to \ell\nu + \gamma\gamma$ gives $0.18 \pm 0.13 \pm 0.18$ events. The first quoted error is a statistical error, and the second error is a systematic error due to the K-factor uncertainty. The combined irreducible background for signal region C is $0.46 \pm 0.16 \pm 0.19$.

10.4 Cosmic Ray Background

The background contribution due to cosmic ray events is estimated using real cosmic events triggered in empty bunches. The estimation technique is based on the

method used in the direct-photon purity estimate [93]. This dataset was collected using the L1_EM3_EMPTY trigger from the 2010 dataset. The 2010 dataset is used for this estimation because of the high prescales present for cosmic triggers in the 2011 data. All luminosity blocks for which this trigger was unprescaled in periods A through F from 2010 are used. The nominal event selection is used with the exceptions of the primary vertex requirement, jet and photon cleaning cuts, and some photon identification variables. Most cosmic events with photons do not have a good reconstructed primary vertex passing our selections. It is assumed that a cosmic event contaminating the collision samples would do so by being overlaid with a real collision event. Photons passing both the loose and tight photon criteria are used, due to the limited statistics of tight photons in the sample.

In this cosmic data sample there are 7395 events with at least one loose photon and 63 events with one tight photon. Two events with two loose photons and zero events with two tight photons are also present. Both of the two loose photon events also passed the $E_{\mathrm{T}}^{\mathrm{miss}}$ cut. A direct estimate of the expected contribution to the pseudo-photon control samples can be obtained from the events with two loose photons. Since no two tight photon events are seen, the rate of such events is estimated using the ratio of events with one tight photon to events with one loose photon multiplied by the number of events with two loose photons. The chance for each photon to pass the tight requirement is conservatively assumed to be fully correlated, hence the multiplication by the ratio instead of the squaring of the ratio. This gives an estimate of 0.017 ± 0.012 (statistical uncertainties only) two tight photon events in the empty-bunch cosmic sample.

The total time in the luminosity blocks used for each run is weighted by the number of empty bunches in that run to obtain a rate per bunch per unit time for each type of event. This rate is then multiplied by the time in good luminosity blocks in periods B through H in the 2011 data weighted by the number of colliding bunches in each run to give an expected background contribution. All events are conservatively assumed to pass the $E_{\mathrm{T}}^{\mathrm{miss}}$ cut. The expected number of events due to cosmics with two loose photons is estimated to be 0.46 ± 0.32. For events with two tight photons the estimate is 0.0039 ± 0.0028 events. Note that the uncertainties assigned are statistical only. Note also that this is merely a conservative upper limit since the rejection power of the cleaning cuts used in the analysis are not taken into account. Based on these numbers the background contributions from cosmics to the two tight photon collision sample is taken to be negligible. Conversely for the pseudo-photon control sample, cosmics are found to possibly contribute, through as seen in the 2010 analysis these events can be removed via timing cuts on the selected photons [93].

10.5 Background Systematic Uncertainties

This section describes the various systematic uncertainties assigned to the background predictions. Sections 10.5.1 and 10.5.2 are systematics applied to the QCD background prediction. There is also an additional 100% systematic uncertainty assessed on the QCD background prediction for signal A and B from the alternative estimation method discussed in Section 10.1.3. The systematics discussed in Sections 10.5.3, 10.5.4,

and 10.5.5 are ones applied to the electroweak background prediction.

10.5.1 Normalization Region

An important component in the estimation of the QCD background is the normalization of the $\mathrm{QCD}_{\gamma\gamma} + \mathrm{QCD}_{\gamma}$ control sample to the diphoton data in the region of $E_{\mathrm{T}}^{\mathrm{miss}} < 20\,\mathrm{GeV}$. The uncertainty on the normalization is derived by observing the effect of different choices for the normalization region on the background estimate. To this end two alternate ranges for the normalization window of $5\,\mathrm{GeV} \leq E_{\mathrm{T}}^{\mathrm{miss}} < 25\,\mathrm{GeV}$ and $10\,\mathrm{GeV} \leq E_{\mathrm{T}}^{\mathrm{miss}} < 30\,\mathrm{GeV}$ are examined. When examining signal region C, the background changes most compared to the nominal for the $10\,\mathrm{GeV} \leq E_{\mathrm{T}}^{\mathrm{miss}} < 30\,\mathrm{GeV}$ window. The predicted number of QCD background events falls from 0.848 events for the nominal normalization window to 0.817 events for the alternative window. This difference of 0.032 events is then taken as a systematic uncertainty on the QCD background estimate for signal region C.

10.5.2 Missing Transverse Energy Template

The systematic error on QCD background due to the shape of the template used in the estimation is determined by substituting the dielectron control sample for that of the $\mathrm{QCD}_{\gamma\gamma} + \mathrm{QCD}_{\gamma}$ control sample. The difference in the resulting background prediction is then taken as systematic uncertainty. This gives an absolute error of 0.71 events on the background prediction for signal region C. Neither the dielectron nor $\mathrm{QCD}_{\gamma\gamma}+\mathrm{QCD}_{\gamma}$ control samples have a non-zero background prediction for signal regions

A and B using the nominal prediction method so this uncertainty is not meaningful.

10.5.3 Control Sample Composition and Overlap

One possibility of uncertainty on the background depends on what fraction of reconstructed diphoton events coming from electroweak sources do not have at least one photon that is actually a fake electron. Contributions from such events will not be accounted for by the electron-photon control sample. In the previous version of this analysis this it was found that such events account for less than 5 % of all reconstructed diphoton events [32]. The photon selection criteria of the current analysis dramatically reduces in the electron-to-photon fake, which may make the contribution of this type of event more pronounced.

A study of using Monte Carlo samples expected to contribute to the electroweak was conducted to assess this. The Monte Carlo samples used are shown in Table 8.2. The nominal diphoton sample selection, with cut on the photon p_{T} of 50 GeV, was performed on those Monte Carlo samples, and the source of the selected photons was determined from the Monte Carlo truth information. This suggests that approximately 75% of all diphoton backgrounds from electroweak sources possess at least one electron faking a photon, and thus are properly accounted for in the electron-photon control sample study.

Examining the 25% of non-electron-faking-photon events of the electroweak background samples suggests that the majority of these should be accounted for in the QCD control sample. Of these non-electron-faking-photon events approximately

20% (25%), for all values of $E_{\mathrm{T}}^{\mathrm{miss}}$ (for $E_{\mathrm{T}}^{\mathrm{miss}} > 50\,\mathrm{GeV}$), are τ lepton decays with fake photons. These events rarely appear to have reconstructed electrons, and thus are likely represented in the QCD control sample. Another 45% (40%) of the non-electron-faking-photon electroweak events, for all values of $E_{\mathrm{T}}^{\mathrm{miss}}$ (for $E_{\mathrm{T}}^{\mathrm{miss}} > 50\,\mathrm{GeV}$), have one real photon and a second photon that is due a jet faking a photon. Again such events should appear in the QCD control samples. Approximately 25% (30%) of the non-electron-faking-photon electroweak events, for all values of $E_{\mathrm{T}}^{\mathrm{miss}}$ (for $E_{\mathrm{T}}^{\mathrm{miss}} > 50\,\mathrm{GeV}$), are due to $W(\rightarrow e\nu) + \gamma$ events where the second photon arises from a jet faking a photon, but the electron was also not reconstructed. Such events are also likely to appear in the QCD control sample. The remaining events are unlikely to be accounted for in any of the background control samples. As a result of this study a 25% systematic uncertainty is assigned to the electroweak background allowing for the possibility of either complete double counting with QCD background or all such events being missed by both.

10.5.4 Electron-Photon Scale Factor Uncertainties

The systematic uncertainties on the values of the scale factors described in Section 10.2.2 are assessed by comparing the results to those obtained via an alternative method. This scale factor comes from a similar 2011 SUSY analysis in ATLAS looking for photons + b-quark jets with $E_{\mathrm{T}}^{\mathrm{miss}}$ events [94, 95]. The primary differences are in the tag-and-probe sample used. These differences are that the *tag* electrons are only required to pass the *ElectronMedium++* identification requirements instead of the *ElectronTight++* requirements. Also, the p_{T} cut on the electrons and photons is only

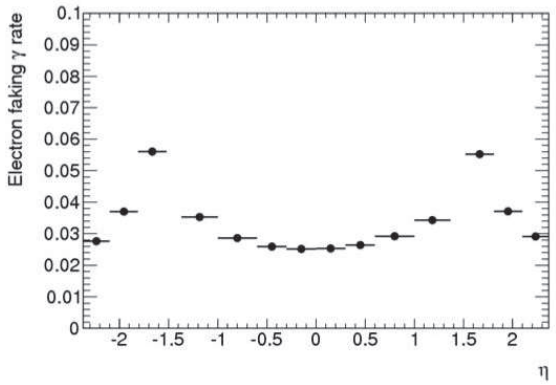

Figure 10.7: The alternative of the electron-to-photon scale factor as function of the η that was used to estimate the systematic uncertainties on the nominal scale factor [94, 95]. The uncertainties were taken as the difference between the two methods for the different η bins of the nominal scale factor.

20 GeV instead of 25 GeV. Lastly, the alternative method makes no require on the amount of $E_{\mathrm{T}}^{\mathrm{miss}}$ in the event.

The nominal scale factor values seen in Fig. 10.6 are compared to those from the independent measurement shown in Fig. 10.7. A slightly finer η binning is used in the other method, so an extrapolation is required to make the comparison. The differences range from 2% to 20% with the largest differences occuring at high η. These differences are used as the bounds for a systematic uncertainty assigned to the value of the scale factor. The uncertainties on the scale factor for each *eta* bin are shown in Table 10.4. This systematic on the electron-to-photon scale factor is then propagated to the electroweak background estimate. This gives a systematic of 6.9%, 7.1%, and 10.0% for signal regions A, B, and C respectively.

10.5.5 QCD Subtraction Uncertainty

The contamination for QCD and $Z \rightarrow ee$ is subtracted from the electron-photon control sample to avoid double counting of backgrounds. The nominal method uses the $E_{\mathrm{T}}^{\mathrm{miss}}$ template from the $\mathrm{QCD}_{\gamma\gamma} + \mathrm{QCD}_{\gamma}$ control sample for the subtraction. This makes the assumption that the contamination purely by events which are hadronic in nature. The counter-case is considered by using the dielectron sample to for the subtraction using the assumption that the events are electromagnetic in nature. The true case is likely some combination of these two possibilities, and therefore these two edge cases should bound the probable true value of the subtraction. By substituting the dielectron template for the $\mathrm{QCD}_{\gamma\gamma} + \mathrm{QCD}_{\gamma}$ one, the difference in the resultant background prediction is taken as a systematic error. No systematic is assigned for signal regions A and B, since the subtraction itself is negligible. For the signal region C the correction to the electroweak background prediction goes from 0.005 to 0.0008 events, so a systematic of 0.004 is assigned.

10.6 Total Background Results

The total expected number of Standard Model background events for each of the three signal regions is taken to be the combination of the expected contributions estimated from the QCD, electroweak, and irreducible control samples. These final numbers and their combination along with the associated statistical and systematic errors can be seen in Table 10.6. In addition $E_{\mathrm{T}}^{\mathrm{miss}}$ distributions of the diphoton sample,

	Signal Region A	Signal Region B	Signal Region C
QCD	$0.07 \pm 0.00 \pm 0.07$	$0.27 \pm 0.00 \pm 0.27$	$0.85 \pm 0.30 \pm 0.71$
Electroweak	$0.03 \pm 0.03 \pm 0.01$	$0.09 \pm 0.05 \pm 0.02$	$0.80 \pm 0.16 \pm 0.22$
$W \to \ell\nu + \gamma\gamma$	0.0	0.0	$0.18 \pm 0.13 \pm 0.18$
$Z \to \nu\nu + \gamma\gamma$	0.0	0.0	$0.27 \pm 0.09 \pm 0.04$
Total Background	$0.10 \pm 0.03 \pm 0.07$	$0.36 \pm 0.05 \pm 0.27$	$2.11 \pm 0.37 \pm 0.77$
Observed Events	0	0	2

Table 10.6: The expected number of background events for each of three signal regions with associated uncertainties. For each background entry the first error is the statistical error due to the limited statistics of the corresponding control samples, and the second error is the associated systematic uncertainty described in Section 10.5.The actual number of $\gamma\gamma$ events observed in the signal regions for $4.8\,\text{fb}^{-1}$ of 2011 collision data is included in the bottom row of the table.

with all the signal region selections applied except for the $E_{\text{T}}^{\text{miss}}$ cut, are shown overlaid with the estimated backgrounds in Fig. 10.8. No excess of events above the Standard Model expectations is observed, which allows limits to be placed on the parameter space of the GGM and SPS8 supersymmetry models discussed in Chapter 3. The theory interpretation of this result will be presented, along with the limit setting procedure used, in Chapter 12.

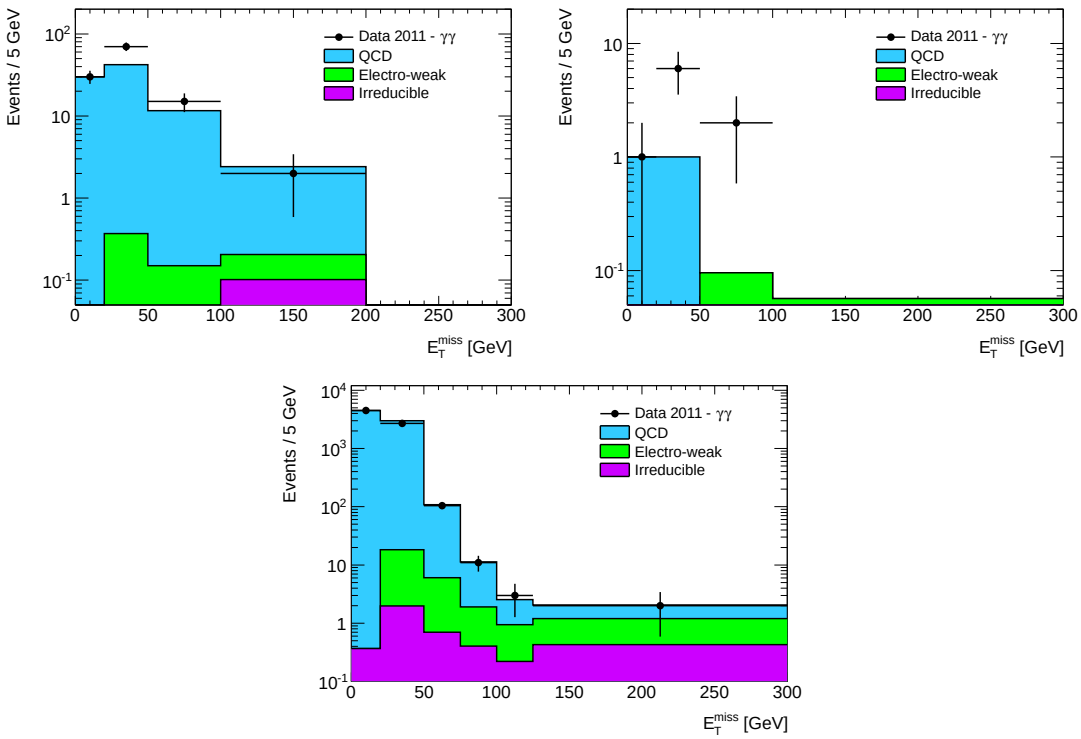

Figure 10.8: The $E_{\mathrm{T}}^{\mathrm{miss}}$ distributions of the diphoton sample after requiring $\Delta\phi > 0.5$ and $H_{\mathrm{T}} > 600\,\mathrm{GeV}$ (top left), $H_{\mathrm{T}} > 1100\,\mathrm{GeV}$ (top left), and $\Delta\phi > 0.5$ (bottom). Each distribution is overlaid with a stacked histogram of the various background contributions.

Chapter 11

Signal Acceptance Uncertainties

This chapter discusses the systematic uncertainties related to the GGM and SPS8 theory interpretations that were used for cross sections and mass limits. The limit setting itself is described in Chapter 12. One of the most important set of uncertainties are those on the acceptance of the cuts of the analysis. These uncertainties are detailed in Section 11.1, and they are used in both the cross section and mass limits. The uncertainty on the official ATLAS integrated luminosity measurement is discussed in Section 11.2. The luminosity uncertainty is also used in the setting of the cross section limits. The final uncertainties considered are those on the theoretical cross sections for the various GGM and SPS8 Monte Carlo points. These play a part in interpreting the experimental result in terms of mass limits in the two theory scenarios. Details on the cross section uncertainties are discussed in Section 11.3.

11.1 Signal Acceptance Uncertainties

This section highlights the uncertainties specifically related to the acceptance of various cuts used in the analysis. Uncertainties are considered for the trigger efficiency, the photon selection and identification cuts, pileup, missing transverse energy, and total transverse energy. The trigger and photon identification uncertainties are the same for both the GGM and SPS8 points, but the isolation and pileup uncertainties differ between the two theory scenarios. The $E_{\mathrm{T}}^{\mathrm{miss}}$ and H_{T} systematics uncertainties are evaluated individually for every Monte Carlo point.

11.1.1 Trigger Efficiency

The efficiency of the *EF_2g20_loose* trigger is estimated via a *Boot Strap* method using a comparable single photon trigger. The efficiency for photons passing the baseline selection is found to be $99.7^{+0.27}_{-0.79}$ % for data in periods D-K and 100^{+0}_{-1} % for periods L-M. The trigger efficiency of the single photon *EF_g20_loose* trigger as a function of the E_{T} of the photons can be seen in Fig. 11.1.

11.1.2 Photon Selection and Identification

Several different uncertainties are assessed on various photon selection and identification cuts, and are discussed below. The largest of these is the uncertainty due to the shifts applied to the photon discriminating variables. Other uncertainties due to bad conversion reconstruction, bad clusters, and the LAr hole are studied, but found to be much smaller. A single value of the uncertainty is used for all Monte Carlo points

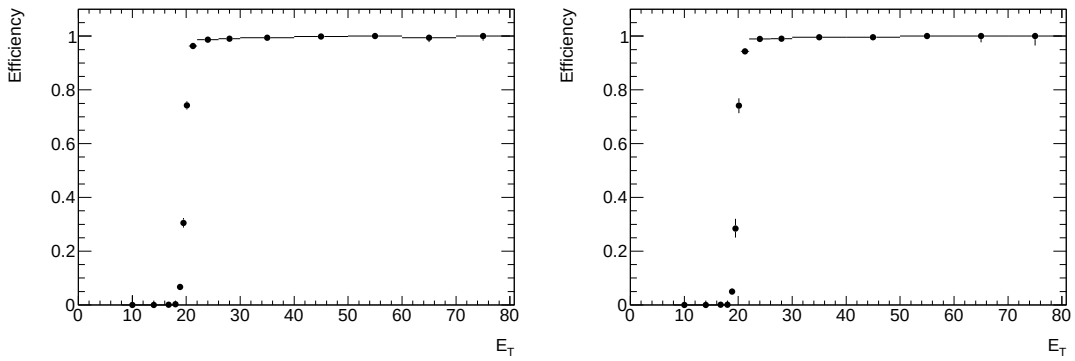

Figure 11.1: Efficiency of the *EF_g20_loose* trigger for one photon as a function of the E_{T} of that photon [96].

for both theory scenarios. Finally, a systematic uncertainty is assessed related to the acceptance of the photon isolation cut. This is applied separately for the GGM and SPS8 Monte Carlo points. Although each of these photon uncertainties are treated as uncorrelated, the uncertainty due to each of the two photons are treated as completely correlated.

11.1.2.1 Discriminating Variable Corrections

A systematic uncertainty is assessed on the Monte Carlo corrections performed on the discriminating variables used in the photon identification, which were described in Section 7.1.2.3. The variable shift method used in this analysis is compared to a data-driven method. Details on this data-driven method called the *matrix method* can be seen in Ref. [97]. The differences between the shifted discriminating variables method and the matrix method, which were evaluated for photons in bins of η and p_{T}, were used to assess an uncertainty. The value of the systematic uncertainty used was 4.0 %

for all the GGM and SPS8 points.

11.1.2.2 Bad Conversions

Another photon-related systematic uncertainty is assessed due to the frequent reconstruction of unconverted photons as converted. Since the cut values used in the photon identification variables described in Section 7.1.2 have a dependence on the conversion status of the photon, this can result in an uncertainty in the photon selection efficiency. A standard ATLAS uncertainty is used for this [98]. The value of this uncertainty is 1.8 %.

11.1.2.3 Object Quality and LAr Hole

As discussed in Section 7.1.6, a set of cleaning cuts are applied to remove photons due to detector problems. There are four distinguishable periods in the 2011 data from the perspective of the calorimeter status:

- Periods B-D: All LAr FEBs were functional and the Tile calorimeter had 5 dead modules
- Period E-H: Six LAr FEBs were non-functional and the Tile calorimeter had 6 dead modules
- Period I-K: Two LAr FEBs were non-functional and the Tile calorimeter had 7 dead modules
- Period L-M: Two LAr FEBs were non-functional and the Tile calorimeter had 9

dead modules

Most of these calorimeter problems have been included in the Monte Carlo simulation, limiting the differences in the inefficiency of the cleaning cuts between the data and the Monte Carlo. The differences of the efficiencies of the cleaning cuts between the data and Monte Carlo is used as a systematic uncertainty. A standard ATLAS systematic uncertainty of 0.1 % per photon is used for this [99]. Since the uncertainties between the two photons are treated as 100 % correlated, a total 0.2 % uncertainty per event is used.

11.1.2.4 Isolation

The mean of the isolation variable for photons and electrons used in the analysis differs between the data and the Monte Carlo. As a result a systematic uncertainty is assessed on the acceptance of the isolation cut (described in Section 7.1.5) applied to photons. This a similar procedure to the one used in the ATLAS Higgs to $\gamma\gamma$ analysis [100]. A sample of $Z \to ee\gamma$ Monte Carlo is used to assess this uncertainty. The distribution of the isolation variable (EtCone20_corrected) for data and Monte Carlo can be seen in Fig. 11.2. The difference in the mean between the data and the Monte Carlo is 0.4 GeV. As can be seen from Fig. 11.3, there appears to be no strong dependence of the mean on either p_{T} or the number of reconstructed primary vertices in the event.

The isolation cut applied to the Monte Carlo is then shifted up by 0.4 GeV, and the uncertainty is taken as the difference in acceptance between the nominal value

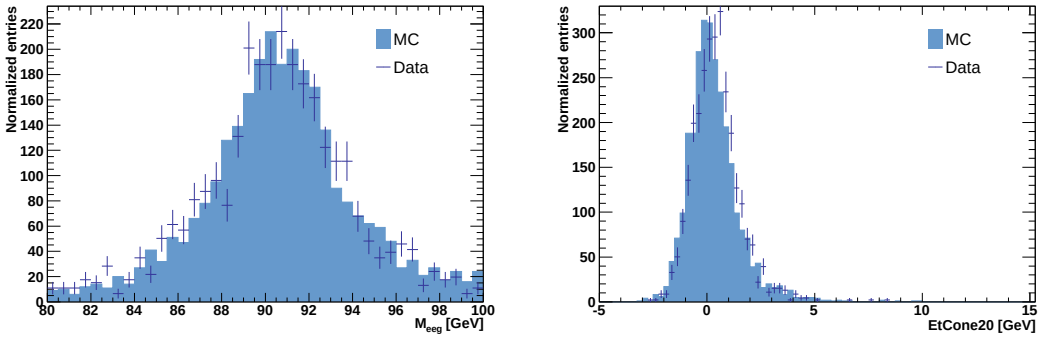

Figure 11.2: The distribution of $M_{ee\gamma}$ after the isolation event selection (left) and distribution of the EtCone20_corrected variable for the same photons (right) comparing data and Monte Carlo [96].

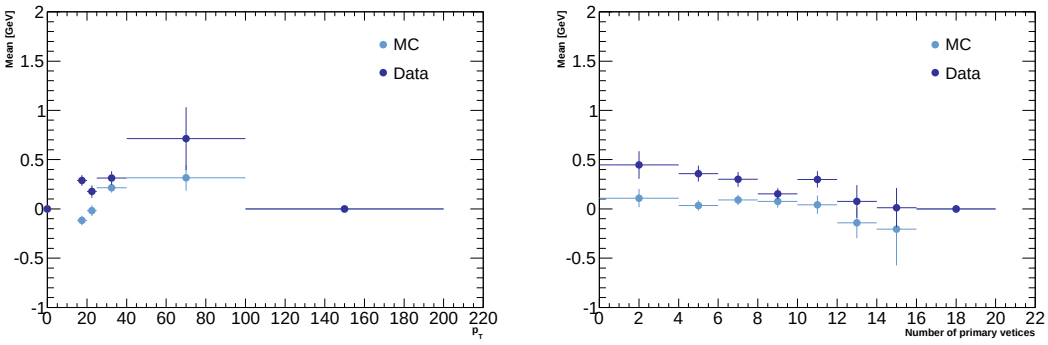

Figure 11.3: Distribution of the mean of the EtCone20_corrected variable as a function of p_{T} (left) and the number of primary vertices (right) after the isolation event selection comparing data and Monte Carlo [96].

and the shifted isolation cut value. This is performed individually for the GGM and SPS8 points, giving relative systematic uncertainties on the acceptance of 0.9 % and 0.2 % respectively.

11.1.3 Pileup

The number of secondary proton-proton interactions in an event can potentially affect any of the selection criteria used for selecting events. The Monte Carlo used for estimating the signal acceptance is generated including secondary collision events to model these effects. However, the pileup configuration in the Monte Carlo does not exactly reproduce that of the actual collision events. This is corrected by using a standard reweighting technique is used to modify the Monte Carlo, so that its average number of pileup interactions per event, $\langle\mu\rangle$, matches that of the data.

These is however some uncertainty on the exact value of $\langle\mu\rangle$. An official ATLAS wide prescription is used to account for this. The Monte Carlo is reweighted to $0.9{\cdot}\langle\mu >\rangle$, where $\langle\mu\rangle$ is the nominal one from the collision data. The resulting change in acceptance is used as a systematic uncertainty. There appears to be no strong correlation of the uncertainty value across the points within each of the theory scenarios examined, so a single uncertainty is used for all the points. The systematic uncertainty for the GGM points is 0.8 % while for the SPS8 points it is a slightly lower 0.5 %.

11.1.4 Missing Transverse Energy

Three primary sources of systematic uncertainties on the $E_{\mathrm{T}}^{\mathrm{miss}}$ selection are considered for this analysis: topocluster energy scale, $E_{\mathrm{T}}^{\mathrm{miss}}$ resolution, and effects from the muon corrections to the $E_{\mathrm{T}}^{\mathrm{miss}}$. Details on these three main contributions can are included in Sections 11.1.4.1, 11.1.4.2, and 11.1.4.3. The techniques used for these were adapted from those used in the inclusive $W^{\pm}$ and Z^{0} cross-section analysis [101]. Additional potential contributions are also investigated, but were found to be negligible. Unlike the signal acceptance systematics highlighted so far, the $E_{\mathrm{T}}^{\mathrm{miss}}$ uncertainties have a very strong dependence on the kinematics of the event. Due to the large variation in kinematics across the various SUSY Monte Carlo points examined, the $E_{\mathrm{T}}^{\mathrm{miss}}$ uncertainties are studied and assigned separately for each GGM and SPS8 point.

All uncertainties presented in this section use the definition of the missing transverse energy from Section 7.5 with muon corrections. The various components of the $E_{\mathrm{T}}^{\mathrm{miss}}$ uncertainty are treated as uncorrelated and are combined in quadrature to obtain the total $E_{\mathrm{T}}^{\mathrm{miss}}$ systematic uncertainty shown in Section 11.1.4.5. The total $E_{\mathrm{T}}^{\mathrm{miss}}$ uncertainty is treated as fully correlated with the uncertainties on the H_{T} described in Section 11.1.5.

11.1.4.1 Topocluster Energy Scale

As described in Section 7.5, the calorimeter portion of the $E_{\mathrm{T}}^{\mathrm{miss}}$ is calculated by summing over the calibrated energies of the reconstructed topoclusters. The uncertainty on the scale of the topocluster energy calibration is the dominant component of the

uncertainty on the $E_{\mathrm{T}}^{\mathrm{miss}}$. The topocluster energy scale uncertainty is taken from the difference between data and MC in E/p studies [102]. This uncertainty is $\sim 20\,\%$ for $p_{\mathrm{T}} \sim 500\,\mathrm{MeV}$ and approximately $5\,\%$ at high p_{T}. To estimate the effect of this uncertainty, the topoclusters' energies are multiplied by a correction factor

$$c = \begin{cases} 1 \pm a \times \left(1 + \frac{b}{p_{\mathrm{T}}}\right) & |\eta_{\mathrm{clus}}| < 2.3 \\ 1 \pm \sqrt{\left(a \times \left(1 + \frac{b}{p_{\mathrm{T}}}\right)\right)^2 + 0.05^2} & 2.3 < |\eta_{\mathrm{clus}}| < 3.2\,, \\ 1 \pm \sqrt{\left(a \times \left(1 + \frac{b}{p_{\mathrm{T}}}\right)\right)^2 + 0.15^2} & 3.2 < |\eta_{\mathrm{clus}}| < 4.5 \end{cases} \tag{11.1}$$

where $a = 5\%$, $b = 1.5$, p_{T} is the cluster transverse momentum in GeV, and the choice of $\pm$ gives the upper and lower uncertainty bounds. The $E_{\mathrm{T}}^{\mathrm{miss}}$ is then recomputed using the altered topoclusters. This is done for both the upper and lower bounds of the topocluster uncertainty. The value assigned as the uncertainty on the $E_{\mathrm{T}}^{\mathrm{miss}}$ acceptance from the topoclusters is taken as the maximum excursion in the $E_{\mathrm{T}}^{\mathrm{miss}}$ acceptance from the bounds on the topocluster uncertainty. Figure 11.4 shows the effect of varying the topocluster energy on the $E_{\mathrm{T}}^{\mathrm{miss}}$ for two GGM signal points.

Signal point		Uncert.[%]	Signal point		Uncert.[%]	Signal point		Uncert.[%]
$m(\tilde{g})$	$m(\tilde{\chi}_1^0)$	A	$m(\tilde{g})$	$m(\tilde{\chi}_1^0)$	A	$m(\tilde{g})$	$m(\tilde{\chi}_1^0)$	A
800	50	11.88	1000	100	7.55	1150	1050	0.58
800	100	11.43	1000	150	8.48	1150	1130	0.68
800	150	7.79	1000	300	5.76	1150	1140	0.70
800	300	6.59	1000	450	3.86	1200	50	8.97
800	450	4.00	1000	600	1.91	1200	100	7.77
800	600	1.66	1000	750	1.11	1200	150	6.49
800	750	1.04	1000	900	1.16	1200	300	4.96
800	780	0.92	1000	980	0.75	1200	450	2.81
800	790	0.88	1000	990	0.80	1200	600	1.50
850	50	15.92	1050	50	10.85	1200	750	1.77
850	100	11.28	1050	100	10.03	1200	900	0.80
850	150	7.21	1050	150	7.81	1200	1050	0.88
850	300	6.53	1050	300	4.92	1200	1180	0.38
850	450	2.96	1050	450	3.66	1200	1190	0.68
850	600	2.28	1050	600	1.69	1250	50	6.71
850	750	1.31	1050	750	1.13	1250	100	7.43
850	830	1.16	1050	900	0.97	1250	150	6.24
850	840	1.04	1050	1030	0.83	1250	300	4.42
900	50	6.60	1050	1040	0.85	1250	450	2.35
900	100	10.16	1100	50	8.68	1250	600	1.38
900	150	11.95	1100	100	11.61	1250	750	1.49
900	300	7.94	1100	150	7.62	1250	900	1.18
900	450	2.47	1100	300	4.06	1250	1050	0.64
900	600	1.35	1100	450	3.73	1250	1200	0.79
900	750	1.45	1100	600	1.85	1250	1230	0.51
900	880	0.87	1100	750	1.04	1250	1240	0.91
900	890	0.99	1100	900	0.73	1300	50	6.41
950	50	10.30	1100	1050	0.62	1300	100	7.48
950	100	14.14	1100	1080	0.59	1300	150	7.34
950	150	8.65	1100	1090	0.36	1300	300	4.51
950	300	5.37	1150	50	11.66	1300	450	3.33
950	450	3.01	1150	100	9.82	1300	600	2.57
950	600	1.68	1150	150	7.13	1300	750	1.39
950	750	0.74	1150	300	4.04	1300	900	0.91
950	900	1.00	1150	450	3.45	1300	1050	0.86
950	930	1.11	1150	600	1.46	1300	1200	0.60
950	940	1.07	1150	750	1.26	1300	1280	0.53
1000	50	16.77	1150	900	0.99	1300	1290	0.42

Table 11.1: The component of the systematic uncertainties on the acceptance, for the gluino GGM points, of the $E_{\mathrm{T}}^{\mathrm{miss}}$ cut of signal region A due to the topocluster energy scale uncertainties.

Signal point		Uncert.[%]	Signal point		Uncert.[%]	Signal point		Uncert.[%]
$m(\tilde{g})$	$m(\tilde{\chi}_1^0)$	B	$m(\tilde{g})$	$m(\tilde{\chi}_1^0)$	B	$m(\tilde{g})$	$m(\tilde{\chi}_1^0)$	B
800	50	4.86	1000	100	2.87	1150	1050	0.17
800	100	4.11	1000	150	2.18	1150	1130	0.19
800	150	4.47	1000	300	1.16	1150	1140	0.18
800	300	1.94	1000	450	1.04	1200	50	2.31
800	450	1.32	1000	600	1.07	1200	100	2.24
800	600	1.07	1000	750	0.15	1200	150	1.81
800	750	0.69	1000	900	0.27	1200	300	1.38
800	780	0.48	1000	980	0.34	1200	450	0.97
800	790	0.35	1000	990	0.60	1200	600	0.42
850	50	3.69	1050	50	2.44	1200	750	0.36
850	100	4.24	1050	100	2.20	1200	900	0.53
850	150	3.21	1050	150	2.19	1200	1050	0.33
850	300	2.20	1050	300	1.40	1200	1180	0.31
850	450	0.88	1050	450	0.83	1200	1190	0.33
850	600	1.11	1050	600	0.55	1250	50	2.13
850	750	0.32	1050	750	0.40	1250	100	1.71
850	830	0.39	1050	900	0.25	1250	150	1.71
850	840	0.56	1050	1030	0.39	1250	300	1.43
900	50	2.87	1050	1040	0.11	1250	450	0.74
900	100	3.46	1100	50	2.03	1250	600	0.34
900	150	1.96	1100	100	2.13	1250	750	0.34
900	300	2.07	1100	150	1.96	1250	900	0.14
900	450	0.88	1100	300	1.34	1250	1050	0.36
900	600	0.45	1100	450	0.55	1250	1200	0.22
900	750	0.36	1100	600	0.40	1250	1230	0.37
900	880	0.49	1100	750	0.58	1250	1240	0.13
900	890	0.72	1100	900	0.25	1300	50	1.52
950	50	2.49	1100	1050	0.31	1300	100	1.41
950	100	3.20	1100	1080	0.31	1300	150	1.83
950	150	2.74	1100	1090	0.62	1300	300	1.41
950	300	1.59	1150	50	2.27	1300	450	0.43
950	450	0.73	1150	100	2.13	1300	600	0.48
950	600	0.73	1150	150	2.42	1300	750	0.52
950	750	0.48	1150	300	1.15	1300	900	0.56
950	900	0.12	1150	450	0.78	1300	1050	0.36
950	930	0.48	1150	600	0.71	1300	1200	0.14
950	940	0.42	1150	750	0.41	1300	1280	0.17
1000	50	2.85	1150	900	0.48	1300	1290	0.12

Table 11.2: The component of the systematic uncertainties on the acceptance, for the gluino GGM points, of the $E_{\mathrm{T}}^{\mathrm{miss}}$ cut of signal region B due to the topocluster energy scale uncertainties.

Signal point		Uncert.[%]	Signal point		Uncert.[%]	Signal point		Uncert.[%]
$m(\tilde{g})$	$m(\tilde{\chi}_1^0)$	C	$m(\tilde{g})$	$m(\tilde{\chi}_1^0)$	C	$m(\tilde{g})$	$m(\tilde{\chi}_1^0)$	C
800	50	9.20	1000	100	4.78	1150	1050	0.25
800	100	6.77	1000	150	4.62	1150	1130	0.24
800	150	5.25	1000	300	2.19	1150	1140	0.22
800	300	3.02	1000	450	1.26	1200	50	2.88
800	450	1.18	1000	600	0.82	1200	100	2.60
800	600	0.89	1000	750	0.84	1200	150	3.84
800	750	0.74	1000	900	0.40	1200	300	1.85
800	780	0.74	1000	980	0.53	1200	450	1.22
800	790	0.47	1000	990	0.56	1200	600	0.37
850	50	6.63	1050	50	5.12	1200	750	0.44
850	100	6.22	1050	100	4.84	1200	900	0.36
850	150	4.85	1050	150	3.06	1200	1050	0.32
850	300	2.45	1050	300	1.90	1200	1180	0.35
850	450	1.50	1050	450	1.54	1200	1190	0.25
850	600	1.13	1050	600	0.92	1250	50	3.89
850	750	0.73	1050	750	0.56	1250	100	4.92
850	830	0.46	1050	900	0.41	1250	150	2.58
850	840	0.46	1050	1030	0.30	1250	300	1.32
900	50	6.49	1050	1040	0.27	1250	450	1.01
900	100	4.43	1100	50	4.15	1250	600	1.01
900	150	4.78	1100	100	5.44	1250	750	0.61
900	300	2.38	1100	150	3.18	1250	900	0.48
900	450	1.77	1100	300	2.25	1250	1050	0.56
900	600	0.95	1100	450	1.38	1250	1200	0.39
900	750	0.66	1100	600	0.74	1250	1230	0.35
900	880	0.36	1100	750	0.35	1250	1240	0.31
900	890	0.29	1100	900	0.33	1300	50	3.68
950	50	4.89	1100	1050	0.13	1300	100	3.71
950	100	7.31	1100	1080	0.39	1300	150	2.21
950	150	3.93	1100	1090	0.52	1300	300	1.12
950	300	2.12	1150	50	4.36	1300	450	0.99
950	450	1.16	1150	100	3.92	1300	600	0.49
950	600	0.84	1150	150	3.37	1300	750	0.51
950	750	0.57	1150	300	1.35	1300	900	0.36
950	900	0.60	1150	450	1.67	1300	1050	0.43
950	930	0.57	1150	600	0.85	1300	1200	0.39
950	940	0.22	1150	750	0.65	1300	1280	0.28
1000	50	5.94	1150	900	0.52	1300	1290	0.11

Table 11.3: The component of the systematic uncertainties on the acceptance, for the gluino GGM points, of the $E_{\mathrm{T}}^{\mathrm{miss}}$ cut of signal region C due to the topocluster energy scale uncertainties.

Signal point		Uncert.[%]	Signal point		Uncert.[%]	Signal point		Uncert.[%]
$m(\tilde{q})$	$m(\tilde{\chi}_1^0)$	A	$m(\tilde{q})$	$m(\tilde{\chi}_1^0)$	A	$m(\tilde{q})$	$m(\tilde{\chi}_1^0)$	A
800	50	7.11	1000	100	4.06	1150	1050	0.73
800	100	8.32	1000	150	5.40	1150	1130	0.84
800	150	5.52	1000	300	3.61	1150	1140	0.57
800	300	4.74	1000	450	2.07	1200	50	3.70
800	450	2.56	1000	600	1.74	1200	100	3.06
800	600	1.13	1000	750	1.32	1200	150	2.99
800	750	1.23	1000	900	0.47	1200	300	2.41
800	780	0.91	1000	980	0.49	1200	450	1.96
800	790	1.46	1000	990	0.60	1200	600	1.45
850	50	8.11	1050	50	5.95	1200	750	1.41
850	100	6.17	1050	100	5.15	1200	900	1.02
850	150	6.12	1050	150	4.03	1200	1050	0.70
850	300	3.88	1050	300	2.49	1200	1180	0.49
850	450	3.15	1050	450	1.86	1200	1190	0.39
850	600	1.33	1050	600	1.78	1250	50	3.21
850	750	1.18	1050	750	0.93	1250	100	3.59
850	830	0.88	1050	900	0.95	1250	150	3.02
850	840	1.12	1050	1030	0.88	1250	300	2.71
900	50	5.26	1050	1040	0.87	1250	450	1.92
900	100	5.67	1100	50	4.85	1250	600	1.64
900	150	4.09	1100	100	3.76	1250	750	1.42
900	300	4.27	1100	150	4.22	1250	900	1.40
900	450	2.60	1100	300	3.23	1250	1050	0.70
900	600	2.06	1100	450	2.22	1250	1200	0.57
900	750	0.89	1100	600	1.20	1250	1230	0.64
900	880	0.90	1100	750	1.12	1250	1240	0.44
900	890	0.59	1100	900	0.70	1300	50	3.66
950	50	5.09	1100	1050	0.89	1300	100	2.99
950	100	5.39	1100	1080	0.67	1300	150	3.01
950	150	3.90	1100	1090	0.52	1300	300	2.57
950	300	3.04	1150	50	4.16	1300	450	2.03
950	450	2.80	1150	100	4.63	1300	600	1.69
950	600	1.80	1150	150	3.47	1300	750	1.14
950	750	1.05	1150	300	2.83	1300	900	0.61
950	900	0.82	1150	450	2.23	1300	1050	0.96
950	930	1.02	1150	600	2.04	1300	1200	0.18
950	940	0.82	1150	750	1.45	1300	1280	0.52
1000	50	6.12	1150	900	0.64	1300	1290	0.67

Table 11.4: The component of the systematic uncertainties on the acceptance, for the squark GGM points, of the $E_{\mathrm{T}}^{\mathrm{miss}}$ cut of signal region A due to the topocluster energy scale uncertainties.

Signal point		Uncert.[%]	Signal point		Uncert.[%]	Signal point		Uncert.[%]
$m(\tilde{q})$	$m(\tilde{\chi}_1^0)$	B	$m(\tilde{q})$	$m(\tilde{\chi}_1^0)$	B	$m(\tilde{q})$	$m(\tilde{\chi}_1^0)$	B
800	50	2.34	1000	100	1.47	1150	1050	0.27
800	100	2.05	1000	150	1.21	1150	1130	0.22
800	150	1.67	1000	300	1.11	1150	1140	0.20
800	300	1.91	1000	450	0.91	1200	50	0.83
800	450	1.33	1000	600	0.81	1200	100	0.88
800	600	0.77	1000	750	0.62	1200	150	0.66
800	750	0.16	1000	900	0.55	1200	300	0.59
800	780	0.00	1000	980	0.24	1200	450	0.98
800	790	0.19	1000	990	0.46	1200	600	0.43
850	50	1.30	1050	50	1.12	1200	750	0.21
850	100	1.89	1050	100	1.19	1200	900	0.61
850	150	2.14	1050	150	1.62	1200	1050	0.42
850	300	1.33	1050	300	0.38	1200	1180	0.37
850	450	1.00	1050	450	0.43	1200	1190	0.23
850	600	0.17	1050	600	0.60	1250	50	1.03
850	750	0.59	1050	750	0.47	1250	100	1.08
850	830	0.44	1050	900	0.13	1250	150	0.75
850	840	0.20	1050	1030	0.40	1250	300	0.47
900	50	1.36	1050	1040	0.21	1250	450	0.53
900	100	1.51	1100	50	0.57	1250	600	0.52
900	150	1.34	1100	100	1.11	1250	750	0.48
900	300	0.83	1100	150	1.03	1250	900	0.34
900	450	0.81	1100	300	1.10	1250	1050	0.22
900	600	0.70	1100	450	0.77	1250	1200	0.21
900	750	0.34	1100	600	0.53	1250	1230	0.17
900	880	0.16	1100	750	0.39	1250	1240	0.18
900	890	0.12	1100	900	0.41	1300	50	0.65
950	50	1.75	1100	1050	0.34	1300	100	0.81
950	100	1.39	1100	1080	0.75	1300	150	0.90
950	150	1.15	1100	1090	0.29	1300	300	0.71
950	300	1.01	1150	50	1.43	1300	450	0.51
950	450	0.85	1150	100	1.15	1300	600	0.40
950	600	0.53	1150	150	0.74	1300	750	0.49
950	750	0.61	1150	300	0.54	1300	900	0.42
950	900	0.40	1150	450	0.64	1300	1050	0.14
950	930	0.22	1150	600	0.41	1300	1200	0.16
950	940	0.53	1150	750	0.25	1300	1280	0.15
1000	50	1.10	1150	900	0.37	1300	1290	0.30

Table 11.5: The component of the systematic uncertainties on the acceptance, for the squark GGM points, of the $E_{\mathrm{T}}^{\mathrm{miss}}$ cut of signal region B due to the topocluster energy scale uncertainties.

Signal point		Uncert.[%]	Signal point		Uncert.[%]	Signal point		Uncert.[%]
$m(\tilde{q})$	$m(\tilde{\chi}_1^0)$	C	$m(\tilde{q})$	$m(\tilde{\chi}_1^0)$	C	$m(\tilde{q})$	$m(\tilde{\chi}_1^0)$	C
800	50	4.71	1000	100	2.36	1150	1050	0.48
800	100	3.18	1000	150	2.45	1150	1130	0.20
800	150	2.74	1000	300	2.28	1150	1140	0.17
800	300	1.81	1000	450	1.26	1200	50	1.44
800	450	1.04	1000	600	0.45	1200	100	2.08
800	600	0.92	1000	750	0.56	1200	150	1.55
800	750	0.52	1000	900	0.49	1200	300	1.17
800	780	0.50	1000	980	0.25	1200	450	0.91
800	790	0.42	1000	990	0.33	1200	600	0.80
850	50	3.72	1050	50	2.32	1200	750	0.47
850	100	3.87	1050	100	2.82	1200	900	0.37
850	150	2.77	1050	150	2.04	1200	1050	0.24
850	300	1.48	1050	300	1.48	1200	1180	0.20
850	450	1.27	1050	450	0.92	1200	1190	0.25
850	600	0.58	1050	600	0.67	1250	50	2.26
850	750	0.78	1050	750	0.44	1250	100	2.10
850	830	0.34	1050	900	0.37	1250	150	2.28
850	840	0.32	1050	1030	0.11	1250	300	1.36
900	50	2.92	1050	1040	0.34	1250	450	0.60
900	100	3.19	1100	50	2.77	1250	600	0.67
900	150	1.92	1100	100	2.12	1250	750	0.51
900	300	1.74	1100	150	2.35	1250	900	0.21
900	450	1.28	1100	300	1.08	1250	1050	0.23
900	600	0.69	1100	450	0.75	1250	1200	0.17
900	750	0.74	1100	600	0.71	1250	1230	0.34
900	880	0.88	1100	750	0.48	1250	1240	0.22
900	890	0.40	1100	900	0.31	1300	50	2.03
950	50	2.99	1100	1050	0.46	1300	100	0.85
950	100	3.04	1100	1080	0.33	1300	150	1.80
950	150	2.63	1100	1090	0.23	1300	300	1.06
950	300	1.47	1150	50	1.37	1300	450	0.79
950	450	0.95	1150	100	1.32	1300	600	0.71
950	600	0.57	1150	150	1.68	1300	750	0.37
950	750	0.76	1150	300	0.87	1300	900	0.32
950	900	0.44	1150	450	0.49	1300	1050	0.49
950	930	0.36	1150	600	0.58	1300	1200	0.26
950	940	0.39	1150	750	0.46	1300	1280	0.36
1000	50	1.75	1150	900	0.79	1300	1290	0.20

Table 11.6: The component of the systematic uncertainties on the acceptance, for the squark GGM points, of the $E_{\mathrm{T}}^{\mathrm{miss}}$ cut of signal region C due to the topocluster energy scale uncertainties.

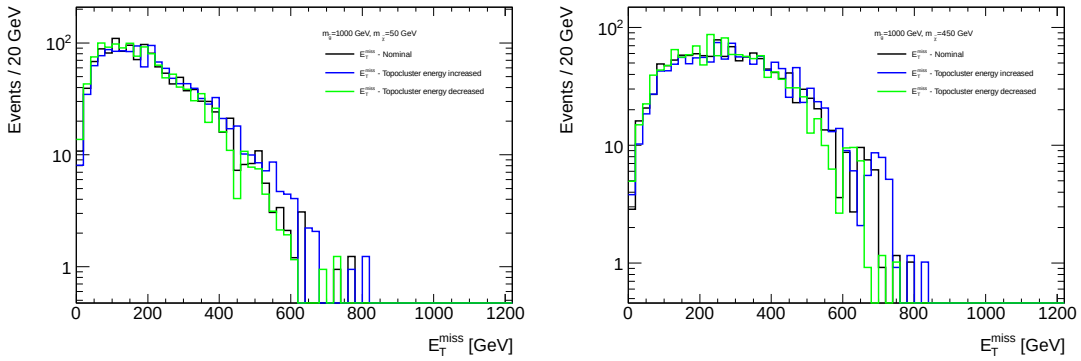

Figure 11.4: Effect of adjusting the topocluster energy scale within its uncertainty bad on the $E_{\mathrm{T}}^{\mathrm{miss}}$ distribution of the $m(\tilde{g}) = 1000\,\mathrm{GeV}$, $m(\tilde{\chi}_1^0) = 50\,\mathrm{GeV}$ (left) and the $m(\tilde{g}) = 1000\,\mathrm{GeV}$, $m(\tilde{\chi}_1^0) = 450\,\mathrm{GeV}$ (right) signal points.

For the GGM model, the estimated uncertainty on the the signal acceptance of the $E_{\mathrm{T}}^{\mathrm{miss}}$ cut due to the topocluster energy uncertainty varies as a function of the signal grid points from 0.4% to 16.8%, 0.1% to 4.9%, and 0.1% to 9.2% for signal regions A, B, and C respectively as shown in Table 11.1 – 11.6. This uncertainty varies most strongly as a function of $m(\tilde{\chi}_1^0)$ because the neutralino mass influences the transverse momentum of the escaping gravitinos. For the very high $m(\tilde{\chi}_1^0)$ signal points, most events have a $E_{\mathrm{T}}^{\mathrm{miss}}$ well above the selection cut, hence the relatively small uncertainty. The points with high uncertainties for signal region A are generally those for which signal B is optimized (with its lower $E_{\mathrm{T}}^{\mathrm{miss}}$ cut). When looking at the optimal analysis for each GGM signal point[1] the $E_{\mathrm{T}}^{\mathrm{miss}}$ uncertainty is less than 5 % across the grid. As an illustration of the effect of the $E_{\mathrm{T}}^{\mathrm{miss}}$ uncertainty, Fig. 11.4 shows the $E_{\mathrm{T}}^{\mathrm{miss}}$ distribution for two different GGM signal points.

[1]The optimal signal region for each point is the one which gives the best expected limit. Details on this can be seen in Chapter 12.

Signal point	Uncertainty [%]		
Λ [TeV]	A	B	C
50	30.78	9.37	13.86
60	19.87	3.19	10.19
70	16.65	3.93	10.34
80	13.88	4.17	14.03
90	14.26	2.22	10.42
100	13.74	2.90	9.65
110	12.59	2.40	9.45
120	12.91	1.87	7.50
130	8.20	1.34	7.34
140	10.65	1.53	6.61
150	9.97	3.06	5.90
160	9.32	0.34	4.01
170	7.63	2.52	3.14
180	9.16	0.65	2.96
190	7.99	1.32	2.81
200	6.79	2.15	2.67
210	6.50	1.69	2.26
220	5.98	1.93	2.63
230	5.21	2.13	2.07
240	5.28	1.18	2.06
250	4.09	0.73	1.59

Table 11.7: The component of the systematic uncertainties on the acceptance, for the SPS8 points, of the $E_{\mathrm{T}}^{\mathrm{miss}}$ cut of signal region A, B, and C due to the topocluster energy scale uncertainties.

For the SPS8 model, the estimated uncertainty on the signal acceptance of the $E_{\mathrm{T}}^{\mathrm{miss}}$ cut due to the topocluster energy uncertainty varies as a function of the signal grid points from 4.1% to 30.8%, 0.3% to 9.4%,and 1.6% to 14.0% for signal regions A, B, and C respectively as shown in Table 11.7. This uncertainty varies strongly as a function of Λ, the effective scale of SUSY breaking, which sets the mass of the lightest neutralino and therefore the $E_{\mathrm{T}}^{\mathrm{miss}}$ in this theory scenario. The topocluster energy uncertainties for a given $m(\tilde{\chi}_1^0)$ are quite similar between the GGM and SPS8 theory scenarios.

11.1.4.2 Missing Transverse Energy Resolution

The $E_{\mathrm{T}}^{\mathrm{miss}}$ resolution can be described by the function $\sigma\left(E_{\mathrm{x}}^{\mathrm{miss}}, E_{\mathrm{y}}^{\mathrm{miss}}\right) = \alpha\sqrt{\sum E_T}$ where α is the resolution parameter. A value of $\alpha = 0.49$ is measured in minimum bias events at $\sqrt{s} = 7\,\mathrm{TeV}$, and a value of $\alpha = 0.53$ is measured in events with at least one jet with $p_{\mathrm{T}} > 20\,\mathrm{GeV}$[101]. For this uncertainty, events from the data with at least two photons passing the *PhotonLoose* requirements and with $p_{\mathrm{T}} > 20\,\mathrm{GeV}$, were used to estimate the resolution of photonic events in the data. The resolution of this sample, as a function of $\sum E_T$, was compared to that of the Monte-Carlo signal samples, and was found to be within 14% for all GGM and SPS8 signal points. The comparison of the resolution between the loose diphoton sample and a Monte Carlo signal point can be seen in Fig. 11.5

The value of 14% for GGM/SPS8 is taken as a conservative uncertainty on the resolution. The $E_{\mathrm{T}}^{\mathrm{miss}}$ resolution is then adjusted using this uncertainty. The $E_{\mathrm{x}}^{\mathrm{miss}}$ and $E_{\mathrm{y}}^{\mathrm{miss}}$ components of the $E_{\mathrm{T}}^{\mathrm{miss}}$ for each event were then smeared using nine variations

Signal point		Uncert.[%]	Signal point		Uncert.[%]	Signal point		Uncert.[%]
$m(\tilde{g})$	$m(\tilde{\chi}_1^0)$	A	$m(\tilde{g})$	$m(\tilde{\chi}_1^0)$	A	$m(\tilde{g})$	$m(\tilde{\chi}_1^0)$	A
800	50	1.89	1000	100	0.81	1150	1050	0.02
800	100	0.90	1000	150	0.75	1150	1130	0.07
800	150	0.97	1000	300	0.51	1150	1140	0.06
800	300	0.17	1000	450	0.27	1200	50	1.91
800	450	0.27	1000	600	0.21	1200	100	1.35
800	600	0.09	1000	750	0.03	1200	150	0.43
800	750	0.11	1000	900	0.12	1200	300	0.15
800	780	0.02	1000	980	0.05	1200	450	0.20
800	790	0.08	1000	990	0.11	1200	600	0.06
850	50	2.48	1050	50	2.70	1200	750	0.10
850	100	1.77	1050	100	1.49	1200	900	0.07
850	150	0.02	1050	150	1.38	1200	1050	0.08
850	300	0.76	1050	300	0.61	1200	1180	0.01
850	450	0.16	1050	450	0.01	1200	1190	0.06
850	600	0.23	1050	600	0.01	1250	50	0.61
850	750	0.13	1050	750	0.11	1250	100	0.99
850	830	0.04	1050	900	0.03	1250	150	0.80
850	840	0.10	1050	1030	0.08	1250	300	0.07
900	50	2.35	1050	1040	0.15	1250	450	0.24
900	100	2.65	1100	50	1.98	1250	600	0.14
900	150	2.70	1100	100	1.28	1250	750	0.01
900	300	0.45	1100	150	1.00	1250	900	0.07
900	450	0.03	1100	300	0.60	1250	1050	0.01
900	600	0.09	1100	450	0.07	1250	1200	0.09
900	750	0.03	1100	600	0.18	1250	1230	0.03
900	880	0.16	1100	750	0.00	1250	1240	0.10
900	890	0.11	1100	900	0.07	1300	50	3.51
950	50	0.20	1100	1050	0.08	1300	100	0.47
950	100	2.36	1100	1080	0.06	1300	150	1.65
950	150	0.21	1100	1090	0.13	1300	300	0.31
950	300	0.81	1150	50	2.07	1300	450	0.07
950	450	0.35	1150	100	3.61	1300	600	0.05
950	600	0.18	1150	150	0.16	1300	750	0.22
950	750	0.10	1150	300	0.32	1300	900	0.02
950	900	0.11	1150	450	0.08	1300	1050	0.06
950	930	0.03	1150	600	0.11	1300	1200	0.03
950	940	0.05	1150	750	0.12	1300	1280	0.08
1000	50	2.41	1150	900	0.00	1300	1290	0.24

Table 11.8: The component of the systematic uncertainties on the acceptance, for the gluino GGM points, of the $E_{\mathrm{T}}^{\mathrm{miss}}$ cut of signal region A due to the $E_{\mathrm{T}}^{\mathrm{miss}}$ resolution uncertainties.

Signal point		Uncert.[%]	Signal point		Uncert.[%]	Signal point		Uncert.[%]
$m(\tilde{g})$	$m(\tilde{\chi}_1^0)$	B	$m(\tilde{g})$	$m(\tilde{\chi}_1^0)$	B	$m(\tilde{g})$	$m(\tilde{\chi}_1^0)$	B
800	50	0.18	1000	100	0.16	1150	1050	0.03
800	100	0.18	1000	150	0.22	1150	1130	0.11
800	150	0.35	1000	300	0.30	1150	1140	0.11
800	300	0.15	1000	450	0.22	1200	50	0.29
800	450	0.42	1000	600	0.21	1200	100	0.26
800	600	0.25	1000	750	0.04	1200	150	0.12
800	750	0.50	1000	900	0.27	1200	300	0.08
800	780	0.09	1000	980	0.13	1200	450	0.15
800	790	0.37	1000	990	0.27	1200	600	0.05
850	50	0.29	1050	50	0.35	1200	750	0.09
850	100	0.34	1050	100	0.28	1200	900	0.08
850	150	0.01	1050	150	0.43	1200	1050	0.10
850	300	0.54	1050	300	0.37	1200	1180	0.02
850	450	0.20	1050	450	0.01	1200	1190	0.09
850	600	0.50	1050	600	0.01	1250	50	0.09
850	750	0.45	1050	750	0.13	1250	100	0.19
850	830	0.16	1050	900	0.05	1250	150	0.24
850	840	0.39	1050	1030	0.19	1250	300	0.04
900	50	0.30	1050	1040	0.31	1250	450	0.18
900	100	0.59	1100	50	0.31	1250	600	0.11
900	150	0.87	1100	100	0.22	1250	750	0.01
900	300	0.30	1100	150	0.31	1250	900	0.06
900	450	0.03	1100	300	0.35	1250	1050	0.01
900	600	0.14	1100	450	0.05	1250	1200	0.12
900	750	0.09	1100	600	0.16	1250	1230	0.04
900	880	0.53	1100	750	0.00	1250	1240	0.14
900	890	0.37	1100	900	0.09	1300	50	0.55
950	50	0.03	1100	1050	0.16	1300	100	0.12
950	100	0.43	1100	1080	0.12	1300	150	0.46
950	150	0.06	1100	1090	0.23	1300	300	0.17
950	300	0.50	1150	50	0.30	1300	450	0.05
950	450	0.32	1150	100	0.67	1300	600	0.04
950	600	0.23	1150	150	0.05	1300	750	0.19
950	750	0.18	1150	300	0.18	1300	900	0.02
950	900	0.33	1150	450	0.06	1300	1050	0.06
950	930	0.09	1150	600	0.09	1300	1200	0.04
950	940	0.15	1150	750	0.11	1300	1280	0.11
1000	50	0.27	1150	900	0.00	1300	1290	0.32

Table 11.9: The component of the systematic uncertainties on the acceptance, for the gluino GGM points, of the $E_{\mathrm{T}}^{\mathrm{miss}}$ cut of signal region B due to the $E_{\mathrm{T}}^{\mathrm{miss}}$ resolution uncertainties.

Signal point		Uncert.[%]	Signal point		Uncert.[%]	Signal point		Uncert.[%]
$m(\tilde{g})$	$m(\tilde{\chi}_1^0)$	C	$m(\tilde{g})$	$m(\tilde{\chi}_1^0)$	C	$m(\tilde{g})$	$m(\tilde{\chi}_1^0)$	C
800	50	0.80	1000	100	0.44	1150	1050	0.02
800	100	0.40	1000	150	0.42	1150	1130	0.06
800	150	0.50	1000	300	0.37	1150	1140	0.06
800	300	0.12	1000	450	0.22	1200	50	1.14
800	450	0.22	1000	600	0.19	1200	100	0.81
800	600	0.08	1000	750	0.03	1200	150	0.28
800	750	0.09	1000	900	0.11	1200	300	0.12
800	780	0.01	1000	980	0.05	1200	450	0.17
800	790	0.06	1000	990	0.10	1200	600	0.05
850	50	1.10	1050	50	1.52	1200	750	0.09
850	100	0.74	1050	100	0.81	1200	900	0.07
850	150	0.01	1050	150	0.83	1200	1050	0.08
850	300	0.50	1050	300	0.45	1200	1180	0.01
850	450	0.13	1050	450	0.01	1200	1190	0.05
850	600	0.21	1050	600	0.01	1250	50	0.39
850	750	0.12	1050	750	0.10	1250	100	0.63
850	830	0.03	1050	900	0.03	1250	150	0.53
850	840	0.08	1050	1030	0.08	1250	300	0.06
900	50	1.15	1050	1040	0.14	1250	450	0.21
900	100	1.39	1100	50	1.22	1250	600	0.12
900	150	1.49	1100	100	0.72	1250	750	0.01
900	300	0.31	1100	150	0.63	1250	900	0.06
900	450	0.02	1100	300	0.45	1250	1050	0.00
900	600	0.08	1100	450	0.06	1250	1200	0.08
900	750	0.03	1100	600	0.16	1250	1230	0.03
900	880	0.14	1100	750	0.00	1250	1240	0.10
900	890	0.10	1100	900	0.07	1300	50	2.25
950	50	0.11	1100	1050	0.08	1300	100	0.32
950	100	1.16	1100	1080	0.06	1300	150	1.08
950	150	0.12	1100	1090	0.12	1300	300	0.24
950	300	0.58	1150	50	1.13	1300	450	0.06
950	450	0.29	1150	100	2.21	1300	600	0.04
950	600	0.16	1150	150	0.11	1300	750	0.20
950	750	0.09	1150	300	0.24	1300	900	0.02
950	900	0.10	1150	450	0.07	1300	1050	0.06
950	930	0.03	1150	600	0.10	1300	1200	0.03
950	940	0.04	1150	750	0.11	1300	1280	0.08
1000	50	1.26	1150	900	0.00	1300	1290	0.23

Table 11.10: The component of the systematic uncertainties on the acceptance, for the gluino GGM points, of the $E_{\mathrm{T}}^{\mathrm{miss}}$ cut of signal region C due to the $E_{\mathrm{T}}^{\mathrm{miss}}$ resolution uncertainties.

Signal point		Uncert.[%]	Signal point		Uncert.[%]	Signal point		Uncert.[%]
$m(\tilde{q})$	$m(\tilde{\chi}_1^0)$	A	$m(\tilde{q})$	$m(\tilde{\chi}_1^0)$	A	$m(\tilde{q})$	$m(\tilde{\chi}_1^0)$	A
800	50	0.63	1000	100	0.03	1150	1050	0.11
800	100	0.73	1000	150	0.13	1150	1130	0.07
800	150	0.93	1000	300	0.05	1150	1140	0.02
800	300	0.50	1000	450	0.02	1200	50	1.75
800	450	0.08	1000	600	0.07	1200	100	0.16
800	600	0.01	1000	750	0.20	1200	150	0.65
800	750	0.10	1000	900	0.05	1200	300	0.03
800	780	0.08	1000	980	0.06	1200	450	0.28
800	790	0.05	1000	990	0.02	1200	600	0.06
850	50	1.29	1050	50	1.88	1200	750	0.19
850	100	1.82	1050	100	0.72	1200	900	0.01
850	150	1.52	1050	150	0.11	1200	1050	0.06
850	300	0.17	1050	300	0.08	1200	1180	0.05
850	450	0.32	1050	450	0.01	1200	1190	0.11
850	600	0.10	1050	600	0.27	1250	50	0.31
850	750	0.12	1050	750	0.02	1250	100	1.13
850	830	0.08	1050	900	0.03	1250	150	0.45
850	840	0.07	1050	1030	0.05	1250	300	0.10
900	50	1.98	1050	1040	0.04	1250	450	0.10
900	100	0.44	1100	50	0.64	1250	600	0.21
900	150	0.29	1100	100	0.16	1250	750	0.16
900	300	0.34	1100	150	0.74	1250	900	0.02
900	450	0.25	1100	300	0.43	1250	1050	0.04
900	600	0.32	1100	450	0.31	1250	1200	0.02
900	750	0.03	1100	600	0.12	1250	1230	0.02
900	880	0.05	1100	750	0.12	1250	1240	0.07
900	890	0.05	1100	900	0.05	1300	50	0.10
950	50	1.05	1100	1050	0.03	1300	100	0.00
950	100	0.18	1100	1080	0.02	1300	150	0.49
950	150	0.14	1100	1090	0.04	1300	300	0.15
950	300	0.23	1150	50	1.10	1300	450	0.04
950	450	0.09	1150	100	1.12	1300	600	0.04
950	600	0.22	1150	150	0.11	1300	750	0.04
950	750	0.15	1150	300	0.35	1300	900	0.09
950	900	0.03	1150	450	0.05	1300	1050	0.11
950	930	0.01	1150	600	0.05	1300	1200	0.04
950	940	0.01	1150	750	0.16	1300	1280	0.00
1000	50	0.81	1150	900	0.05	1300	1290	0.10

Table 11.11: The component of the systematic uncertainties on the acceptance, for the squark GGM points, of the $E_{\mathrm{T}}^{\mathrm{miss}}$ cut of signal region A due to the $E_{\mathrm{T}}^{\mathrm{miss}}$ resolution uncertainties.

Signal point		Uncert.[%]	Signal point		Uncert.[%]	Signal point		Uncert.[%]
$m(\tilde{q})$	$m(\tilde{\chi}_1^0)$	B	$m(\tilde{q})$	$m(\tilde{\chi}_1^0)$	B	$m(\tilde{q})$	$m(\tilde{\chi}_1^0)$	B
800	50	0.13	1000	100	0.01	1150	1050	0.14
800	100	0.21	1000	150	0.04	1150	1130	0.12
800	150	0.44	1000	300	0.03	1150	1140	0.03
800	300	0.43	1000	450	0.01	1200	50	0.33
800	450	0.11	1000	600	0.07	1200	100	0.04
800	600	0.03	1000	750	0.27	1200	150	0.19
800	750	0.38	1000	900	0.09	1200	300	0.02
800	780	0.30	1000	980	0.13	1200	450	0.20
800	790	0.19	1000	990	0.04	1200	600	0.05
850	50	0.25	1050	50	0.34	1200	750	0.17
850	100	0.45	1050	100	0.17	1200	900	0.02
850	150	0.57	1050	150	0.03	1200	1050	0.07
850	300	0.13	1050	300	0.05	1200	1180	0.07
850	450	0.34	1050	450	0.01	1200	1190	0.17
850	600	0.18	1050	600	0.26	1250	50	0.06
850	750	0.32	1050	750	0.02	1250	100	0.25
850	830	0.25	1050	900	0.04	1250	150	0.13
850	840	0.26	1050	1030	0.10	1250	300	0.05
900	50	0.36	1050	1040	0.08	1250	450	0.07
900	100	0.11	1100	50	0.12	1250	600	0.17
900	150	0.11	1100	100	0.04	1250	750	0.14
900	300	0.25	1100	150	0.23	1250	900	0.02
900	450	0.25	1100	300	0.24	1250	1050	0.04
900	600	0.43	1100	450	0.24	1250	1200	0.03
900	750	0.06	1100	600	0.11	1250	1230	0.03
900	880	0.13	1100	750	0.13	1250	1240	0.10
900	890	0.14	1100	900	0.06	1300	50	0.02
950	50	0.18	1100	1050	0.06	1300	100	0.00
950	100	0.04	1100	1080	0.03	1300	150	0.13
950	150	0.05	1100	1090	0.08	1300	300	0.08
950	300	0.15	1150	50	0.24	1300	450	0.03
950	450	0.08	1150	100	0.26	1300	600	0.03
950	600	0.25	1150	150	0.03	1300	750	0.04
950	750	0.23	1150	300	0.20	1300	900	0.09
950	900	0.07	1150	450	0.04	1300	1050	0.10
950	930	0.04	1150	600	0.04	1300	1200	0.04
950	940	0.02	1150	750	0.15	1300	1280	0.00
1000	50	0.15	1150	900	0.06	1300	1290	0.13

Table 11.12: The component of the systematic uncertainties on the acceptance, for the squark GGM points, of the $E_{\mathrm{T}}^{\mathrm{miss}}$ cut of signal region B due to the $E_{\mathrm{T}}^{\mathrm{miss}}$ resolution uncertainties.

Signal point		Uncert.[%]	Signal point		Uncert.[%]	Signal point		Uncert.[%]
$m(\tilde{q})$	$m(\tilde{\chi}_1^0)$	C	$m(\tilde{q})$	$m(\tilde{\chi}_1^0)$	C	$m(\tilde{q})$	$m(\tilde{\chi}_1^0)$	C
800	50	0.38	1000	100	0.02	1150	1050	0.10
800	100	0.46	1000	150	0.09	1150	1130	0.07
800	150	0.64	1000	300	0.04	1150	1140	0.02
800	300	0.36	1000	450	0.02	1200	50	1.36
800	450	0.06	1000	600	0.06	1200	100	0.13
800	600	0.01	1000	750	0.19	1200	150	0.52
800	750	0.09	1000	900	0.04	1200	300	0.03
800	780	0.06	1000	980	0.06	1200	450	0.25
800	790	0.04	1000	990	0.02	1200	600	0.05
850	50	0.85	1050	50	1.40	1200	750	0.17
850	100	1.22	1050	100	0.54	1200	900	0.01
850	150	1.03	1050	150	0.09	1200	1050	0.05
850	300	0.13	1050	300	0.07	1200	1180	0.04
850	450	0.26	1050	450	0.01	1200	1190	0.11
850	600	0.09	1050	600	0.25	1250	50	0.25
850	750	0.10	1050	750	0.02	1250	100	0.88
850	830	0.07	1050	900	0.02	1250	150	0.37
850	840	0.06	1050	1030	0.04	1250	300	0.08
900	50	1.36	1050	1040	0.04	1250	450	0.09
900	100	0.31	1100	50	0.48	1250	600	0.19
900	150	0.21	1100	100	0.12	1250	750	0.14
900	300	0.27	1100	150	0.58	1250	900	0.02
900	450	0.21	1100	300	0.35	1250	1050	0.03
900	600	0.28	1100	450	0.27	1250	1200	0.02
900	750	0.03	1100	600	0.11	1250	1230	0.02
900	880	0.04	1100	750	0.12	1250	1240	0.07
900	890	0.04	1100	900	0.04	1300	50	0.08
950	50	0.71	1100	1050	0.03	1300	100	0.00
950	100	0.13	1100	1080	0.02	1300	150	0.39
950	150	0.10	1100	1090	0.04	1300	300	0.13
950	300	0.18	1150	50	0.91	1300	450	0.03
950	450	0.08	1150	100	0.88	1300	600	0.04
950	600	0.19	1150	150	0.09	1300	750	0.04
950	750	0.14	1150	300	0.30	1300	900	0.09
950	900	0.03	1150	450	0.04	1300	1050	0.10
950	930	0.01	1150	600	0.04	1300	1200	0.04
950	940	0.01	1150	750	0.14	1300	1280	0.00
1000	50	0.62	1150	900	0.05	1300	1290	0.10

Table 11.13: The component of the systematic uncertainties on the acceptance, for the squark GGM points, of the $E_{\mathrm{T}}^{\mathrm{miss}}$ cut of signal region C due to the $E_{\mathrm{T}}^{\mathrm{miss}}$ resolution uncertainties.

Signal point	Uncertainty [%]		
Λ [TeV]	A	B	C
50	1.68	0.78	0.28
60	2.05	0.71	0.61
70	1.62	0.49	0.48
80	2.16	0.73	0.68
90	2.59	0.82	0.63
100	1.32	0.49	0.27
110	1.70	0.80	0.29
120	0.85	0.59	0.13
130	1.67	1.79	0.30
140	0.51	0.60	0.08
150	0.79	1.42	0.14
160	0.28	0.72	0.06
170	0.51	1.85	0.14
180	0.22	0.77	0.07
190	0.58	2.47	0.21
200	0.02	0.10	0.01
210	0.49	1.90	0.22
220	0.09	0.32	0.04
230	0.01	0.04	0.01
240	0.21	0.76	0.12
250	0.26	0.83	0.16

Table 11.14: The component of the systematic uncertainties on the acceptance, for the SPS8 points, of the $E_{\mathrm{T}}^{\mathrm{miss}}$ cut of signal region A, B, and C due to the $E_{\mathrm{T}}^{\mathrm{miss}}$ resolution uncertainties.

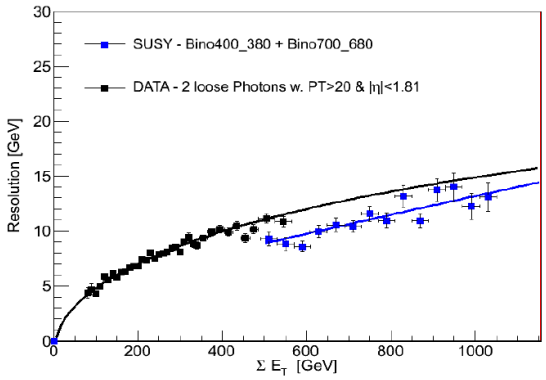

Figure 11.5: $E_{\mathrm{T}}^{\mathrm{miss}}$ resolution as a function of the $\sum E_T$ of a loose (*PhotonLoose*) diphoton sample from the 2010 data compared to GGM Monte Carlo. The difference in resolution between the data and MC are within 14% for all GGM signal points.

on $\Delta\alpha$ in the range $[-0.16, 0.16]$, with respect to the measured nominal value. A new acceptance of the $E_{\mathrm{T}}^{\mathrm{miss}}$ cut was then measured for each value of $\Delta\alpha$. These new acceptances were then fit with a linear function. This fitted function was then used to extract the change in acceptance of the $E_{\mathrm{T}}^{\mathrm{miss}}$ corresponding to a 14% change in α. This yields an uncertainty on the efficiency of the $E_{\mathrm{T}}^{\mathrm{miss}}$ cut due to the resolution of less than 5.4% for all points in the GGM and SPS8 samples. See Tables 11.8 – 11.13 and Table 11.14 for the numbers for all points in both GGM and SPS8 signal grids respectively.

11.1.4.3 Muon Terms Uncertainties

The two uncertainty components discussed so far dealt with the calorimeter component of the $E_{\mathrm{T}}^{\mathrm{miss}}$. Uncertainties on the muon terms come primarily from the uncertainties on the muons themselves. The systematic uncertainties on the p_{T} of

reconstructed muons were considered using a tool provided by the Muon Combined Performance group [66]. The primary effect is on the p_{T} resolution of the reconstructed muons. These uncertainties were then propagated into the muon terms used in the definition of the $E_{\mathrm{T}}^{\mathrm{miss}}$. The effect of these uncertainties on the acceptance of the $E_{\mathrm{T}}^{\mathrm{miss}}$ cut acceptance for all signal regions was found to be negligible for all the GGM and SPS8 Monte Carlo points.

11.1.4.4 Other Missing Transverse Energy Uncertainties

The Monte Carlo samples used in this analysis have been simulated with the LAr calorimeter hole included. As a result the inefficiency of the smart veto, which was described in Section 9.1.4, agrees very well between the Monte Carlo and the actual data. As a result a systematic uncertainty is not assigned, unlike the previous analysis [32]. In the previous analysis this uncertainty was only 1 % for the GGM points and slightly less for SPS8.

11.1.4.5 Total Missing Transverse Energy Uncertainties

The total uncertainty on the acceptance arising from the $E_{\mathrm{T}}^{\mathrm{miss}}$ is obtained from combining in quadrature the components discussed in this section. The only non-negligible components are the topocluster energy scale uncertainty from Section 11.1.4.1 and $E_{\mathrm{T}}^{\mathrm{miss}}$ resolution uncertainty from Section 11.1.4.2. The total relative uncertainty from the $E_{\mathrm{T}}^{\mathrm{miss}}$ acceptance for the GGM points can be seen in Tables 11.15 – 11.20. The same numbers for the SPS8 signal points are included in Table 11.21.

Signal point		Uncert.[%]	Signal point		Uncert.[%]	Signal point		Uncert.[%]
$m(\tilde{g})$	$m(\tilde{\chi}_1^0)$	A	$m(\tilde{g})$	$m(\tilde{\chi}_1^0)$	A	$m(\tilde{g})$	$m(\tilde{\chi}_1^0)$	A
800	50	12.13	1000	100	7.61	1150	1050	0.58
800	100	11.57	1000	150	8.52	1150	1130	0.68
800	150	7.85	1000	300	5.78	1150	1140	0.70
800	300	6.61	1000	450	3.87	1200	50	9.21
800	450	4.01	1000	600	1.92	1200	100	7.89
800	600	1.67	1000	750	1.11	1200	150	6.51
800	750	1.04	1000	900	1.17	1200	300	4.97
800	780	0.92	1000	980	0.75	1200	450	2.82
800	790	0.88	1000	990	0.81	1200	600	1.50
850	50	16.11	1050	50	11.18	1200	750	1.78
850	100	11.42	1050	100	10.15	1200	900	0.80
850	150	7.22	1050	150	7.94	1200	1050	0.89
850	300	6.58	1050	300	4.96	1200	1180	0.39
850	450	2.97	1050	450	3.66	1200	1190	0.68
850	600	2.30	1050	600	1.70	1250	50	6.83
850	750	1.32	1050	750	1.14	1250	100	7.56
850	830	1.16	1050	900	0.97	1250	150	6.29
850	840	1.04	1050	1030	0.83	1250	300	4.42
900	50	7.20	1050	1040	0.87	1250	450	2.36
900	100	10.52	1100	50	8.90	1250	600	1.40
900	150	12.26	1100	100	11.69	1250	750	1.49
900	300	7.96	1100	150	7.69	1250	900	1.18
900	450	2.47	1100	300	4.11	1250	1050	0.64
900	600	1.35	1100	450	3.73	1250	1200	0.80
900	750	1.45	1100	600	1.87	1250	1230	0.51
900	880	0.89	1100	750	1.04	1250	1240	0.91
900	890	1.00	1100	900	0.73	1300	50	7.30
950	50	10.30	1100	1050	0.63	1300	100	7.60
950	100	14.35	1100	1080	0.59	1300	150	7.53
950	150	8.66	1100	1090	0.38	1300	300	4.52
950	300	5.43	1150	50	11.86	1300	450	3.35
950	450	3.03	1150	100	10.48	1300	600	2.57
950	600	1.69	1150	150	7.14	1300	750	1.41
950	750	0.74	1150	300	4.07	1300	900	0.91
950	900	1.01	1150	450	3.47	1300	1050	0.86
950	930	1.11	1150	600	1.47	1300	1200	0.60
950	940	1.07	1150	750	1.27	1300	1280	0.54
1000	50	17.04	1150	900	1.01	1300	1290	0.49

Table 11.15: The total systematic uncertainties on the acceptance, for the gluino GGM points, of the $E_{\mathrm{T}}^{\mathrm{miss}}$ cut of signal region A. The total uncertainty is a combination of the uncertainties from the topocluster energy scale and the $E_{\mathrm{T}}^{\mathrm{miss}}$ resolution.

Signal point		Uncert.[%]	Signal point		Uncert.[%]	Signal point		Uncert.[%]
$m(\tilde{g})$	$m(\tilde{\chi}_1^0)$	B	$m(\tilde{g})$	$m(\tilde{\chi}_1^0)$	B	$m(\tilde{g})$	$m(\tilde{\chi}_1^0)$	B
800	50	4.89	1000	100	2.88	1150	1050	0.17
800	100	4.12	1000	150	2.19	1150	1130	0.22
800	150	4.49	1000	300	1.20	1150	1140	0.21
800	300	1.96	1000	450	1.07	1200	50	2.33
800	450	1.39	1000	600	1.10	1200	100	2.26
800	600	1.10	1000	750	0.15	1200	150	1.82
800	750	0.85	1000	900	0.38	1200	300	1.38
800	780	0.49	1000	980	0.37	1200	450	0.98
800	790	0.51	1000	990	0.66	1200	600	0.43
850	50	3.72	1050	50	2.49	1200	750	0.37
850	100	4.27	1050	100	2.24	1200	900	0.54
850	150	3.21	1050	150	2.23	1200	1050	0.34
850	300	2.27	1050	300	1.45	1200	1180	0.31
850	450	0.95	1050	450	0.85	1200	1190	0.34
850	600	1.22	1050	600	0.55	1250	50	2.13
850	750	0.56	1050	750	0.42	1250	100	1.73
850	830	0.43	1050	900	0.26	1250	150	1.73
850	840	0.68	1050	1030	0.43	1250	300	1.43
900	50	2.89	1050	1040	0.33	1250	450	0.76
900	100	3.52	1100	50	2.05	1250	600	0.37
900	150	2.17	1100	100	2.16	1250	750	0.34
900	300	2.10	1100	150	1.98	1250	900	0.15
900	450	0.88	1100	300	1.39	1250	1050	0.36
900	600	0.47	1100	450	0.56	1250	1200	0.25
900	750	0.37	1100	600	0.44	1250	1230	0.37
900	880	0.72	1100	750	0.58	1250	1240	0.20
900	890	0.81	1100	900	0.29	1300	50	1.65
950	50	2.50	1100	1050	0.35	1300	100	1.43
950	100	3.23	1100	1080	0.34	1300	150	1.89
950	150	2.75	1100	1090	0.66	1300	300	1.43
950	300	1.67	1150	50	2.33	1300	450	0.44
950	450	0.79	1150	100	2.31	1300	600	0.48
950	600	0.77	1150	150	2.42	1300	750	0.56
950	750	0.51	1150	300	1.16	1300	900	0.56
950	900	0.35	1150	450	0.78	1300	1050	0.37
950	930	0.49	1150	600	0.72	1300	1200	0.15
950	940	0.45	1150	750	0.43	1300	1280	0.21
1000	50	2.90	1150	900	0.48	1300	1290	0.34

Table 11.16: The total systematic uncertainties on the acceptance, for the gluino GGM points, of the $E_{\mathrm{T}}^{\mathrm{miss}}$ cut of signal region B. The total uncertainty is a combination of the uncertainties from the topocluster energy scale and the $E_{\mathrm{T}}^{\mathrm{miss}}$ resolution.

Signal point		Uncert.[%]	Signal point		Uncert.[%]	Signal point		Uncert.[%]
$m(\tilde{g})$	$m(\tilde{\chi}_1^0)$	C	$m(\tilde{g})$	$m(\tilde{\chi}_1^0)$	C	$m(\tilde{g})$	$m(\tilde{\chi}_1^0)$	C
800	50	9.29	1000	100	4.82	1150	1050	0.26
800	100	6.78	1000	150	4.65	1150	1130	0.25
800	150	5.27	1000	300	2.25	1150	1140	0.23
800	300	3.03	1000	450	1.29	1200	50	3.12
800	450	1.20	1000	600	0.86	1200	100	2.73
800	600	0.89	1000	750	0.84	1200	150	3.88
800	750	0.74	1000	900	0.41	1200	300	1.86
800	780	0.74	1000	980	0.54	1200	450	1.24
800	790	0.47	1000	990	0.57	1200	600	0.39
850	50	6.75	1050	50	5.34	1200	750	0.46
850	100	6.26	1050	100	4.95	1200	900	0.38
850	150	4.85	1050	150	3.17	1200	1050	0.33
850	300	2.50	1050	300	1.96	1200	1180	0.35
850	450	1.50	1050	450	1.54	1200	1190	0.26
850	600	1.15	1050	600	0.92	1250	50	3.92
850	750	0.74	1050	750	0.57	1250	100	4.96
850	830	0.46	1050	900	0.41	1250	150	2.63
850	840	0.47	1050	1030	0.31	1250	300	1.33
900	50	6.61	1050	1040	0.31	1250	450	1.04
900	100	4.69	1100	50	4.33	1250	600	1.03
900	150	5.01	1100	100	5.51	1250	750	0.61
900	300	2.41	1100	150	3.24	1250	900	0.49
900	450	1.77	1100	300	2.30	1250	1050	0.56
900	600	0.96	1100	450	1.38	1250	1200	0.41
900	750	0.68	1100	600	0.75	1250	1230	0.35
900	880	0.38	1100	750	0.35	1250	1240	0.33
900	890	0.30	1100	900	0.34	1300	50	4.35
950	50	4.90	1100	1050	0.15	1300	100	3.72
950	100	7.40	1100	1080	0.40	1300	150	2.47
950	150	3.93	1100	1090	0.53	1300	300	1.16
950	300	2.24	1150	50	4.56	1300	450	1.00
950	450	1.20	1150	100	4.54	1300	600	0.52
950	600	0.86	1150	150	3.38	1300	750	0.55
950	750	0.58	1150	300	1.41	1300	900	0.36
950	900	0.61	1150	450	1.67	1300	1050	0.44
950	930	0.57	1150	600	0.86	1300	1200	0.39
950	940	0.22	1150	750	0.67	1300	1280	0.29
1000	50	6.20	1150	900	0.53	1300	1290	0.25

Table 11.17: The total systematic uncertainties on the acceptance, for the gluino GGM points, of the $E_{\mathrm{T}}^{\mathrm{miss}}$ cut of signal region C. The total uncertainty is a combination of the uncertainties from the topocluster energy scale and the $E_{\mathrm{T}}^{\mathrm{miss}}$ resolution.

Signal point		Uncert.[%]	Signal point		Uncert.[%]	Signal point		Uncert.[%]
$m(\tilde{q})$	$m(\tilde{\chi}_1^0)$	A	$m(\tilde{q})$	$m(\tilde{\chi}_1^0)$	A	$m(\tilde{q})$	$m(\tilde{\chi}_1^0)$	A
800	50	7.14	1000	100	4.06	1150	1050	0.73
800	100	8.36	1000	150	5.40	1150	1130	0.85
800	150	5.61	1000	300	3.63	1150	1140	0.58
800	300	4.76	1000	450	2.07	1200	50	4.11
800	450	2.56	1000	600	1.74	1200	100	3.07
800	600	1.13	1000	750	1.33	1200	150	3.06
800	750	1.23	1000	900	0.47	1200	300	2.41
800	780	0.92	1000	980	0.49	1200	450	1.98
800	790	1.46	1000	990	0.60	1200	600	1.45
850	50	8.22	1050	50	6.24	1200	750	1.42
850	100	6.45	1050	100	5.21	1200	900	1.02
850	150	6.30	1050	150	4.03	1200	1050	0.70
850	300	3.88	1050	300	2.50	1200	1180	0.49
850	450	3.17	1050	450	1.87	1200	1190	0.40
850	600	1.34	1050	600	1.80	1250	50	3.24
850	750	1.18	1050	750	0.93	1250	100	3.77
850	830	0.88	1050	900	0.95	1250	150	3.06
850	840	1.13	1050	1030	0.88	1250	300	2.72
900	50	5.62	1050	1040	0.87	1250	450	1.93
900	100	5.69	1100	50	4.91	1250	600	1.65
900	150	4.13	1100	100	3.76	1250	750	1.43
900	300	4.28	1100	150	4.29	1250	900	1.40
900	450	2.63	1100	300	3.26	1250	1050	0.70
900	600	2.09	1100	450	2.24	1250	1200	0.57
900	750	0.89	1100	600	1.21	1250	1230	0.64
900	880	0.91	1100	750	1.12	1250	1240	0.44
900	890	0.59	1100	900	0.70	1300	50	3.68
950	50	5.20	1100	1050	0.89	1300	100	2.99
950	100	5.40	1100	1080	0.67	1300	150	3.05
950	150	3.91	1100	1090	0.53	1300	300	2.58
950	300	3.05	1150	50	4.30	1300	450	2.04
950	450	2.80	1150	100	4.83	1300	600	1.70
950	600	1.81	1150	150	3.48	1300	750	1.14
950	750	1.06	1150	300	2.86	1300	900	0.62
950	900	0.82	1150	450	2.23	1300	1050	0.97
950	930	1.02	1150	600	2.04	1300	1200	0.18
950	940	0.82	1150	750	1.47	1300	1280	0.52
1000	50	6.17	1150	900	0.65	1300	1290	0.68

Table 11.18: The total systematic uncertainties on the acceptance, for the squark GGM points, of the $E_{\mathrm{T}}^{\mathrm{miss}}$ cut of signal region A. The total uncertainty is a combination of the uncertainties from the topocluster energy scale and the $E_{\mathrm{T}}^{\mathrm{miss}}$ resolution.

Signal point		Uncert.[%]	Signal point		Uncert.[%]	Signal point		Uncert.[%]
$m(\tilde{q})$	$m(\tilde{\chi}_1^0)$	B	$m(\tilde{q})$	$m(\tilde{\chi}_1^0)$	B	$m(\tilde{q})$	$m(\tilde{\chi}_1^0)$	B
800	50	2.34	1000	100	1.48	1150	1050	0.31
800	100	2.06	1000	150	1.21	1150	1130	0.25
800	150	1.74	1000	300	1.11	1150	1140	0.20
800	300	1.95	1000	450	0.91	1200	50	0.90
800	450	1.34	1000	600	0.82	1200	100	0.88
800	600	0.77	1000	750	0.68	1200	150	0.70
800	750	0.41	1000	900	0.56	1200	300	0.59
800	780	0.30	1000	980	0.28	1200	450	1.00
800	790	0.27	1000	990	0.46	1200	600	0.43
850	50	1.34	1050	50	1.18	1200	750	0.29
850	100	1.94	1050	100	1.20	1200	900	0.61
850	150	2.21	1050	150	1.62	1200	1050	0.43
850	300	1.35	1050	300	0.38	1200	1180	0.37
850	450	1.06	1050	450	0.43	1200	1190	0.29
850	600	0.25	1050	600	0.66	1250	50	1.04
850	750	0.67	1050	750	0.47	1250	100	1.11
850	830	0.51	1050	900	0.14	1250	150	0.77
850	840	0.33	1050	1030	0.41	1250	300	0.48
900	50	1.41	1050	1040	0.23	1250	450	0.54
900	100	1.52	1100	50	0.59	1250	600	0.55
900	150	1.34	1100	100	1.11	1250	750	0.50
900	300	0.87	1100	150	1.06	1250	900	0.34
900	450	0.86	1100	300	1.13	1250	1050	0.23
900	600	0.82	1100	450	0.81	1250	1200	0.22
900	750	0.35	1100	600	0.54	1250	1230	0.21
900	880	0.20	1100	750	0.41	1250	1240	0.20
900	890	0.18	1100	900	0.41	1300	50	0.65
950	50	1.77	1100	1050	0.35	1300	100	0.81
950	100	1.40	1100	1080	0.75	1300	150	0.91
950	150	1.15	1100	1090	0.30	1300	300	0.72
950	300	1.03	1150	50	1.47	1300	450	0.53
950	450	0.86	1150	100	1.18	1300	600	0.41
950	600	0.59	1150	150	0.76	1300	750	0.49
950	750	0.65	1150	300	0.57	1300	900	0.43
950	900	0.41	1150	450	0.65	1300	1050	0.17
950	930	0.22	1150	600	0.45	1300	1200	0.16
950	940	0.53	1150	750	0.29	1300	1280	0.15
1000	50	1.11	1150	900	0.37	1300	1290	0.33

Table 11.19: The total systematic uncertainties on the acceptance, for the squark GGM points, of the $E_{\mathrm{T}}^{\mathrm{miss}}$ cut of signal region B. The total uncertainty is a combination of the uncertainties from the topocluster energy scale and the $E_{\mathrm{T}}^{\mathrm{miss}}$ resolution.

Signal point		Uncert.[%]	Signal point		Uncert.[%]	Signal point		Uncert.[%]
$m(\tilde{q})$	$m(\tilde{\chi}_1^0)$	C	$m(\tilde{q})$	$m(\tilde{\chi}_1^0)$	C	$m(\tilde{q})$	$m(\tilde{\chi}_1^0)$	C
800	50	4.74	1000	100	2.41	1150	1050	0.49
800	100	3.22	1000	150	2.45	1150	1130	0.21
800	150	2.82	1000	300	2.29	1150	1140	0.17
800	300	1.86	1000	450	1.26	1200	50	1.99
800	450	1.04	1000	600	0.45	1200	100	2.08
800	600	0.92	1000	750	0.59	1200	150	1.65
800	750	0.52	1000	900	0.49	1200	300	1.17
800	780	0.51	1000	980	0.25	1200	450	0.95
800	790	0.42	1000	990	0.33	1200	600	0.80
850	50	3.83	1050	50	2.73	1200	750	0.50
850	100	4.06	1050	100	2.87	1200	900	0.37
850	150	2.97	1050	150	2.04	1200	1050	0.25
850	300	1.49	1050	300	1.48	1200	1180	0.20
850	450	1.30	1050	450	0.92	1200	1190	0.28
850	600	0.59	1050	600	0.72	1250	50	2.29
850	750	0.79	1050	750	0.44	1250	100	2.28
850	830	0.35	1050	900	0.37	1250	150	2.31
850	840	0.32	1050	1030	0.12	1250	300	1.36
900	50	3.22	1050	1040	0.34	1250	450	0.60
900	100	3.23	1100	50	2.83	1250	600	0.69
900	150	1.93	1100	100	2.16	1250	750	0.53
900	300	1.80	1100	150	2.43	1250	900	0.21
900	450	1.32	1100	300	1.13	1250	1050	0.24
900	600	0.75	1100	450	0.82	1250	1200	0.17
900	750	0.74	1100	600	0.72	1250	1230	0.34
900	880	0.88	1100	750	0.50	1250	1240	0.23
900	890	0.40	1100	900	0.32	1300	50	2.05
950	50	3.08	1100	1050	0.46	1300	100	0.87
950	100	3.04	1100	1080	0.33	1300	150	1.85
950	150	2.64	1100	1090	0.23	1300	300	1.06
950	300	1.49	1150	50	1.64	1300	450	0.79
950	450	0.96	1150	100	1.59	1300	600	0.71
950	600	0.61	1150	150	1.70	1300	750	0.38
950	750	0.77	1150	300	0.92	1300	900	0.33
950	900	0.44	1150	450	0.49	1300	1050	0.50
950	930	0.36	1150	600	0.58	1300	1200	0.26
950	940	0.39	1150	750	0.48	1300	1280	0.36
1000	50	1.86	1150	900	0.79	1300	1290	0.22

Table 11.20: The total systematic uncertainties on the acceptance, for the squark GGM points, of the $E_{\mathrm{T}}^{\mathrm{miss}}$ cut of signal region C. The total uncertainty is a combination of the uncertainties from the topocluster energy scale and the $E_{\mathrm{T}}^{\mathrm{miss}}$ resolution.

Signal point	Uncertainty [%]		
Λ [TeV]	A	B	C
50	30.82	9.40	13.91
60	20.14	3.38	10.74
70	16.78	3.97	10.43
80	14.16	4.24	14.04
90	14.52	2.43	10.44
100	13.90	2.97	9.66
110	12.70	2.65	9.45
120	12.94	2.16	7.50
130	8.37	2.30	7.34
140	10.71	1.76	6.62
150	10.01	3.47	5.91
160	9.36	1.00	4.01
170	7.70	3.12	3.14
180	9.20	1.22	2.96
190	8.09	2.80	2.82
200	6.80	2.17	2.67
210	6.53	2.55	2.27
220	5.98	1.95	2.64
230	5.22	2.16	2.08
240	5.29	1.52	2.08
250	4.11	1.10	1.60

Table 11.21: The total systematic uncertainties on the acceptance, for SPS8, of the $E_{\mathrm{T}}^{\mathrm{miss}}$ cut of signal region A, B, and C. The total uncertainty is a combination of the uncertainties from the topocluster energy scale and the $E_{\mathrm{T}}^{\mathrm{miss}}$ resolution.

11.1.5 Total Visible Transverse Energy

As described in Section 7.7 the observable H_{T} is defined as the scalar sum of the transverse energy of all individual selected objects of the analysis. The uncertainties on the energies of these objects was then propagated to the H_{T}. The primary uncertainties considered were the energy scale and resolution for photons and electrons and the jet energy scale. The uncertainty on the H_{T} from each component is evaluated individually. These individual uncertainties are then added in quadrature to obtain the final systematic uncertainty. The uncertainties for the various signal grids are shown in Table 11.22 and 11.23.

The jet and photon energy scale uncertainties are the only non-negligible components in the final H_{T} uncertainty. The jet energy scale is by far the dominant of these two components. This uncertainty is treated as fully correlated with the uncertainties on the $E_{\mathrm{T}}^{\mathrm{miss}}$ described in Section 11.1.4.

Signal point		H_T Uncert		Signal point		H_T Uncert		Signal point		H_T Uncert	
$m(\tilde{g})$	$m(\tilde{\chi}_1^0)$	A	B	$m(\tilde{g})$	$m(\tilde{\chi}_1^0)$	A	B	$m(\tilde{g})$	$m(\tilde{\chi}_1^0)$	A	B
800	50	0.00	3.91	1000	100	0.00	1.10	1150	1050	0.04	2.08
800	100	0.00	3.87	1000	150	0.00	1.37	1150	1130	0.10	1.75
800	150	0.00	4.66	1000	300	0.00	1.42	1150	1140	0.28	1.74
800	300	0.08	5.34	1000	450	0.00	2.11	1200	50	0.00	0.13
800	450	0.14	7.25	1000	600	0.00	2.61	1200	100	0.00	0.14
800	600	0.29	4.90	1000	750	0.00	4.98	1200	150	0.00	0.22
800	750	0.62	3.91	1000	900	0.14	3.95	1200	300	0.00	0.37
800	780	0.84	2.89	1000	980	0.22	2.54	1200	450	0.00	0.45
800	790	0.35	3.28	1000	990	0.00	1.22	1200	600	0.00	0.68
850	50	0.00	3.21	1050	50	0.00	0.42	1200	750	0.00	1.09
850	100	0.00	2.26	1050	100	0.00	0.80	1200	900	0.00	1.85
850	150	0.00	3.00	1050	150	0.00	0.91	1200	1050	0.04	1.58
850	300	0.00	4.55	1050	300	0.00	1.45	1200	1180	0.00	1.84
850	450	0.05	5.42	1050	450	0.00	1.62	1200	1190	0.05	1.51
850	600	0.00	6.59	1050	600	0.00	2.23	1250	50	0.00	0.14
850	750	0.45	6.65	1050	750	0.00	3.45	1250	100	0.00	0.31
850	830	0.25	6.66	1050	900	0.09	3.58	1250	150	0.00	0.19
850	840	0.27	1.63	1050	1030	0.33	1.67	1250	300	0.00	0.16
900	50	0.00	1.97	1050	1040	0.16	2.31	1250	450	0.00	0.13
900	100	0.00	1.94	1100	50	0.00	0.49	1250	600	0.00	0.50
900	150	0.00	2.57	1100	100	0.00	0.67	1250	750	0.00	0.76
900	300	0.00	3.37	1100	150	0.00	0.65	1250	900	0.00	1.04
900	450	0.00	3.84	1100	300	0.00	0.85	1250	1050	0.05	1.88
900	600	0.00	5.29	1100	450	0.00	0.94	1250	1200	0.00	2.14
900	750	0.13	4.57	1100	600	0.00	1.20	1250	1230	0.06	1.07
900	880	0.31	4.31	1100	750	0.00	2.58	1250	1240	0.00	1.17
900	890	0.31	3.20	1100	900	0.04	3.29	1300	50	0.00	0.12
950	50	0.00	1.74	1100	1050	0.07	3.16	1300	100	0.00	0.15
950	100	0.00	1.44	1100	1080	0.10	2.77	1300	150	0.00	0.04
950	150	0.00	1.66	1100	1090	0.13	1.60	1300	300	0.00	0.32
950	300	0.00	2.51	1150	50	0.00	0.51	1300	450	0.00	0.25
950	450	0.00	2.45	1150	100	0.00	0.22	1300	600	0.00	0.26
950	600	0.00	4.86	1150	150	0.00	0.45	1300	750	0.00	0.45
950	750	0.00	4.74	1150	300	0.00	0.65	1300	900	0.00	0.81
950	900	0.29	3.70	1150	450	0.00	0.75	1300	1050	0.00	0.97
950	930	0.18	2.37	1150	600	0.00	1.12	1300	1200	0.00	1.57
950	940	0.36	3.32	1150	750	0.00	1.42	1300	1280	0.00	1.08
1000	50	0.00	0.85	1150	900	0.00	2.32	1300	1290	0.00	0.88

Table 11.22: The systematic uncertainty on the gluino GGM signal region A and B acceptances due to the H_T cut.

Signal point	H_{T} uncertainty	
Λ [TeV]	A	B
50	4.28	8.29
60	0.00	8.34
70	0.63	5.90
80	0.43	5.71
90	0.48	3.65
100	1.31	1.60
110	0.37	2.19
120	3.08	1.67
130	1.79	3.35
140	3.47	1.77
150	3.23	5.22
160	3.25	6.25
170	3.44	5.19
180	3.17	7.01
190	2.48	4.36
200	1.79	8.00
210	2.20	8.97
220	1.75	6.90
230	1.38	7.92
240	1.14	6.88
250	0.76	6.08

Table 11.23: The systematic uncertainties on the SPS8 signal region A and B acceptances due to the H_{T} cut.

11.1.6 Monte Carlo Statistics

The signal acceptances measured from the Monte Carlo have a statistical uncertainty due to the limited number of events in the samples. This uncertainty is treated as systematic uncertainty when used to interpret the experiment result since its value is not a function of the collision data set size. The uncertainty is calculated as a binomial error since this is an efficiency. The formula used is

$$\sigma = (1/N)\sqrt{k(1-k/N)}, \tag{11.2}$$

where N is the total number of events in the Monte Carlo sample, and k is the number of events passing the cuts. Since this uncertainty varies across the Monte Carlo points, it is assessed individually for each point.

Each GGM signal point has $\sim$ 5000 generated events. For analysis A the acceptance of all cuts ranges from 0.257 ± 0.006 to 0.012 ± 0.002, corresponding to respective relative uncertainties of 2.4% and 12.9%. Note that points with very low efficiency for signal region A are those meant to be covered by signal region B. For signal region B the final acceptance on the GGM points ranges from 0.259 ± 0.006 to 0.028 ± 0.002, corresponding to respective relative uncertainties of 2.4% and 8.3%. Finally, for analysis C the acceptance of all cuts on the GGM points ranges from 0.269 ± 0.006 to 0.028 ± 0.002, corresponding to respective relative uncertainties of 2.3% and 8.3%. The acceptances and uncertainties for each signal region on all GGM Monte Carlo points can be seen in Tables A.5 – A.10 from Appendix A.

Approximately $\sim$ 10000 events were generated for each SPS8 signal point. The

acceptance of all cuts for signal region A for SPS8 ranged from 0.131 ± 0.003 to 0.0013 ± 0.0004, corresponding to respective relative uncertainties of 2.6% and 27.8%. For signal region B the acceptance of all cuts on the SPS8 points ranges from 0.041 ± 0.002 to 0.0029 ± 0.0005, corresponding to respective relative uncertainties of 4.9% and 19.0%. Lastly, the acceptances of signal region C of for SPS8 Monte Carlo points ranges from 0.215 ± 0.004 to 0.0079 ± 0.0009, corresponding to respective relative uncertainties of 1.9% and 11.3%. Note signal region C is the most sensitive analysis for the SPS8 theory scenario. The acceptances and uncertainties per SPS8 signal point for each signal region are given in Table A.17 from Appendix A.

11.2 Luminosity Uncertainty

An uncertainty on the total integrated luminosity is necessary when interpreting results in terms of cross sections and mass limits. The uncertainty used on the luminosity of the collision data set is 3.7 %[70]. This value is the standard one used across ATLAS for the 2011 data.

11.3 Cross Section Uncertainty

The methodology for calculating the cross sections used for the SUSY signal Monte Carlo was described in detail in Section 3.6. The central value of the cross section is taken as the mid-point of an envelope derived from a set of PDF error sets, including a variation in α_s. The error on that central value was taken as half the extent of the

envelope.

The errors on the cross sections for the GGM signal are included in Tables 8.5 and 8.6. The relative uncertainties vary from 23.1 % to 42.7 % for the gluino GGM points. In the case of the squark GGM points the relative uncertainties vary from 28.5 % to 54.3 %. The uncertainties for the GGM are highest for the points where the gluino or squark mass is the largest. The cross section errors for the SPS8 can be seen in Table 8.7. The SPS8 points, which are dominated by electroweak instead of strong production, have substantially smaller errors. These relative uncertainties vary from 5.2 % to 6.1 %. Unlike the GGM points, the errors on the SPS8 cross sections are smallest for the lowest values of Λ, and decrease with increasing Λ.

11.4 Uncertainty Summary

This section is a summary of the various systematic presented in this chapter. The uncertainties for the GGM points are show in Table 11.24 and the SPS8 points in Table 11.25. All uncertainties except the $E_{\mathrm{T}}^{\mathrm{miss}}$ and H_{T} are treated as uncorrelated and added in quadrature to obtain the final values. The H_{T} and $E_{\mathrm{T}}^{\mathrm{miss}}$ are taken to be 100 % correlated, and are added together before being combined with the remaining uncertainties in quadrature.

Source of the systematic	Systematic Uncertainty - GGM		
Luminosity	3.7 %		
Trigger	0.5 %		
Discriminating variables	4.0 %		
Bad conversions	1.8 %		
Photon cleaning	0.2 %		
Sum photon syst.	4.4 %		
Photon isolation	0.9 %		
Pileup	0.8 %		
	A	B	C
MET	$0.4 - 17.0$ %	$0.1 - 4.9$ %	$0.1 - 9.3$ %
HT	$0.0 - 0.8$ %	$0.0 - 7.3$ %	–
	A	B	C
MC statistics	$2.4 - 12.9$ %	$2.4 - 8.3$ %	$2.3 - 8.3$ %
PDF/Scale uncertainty	$23 - 43$ %		
	A	B	C
Total (w/o PDF/scale)	8-21 %	8-12 %	8-14 %
Total (with PDF/scale)	24-44 %	25-43 %	24-44 %

Table 11.24: Summary of the systematic uncertainties for the GGM Monte Carlo points. The uncertainties are relative and given as percentages. Uncertainties that vary over the Monte Carlo points list the range.

Source of the systematic	Systematic Uncertainty - SPS8		
Luminosity	3.7 %		
Trigger	0.5 %		
Discriminating variables	4.0 %		
Bad conversions	1.8 %		
Photon cleaning	0.2 %		
Sum photon syst.	4.4 %		
Photon isolation	0.2 %		
Pileup	0.5 %		
	A	B	C
MET	$4.1 - 30.8$ %	$1.0 - 9.4$ %	$1.6 - 14.0$ %
HT	$0.0 - 4.3$ %	$1.6 - 9.0$ %	0.0 %
	A	B	C
MC statistics	$2.6 - 27.8$ %	$4.9 - 19.0$ %	$1.9 - 11.3$ %
PDF/Scale uncertainty	$4.7 - 6.4$ %		
	A	B	C
Total (w/o PDF/scale)	8-21 %	8-12 %	8-14 %
Total (with PDF/scale)	24-44 %	25-43 %	24-44 %

Table 11.25: Summary of the systematic uncertainties for the SPS8 Monte Carlo points. The uncertainties are relative and given as percentages. Uncertainties that vary over the Monte Carlo points list the range.

Chapter 12

Results and Interpretation

This chapter discusses the interpretation of the experimental results in terms of the two SUSY scenarios investigated in this analysis. As can be seen in Table 10.6, no apparent excess is observed in any of the signal regions compared to the Standard Model background. The frequentist CL_s limit setting technique [103] is used to interpret the results. Limits are set using each signal region for each point in the theory parameter space. Three different types of limits are set: model independent limits on the number of signal events, upper limits on the production cross sections, and lower limits on particle masses.

Details on the limit setting formalism are presented in Section 12.1. The methodology and results of the model independent limits are described in Section 12.2. The cross section and mass limits for both the gluino and squark production GGM grids are discussed in Section 12.3. Mass limits in the SPS8 scenario are included in Section 12.4.

12.1 Limit Setting Technique

The CL_s method is based upon a profile likelihood ratio technique. The likelihood function is written as

$$L\left(n|\mu,\sigma\right) = P_{\text{signal}} \times P_{\text{syst}} = P\left(n_S|\lambda_S\left(\mu,B,\theta\right)\right) \times P_{\text{syst}}\left(\theta\right), \tag{12.1}$$

where P_{signal} is a Poisson distribution representing the signal, P_{syst} is a probability distribution incorporating the systematics. The parameter n_S is the observed number of signal events, μ defines the hypothesized signal strength (0 for a background only model and 1 for signal), B is the expected number of background events, and θ are the nuisance parameters for the various systematic uncertainties.

The signal Poisson distribution represents the likelihood of observing n_S, based on a Poisson distribution with expected mean λ_S. The probability distribution P_{syst} for the systematics is represented by two Gaussians, one for the signal systematics and one for the background systematic uncertainties. The functional form of P_{syst} is given by

$$P_{syst}\left(\theta\right) = G\left(\theta_S,\theta_S^0,\sigma_S\right) \times G\left(\theta_B,\theta_B^0,\sigma_B\right), \tag{12.2}$$

where $G\left(\theta_i,\theta_i^0,\sigma_i\right)$ are Gaussian functions with mean θ_i^0 and width σ_i, for the signal and background systematics respectively. The background systematics that will be used here are those taken from Section 10.5, and the signal systematics are those from Section 11.4. There are no common systematics between the signal acceptance and the background estimation.

Using likelihood functions of the form Eq. 12.1 a limit can be extracted using

a likelihood ratio with the form

$$\Lambda(\mu) = -2\left(\ln\left(\mu, B'', \theta''\right) - \ln\left(\mu', B', \theta'\right)\right), \tag{12.3}$$

where μ', B', θ' are the values that maximize the likelihood function, and B'', θ'' are the values that maximize the likelihood function for a specific value of μ. The value of μ is set to one when testing a signal scenario. The p-value based upon the likelihood ratio is defined as

$$p = \begin{cases} P_{\chi^2}(\Lambda(\mu)) & \mu' \geq 1 \\ 1 - P_{\chi^2}(\Lambda(\mu)) & \mu' < 1 \end{cases}, \tag{12.4}$$

where P_{χ^2} is a function that produces a one-side p-value. This is done using a χ^2 test with one degree of freedom, which produces a two-sided p-value that is converted to a one-sided by dividing by two.

In order to obtain the p-values, the likelihood ratio must be evaluated. This is performed using pseudo-experiments. The final p-value of the CL_s technique, which is used for the limits, is given by

$$p' = \frac{p_{s+b}}{1 - p_b}, \tag{12.5}$$

where p_{s+b} is the p-value of the signal plus background hypothesis and p_b is that of the background only hypothesis.

12.2 Model Independent Limits

A set of model-independent limits are set for each of the three signal regions. These limits used only the total uncertainties of the background. The model-

independent limits on the number of events beyond the standard model can be seen in Table 12.1.

	Expected limit	Observed limit
SR A	3.1	3.1
SR B	3.1	3.1
SR C	4.9	4.9

Table 12.1: The expected and observed 95 %CL limits on the number of events not coming from the Standard Model.

12.3 GGM Limits

Model-dependent limits are set on the GGM signal points. Two types of limits are set: cross section limits and mass limits. In the case of the cross section limits all background uncertainties and all signal uncertainties except the theory uncertainties on the production cross sections are used. Cross section limits are set only for the gluino production points. In the case of actual mass limits, all background and signal uncertainties are applied. The p-values from the limiting setting can be see for the GGM points with gluino production in Table 12.1 and with squark production in Table 12.2. The lower limits on the cross sections for the gluino production points for all three signal regions are shown in Table 12.3. A combined plot showing the cross section lower limits using the result from the signal region A or B which gives the best expected limit is included in Fig. 12.4.

Mass limits are placed for both squark and gluino production points. The limits set for signal regions A, B, and C on the gluino mass versus neutralino mass

plane are shown in Fig. 12.5, 12.6, and 12.7. Note that signal region C is included here only for the purposes of completeness and is not used in the final combined limit. Fig. 12.8 shows which signal region gives the best expected limit for each point. These are the signal regions used for each point to obtain the exclusion plot in Fig. 12.9. With this combined limit gluino masses up to 1070 GeV are excluded at 95 % CL where the lightest neutralino mass is between 50 GeV and the gluino mass.

A very similar set of plots is also shown for squark production points. The CL_S limits for the three signal regions are shown in Fig. 12.10, 12.11, and 12.12. The plot showing the signal region with the best expected limit is in Fig. 12.13, and the final combined limit plot for the squark production is in Fig. 12.14. The cutoff appearing at a squark mass of 800 GeV that can be observed in both Fig. 12.10 and 12.11 is due to a lack of Monte Carlo points with squark mass below 800 GeV. For both signal region A and B this problem area is in the region covered by the other analysis, so the problem has no effect on the combined limit. Squark masses are excluded in this model up to 910 GeV at 95 % CL for lightest neutralino masses between 50 GeV and the squark mass. This is somewhat worse than the gluino production case, but this is due to a lower cross section for these points.

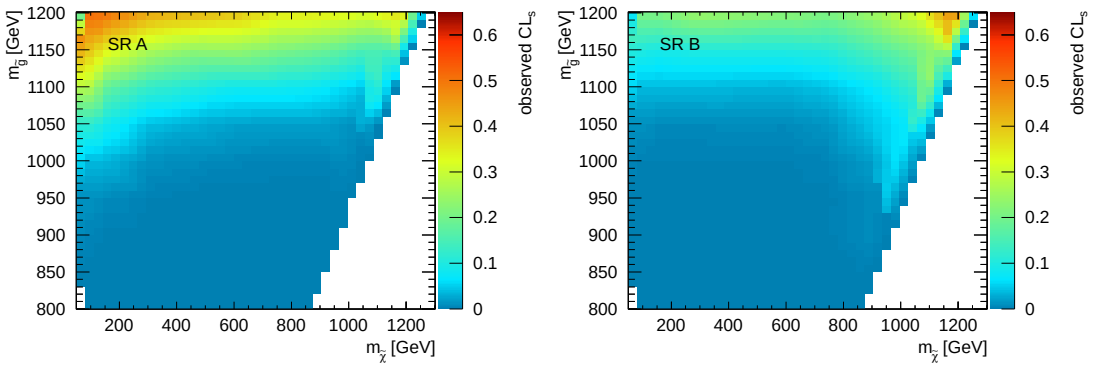

Figure 12.1: Observed CL_s p-value for signal region A (left) and B (right) on GGM signal points as a function of gluino and lightest neutralino mass.

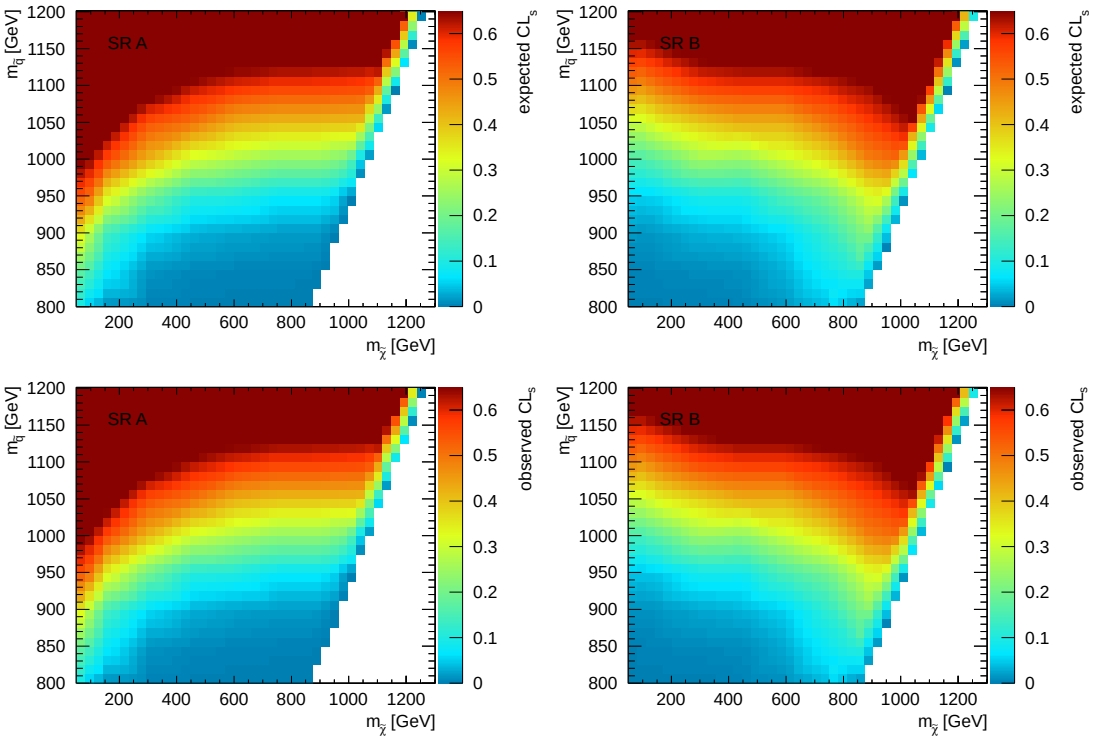

Figure 12.2: Expected (top) and observed (bottom) CL_s p-value for signal region A (left) and B (right) on GGM signal points as a function of squark and lightest neutralino mass.

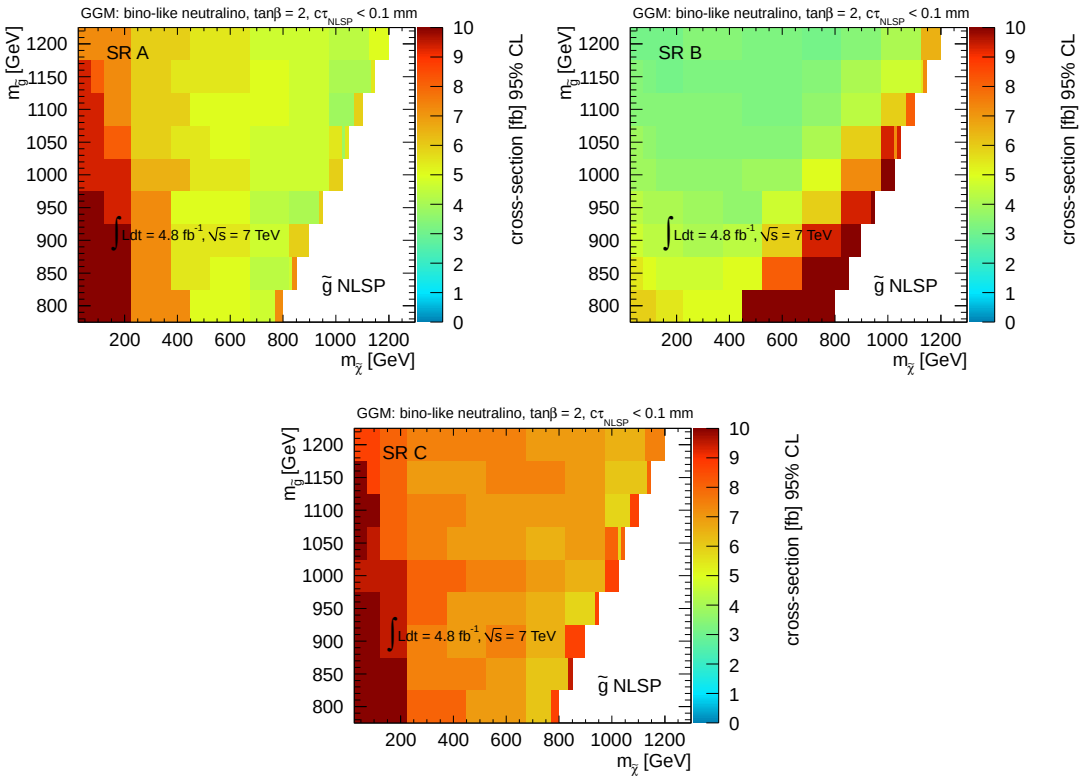

Figure 12.3: Observed frequentist CL_s 95 % CL upper limit as a function of gluino and lightest neutralino mass using signal region A (upper left), B (upper right), and C (bottom).

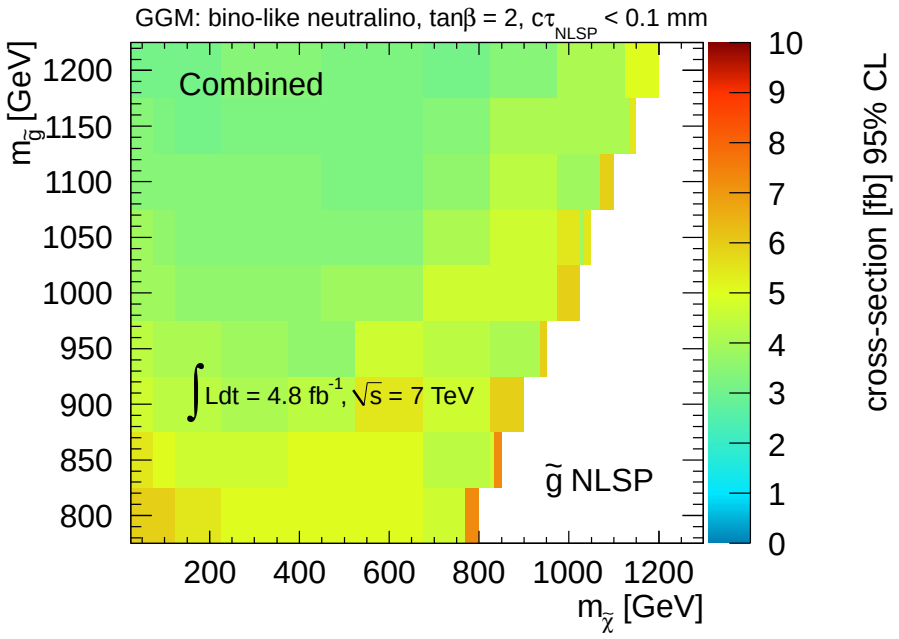

Figure 12.4: Combined observed frequentist CL_s 95 % CL upper limit as a function of gluino and lightest neutralino mass using the signal region which gives the best expected limit.

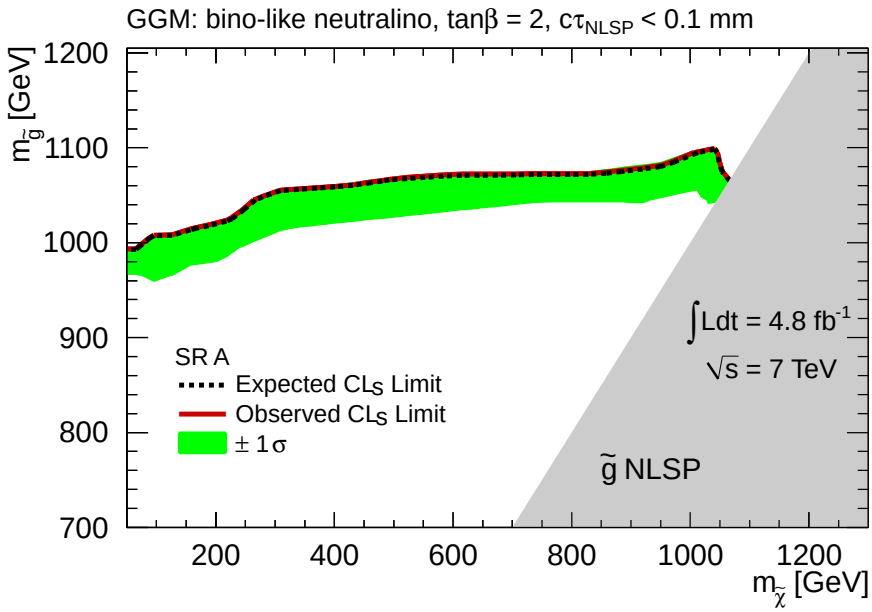

Figure 12.5: Observed and expected frequentist CL_s 95 % CL lower limit on the mass of the gluino as a function of the lightest neutralino mass using signal region A.

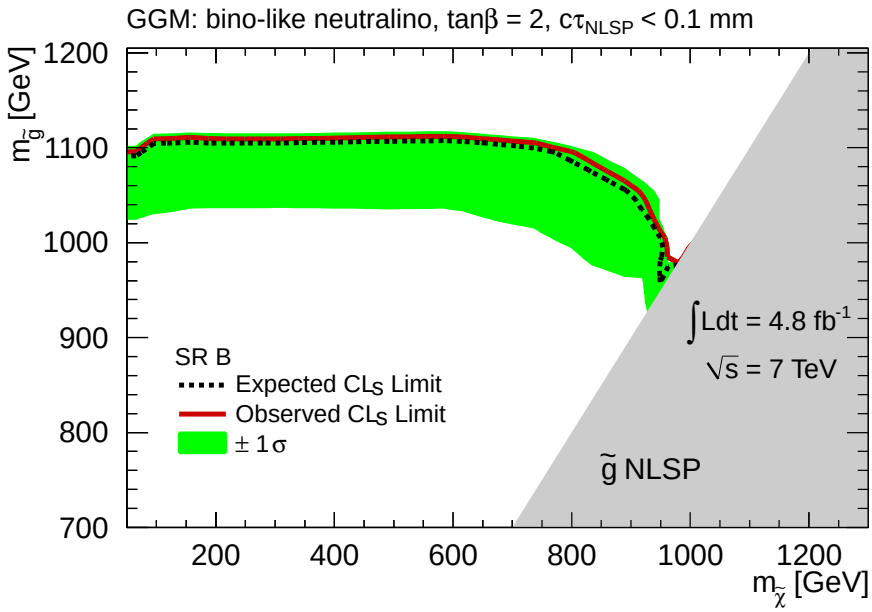

Figure 12.6: Observed and expected frequentist CL_s 95 % CL lower limit on the mass of the gluino as a function of the lightest neutralino mass using signal region B.

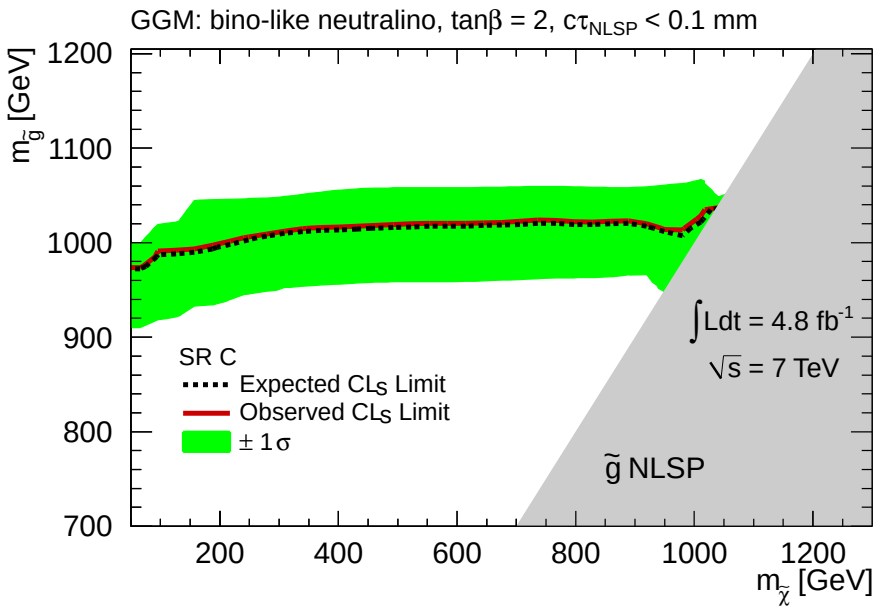

Figure 12.7: Observed and expected frequentist CL_s 95 % CL lower limit on the mass of the gluino as a function of the lightest neutralino mass using signal region C.

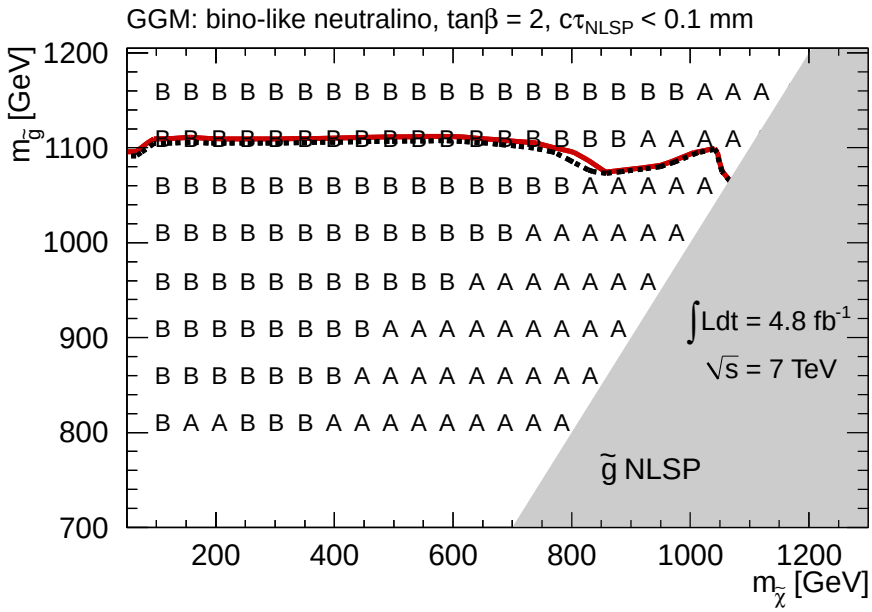

Figure 12.8: Signal region with the best expected CL_s 95 % CL lower limit on the mass of the gluino as a function of the lightest neutralino mass.

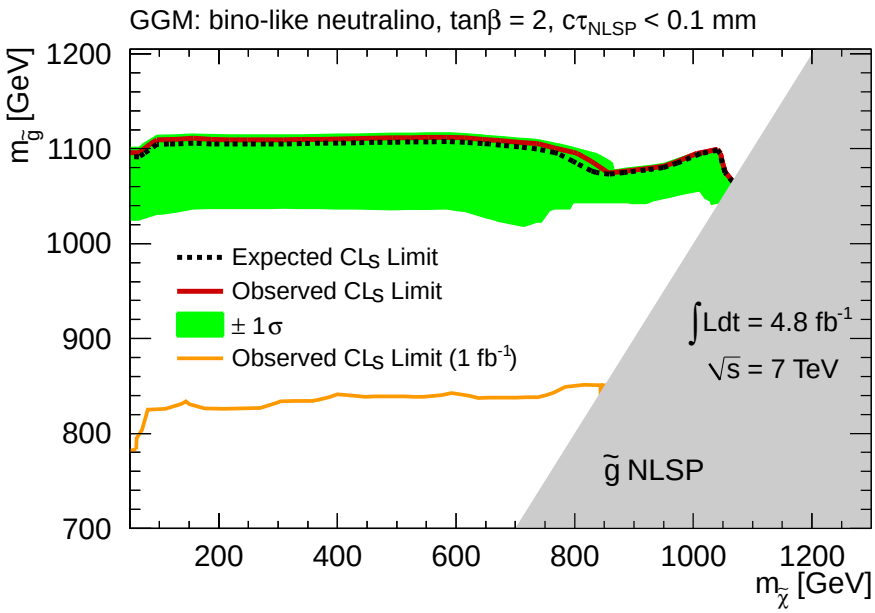

Figure 12.9: Observed and expected frequentist CL_s 95 % CL lower limit on the mass of the gluino as a function of the lightest neutralino mass using the signal region which gives the best expected limit.

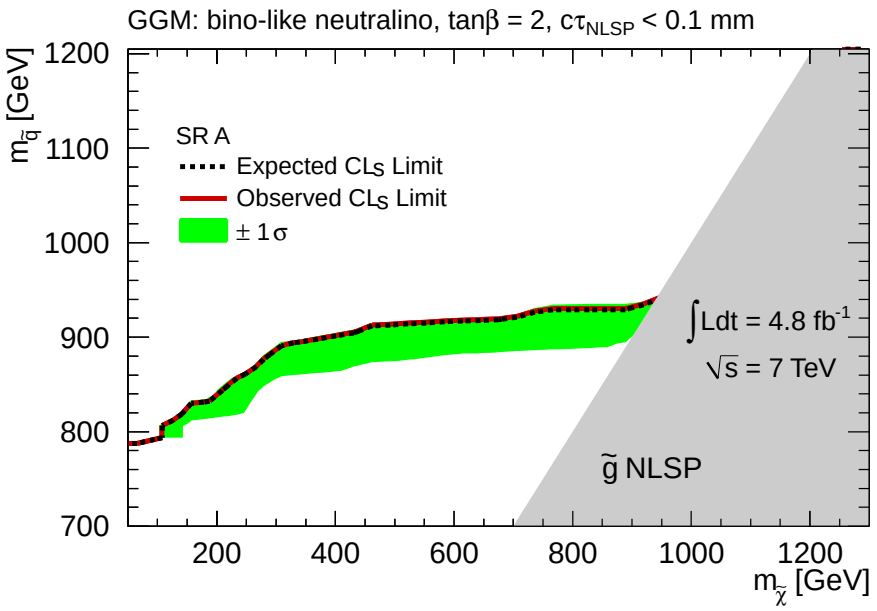

Figure 12.10: Observed and expected frequentist CL_s 95 % CL lower limit on the mass of the squark as a function of the lightest neutralino mass using signal region A.

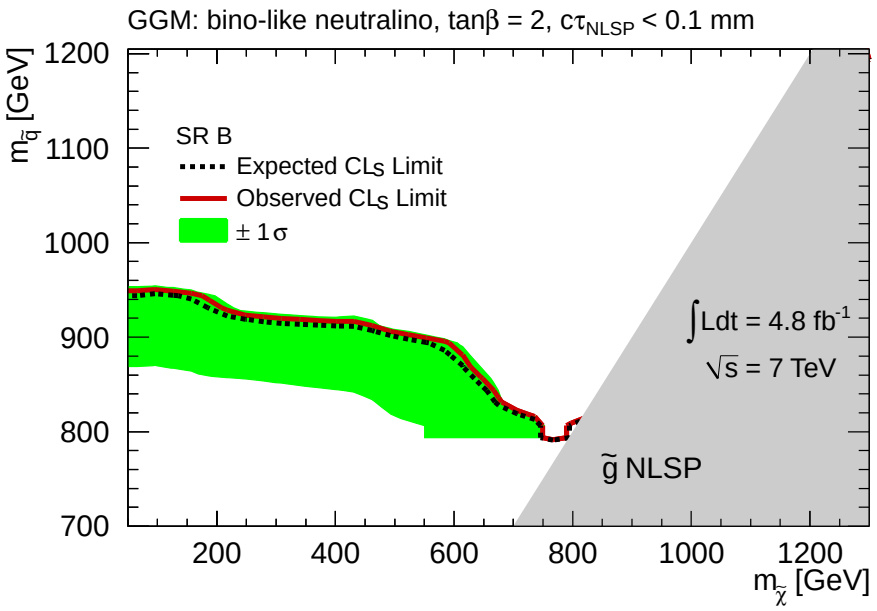

Figure 12.11: Observed and expected frequentist CL_s 95 % CL lower limit on the mass of the squark as a function of the lightest neutralino mass using signal region B.

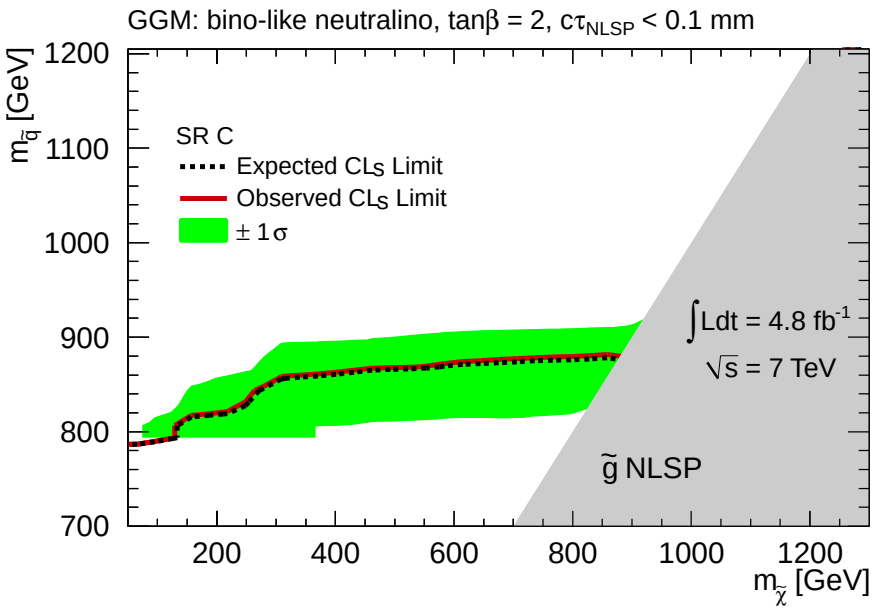

Figure 12.12: Observed and expected frequentist CL_s 95 % CL lower limit on the mass of the squark as a function of the lightest neutralino mass using signal region C.

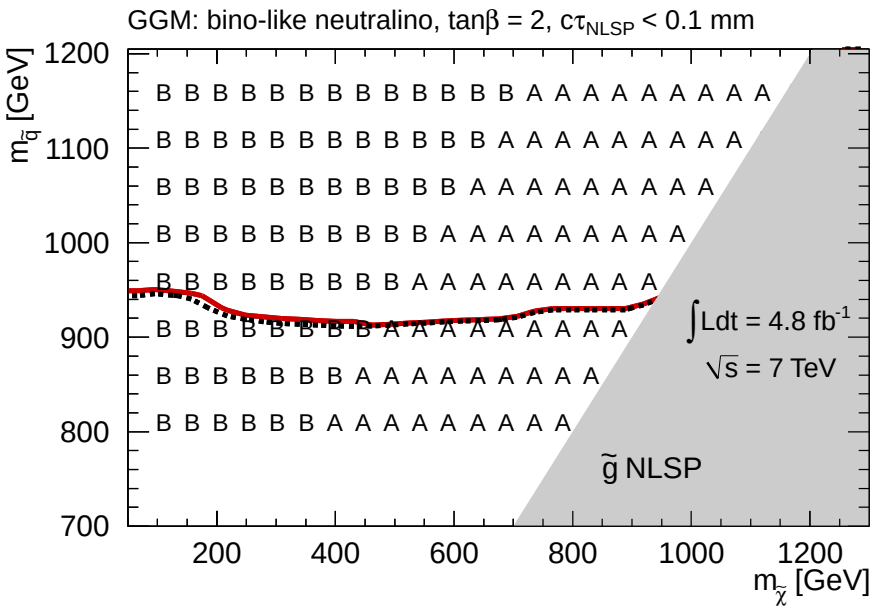

Figure 12.13: Signal region with the best expected CL_s 95 % CL lower limit on the mass of the squark as a function of the lightest neutralino mass.

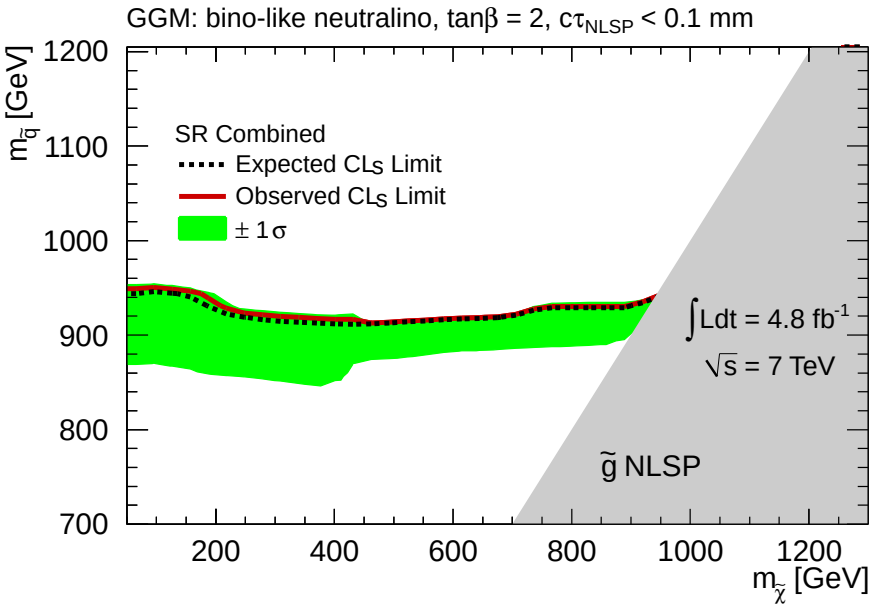

Figure 12.14: Observed and expected frequentist CL_s 95 % CL lower limit on the mass of the squark as a function of the lightest neutralino mass using the signal region which gives the best expected limit.

12.4 SP8 Limits

Unlike the GGM scenario only limits in terms of the parameter Λ are set for the SPS8. The exclusion plots for all three signal regions can be seen in Fig. 12.15, 12.16, and 12.17. As expected, signal region C gives the best limit, and as a result a lower limit at 95 % CL can be placed on Λ of 197 TeV.

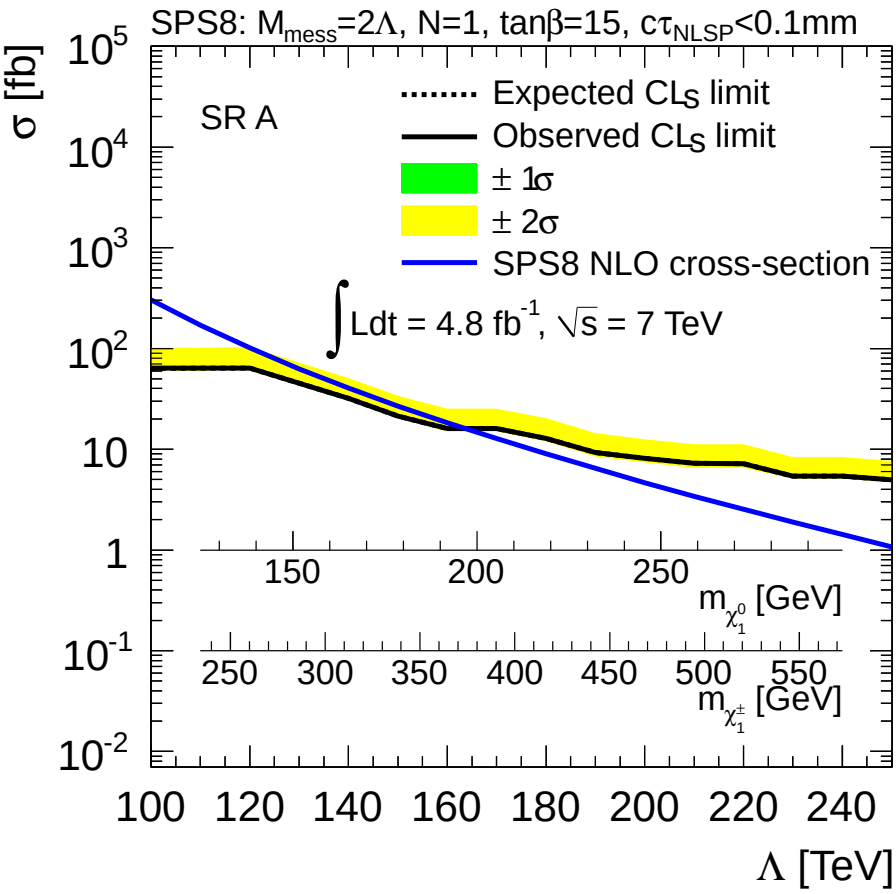

Figure 12.15: NLO cross section versus Λ for SPS8 (blue line). Superimposed are the observed (solid black line) and expected (dashed line) frequentist CL_s 95% CL upper limits as well as the $\pm 1, 2\sigma$ expected error bands for an integrated luminosity of $4.8\,\mathrm{fb}^{-1}$ for analysis A.

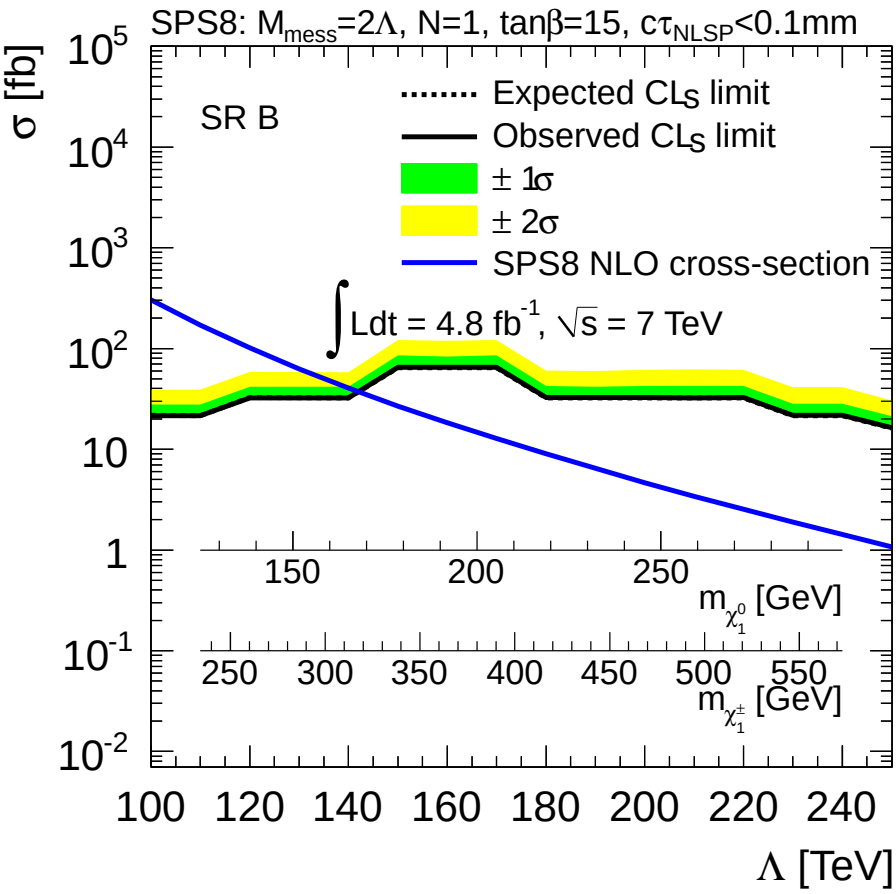

Figure 12.16: NLO cross section versus Λ for SPS8 (blue line). Superimposed are the observed (solid black line) and expected (dashed line) frequentist CL_s 95% CL upper limits as well as the $\pm 1, 2\sigma$ expected error bands for an integrated luminosity of $4.8\,\mathrm{fb}^{-1}$ for analysis B.

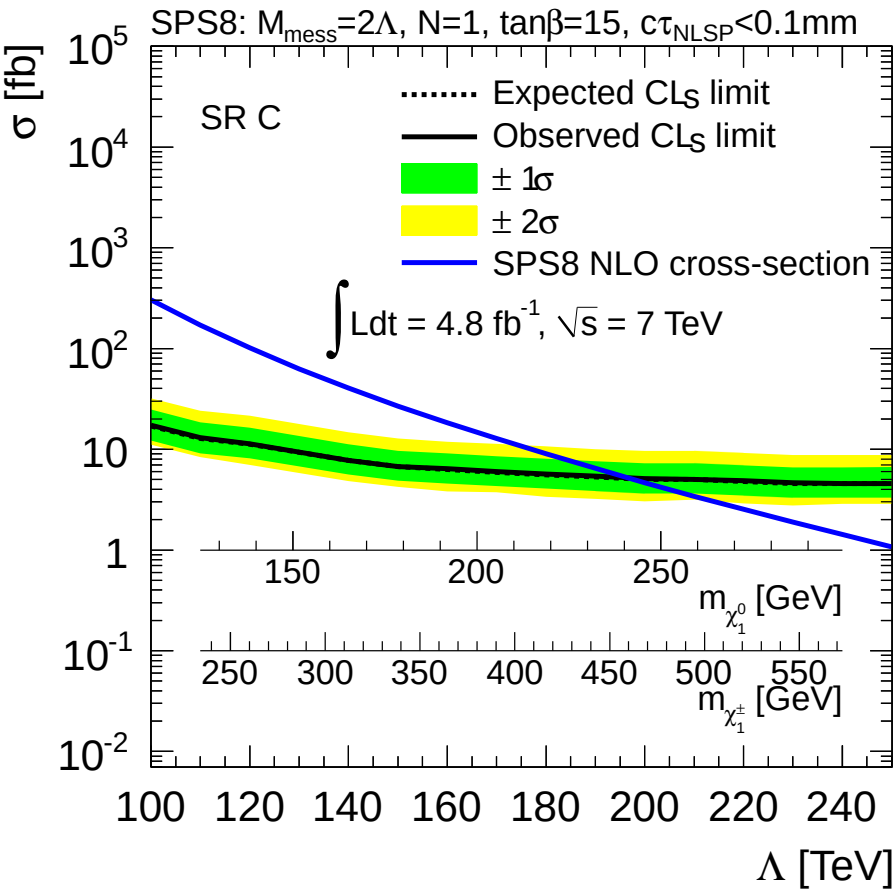

Figure 12.17: NLO cross section versus Λ for SPS8 (blue line). Superimposed are the observed (solid black line) and expected (dashed line) frequentist CL_s 95% CL upper limits as well as the $\pm 1, 2\sigma$ expected error bands for an integrated luminosity of $4.8\,\mathrm{fb}^{-1}$ for analysis C.

12.5 Conclusion

No excess over Standard Model expectations were observed in this analysis. The number of background events for the three signal regions examined were $0.10 \pm 0.03 \pm 0.07$, $0.36 \pm 0.05 \pm 0.27$, and $2.11 \pm 0.37 \pm 0.77$ events for signal regions A, B, and, C respectively. No events were observed in either signal regions A or B. Two events were observed in signal region C. The lack of excess is interpreted in both the GGM and SPS8 scenario scenarios. For the gluino production GGM scenario, gluino masses up to 1070 GeV are excluded at 95 % CL where the lightest neutralino mass is between 50 GeV and the gluino mass. Squark masses are also excluded in this model up to 910 GeV at 95 % CL for lightest neutralino masses between 50 GeV and the squark mass. In the SPS8 scenario values of Λ up to 197 TeV is excluded at 95 % CL.

Bibliography

[1] S. Weinberg, "A Model of Leptons," *Phys.Rev.Lett.* **19** (1967) 1264–1266.

[2] A. Salam, "Weak and electromagnetic interactions," in *Elementary particle theory*, N. Svartholm, ed., pp. 367–377. Almquist & Wiksell, Stockholm, 1968.

[3] S. Glashow, J. Iliopoulos, and L. Maiani, "Weak Interactions with Lepton-Hadron Symmetry," *Phys.Rev.* **D2** (1970) 1285–1292.

[4] F. Englert and R. Brout, "Broken Symmetry and the Mass of Gauge Vector Mesons," *Phys.Rev.Lett.* **13** (1964) 321–323.

[5] P. W. Higgs, "Broken symmetries, massless particles and gauge fields," *Phys.Lett.* **12** (1964) 132–133.

[6] G. Guralnik, C. Hagen, and T. Kibble, "Global Conservation Laws and Massless Particles," *Phys.Rev.Lett.* **13** (1964) 585–587.

[7] M. Dine, *Supersymmetry and String Theory.* Cambridge University Press, 2007.

[8] **ATLAS** Collaboration, G. Aad *et al.*, "Combined search for the Standard

Model Higgs boson using up to 4.9 fb-1 of pp collision data at sqrt(s) = 7 TeV with the ATLAS detector at the LHC," *Phys.Lett.* **B710** (2012) 49–66.

[9] **CMS** Collaboration, S. Chatrchyan *et al.*, "Combined results of searches for the standard model Higgs boson in pp collisions at sqrt(s) = 7 TeV," *Phys.Lett.* **B710** (2012) 26–48.

[10] Y. Fukuda *et al.*, "Solar neutrino data covering solar cycle 22," *Phys. Rev. Lett.* **77** (Aug, 1996) 1683–1686.

[11] P. Minkowski, "$\mu \to e\gamma$ at a Rate of One Out of 1-Billion Muon Decays?," *Phys.Lett.* **B67** (1977) 421.

[12] D. Gross and F. Wilczek, "Ultraviolet Behavior of Nonabelian Gauge Theories," *Phys.Rev.Lett.* **30** (1973) 1343–1346.

[13] A. Seiden, *Particle physics: a comprehensive introduction.* Addison Wesley, 2005.

[14] K. Nakamura and P. D. Group, "Review of Particle Physics," *Journal of Physics G: Nuclear and Particle Physics* **37** no. 7A, 075021.

[15] S. Weinberg, "Implications of Dynamical Symmetry Breaking," *Phys. Rev.* **D13** (1976) 974–996.

[16] E. Gildener, "Gauge Symmetry Hierarchies," *Phys. Rev.* **D14** (1976) 1667.

[17] S. Weinberg, "Implications of Dynamical Symmetry Breaking: An Addendum," *Phys. Rev.* **D19** (1979) 1277–1280.

[18] L. Susskind, "Dynamics of Spontaneous Symmetry Breaking in the Weinberg-Salam Theory," *Phys. Rev.* **D20** (1979) 2619–2625.

[19] S. P. Martin, "A Supersymmetry Primer," `arXiv:hep-ph/9709356 [hep-ph]`.

[20] **WMAP** Collaboration, E. Komatsu *et al.*, "Seven-Year Wilkinson Microwave Anisotropy Probe (WMAP) Observations: Cosmological Interpretation," *Astrophys.J.Suppl.* **192** (2011) 18.

[21] H. Goldberg, "Constraint on the photino mass from cosmology," *Phys. Rev. Lett.* **50** (1983) 1419.

[22] J. Ellis *et al.*, "Supersymmetric relics from the big bang," *Nucl. Phys.* **B238** (1984) 453–476.

[23] M. Dine and W. Fischler, "A Phenomenological Model of Particle Physics Based on Supersymmetry," *Phys. Lett.* **B110** (1982) 227.

[24] L. Alvarez-Gaume, M. Claudson, and M. B. Wise, "Low-Energy Supersymmetry," *Nucl. Phys.* **B207** (1982) 96.

[25] C. R. Nappi and B. A. Ovrut, "Supersymmetric Extension of the SU(3) x SU(2) x U(1) Model," *Phys. Lett.* **B113** (1982) 175.

[26] M. Dine and A. E. Nelson, "Dynamical supersymmetry breaking at low-energies," *Phys. Rev.* **D48** (1993) 1277–1287.

[27] M. Dine, A. E. Nelson, and Y. Shirman, "Low-energy dynamical supersymmetry breaking simplified," *Phys. Rev.* **D51** (1995) 1362–1370.

[28] M. Dine *et al.*, "New tools for low-energy dynamical supersymmetry breaking," *Phys. Rev.* **D53** (1996) 2658–2669.

[29] **CDF** Collaboration, T. Aaltonen *et al.*, "Search for Supersymmetry with Gauge-Mediated Breaking in Diphoton Events with Missing Transverse Energy at CDF II," *Phys.Rev.Lett.* **104** (2010) 011801.

[30] **D0** Collaboration, V. M. Abazov *et al.*, "Search for diphoton events with large missing transverse energy in 6.3 fb^{-1} of $\mathbf{p\bar{p}}$ collisions at $\sqrt{\mathbf{s}} = \mathbf{1.96}$ TeV," *Phys.Rev.Lett.* **105** (2010) 221802.

[31] **CMS** Collaboration, "Search for Supersymmetry in Events with Photons and Missing Energy," Tech. Rep. CMS-PAS-SUS-12-001, CERN, Geneva, Apr, 2012.

[32] **ATLAS** Collaboration, G. Aad *et al.*, "Search for Diphoton Events with Large Missing Transverse Momentum in 1 fb^{-1} of 7 TeV Proton-Proton Collision Data with the ATLAS Detector," *Phys. Lett.* **B710** (2012) 519–537.

[33] B. Allanach *et al.*, "The Snowmass points and slopes: Benchmarks for SUSY searches," *Eur.Phys.J.* **C25** (2002) 113–123.

[34] P. Meade, N. Seiberg, and D. Shih, "General Gauge Mediation," *Prog. Theor. Phys. Suppl.* **177** (2009) 143–158.

[35] M. Buican, P. Meade, N. Seiberg, and D. Shih, "Exploring General Gauge Mediation," *JHEP* **03** (2009) 016.

[36] "ATLAS SUSY ETmiss Subgroup Twiki." `https://twiki.cern.ch/twiki/bin/viewauth/AtlasProtected/SUSYSignalUncertainties`, 2012.

[37] M. Botje *et al.*, "The PDF4LHC Working Group Interim Recommendations," `arXiv:1101.0538 [hep-ph]`.

[38] W. Beenakker *et al.*, "Squark and gluino production at hadron colliders," *Nucl.Phys.* **B492** (1997) 51–103.

[39] A. Kulesza and L. Motyka, "Threshold resummation for squark-antisquark and gluino-pair production at the LHC," *Phys.Rev.Lett.* **102** (2009) 111802.

[40] A. Kulesza and L. Motyka, "Soft gluon resummation for the production of gluino-gluino and squark-antisquark pairs at the LHC," *Phys.Rev.* **D80** (2009) 095004.

[41] W. Beenakker *et al.*, "Soft-gluon resummation for squark and gluino hadroproduction," *JHEP* **0912** (2009) 041.

[42] W. Beenakker *et al.*, "Squark and gluino hadroproduction," *Int.J.Mod.Phys.* **A26** (2011) 2637–2664.

[43] P. M. Nadolsky *et al.*, "Implications of CTEQ global analysis for collider observables," *Phys.Rev.* **D78** (2008) 013004.

[44] A. Martin, W. Stirling, R. Thorne, and G. Watt, "Parton distributions for the LHC," *Eur.Phys.J.* **C63** (2009) 189–285.

[45] **CMS** Collaboration, S. Chatrchyan *et al.*, "Search for Supersymmetry in pp Collisions at $\sqrt{s} = 7$ TeV in Events with Two Photons and Missing Transverse Energy," *Phys.Rev.Lett.* **106** (2011) 211802.

[46] **ATLAS** Collaboration, G. Aad *et al.*, "Search for Diphoton Events with Large Missing Transverse Energy with 36 pb^{-1} of 7 TeV Proton-Proton Collision Data with the ATLAS Detector," *Eur.Phys.J.* **C71** (2011) 1744.

[47] L. Evans and P. Bryant, "LHC Machine," *Journal of Instrumentation* **3** no. 08, (2008) S08001.

[48] *Proceedings of the 2nd Evian 2010 Workshop on LHC Beam Operation*. CERN, Geneva, 2011. CERN-ATS-2011-017.

[49] M. Bajko *et al.*, "Report of the Task Force on the Incident of 19th September 2008 at the LHC," Tech. Rep. CERN-LHC-PROJECT-Report-1168, CERN, Geneva, Mar, 2009.

[50] F. Bertinelli *et al.*, "Towards a Consolidation of LHC Superconducting Splices for 7 TeV Operation," Tech. Rep. CERN-ATS-2010-144, Jun, 2010.

[51] "LHC Commissioning with Beam." `http://lhc-commissioning.web.cern.ch/lhc-commissioning/`, 2012.

[52] **ATLAS** Collaboration, G. Aad *et al.*, "The atlas experiment at the cern large hadron collider," *JINST* **3** (2008) S08003.

[53] "ATLAS Website - Photos Section." `http://www.atlas.ch/photos`, 2012.

[54] **ATLAS** Collaboration, *Atlas Computing: Technical Design Report*. CERN, Geneva, 2005. `http://cdsweb.cern.ch/record/837738`.

[55] W. Lampl *et al.*, "Calorimeter clustering algorithms: Description and performance," Tech. Rep. ATL-LARG-PUB-2008-002, CERN, Geneva, Apr, 2008.

[56] **ATLAS** Collaboration, "Expected photon performance in the ATLAS experiment," Tech. Rep. ATL-PHYS-PUB-2011-007, CERN, Geneva, Apr, 2011.

[57] **ATLAS** Collaboration, G. Aad *et al.*, "Expected Performance of the ATLAS Experiment - Detector, Trigger and Physics," `arXiv:0901.0512 [hep-ex]`.

[58] L. Carminati *et al.*, "Reconstruction and Identification Efficiency of Inclusive Isolated Photons," Tech. Rep. ATL-PHYS-INT-2011-014, CERN, Geneva, Mar, 2011.

[59] **ATLAS** Collaboration, G. Aad *et al.*, "Electron performance measurements with the ATLAS detector using the 2010 LHC proton-proton collision data," *Eur.Phys.J.* **C72** (2012) 1909.

[60] "ATLAS Egamma Combined Performance Group Twiki." `https:`

//twiki.cern.ch/twiki/bin/viewauth/AtlasProtected/ElectronGamma, 2012.

[61] M. Hance, D. Olivito, and H. Williams, "Performance Studies for e/gamma Calorimeter Isolation," Tech. Rep. ATL-COM-PHYS-2011-1186, CERN, Geneva, Sep, 2011.

[62] **ATLAS** Collaboration, "Expected electron performance in the ATLAS experiment," Tech. Rep. ATL-PHYS-PUB-2011-006, CERN, Geneva, Apr, 2011.

[63] M. Cacciari, G. Salam, and G. Soyez, "The anti-k$_t$ jet clustering algorithm," *JHEP* **04** (2008) 063.

[64] **ATLAS** Collaboration, G. Aad *et al.*, "Jet energy measurement with the ATLAS detector in proton-proton collisions at sqrt(s) = 7 TeV," arXiv:1112.6426 [hep-ex].

[65] "ATLAS SUSY ETmiss Subgroup Twiki." https://twiki.cern.ch/twiki/bin/viewauth/AtlasProtected/SusyEtMissSubGroup, 2012.

[66] "ATLAS Muon Combined Performance Guidelines." https://twiki.cern.ch/twiki/bin/viewauth/AtlasProtected/MCPAnalysisGuidelinesRel17MC11a, 2012.

[67] T. Barillari *et al.*, "Local hadronic calibration," Tech. Rep. ATL-LARG-PUB-2009-001-2, CERN, Geneva, Jun, 2008.

[68] **ATLAS** Collaboration, "Performance of the missing transverse energy reconstruction and calibration in proton-proton collisions at a center-of-mass energy of 7 tev with the atlas detector," Tech. Rep. ATLAS-CONF-2010-057, CERN, Geneva, Jul, 2010.

[69] **ATLAS** Collaboration, G. Aad *et al.*, "Performance of Missing Transverse Momentum Reconstruction in Proton-Proton Collisions at 7 TeV with ATLAS," *Eur.Phys.J.* **C72** (2012) 1844.

[70] **ATLAS** Collaboration, "Luminosity Determination in pp Collisions at $\sqrt{s} = 7$ TeV using the ATLAS Detector in 2011," Tech. Rep. ATLAS-CONF-2011-116, CERN, Geneva, Aug, 2011.

[71] M. Mangano *et al.*, "ALPGEN, a generator for hard multiparton processes in hadronic collisions," *JHEP* **07** (2003) 001.

[72] G. Corcella *et al.*, "HERWIG 6: An event generator for hadron emission reactions with interfering gluons (including supersymmetric processes)," *JHEP* **01** (2001) 010.

[73] G. Corcella *et al.*, "HERWIG 6.5 release note," `arXiv:hep-ph/0210213 [hep-ph]`.

[74] J. F. J. Butterworth and M. Seymour, "Multiparton interactions in photoproduction at hera," *Z. Phys.* **C72** (1996) 637–646.

[75] C. Anastasiou *et al.*, "High precision QCD at hadron colliders: Electroweak gauge boson rapidity distributions at NNLO," *Phys. Rev.* **D69** (2004) 094008.

[76] J. Alwall *et al.*, "MadGraph/MadEvent v4: The New Web Generation," *JHEP* **09** (2007) 028.

[77] T. Sjostrand, S. Mrenna, and P. Skands, "PYTHIA 6.4 physics and manual," *JHEP* **05** (2006) 026.

[78] S. Frixione and B. R. Webber, "The MC@NLO 3.2 event generator," `arXiv:hep-ph/0601192`.

[79] S. Frixione and B. R. Webber, "Matching NLO QCD computations and parton shower simulations," *JHEP* **06** (2002) 029.

[80] S. Moch and P. Uwer, "Heavy-quark pair production at two loops in QCD," *Nucl. Phys. Proc. Suppl.* **183** (2008) 75–80.

[81] G. Bozzi *et al.*, "$Z\gamma\gamma$ production with leptonic decays and triple photon production at NLO QCD," *Phys.Rev.* **D84** (2011) 074028.

[82] G. Bozzi *et al.*, "$W\gamma\gamma$ production with leptonic decays at NLO QCD," *Phys. Rev.* **D83** (2011) 114035.

[83] A. Djouadi, J.-L. Kneur, and G. Moultaka, "SuSpect: A Fortran code for the supersymmetric and Higgs particle spectrum in the MSSM," *Comput.Phys.Commun.* **176** (2007) 426–455.

[84] M. Muhlleitner, A. Djouadi, and Y. Mambrini, "SDECAY: A Fortran code for the decays of the supersymmetric particles in the MSSM," *Comput.Phys.Commun.* **168** (2005) 46–70.

[85] M. Bahr *et al.*, "Herwig++ Physics and Manual," *Eur. Phys. J.* **C58** (2008) 639–707.

[86] A. Sherstnev and R. S. Thorne, "Parton Distributions for LO Generators," *Eur. Phys. J.* **C55** (2008) 553–575.

[87] F. E. Paige *et al.*, "ISAJET 7.69: A Monte Carlo event generator for p p, anti-p p, and e+ e- reactions," `arXiv:hep-ph/0312045`.

[88] **ATLAS** Collaboration, "Data-Quality Requirements and Event Cleaning for Jets and Missing Transverse Energy Reconstruction with the ATLAS Detector in Proton-Proton Collisions at a Center-of-Mass Energy of $\sqrt{s} = 7$ TeV," Tech. Rep. ATLAS-CONF-2010-038, CERN, Geneva, Jul, 2010.

[89] "ATLAS JetEtMiss Combined Performance Group Twiki." `https://twiki.cern.ch/twiki/bin/viewauth/AtlasProtected/JetEtMiss`, 2012.

[90] S. Asai *et al.*, "Search for Supersymmetry with jets and missing transverse momentum and one lepton at $\sqrt{s} = 7$ TeV," Tech. Rep. ATL-COM-PHYS-2011-848, CERN, Geneva, Jul, 2011.

[91] "SUSY Fake Met Estimator." `https:`

//twiki.cern.ch/twiki/bin/viewauth/AtlasProtected/FakeMetEstimator, 2012.

[92] J. Alasia *et al.*, "Search for a diphoton and E_T^{miss} final state in $\sqrt{s} = 7$ TeV pp collisions at the LHC using the ATLAS detector," Tech. Rep. ATL-PHYS-INT-2011-095, CERN, Geneva, Nov, 2011.

[93] H. Abreu *et al.*, "Purity estimates for the inclusive isolated photons," Tech. Rep. ATL-PHYS-INT-2011-015, CERN, Geneva, Mar, 2011.

[94] "SUSY Photon+B+ETmiss Meeting Agenda: Feb 1st." https://indico.cern.ch/conferenceDisplay.py?confId=164758, 2012.

[95] "SUSY Photon+B+ETmiss Meeting Agenda: Feb 14th." https://indico.cern.ch/conferenceDisplay.py?confId=176499, 2012.

[96] F. Alonso *et al.*, "Search for a diphoton and $E_{\mathrm{T}}^{\mathrm{miss}}$ final state in $\sqrt{s} = 7$ TeV pp collisions at the LHC using the ATLAS detector," Tech. Rep. ATL-COM-PHYS-2012-463, CERN, Geneva, Apr, 2012. 5fb-1 Diphoton plus missing et supporting note.

[97] K. Liu, Y. Liu, and G. Marchiori, "Measurement of the identification efficiency of isolated prompt photons using the matrix method and 4.9 fb^{-1} of atlas data," Tech. Rep. ATL-COM-PHYS-2012-242, CERN, Geneva, Mar, 2012.

[98] **ATLAS** Collaboration, G. Aad *et al.*, "Measurement of W gamma and Z gamma production cross sections in pp collisions at sqrt(s) = 7 TeV and limits

on anomalous triple gauge couplings with the ATLAS detector," arXiv:1205.2531 [hep-ex].

[99] "LAr Cleaning And Object Quality Twiki." https://twiki.cern.ch/twiki/bin/view/AtlasProtected/LArCleaningAndObjectQuality, 2012.

[100] **ATLAS** Collaboration, G. Aad *et al.*, "Search for the Standard Model Higgs boson in the diphoton decay channel with 4.9 fb-1 of pp collisions at sqrt(s)=7 TeV with ATLAS," *Phys.Rev.Lett.* **108** (2012) 111803.

[101] **Atlas** Collaboration, G. Aad *et al.*, "Measurement of the $W \to l\nu$ and $Z/\gamma^* \to ll$ production cross sections in proton-proton collisions at $\sqrt{s} = 7$ TeV with the ATLAS detector," *JHEP* **12** (2010) 060.

[102] "Atlas calorimeter response to single isolated hadrons and estimation of the calorimeter jet scale uncertainty," Tech. Rep. ATLAS-CONF-2010-052, CERN, Geneva, Jul, 2010.

[103] A. L. Read, "Presentation of search results: The CL_s technique," *J.Phys.G* **G28** (2002) 2693.

Part IV

Appendices

Appendix A

Monte Carlo Sample Details

This appendix section highlights various details about both the GGM and SPS8 signal samples that were produced for this analysis. Details on the GGM samples is contained in Section A.1. The information includes leading-order production cross sections taken from the `HERWIG++` event generator, detailed tables of the signal region selection acceptances of all points, and a detailed mass spectrum for a selection of points. Similar information is included for the SPS8 samples in Section A.2, but additional info is included on the breakdown of the various contributing production processes.

A.1 GGM Signal Samples

This section collects detailed information about the GGM signal samples. The gluino/squark and lightest neutralino mass combinations used for the GGM samples and the corresponding cross sections are listed in Table A.1 and A.2. The other GGM model parameters are fixed to $M_2 = 2.5\,\text{TeV}$, $\tan\beta = 1.5$, $\mu = 2.5\,\text{TeV}$ and $c\tau_{\text{NLSP}} < 0.1\,\text{mm}$.

Table A.3 shows the full SUSY mass spectrum for an example point of $m(\tilde{\chi}_1^0) = 450\,\text{GeV}$ and $m(\tilde{g}) = 1000\,\text{GeV}$. Similarly, Table A.4 shows the full SUSY mass spectrum for an example point of $m(\tilde{\chi}_1^0) = 450\,\text{GeV}$ and $m(\tilde{q}) = 1000\,\text{GeV}$.

$M(\tilde{g})$ [GeV]	Cross Section (LO) [pb]
800	0.027
850	0.016
900	8.9×10^{-3}
950	5.1×10^{-3}
1000	3.0×10^{-3}
1050	1.8×10^{-3}
1100	1.0×10^{-3}
1150	0.6×10^{-3}
1200	0.4×10^{-3}
1250	0.2×10^{-3}
1300	0.1×10^{-3}

Table A.1: The LO cross sections for GGM from `HERWIG++` as a function of gluino mass in GeV.

$M(\tilde{q})$ [GeV]	Cross Section (LO) [pb]
800	0.050
850	0.035
900	0.025
950	0.017
1000	0.012
1050	8.7×10^{-3}
1100	6.2×10^{-3}
1150	4.4×10^{-3}
1200	3.1×10^{-3}
1250	2.2×10^{-3}
1300	1.5×10^{-3}

Table A.2: The LO cross sections for GGM from `HERWIG++` as a function of squark mass in GeV.

Sparticle	Mass Eigenstates	M [GeV]
squarks	$\tilde{u}_L$	2499.78
	$\tilde{u}_R$	2499.90
	$\tilde{d}_L$	2500.27
	$\tilde{d}_R$	2500.05
	$\tilde{s}_L$	2500.27
	$\tilde{s}_R$	2500.05
	$\tilde{c}_L$	2499.78
	$\tilde{c}_R$	2499.90
	$\tilde{b}_1$	2498.13
	$\tilde{b}_2$	2502.19
	$\tilde{t}_1$	2452.85
	$\tilde{t}_2$	2555.25
sleptons	$\tilde{e}_L$	2500.17
	$\tilde{e}_R$	2500.15
	$\tilde{\mu}_L$	2500.17
	$\tilde{\mu}_R$	2500.15
	$\tilde{\tau}_1$	2498.82
	$\tilde{\tau}_2$	2501.49
sneutrinos	$\tilde{\nu}_e$	2499.68
	$\tilde{\nu}_\mu$	2499.68
	$\tilde{\nu}_\tau$	2499.68
neutralinos	$\tilde{\chi}_1^0$	449.09
	$\tilde{\chi}_2^0$	2422.69
	$\tilde{\chi}_3^0$	2500.07
	$\tilde{\chi}_4^0$	2578.29
charginos	$\chi_1^\pm$	2422.24
	$\chi_2^\pm$	2577.86
gluino	$\tilde{g}$	1000.0
gravitino	$\tilde{G}$	3.8×10^{-9}
Higgs bosons	$\tilde{h}^0$	120.00
	$\tilde{H}^0$	2003.78
	$\tilde{A}^0$	2000.00
	$\tilde{H}^\pm$	2001.43

Table A.3: SUSY particle mass spectrum for the GGM model which is characterized by the following parameters: $m(\tilde{\chi}_1^0) = 450\,\text{GeV}, m(\tilde{g}) = 1000\,\text{GeV}$.

Sparticle	Mass Eigenstates	M [GeV]
squarks	$\tilde{u}_L$	999.45
	$\tilde{u}_R$	2499.90
	$\tilde{d}_L$	1000.67
	$\tilde{d}_R$	1000.13
	$\tilde{s}_L$	1000.67
	$\tilde{s}_R$	1000.13
	$\tilde{c}_L$	999.45
	$\tilde{c}_R$	2499.90
	$\tilde{b}_1$	995.42
	$\tilde{b}_2$	1005.36
	$\tilde{t}_1$	1005.02
	$\tilde{t}_2$	2507.11
sleptons	$\tilde{e}_L$	2500.17
	$\tilde{e}_R$	2500.15
	$\tilde{\mu}_L$	2500.17
	$\tilde{\mu}_R$	2500.15
	$\tilde{\tau}_1$	2498.83
	$\tilde{\tau}_2$	2501.50
sneutrinos	$\tilde{\nu}_e$	2499.68
	$\tilde{\nu}_\mu$	2499.68
	$\tilde{\nu}_\tau$	2499.68
neutralinos	$\tilde{\chi}_1^0$	449.09
	$\tilde{\chi}_2^0$	2422.46
	$\tilde{\chi}_3^0$	2500.07
	$\tilde{\chi}_4^0$	2578.23
charginos	$\chi_1^\pm$	2422.00
	$\chi_2^\pm$	2578.10
gluino	$\tilde{g}$	2500.0
gravitino	$\tilde{G}$	9.5×10^{-10}
Higgs bosons	$\tilde{h}^0$	120.00
	$\tilde{H}^0$	2003.09
	$\tilde{A}^0$	2000.00
	$\tilde{H}^\pm$	2001.08

Table A.4: SUSY particle mass spectrum for the GGM model which is characterized by the following parameters: $m(\tilde{\chi}_1^0) = 450\,\text{GeV}, m(\tilde{q}) = 1000\,\text{GeV}$.

A.1.1 GGM Signal Acceptances

The acceptances of the cuts defining the three signal regions from Section 9.4 for the GGM Monte Carlo signal points are shown in this section. The acceptances for the various GGM signal points where gluinos are the sparticles produced are given in Tables A.5, A.6, and A.7. The acceptances for the points in which squarks are the sparticles produced can be seen in Tables A.8, A.9, and A.10. The uncertainties shown in these tables are those due to the limited MC statistics. Visual representations of these numbers can be seen in the main body of the document in Section 9.4.1.

$m(\tilde{g})$	$m(\tilde{\chi}_1^0)$	Acceptance [%]	$m(\tilde{g})$	$m(\tilde{\chi}_1^0)$	Acceptance [%]	$m(\tilde{g})$	$m(\tilde{\chi}_1^0)$	Acceptance [%]
800	50	1.2 ± 0.2	1000	100	3.9 ± 0.3	1150	1050	22.7 ± 0.6
800	100	2.5 ± 0.2	1000	150	5.9 ± 0.3	1150	1130	24.3 ± 0.6
800	150	4.8 ± 0.3	1000	300	12.2 ± 0.5	1150	1140	18.1 ± 0.5
800	300	12.1 ± 0.5	1000	450	16.4 ± 0.5	1200	50	3.5 ± 0.3
800	450	15.9 ± 0.5	1000	600	18.7 ± 0.6	1200	100	4.8 ± 0.3
800	600	19.7 ± 0.6	1000	750	20.4 ± 0.6	1200	150	6.8 ± 0.4
800	750	21.4 ± 0.6	1000	900	21.7 ± 0.6	1200	300	12.1 ± 0.5
800	780	19.5 ± 0.6	1000	980	23 ± 0.6	1200	450	17.1 ± 0.5
800	790	13.3 ± 0.5	1000	990	15.3 ± 0.5	1200	600	18.5 ± 0.6
850	50	1.5 ± 0.2	1050	50	2.5 ± 0.2	1200	750	21.6 ± 0.6
850	100	2.9 ± 0.2	1050	100	3.9 ± 0.3	1200	900	22 ± 0.6
850	150	5.3 ± 0.3	1050	150	6.8 ± 0.4	1200	1050	22.8 ± 0.6
850	300	11.6 ± 0.5	1050	300	13.1 ± 0.5	1200	1180	24.5 ± 0.6
850	450	17.3 ± 0.5	1050	450	17.2 ± 0.5	1200	1190	19 ± 0.6
850	600	19.9 ± 0.6	1050	600	20 ± 0.6	1250	50	3.6 ± 0.3
850	750	21.3 ± 0.6	1050	750	21.1 ± 0.6	1250	100	4.6 ± 0.3
850	830	20.5 ± 0.6	1050	900	20.6 ± 0.6	1250	150	7.5 ± 0.4
850	840	13.1 ± 0.5	1050	1030	24.3 ± 0.6	1250	300	12.9 ± 0.5
900	50	2 ± 0.2	1050	1040	17.5 ± 0.5	1250	450	16.9 ± 0.5
900	100	3.7 ± 0.3	1100	50	3.3 ± 0.3	1250	600	19.5 ± 0.6
900	150	5.6 ± 0.3	1100	100	3.7 ± 0.3	1250	750	20.3 ± 0.6
900	300	12.1 ± 0.5	1100	150	7 ± 0.4	1250	900	21.2 ± 0.6
900	450	17.1 ± 0.5	1100	300	12.7 ± 0.5	1250	1050	22.9 ± 0.6
900	600	19.5 ± 0.6	1100	450	16.6 ± 0.5	1250	1200	23.9 ± 0.6
900	750	21.1 ± 0.6	1100	600	19.3 ± 0.6	1250	1230	25.7 ± 0.6
900	880	21.6 ± 0.6	1100	750	20.9 ± 0.6	1250	1240	19.5 ± 0.6
900	890	14.7 ± 0.5	1100	900	21.5 ± 0.6	1300	50	4.1 ± 0.3
950	50	2.3 ± 0.2	1100	1050	23.9 ± 0.6	1300	100	6.4 ± 0.3
950	100	3.2 ± 0.3	1100	1080	24.6 ± 0.6	1300	150	6.8 ± 0.4
950	150	5.6 ± 0.3	1100	1090	16.8 ± 0.5	1300	300	12.4 ± 0.5
950	300	11.9 ± 0.5	1150	50	3.2 ± 0.2	1300	450	16.2 ± 0.5
950	450	17.8 ± 0.5	1150	100	4.4 ± 0.3	1300	600	18.9 ± 0.6
950	600	20.1 ± 0.6	1150	150	7.1 ± 0.4	1300	750	19.1 ± 0.6
950	750	21.3 ± 0.6	1150	300	13 ± 0.5	1300	900	20.9 ± 0.6
950	900	23 ± 0.6	1150	450	15.9 ± 0.5	1300	1050	22.7 ± 0.6
950	930	22.1 ± 0.6	1150	600	18.9 ± 0.6	1300	1200	23.1 ± 0.6
950	940	15.1 ± 0.5	1150	750	19.4 ± 0.6	1300	1280	25.4 ± 0.6
1000	50	2.2 ± 0.2	1150	900	20.7 ± 0.6	1300	1290	20 ± 0.6

Table A.5: The acceptance of signal region A, including the error due to limited Monte Carlo statistics, for each GGM grid point with gluino production. Other systematics are not included.

$m(\tilde{g})$	$m(\tilde{\chi}_1^0)$	Acceptance [%]	$m(\tilde{g})$	$m(\tilde{\chi}_1^0)$	Acceptance [%]	$m(\tilde{g})$	$m(\tilde{\chi}_1^0)$	Acceptance [%]
800	50	12.5 ± 0.5	1000	100	19.6 ± 0.6	1150	1050	15.5 ± 0.5
800	100	12.2 ± 0.5	1000	150	20.5 ± 0.6	1150	1130	14.3 ± 0.5
800	150	13.5 ± 0.5	1000	300	20.4 ± 0.6	1150	1140	10.6 ± 0.4
800	300	14 ± 0.5	1000	450	19.8 ± 0.6	1200	50	22.9 ± 0.6
800	450	10.2 ± 0.4	1000	600	18.6 ± 0.6	1200	100	24.3 ± 0.6
800	600	6.9 ± 0.4	1000	750	14.5 ± 0.5	1200	150	23.7 ± 0.6
800	750	4.7 ± 0.3	1000	900	10.1 ± 0.4	1200	300	22.3 ± 0.6
800	780	4.1 ± 0.3	1000	980	8.6 ± 0.4	1200	450	23.4 ± 0.6
800	790	2.8 ± 0.2	1000	990	6.4 ± 0.3	1200	600	22.2 ± 0.6
850	50	13.1 ± 0.5	1050	50	19.5 ± 0.6	1200	750	23.6 ± 0.6
850	100	15.2 ± 0.5	1050	100	20.8 ± 0.6	1200	900	21.3 ± 0.6
850	150	15.5 ± 0.5	1050	150	21.5 ± 0.6	1200	1050	18.4 ± 0.6
850	300	16.3 ± 0.5	1050	300	21.7 ± 0.6	1200	1180	16.7 ± 0.5
850	450	13.9 ± 0.5	1050	450	21.9 ± 0.6	1200	1190	11.9 ± 0.5
850	600	9.4 ± 0.4	1050	600	21.2 ± 0.6	1250	50	23.7 ± 0.6
850	750	6.2 ± 0.3	1050	750	17.5 ± 0.5	1250	100	24.3 ± 0.6
850	830	5.2 ± 0.3	1050	900	12.3 ± 0.5	1250	150	25 ± 0.6
850	840	3.3 ± 0.3	1050	1030	10.7 ± 0.4	1250	300	23.1 ± 0.6
900	50	16 ± 0.5	1050	1040	8.4 ± 0.4	1250	450	23.3 ± 0.6
900	100	16.6 ± 0.5	1100	50	21.1 ± 0.6	1250	600	23.6 ± 0.6
900	150	17.3 ± 0.5	1100	100	21.6 ± 0.6	1250	750	23.3 ± 0.6
900	300	18.1 ± 0.5	1100	150	22.3 ± 0.6	1250	900	22.4 ± 0.6
900	450	17.1 ± 0.5	1100	300	21.9 ± 0.6	1250	1050	21.4 ± 0.6
900	600	12.7 ± 0.5	1100	450	22 ± 0.6	1250	1200	17.2 ± 0.5
900	750	8 ± 0.4	1100	600	22.1 ± 0.6	1250	1230	18.4 ± 0.5
900	880	6.4 ± 0.3	1100	750	20 ± 0.6	1250	1240	14 ± 0.5
900	890	4.4 ± 0.3	1100	900	16.4 ± 0.5	1300	50	25.9 ± 0.6
950	50	16.9 ± 0.5	1100	1050	12.6 ± 0.5	1300	100	25.8 ± 0.6
950	100	17.8 ± 0.5	1100	1080	12.7 ± 0.5	1300	150	24.4 ± 0.6
950	150	18.3 ± 0.5	1100	1090	9 ± 0.4	1300	300	22.1 ± 0.6
950	300	19.3 ± 0.6	1150	50	22.1 ± 0.6	1300	450	23.1 ± 0.6
950	450	19.5 ± 0.6	1150	100	23.3 ± 0.6	1300	600	23.7 ± 0.6
950	600	15.8 ± 0.5	1150	150	23.5 ± 0.6	1300	750	22.4 ± 0.6
950	750	11.8 ± 0.5	1150	300	22.7 ± 0.6	1300	900	23 ± 0.6
950	900	7.8 ± 0.4	1150	450	22.3 ± 0.6	1300	1050	23.1 ± 0.6
950	930	8 ± 0.4	1150	600	22.5 ± 0.6	1300	1200	19.7 ± 0.6
950	940	4.7 ± 0.3	1150	750	20.4 ± 0.6	1300	1280	19.1 ± 0.6
1000	50	19 ± 0.6	1150	900	18.6 ± 0.6	1300	1290	14.8 ± 0.5

Table A.6: The acceptance of signal region B, including the error due to limited Monte Carlo statistics, for each GGM grid point with gluino production. Other systematics are not included.

$m(\tilde{g})$	$m(\tilde{\chi}_1^0)$	Acceptance [%]	$m(\tilde{g})$	$m(\tilde{\chi}_1^0)$	Acceptance [%]	$m(\tilde{g})$	$m(\tilde{\chi}_1^0)$	Acceptance [%]
800	50	2.8 ± 0.2	1000	100	7.2 ± 0.4	1150	1050	23.8 ± 0.6
800	100	5.5 ± 0.3	1000	150	10.5 ± 0.4	1150	1130	25.6 ± 0.6
800	150	9.4 ± 0.4	1000	300	16.8 ± 0.5	1150	1140	19 ± 0.6
800	300	17.6 ± 0.5	1000	450	20 ± 0.6	1200	50	5.9 ± 0.3
800	450	19.8 ± 0.6	1000	600	21.4 ± 0.6	1200	100	7.9 ± 0.4
800	600	22.3 ± 0.6	1000	750	22.1 ± 0.6	1200	150	10.3 ± 0.4
800	750	25.7 ± 0.6	1000	900	23.6 ± 0.6	1200	300	16.1 ± 0.5
800	780	24.3 ± 0.6	1000	980	25.3 ± 0.6	1200	450	20.3 ± 0.6
800	790	16.4 ± 0.5	1000	990	16.7 ± 0.5	1200	600	20.7 ± 0.6
850	50	3.4 ± 0.3	1050	50	4.5 ± 0.3	1200	750	23.1 ± 0.6
850	100	6.9 ± 0.4	1050	100	7.1 ± 0.4	1200	900	23.2 ± 0.6
850	150	9.9 ± 0.4	1050	150	11.2 ± 0.4	1200	1050	24.1 ± 0.6
850	300	17.6 ± 0.5	1050	300	17.7 ± 0.5	1200	1180	25.8 ± 0.6
850	450	20.9 ± 0.6	1050	450	20.7 ± 0.6	1200	1190	20 ± 0.6
850	600	22.5 ± 0.6	1050	600	22.5 ± 0.6	1250	50	5.6 ± 0.3
850	750	24.1 ± 0.6	1050	750	22.7 ± 0.6	1250	100	7.2 ± 0.4
850	830	24.3 ± 0.6	1050	900	22.1 ± 0.6	1250	150	11.3 ± 0.4
850	840	15.4 ± 0.5	1050	1030	26.1 ± 0.6	1250	300	16.4 ± 0.5
900	50	4.2 ± 0.3	1050	1040	18.6 ± 0.6	1250	450	19.6 ± 0.6
900	100	7.1 ± 0.4	1100	50	5.4 ± 0.3	1250	600	21.6 ± 0.6
900	150	10.2 ± 0.4	1100	100	6.7 ± 0.4	1250	750	22.1 ± 0.6
900	300	17.5 ± 0.5	1100	150	11.1 ± 0.4	1250	900	22.6 ± 0.6
900	450	21.1 ± 0.6	1100	300	17.1 ± 0.5	1250	1050	23.9 ± 0.6
900	600	21.7 ± 0.6	1100	450	20.1 ± 0.6	1250	1200	25.2 ± 0.6
900	750	22.9 ± 0.6	1100	600	21.7 ± 0.6	1250	1230	26.9 ± 0.6
900	880	24.5 ± 0.6	1100	750	22.6 ± 0.6	1250	1240	20.5 ± 0.6
900	890	16.8 ± 0.5	1100	900	22.8 ± 0.6	1300	50	6.3 ± 0.3
950	50	4.4 ± 0.3	1100	1050	25.3 ± 0.6	1300	100	9.4 ± 0.4
950	100	6.6 ± 0.4	1100	1080	26.2 ± 0.6	1300	150	10.3 ± 0.4
950	150	9.9 ± 0.4	1100	1090	17.9 ± 0.5	1300	300	15.9 ± 0.5
950	300	16.6 ± 0.5	1150	50	5.8 ± 0.3	1300	450	19.1 ± 0.6
950	450	21.5 ± 0.6	1150	100	7.1 ± 0.4	1300	600	21 ± 0.6
950	600	22.5 ± 0.6	1150	150	10.8 ± 0.4	1300	750	20.9 ± 0.6
950	750	23.2 ± 0.6	1150	300	17.2 ± 0.5	1300	900	22.4 ± 0.6
950	900	25.3 ± 0.6	1150	450	19.5 ± 0.6	1300	1050	23.9 ± 0.6
950	930	25 ± 0.6	1150	600	21.2 ± 0.6	1300	1200	24.3 ± 0.6
950	940	16.6 ± 0.5	1150	750	21.1 ± 0.6	1300	1280	26.5 ± 0.6
1000	50	4.1 ± 0.3	1150	900	22.1 ± 0.6	1300	1290	20.9 ± 0.6

Table A.7: The acceptance of signal region C, including the error due to limited Monte Carlo statistics, for each GGM grid point with gluino production. Other systematics are not included.

$m(\tilde{g})$	$m(\tilde{\chi}_1^0)$	Acceptance [%]	$m(\tilde{g})$	$m(\tilde{\chi}_1^0)$	Acceptance [%]	$m(\tilde{g})$	$m(\tilde{\chi}_1^0)$	Acceptance [%]
800	50	4.2 ± 0.3	1000	100	7.4 ± 0.4	1150	1050	24.4 ± 0.6
800	100	6.4 ± 0.3	1000	150	9.1 ± 0.4	1150	1130	23.8 ± 0.6
800	150	9.1 ± 0.4	1000	300	14.0 ± 0.5	1150	1140	25.0 ± 0.6
800	300	14.3 ± 0.5	1000	450	19.5 ± 0.6	1200	50	6.7 ± 0.4
800	450	18.2 ± 0.5	1000	600	21.4 ± 0.6	1200	100	8.0 ± 0.4
800	600	20.7 ± 0.6	1000	750	22.8 ± 0.6	1200	150	9.5 ± 0.4
800	750	21.6 ± 0.6	1000	900	22.5 ± 0.6	1200	300	14.0 ± 0.5
800	780	21.3 ± 0.6	1000	980	25.2 ± 0.6	1200	450	19.0 ± 0.6
800	790	21.9 ± 0.6	1000	990	24.4 ± 0.6	1200	600	20.4 ± 0.6
850	50	4.8 ± 0.3	1050	50	5.8 ± 0.3	1200	750	22.0 ± 0.6
850	100	5.9 ± 0.3	1050	100	7.3 ± 0.4	1200	900	23.5 ± 0.6
850	150	8.4 ± 0.4	1050	150	9.2 ± 0.4	1200	1050	22.9 ± 0.6
850	300	14.7 ± 0.5	1050	300	15.7 ± 0.5	1200	1180	25.1 ± 0.6
850	450	18.4 ± 0.6	1050	450	18.4 ± 0.5	1200	1190	25.3 ± 0.6
850	600	21.7 ± 0.6	1050	600	21.8 ± 0.6	1250	50	6.5 ± 0.3
850	750	22.9 ± 0.6	1050	750	23.0 ± 0.6	1250	100	7.8 ± 0.4
850	830	22.9 ± 0.6	1050	900	22.7 ± 0.6	1250	150	9.7 ± 0.4
850	840	21.6 ± 0.6	1050	1030	24.3 ± 0.6	1250	300	15.6 ± 0.5
900	50	4.7 ± 0.3	1050	1040	23.9 ± 0.6	1250	450	18.9 ± 0.6
900	100	6.9 ± 0.4	1100	50	6.2 ± 0.3	1250	600	20.8 ± 0.6
900	150	9.6 ± 0.4	1100	100	7.4 ± 0.4	1250	750	21.8 ± 0.6
900	300	15.4 ± 0.5	1100	150	9.5 ± 0.4	1250	900	24.0 ± 0.6
900	450	18.9 ± 0.6	1100	300	14.3 ± 0.5	1250	1050	22.6 ± 0.6
900	600	21.5 ± 0.6	1100	450	18.7 ± 0.6	1250	1200	25.0 ± 0.6
900	750	22.5 ± 0.6	1100	600	22.1 ± 0.6	1250	1230	24.8 ± 0.6
900	880	22.7 ± 0.6	1100	750	22.7 ± 0.6	1250	1240	24.5 ± 0.6
900	890	24.2 ± 0.6	1100	900	23.3 ± 0.6	1300	50	7.0 ± 0.4
950	50	4.9 ± 0.3	1100	1050	24.4 ± 0.6	1300	100	8.8 ± 0.4
950	100	6.4 ± 0.3	1100	1080	25.0 ± 0.6	1300	150	8.5 ± 0.4
950	150	9.3 ± 0.4	1100	1090	24.3 ± 0.6	1300	300	13.8 ± 0.5
950	300	14.3 ± 0.5	1150	50	7.5 ± 0.4	1300	450	18.9 ± 0.6
950	450	19.4 ± 0.6	1150	100	8.1 ± 0.4	1300	600	21.3 ± 0.6
950	600	20.4 ± 0.6	1150	150	9.7 ± 0.4	1300	750	22.7 ± 0.6
950	750	22.6 ± 0.6	1150	300	14.6 ± 0.5	1300	900	22.6 ± 0.6
950	900	23.2 ± 0.6	1150	450	19.0 ± 0.6	1300	1050	23.0 ± 0.6
950	930	24.1 ± 0.6	1150	600	22.0 ± 0.6	1300	1200	25.0 ± 0.6
950	940	24.1 ± 0.6	1150	750	22.4 ± 0.6	1300	1280	25.6 ± 0.6
1000	50	5.6 ± 0.3	1150	900	23.7 ± 0.6	1300	1290	26.0 ± 0.6

Table A.8: The acceptance of signal region A, including the error due to limited Monte Carlo statistics, for each GGM grid point with squark production. Other systematics are not included.

$m(\tilde{g})$	$m(\tilde{\chi}_1^0)$	Acceptance [%]	$m(\tilde{g})$	$m(\tilde{\chi}_1^0)$	Acceptance [%]	$m(\tilde{g})$	$m(\tilde{\chi}_1^0)$	Acceptance [%]
800	50	21.1 ± 0.6	1000	100	30.6 ± 0.7	1150	1050	17.9 ± 0.5
800	100	22.3 ± 0.6	1000	150	29.4 ± 0.6	1150	1130	14.9 ± 0.5
800	150	19.5 ± 0.6	1000	300	22.5 ± 0.6	1150	1140	15.6 ± 0.5
800	300	16.7 ± 0.5	1000	450	23.7 ± 0.6	1200	50	34.9 ± 0.7
800	450	12.6 ± 0.5	1000	600	20.0 ± 0.6	1200	100	35.3 ± 0.7
800	600	9.1 ± 0.4	1000	750	17.4 ± 0.5	1200	150	32.5 ± 0.7
800	750	5.9 ± 0.3	1000	900	11.9 ± 0.5	1200	300	26.7 ± 0.6
800	780	5.5 ± 0.3	1000	980	11.4 ± 0.5	1200	450	26.4 ± 0.6
800	790	6.0 ± 0.3	1000	990	10.4 ± 0.4	1200	600	24.5 ± 0.6
850	50	24.8 ± 0.6	1050	50	32.0 ± 0.7	1200	750	23.4 ± 0.6
850	100	24.1 ± 0.6	1050	100	31.9 ± 0.7	1200	900	23.3 ± 0.6
850	150	22.3 ± 0.6	1050	150	30.0 ± 0.7	1200	1050	19.3 ± 0.6
850	300	19.1 ± 0.6	1050	300	25.4 ± 0.6	1200	1180	16.7 ± 0.5
850	450	17.1 ± 0.5	1050	450	23.1 ± 0.6	1200	1190	16.7 ± 0.5
850	600	12.4 ± 0.5	1050	600	22.6 ± 0.6	1250	50	35.8 ± 0.7
850	750	8.4 ± 0.4	1050	750	19.3 ± 0.6	1250	100	35.2 ± 0.7
850	830	7.0 ± 0.4	1050	900	14.8 ± 0.5	1250	150	33.1 ± 0.7
850	840	5.8 ± 0.3	1050	1030	12.3 ± 0.5	1250	300	28.1 ± 0.6
900	50	25.3 ± 0.6	1050	1040	12.4 ± 0.5	1250	450	26.9 ± 0.6
900	100	27.9 ± 0.6	1100	50	32.6 ± 0.7	1250	600	25.8 ± 0.6
900	150	25.7 ± 0.6	1100	100	32.9 ± 0.7	1250	750	24.8 ± 0.6
900	300	21.3 ± 0.6	1100	150	30.4 ± 0.7	1250	900	24.5 ± 0.6
900	450	19.0 ± 0.6	1100	300	25.5 ± 0.6	1250	1050	21.1 ± 0.6
900	600	16.0 ± 0.5	1100	450	24.3 ± 0.6	1250	1200	19.3 ± 0.6
900	750	11.4 ± 0.5	1100	600	24.5 ± 0.6	1250	1230	17.6 ± 0.5
900	880	8.0 ± 0.4	1100	750	22.1 ± 0.6	1250	1240	17.7 ± 0.5
900	890	8.1 ± 0.4	1100	900	19.0 ± 0.6	1300	50	37.9 ± 0.7
950	50	28.6 ± 0.6	1100	1050	14.3 ± 0.5	1300	100	37.5 ± 0.7
950	100	29.3 ± 0.6	1100	1080	14.3 ± 0.5	1300	150	33.2 ± 0.7
950	150	27.7 ± 0.6	1100	1090	13.3 ± 0.5	1300	300	27.2 ± 0.6
950	300	22.4 ± 0.6	1150	50	34.6 ± 0.7	1300	450	27.0 ± 0.6
950	450	21.7 ± 0.6	1150	100	34.5 ± 0.7	1300	600	26.8 ± 0.6
950	600	17.4 ± 0.5	1150	150	31.8 ± 0.7	1300	750	25.9 ± 0.6
950	750	14.4 ± 0.5	1150	300	26.2 ± 0.6	1300	900	24.3 ± 0.6
950	900	10.2 ± 0.4	1150	450	25.4 ± 0.6	1300	1050	23.5 ± 0.6
950	930	9.9 ± 0.4	1150	600	24.8 ± 0.6	1300	1200	21.6 ± 0.6
950	940	10.2 ± 0.4	1150	750	23.3 ± 0.6	1300	1280	19.8 ± 0.6
1000	50	31.0 ± 0.7	1150	900	21.3 ± 0.6	1300	1290	20.1 ± 0.6

Table A.9: The acceptance of signal region B, including the error due to limited Monte Carlo statistics, for each GGM grid point with squark production. Other systematics are not included.

$m(\tilde{g})$	$m(\tilde{\chi}_1^0)$	Acceptance [%]	$m(\tilde{g})$	$m(\tilde{\chi}_1^0)$	Acceptance [%]	$m(\tilde{g})$	$m(\tilde{\chi}_1^0)$	Acceptance [%]
800	50	7.0 ± 0.4	1000	100	10.1 ± 0.4	1150	1050	25.8 ± 0.6
800	100	10.2 ± 0.4	1000	150	12.6 ± 0.5	1150	1130	25.4 ± 0.6
800	150	13.2 ± 0.5	1000	300	17.5 ± 0.5	1150	1140	26.5 ± 0.6
800	300	19.5 ± 0.6	1000	450	22.7 ± 0.6	1200	50	8.5 ± 0.4
800	450	22.2 ± 0.6	1000	600	23.5 ± 0.6	1200	100	10.2 ± 0.4
800	600	23.8 ± 0.6	1000	750	24.8 ± 0.6	1200	150	11.9 ± 0.5
800	750	25.5 ± 0.6	1000	900	24.5 ± 0.6	1200	300	16.7 ± 0.5
800	780	26.3 ± 0.6	1000	980	27.4 ± 0.6	1200	450	21.6 ± 0.6
800	790	27.2 ± 0.6	1000	990	27.2 ± 0.6	1200	600	22.3 ± 0.6
850	50	7.2 ± 0.4	1050	50	7.7 ± 0.4	1200	750	23.5 ± 0.6
850	100	8.8 ± 0.4	1050	100	9.8 ± 0.4	1200	900	25.0 ± 0.6
850	150	12.4 ± 0.5	1050	150	12.3 ± 0.5	1200	1050	24.2 ± 0.6
850	300	19.3 ± 0.6	1050	300	18.8 ± 0.6	1200	1180	26.5 ± 0.6
850	450	22.4 ± 0.6	1050	450	21.1 ± 0.6	1200	1190	26.3 ± 0.6
850	600	24.4 ± 0.6	1050	600	24.3 ± 0.6	1250	50	7.9 ± 0.4
850	750	25.6 ± 0.6	1050	750	24.6 ± 0.6	1250	100	9.9 ± 0.4
850	830	26.5 ± 0.6	1050	900	24.3 ± 0.6	1250	150	12.1 ± 0.5
850	840	25.6 ± 0.6	1050	1030	26.2 ± 0.6	1250	300	18.3 ± 0.5
900	50	6.8 ± 0.4	1050	1040	25.8 ± 0.6	1250	450	21.2 ± 0.6
900	100	9.7 ± 0.4	1100	50	8.2 ± 0.4	1250	600	23.0 ± 0.6
900	150	13.0 ± 0.5	1100	100	9.7 ± 0.4	1250	750	23.6 ± 0.6
900	300	19.6 ± 0.6	1100	150	12.1 ± 0.5	1250	900	25.3 ± 0.6
900	450	22.7 ± 0.6	1100	300	17.7 ± 0.5	1250	1050	23.9 ± 0.6
900	600	24.4 ± 0.6	1100	450	21.5 ± 0.6	1250	1200	26.1 ± 0.6
900	750	24.8 ± 0.6	1100	600	24.2 ± 0.6	1250	1230	25.9 ± 0.6
900	880	26.0 ± 0.6	1100	750	24.2 ± 0.6	1250	1240	25.6 ± 0.6
900	890	27.1 ± 0.6	1100	900	24.7 ± 0.6	1300	50	8.6 ± 0.4
950	50	7.3 ± 0.4	1100	1050	26.1 ± 0.6	1300	100	10.7 ± 0.4
950	100	8.8 ± 0.4	1100	1080	26.6 ± 0.6	1300	150	10.8 ± 0.4
950	150	12.6 ± 0.5	1100	1090	25.9 ± 0.6	1300	300	16.0 ± 0.5
950	300	18.4 ± 0.5	1150	50	9.0 ± 0.4	1300	450	21.4 ± 0.6
950	450	22.9 ± 0.6	1150	100	10.4 ± 0.4	1300	600	23.5 ± 0.6
950	600	23.0 ± 0.6	1150	150	12.2 ± 0.5	1300	750	24.0 ± 0.6
950	750	24.7 ± 0.6	1150	300	17.1 ± 0.5	1300	900	23.8 ± 0.6
950	900	25.5 ± 0.6	1150	450	21.6 ± 0.6	1300	1050	24.2 ± 0.6
950	930	26.8 ± 0.6	1150	600	24.5 ± 0.6	1300	1200	25.8 ± 0.7
950	940	27.3 ± 0.6	1150	750	24.1 ± 0.6	1300	1280	26.9 ± 0.6
1000	50	7.3 ± 0.4	1150	900	25.3 ± 0.6	1300	1290	27.1 ± 0.6

Table A.10: The acceptance of signal region C, including the error due to limited Monte Carlo statistics, for each GGM grid point with squark production. Other systematics are not included.

A.2 SPS8 Signal Samples

This section collects detailed information about the SPS8 signal samples. Λ, the only free SPS8 model parameter and the corresponding cross sections are listed in Table A.11. The other minimal GMSB model parameters are fixed to $M_{\texttt{mess}} = 2 \times \Lambda$, $N_{\texttt{mess}} = 1$, $\tan\beta = 15$, $\mathrm{sgn}\mu = 1$ and $c\tau_{\mathrm{NLSP}} < 0.1\,\mathrm{mm}$.

Table A.12 shows the full SUSY mass spectrum for an example point of $\Lambda = 140\,\mathrm{TeV}$.

Λ TeV	Cross Section (LO) [pb]
50	15.6
60	5.53
70	2.25
80	1.03
90	0.528
100	0.288
110	0.166
120	0.103
130	64.7×10^{-3}
140	43.2×10^{-3}
150	29.8×10^{-3}
160	20.8×10^{-3}
170	14.7×10^{-3}
180	10.6×10^{-3}
190	7.75×10^{-3}
200	5.70×10^{-3}
210	4.27×10^{-3}
220	3.19×10^{-3}
230	2.41×10^{-3}
240	1.82×10^{-3}
250	1.39×10^{-3}

Table A.11: The LO cross sections for SPS8 from HERWIG++ as a function of Λ in TeV.

Sparticle	Mass Eigenstates	M [GeV]
squarks	$\tilde{u}_L$	1528.0
	$\tilde{u}_R$	1461.9
	$\tilde{d}_L$	1530.1
	$\tilde{d}_R$	1455.9
	$\tilde{s}_L$	1530.1
	$\tilde{s}_R$	1455.9
	$\tilde{c}_L$	1528.0
	$\tilde{c}_R$	1461.9
	$\tilde{t}_1$	1332.3
	$\tilde{t}_2$	1485.1
	$\tilde{b}_1$	1446.6
	$\tilde{b}_2$	1472.4
sleptons	$\tilde{e}_L$	498.8
	$\tilde{e}_R$	243.3
	$\tilde{\mu}_L$	498.8
	$\tilde{\mu}_R$	243.3
	$\tilde{\tau}_1$	242.8
	$\tilde{\tau}_2$	497.0
sneutrinos	$\tilde{\nu}_e$	489.2
	$\tilde{\nu}_\mu$	489.2
	$\tilde{\nu}_\tau$	486.4
neutralinos	$\tilde{\chi}_1^0$	197.6
	$\tilde{\chi}_2^0$	376.1
	$\tilde{\chi}_3^0$	555.6
	$\tilde{\chi}_4^0$	573.8
charginos	$\chi_1^\pm$	376.6
	$\chi_2^\pm$	573.6
gluino	$\tilde{g}$	1133.9
gravitino	$\tilde{G}$	9.4×10^{-9}
Higgs bosons	$\tilde{h}^0$	114.6
	$\tilde{H}^0$	724.9
	$\tilde{A}^0$	720.0
	$\tilde{H}^\pm$	729.2

Table A.12: SUSY particle mass spectrum for the SPS8 model which is characterized by the free model parameter $\Lambda = 140\,\text{TeV}$.

A.2.1 SPS8 Production Processes

The breakdown of the various processes, as taken from Prospino, in the production of the $\Lambda = 200\,\text{GeV}$ point at $\sqrt{s} = 7\,\text{TeV}$ can be seen in Tables A.13 and A.14. The breakdown at LO and NLO of all possible production processes is included in Table A.13. In Table A.14 the fractions of the total neutralino/chargino production that are due to various sub-processes is shown. A similar breakdown can be seen for the $\Lambda = 140\,\text{GeV}$ point in Tables A.15 and A.16.

Prospino Process	Fraction at LO	Fraction at NLO
nn	0.906	0.897
ll	0.083	0.084
ng	0.0056	0.0050
sg	0.0019	0.0061
ns	0.0015	0.0020
ss	0.0010	0.0010
gg	0.0007	0.0051
sb	1.4×10^{-5}	4.5×10^{-5}
tb	3.8×10^{-6}	2.1×10^{-5}
bb	5.7×10^{-7}	4.3×10^{-6}

Table A.13: The breakdown of the various processes in the production of the $\Lambda = 200\,\text{GeV}$ point at $\sqrt{s} = 7\,\text{TeV}$ for LO and NLO as taken from Prospino.

Production Process	Fraction at LO	Fraction at NLO
$\tilde{\chi}_1^0\tilde{\chi}_1^\pm$	0.002	0.002
$\tilde{\chi}_1^+\tilde{\chi}_1^-$	0.277	0.288
$\tilde{\chi}_2^0\tilde{\chi}_1^0$	0.0002	0.0002
$\tilde{\chi}_2^0\tilde{\chi}_1^\pm$	0.624	0.616
$\tilde{\chi}_2^0\tilde{\chi}_2^0$	0.002	0.002
Others processes	0.095	0.092

Table A.14: The breakdown of the various neutralino/chargino production processes of the $\Lambda = 200\,\text{GeV}$ point at $\sqrt{s} = 7\,\text{TeV}$ for LO and NLO as taken from Prospino.

Prospino Process	Fraction at LO	Fraction at NLO
nn	0.850	0.794
ll	0.068	0.063
ng	0.016	0.013
sg	0.031	0.065
ns	0.006	0.006
ss	0.019	0.018
gg	0.009	0.038
sb	0.001	0.002
tb	0.0001	0.0003
bb	3.6×10^{-5}	9.4×10^{-5}

Table A.15: The breakdown of the various processes in the production of the $\Lambda = 140\,\text{GeV}$ point at $\sqrt{s} = 7\,\text{TeV}$ for LO and NLO as taken from Prospino.

Production Process	Fraction at LO	Fraction at NLO
$\tilde{\chi}_1^0\tilde{\chi}_1^\pm$	0.003	0.003
$\tilde{\chi}_1^+\tilde{\chi}_1^-$	0.286	0.291
$\tilde{\chi}_2^0\tilde{\chi}_1^0$	0.0001	0.0002
$\tilde{\chi}_2^0\tilde{\chi}_1^\pm$	0.612	0.610
$\tilde{\chi}_2^0\tilde{\chi}_2^0$	0.002	0.002
Others processes	0.096	0.093

Table A.16: The breakdown of the various neutralino/chargino production processes of the $\Lambda = 140\,\text{GeV}$ point at $\sqrt{s} = 7\,\text{TeV}$ for LO and NLO as taken from Prospino.

A.2.2 SPS8 Signal Acceptances

The acceptances of the cuts defining the three signal regions from Section 9.4 for the SPS8 Monte Carlo signal points are shown in this section. These acceptances are given in Table A.17. The uncertainties shown in this table are those due to the limited MC statistics. Visual representations of these numbers can be seen in the main body of the document in Section 9.4.1.

	Acceptance [%]		
Λ [TeV]	SR A	SR B	SR C
50	0.1 ± 0.0	0.3 ± 0.1	0.8 ± 0.1
60	0.5 ± 0.1	1.3 ± 0.1	1.5 ± 0.1
70	0.7 ± 0.1	2.4 ± 0.2	2.4 ± 0.2
80	1.1 ± 0.1	3.1 ± 0.2	3.3 ± 0.2
90	1.1 ± 0.1	3.3 ± 0.2	4.3 ± 0.2
100	1.2 ± 0.1	3.2 ± 0.2	5.9 ± 0.2
110	1.3 ± 0.1	2.8 ± 0.2	7.7 ± 0.3
120	1.5 ± 0.1	2.1 ± 0.1	9.4 ± 0.3
130	2.1 ± 0.1	2.0 ± 0.1	11.8 ± 0.3
140	1.9 ± 0.1	1.7 ± 0.1	13.1 ± 0.3
150	2.6 ± 0.2	1.4 ± 0.1	14.5 ± 0.4
160	3.5 ± 0.2	1.4 ± 0.1	16.0 ± 0.4
170	4.5 ± 0.2	1.2 ± 0.1	16.8 ± 0.4
180	5.4 ± 0.2	1.5 ± 0.1	17.8 ± 0.4
190	6.7 ± 0.3	1.6 ± 0.1	18.7 ± 0.4
200	7.7 ± 0.3	1.9 ± 0.1	19.7 ± 0.4
210	9.2 ± 0.3	2.4 ± 0.2	20.2 ± 0.4
220	9.4 ± 0.3	2.5 ± 0.2	20.5 ± 0.4
230	11.8 ± 0.3	3.2 ± 0.2	21.6 ± 0.4
240	12.2 ± 0.3	3.4 ± 0.2	21.7 ± 0.4
250	13.1 ± 0.3	4.1 ± 0.2	21.5 ± 0.4

Table A.17: The acceptances of signal region A, B, and C, including the error due to limited Monte Carlo statistics, for each SPS8 signal point. Other systematics are not included.

Appendix B

Scale Factor Equation Derivation

This appendix highlights the derivation of Eq. 10.1, which is that of the electron-to-photon scale factor, from Chapter 10. This is a condensed version of the derivation found in the supporting note for this analysis [96], which is placed in this document merely because that note is not publicly viewable to those outside of the ATLAS Collaboration. Starting from N_z, the true number of $Z \to ee$ events where m_{ee} is within the chosen mass window and ϵ_e, the efficiency with which a true electron passes the chosen identification criteria, the number of selected electron-electron events from the $Z \to ee$ decay is given by Eq. B.1.

$$N_{ee} = \epsilon_e \epsilon_e N_z \tag{B.1}$$

Let $P_{e\to\gamma}$ be the probability for a true electron to be reconstructed as a photon passing the chosen identification criteria. From this the following expressions can be

derived:

$$N_{\gamma e} = \epsilon_e P_{e\to\gamma} N_z \quad (E_T^\gamma > E_T^e) \tag{B.2}$$

$$N_{e\gamma} = \epsilon_e P_{e\to\gamma} N_z \quad (E_T^\gamma < E_T^e) \tag{B.3}$$

Combining Eq. B.2 with Eq. B.3 and then substituting in Eq. B.1 yields:

$$N_{\gamma e} + N_{e\gamma} = 2\epsilon_e P_{e\to\gamma} N_z = 2P_{e\to\gamma}\frac{N_{ee}}{\epsilon_e} \tag{B.4}$$

From Eq. B.4 the probability of a true electron to be reconstructed as a photon passing the selection criteria is:

$$P_{e\to\gamma} = \epsilon_e \left(\frac{N_{\gamma e} + N_{e\gamma}}{2N_{ee}}\right) \tag{B.5}$$

The next step is to transform this into a scale factor that relates the number of observed electron-photon events to the number of events of that type which are expected to be observed as photon-photon events. Let N_W be the number of events with a true electron. Also let ϵ_γ be the fraction of those events where an observed photon, which is not from the truth electron, passes the chosen selection criteria. The number of observed electron-photon events is then given by:

$$N_{e\gamma}^{\text{obs}} = \epsilon_e \epsilon_\gamma N_W \tag{B.6}$$

The observed number of photon-photon events coming from N_W is given by:

$$N_{\gamma\gamma}^{\text{obs}} = P_{e\to\gamma}\epsilon_\gamma N_W = \frac{P_{e\to\gamma}}{\epsilon_e} N_{e\gamma}^{\text{obs}} \tag{B.7}$$

Substituting in the expression for $P_{e\to\gamma}$ from Eq. B.5 into Eq. B.7 leads to:

$$N_{\gamma\gamma}^{\text{obs}} = \left(\frac{N_{\gamma e} + N_{e\gamma}}{2N_{ee}}\right) N_{e\gamma}^{\text{obs}} \tag{B.8}$$

The scale factor relating the number of observed electron-photon events to the expected number of photon-photon events is then simply:

$$f = \frac{N_{\gamma e} + N_{e\gamma}}{2N_{ee}} \tag{B.9}$$